Sarina Bao

Filtration of Aluminium-Experiments, Wetting, and Modelling

Thesis for the degree of Philosophiae Doctor

Trondheim, October 2011

Norwegian University of Science and Technology
Faculty of Natural Sciences and Technology
Department of Materials Science and Engineering

NTNU – Trondheim
Norwegian University of
Science and Technology

NTNU
Norwegian University of Science and Technology

Thesis for the degree of Philosophiae Doctor

Faculty of Natural Sciences and Technology
Department of Materials Science and Engineering

ISBN 978-82-471-3175-6 (printed ver.)
ISBN 978-82-471-3176-3 (electronic ver.)
ISSN 1503-8181

Doctoral thesis at NTNU, 2011:301
IMT-Report 2011:142

Printed in Norway by NTNU-trykk

Preface

This thesis is submitted to the Norwegian University of Science and Technology (NTNU) for partial fulfilment of the requirements for the degree of philosophiae doctor.

This doctoral work has been performed at the Department of Material Science and Engineering, Norwegian University of Science and Technology (NTNU), Trondheim, with Merete Tangstad as main supervisor and with co-supervisor Thorvald Abel Engh.

This research was carried out as a part of the Norwegian Research Council (NRC) funded BIP Project (No.179947/I40) RIRA (Remelting and Inclusion Refining of Aluminium). It includes the partners: Hydro Aluminium AS, SAPA Heat Transfer AB, Alcoa Norway ANS, NTNU and SINTEF.

Acknowledgements

I am deeply grateful to my main supervisor Prof. Merete Tangstad. From 2008, when I became her student, to this day she has believed in me and my work. She gave me freedom to explore the challenges in process metallurgy, providing guidance whenever it was necessary. I would like to acknowledge her great patience and support. She pays a lot care on her students, and lets us enjoy and learn in the SiMnTiAl group.

I am greatly thankful to my co-supervisor Prof. Thorvald Engh for successful guidance, useful suggestions and fruitful discussions. I would like to profoundly thank him for his guidance in problems and help to overcome the challenges. Thanks are also for his work during holidays in Spain and reading my thesis in the cottage on the coast.

Prof. Lifeng Zhang is acknowledged for introducing me into this field and guiding me with the literature survey.

I am very grateful for the open environment at NTNU/SINTEF. I would like to acknowledge Dr. Anne Kvithyld in SINTEF for giving me huge support on wetting trials and preparation of plant experiments. I learned a lot from her, not only research work, but also the social part.

Particular recognition is deserved by Dr. Martin Syvertsen in SINTEF for fruitful discussion and his support in plant experiments. It was a very happy experience working with him.

I also like to give special thanks to Kai Tang in SINTEF, who guided me in the contact angle extrapolation.

Members in RIRA project are acknowledged for fruitful suggestions and discussion during this work. I would like to thank Dr. Bjørn Rasch at Hydro Sunndalsøra, for support and help in arranging the industrial experiments in Sunndalsøra. Dr. Mark Badowski in Hydro Bonn is thanked for discussions and teaching concerning inclusion measurement methods.

Drache GmbH is acknowledged for its supply of ceramic foam filters.

Thanks are also given to Tone Anzjøn for assisting in the sessile drop tests and Jan Arve Baatnes and Pål Ulseth for always being available.

Many thanks go to all friends in the SiMnTiAl family. I will always remember the delightful moments we shared together.

Last but not the least, I am very grateful and obliged to my parents and siblings. They are my inspiration to achieve. Thanks are also given to my dear Lufeng for encouraging me all the time.

Summary

The present work deals with the inclusion removal mechanism in aluminium filtration and the use of alternative filter materials. Four routes are investigated.

First, an overview of previous research on filtration knowledge is summarized. The filtration mechanism comprises two parts: transport of inclusions to the filter wall and attachment of inclusions on the wall. We have mainly investigated collision by interception and the wetting (surface tension) of inclusion-Al and Al-filter in this work.

Second, the wetting behaviour of inclusion-Al and Al-filter is measured in the laboratory.

In filtration it is important that particles to be removed contact, or come close to the filter walls. Therefore the metal carrying the inclusions must come into close contact, i.e. wet the filter material. A systematic and comprehensive investigation of the wetting behaviour in the molten aluminium-filter system is presented. In aluminium filtration, alumina is the most common filter material, even though alumina is not wetted by aluminium. Therefore we have investigated the use of alternative filter materials with improved wetting. In the laboratory, SiC and graphite demonstrate good wetting by molten aluminium. Problems with these materials exist, as SiC is easily oxidized to SiO_2 and both react with aluminium to give Al_4C_3. However, SiO_2 and SiC react slowly with aluminium, but this does not seem to influence the wetting.

The wettability of the inclusion-Al may play a key role in aluminium filtration. Particles to be removed should ideally have poor wetting with aluminium and filter should has good wetting with aluminium. A challenge is that SiC and Al_4C_3 inclusions show better wetting with aluminium than alumina.

Third, plant scale filtration experiments were carried out with Al_2O_3 and SiC industrial filters. Metal composition was not changed by the industrial filters. Improved wetting of aluminium on filter materials is an advantage in getting molten metal to infiltrate filters and thus to improve the filtration efficiency. A SiC filter gives better filtration efficiency. Filtration efficiency increases with particle size. SiC reacts with aluminium so slowly that no carbide inclusions were produced in the industrial SiC filter with approximately 60% of SiC. SiC filters have better wetting than Al_2O_3 filters with aluminium. Thus SiC could be a good alternative filter material.

Fourth, a theoretical model is developed regarding the interceptional and gravitational collision considering the filter as a collection of branches (cylinders). A filtration efficiency equation is derived based on particle diameter, branch diameter, porosity, filter thickness, filter specific surface area, and Reynolds number.

The filtration efficiency decreases with the flow rate until it reaches a minimum, and then increases. Gravitational collision must be taken into account at the lower flow rates. The greater the velocity the less time particles have to settle. Thus gravitational collision efficiency decays with increasing flow rate. The interceptional collision efficiency increases with the velocity since then more liquid and particles come into

contact with the collector. The interceptional collision efficiency that dominates at high velocities is the main topic of the model.

Contents

List of Symbols

a	The inclusion area fraction	
A	The cross section area of the control volume in direction z	m^2
A	The constant in Equ.(5.11)	
A_P	The projected area of the particle in the flow direction	m^2
A_r	The mean measured residue area	mm^2
a_s	The surface area per unit volume of melt	m^{-1}
A_x	The filter cross section area	m^2
b	Ratio between projected area in the flow direction and the surface area, i.e. b=1/4 for spherical collectors.	
b	The curvature radius at the drop apex	m
B	The magnetic flux density vector	
c or c(z)	The particle concentration (at z direction)	$\#/m^3$
C	The drag coefficient which depends on the shape of the body and the wall effects	
c_{in}	The inclusion concentrations at the inlet	$\#/m^3$
c_{out}	The inclusion concentrations at the outlet	$\#/m^3$
C_v	Vitreous carbon, which is a graphitic although imperfectly crystallized form of carbon [1]	
c_∞	The particle concentration far from the collector	$\#/m^3$
D	Sessile drop base diameter	m
d_c	Pore diameter	m
d_{pore}	The filter pore diameter	m
d_s	A structural parameter, the strut diameter in the models	m
d_w	The average diameter of the filter web	m
d_{win}	The average diameter of the filter window	m
E	The filtration efficiency	
E_f	Inclusion removal efficiency by flotation	
E_0	The initial filtration efficiency	
f	The friction coefficient	
$f_1, f_3, f_5, f_7 \ldots$	The function of λ or y, see Appendix A.	
F_d	The drag force on the particle	N
F_g	The gravity force acting on the particle	N
F_A	The adhesion force	N
F_f	The viscous drag exerted by the fluid	N
F_l	The electromagnetic force acting on a unit volume of melt	N/m^3
F_{LV}	Total free energy of the liquid-vapour system	J
F_P	The electromagnetic force acting on particle	N
F_{SV}	Total free energy of the solid-vapour system	J
g	The acceleration due to gravity, 9.18	m/s^2
G	The gravity [2]	N
G_m	Specific gas sparging rate, volume flow rate gas per	m^3/kg

	unit mass treatment zone	
ΔG	Gibbs free energy	J/m^2
H	The potential energy of an atom in bulk	J
H	The height of sessile drop	m
H`	The potential energy of an atom at the surface	J
i	Element	
j	The current density	A/m^2
k	The Boltzmann constant	
K	The cohesion force	N
K	The constant in Equ.(3.14)	
K	A factor, see Equ.(5.31)	
k_t	The mass transfer coefficient for deposition	m/s
k_1	Darcian permeability	m^2
k_2	Non-Darcian permeability	m
l	The characteristic length of the foam structure	m
L	The filter thickness	m
L_c	The length of the cylinder	m
L_m	The measured chord length	mm
L_n	The nominal chord length	mm
m	Total number of elements	
M	The filtrated metal mass	kg
m_{Al2O}	The mass of a molecule of Al_2O	kg
m_d	The liquid drop mass	kg
m_{O2}	The mass of a molecule of O_2	kg
n	Exponent of $R^n \sim t$	
n_o	The number of particles in unit volume of fluid	$\#/m^3$
N_G	The gravity number, see Equ.(2.16)	
n_i	The number of moles of component i	mol
N_R	Relative size number, $N_R = R_p / R$	
P_{Al2O}^{eq}	The equilibrium vapour pressure of Al_2O in reaction (2.42)	Pa
P_{O2}^{w}	The oxygen partial pressure in chamber	Pa
ΔP	The pressure drop across the filter	Pa
q	The adhesion efficiency	
Q	The volumetric flow rate	m^3/s
Q_m	The mass flow rate	ton/h
r	The distance between the particle and the axis of rotation Polar coordinate, r=R+y	m
R	The surface roughness factor	
R	Sessile drop base radius	m
R	The cylinder radius	m
R^2	The correlation coefficient of the curve fitting	
R`	The cylinder radius considering the coating, $R=R'+2.5\times10^{-3}$ m in Palmer's case [3]	m
r_b	Bubble equivalent radius	m
R_0	The initial sessile drop base radius	m

Re	Reynolds number	
Re_c	Reynolds number for a cylinder	
Re_c`	The Reynolds number for a cylinder considering the coating	
Re_f	Reynolds number of a filter	
Re_p	Reynolds number of a particle	
Re_{pore}	Reynolds number of a pore	
R_p	The particle/inclusion radius	m
s	Interface area	m^2
S^σ	Entropy of interface	J/K
t	The time	s
T	Temperature	K
T_{cs}	The critical temperature for spreading, i.e. the temperature at which contact angle approaches zero.	K
t_d	The de-oxidation time of oxide film on aluminium drop	s
T.[inclusion]	The total inclusion	mm^2/kg
T_{liq}	The aluminium drop temperature	K
T_w	The chamber wall temperature	K
T*	A threshold temperature, below which the oxide film thickens and above which it is eroded.	K
u_i	The chemical potential of element i	J/mol
u_τ	The shear velocity in the boundary layer	m/s
U_1,U_3, U_5,U_7….	The fluid flux coefficients, depend only on the shape of the body	
U_d	The turbulent deposition rate for a smooth surface	m/s
U_r	The fluid velocity in the radial direction	m/s
U_s	The relative velocity of particle and metal	m/s
U_θ	The fluid velocity along the cylinder	m/s
U_∞	The approach or superfial velocity of the fluid	m/s
v	The drop volume	m^3
V	The volume	m^3
V_r	The particle velocity in the radial direction	m/s
V_θ	The particle velocity along the cylinder	m/s
W_a	Work of adhesion	J
W_c, W_c^A	Work of cohesion, cohesion work of phase A	J
x	The distance along cylinder measured from stagnation point and $x=R\theta$	m
y	The normal distance from the cylinder surface	m
z	The starting point of a control volume	m
Δz	The length of the control volume	m

Greek letters

α	The specific cake resistance	m/kg
α	The angle between the flow direction and the gravity	Degree
α_{Al2O}	The evaporation coefficient which takes into account a possible departure from equilibrium (reaction(2.42))	

	at the surface of oxide film on the drop, α_{Al2O} <1.	
β	Parameter in Equ.(2.25)	
β	The angle made by the cylinder with the normal to the flow	Degree
γ_{if}	Interfacial energy of inclusion/ filter surface	J/m^2
γ_{mf}	Interfacial energy of metal/filter surface	J/m^2
γ_{mi}	Interfacial energy of metal/inclusion surface	J/m^2
δd	An element length	m
ε	Filter porosity	%
η	The collision efficiency	%
η_i	The collision efficiency due to interception	
$\eta_{i\text{-}avg}$	Average collision efficiency due to interception	
η_g	The collision efficiency due to gravity	
θ	The polar coordinate	Degree
θ	Contact angle	Degree
θ_a	Advancing contact angle	Degree
θ_c	The collection angle	Degree
θ_{c+}, θ_{c-}	The upper, lower collection angle	Degree
θ_r	Receding contact angle	Degree
θ_t	Instantaneous contact angle with time	Degree
θ_Y	Young contact angle	Degree
θ`	The apparent contact angle on a rough surface	Degree
φ	The angle between the gravity and the tangent line of the cylinder	Degree
λ	The filtration coefficient or the probability of retention	m^{-1}
λ_0	The initial filtration coefficient	m^{-1}
μ	The fluid dynamic viscosity	kg/(m·s)
μ_s	The viscosity of suspension	m^2/s
ν	The kinematic viscosity	m^2/s
ρ	The density	kg/m^3
ρ_l	The density of the liquid metal	$kg{\cdot}m^{-3}$
ρ_p	The density of the particle	$kg{\cdot}m^{-3}$
$\Delta\rho$	Density difference between inclusion and melt	kg/m^3
ψ	The fluid flux	
ξ	The dimensionless surface vorticity at the collection angle	
σ	The solid inclusion mass captured per unit filtrate volume	kg/m^3
σ	The surface tension or the interfacial tension	J/m^2
σ_{inter}	The interface surface energy	J/m^2
σ_l	Electrical conductivity of melt	S/m
σ_p	Electrical conductivity of particle	S/m
σ_{LV}	The liquid/vapour surface energy	J/m^2
σ_{SL}	The solid/liquid surface energy	J/m^2
σ_{SV}	The solid/vapour surface energy	J/m^2
τ	A characteristic time factor in Equ.(3.11)	

τ	The frictional shearing stress	N/m^2
Φ	The angle in Figure 2.33	degree
Φ_o^{ev}	The flow of oxygen resulting from all evaporation process	
Φ_o^{i}	The impinging flow of oxygen	
ω	The surface area per atom	m^2
ω	The rotational velocity	radian/s
Ω	The surface area	m^2
Ω_m	The molar surface area of the oxide	m^2
Γ_i	Mole of element i on a unit interface area	mol

Chapter 1 INTRODUCTION

1.1 Research Motivation

Due to the continuously increasing energy prices in Europe and globally, the importance of recycling of aluminium is increasing. Representing a value of about 2.7 billions NOK annually, aluminium cast house products are of primary importance for the Norwegian industry and national economy. During the last decade the aluminium industry has changed to a global industry with increasing competition from other materials, and increasing demands on quality and price. The Far East, with low cost countries, such as China, India, Indonesia is able to compete, in spite of the substantial transportation cost, with the European aluminium industry. In addition, production of cast house products is a big industry in Russia (RusAl), and as soon as they solve the logistic challenges they will overload the European market with standard Al cast house products. This means that within a few years, standard products in aluminium will be produced in these low-cost countries.

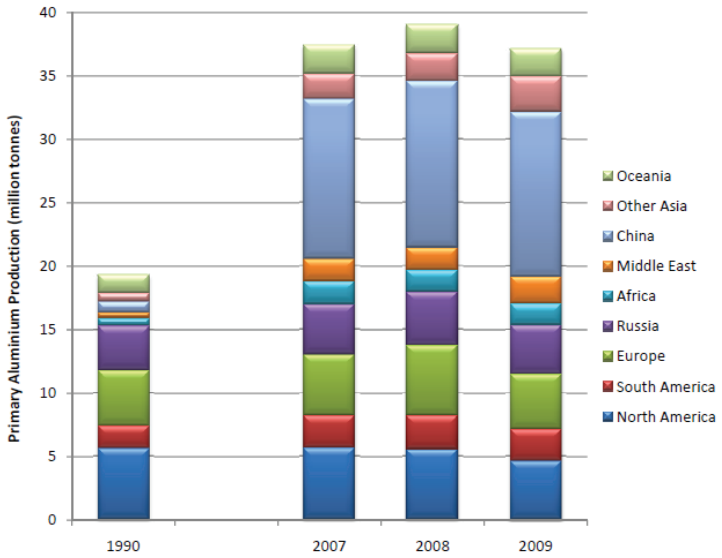

Figure 1.1 Geographical location of primary Al production, 1990 & 2007-2009 [4]

To meet these future demands it is evident that not only the efficiency of the refining technologies has to be improved, but also the remelting/recycling technology must improve regarding contaminant introduction and removal to keep the load on the refining equipment on an acceptable level.

Various refining techniques have to be applied in order to remove inclusions from molten aluminium before casting. Examples of conventionally used, or more novel methods are: gravity sedimentation, gas flotation, centrifugal separation, filtration, and electromagnetic separation. Gravity sedimentation methods are limited to large size inclusions. This is also the case for gas flotation and centrifugal separation. These methods are not effective for small inclusions and/or small difference in density between particle and metal. Thus the most feasible method to remove inclusions from aluminium is filtration.

Figure 1.2 illustrates a general flow sheet for primary and secondary aluminium processing. Not every refining facility uses all the five steps shown here. For example, a melting furnace and the casting furnace are the same unit at some cases. Metal from the casting furnace goes through the refining unit, e.g. degasser and filter, and is finally transported to casting. Filters work as a crucial step to remove inclusions, bubbles, and even dissolved elements.

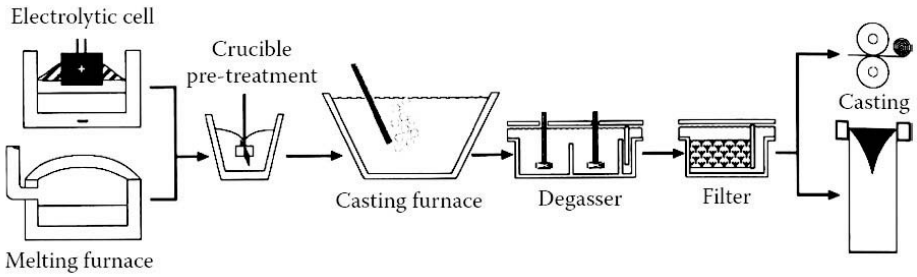

Figure 1.2 Flow sheet for Al melting and refining [5]

The main goal of this thesis is to study the fundamentals of removing inclusions by filtration and to investigate the characteristics of several filter materials. Inclusions in aluminium have to go through two steps to be captured by the filter. First, particles must be transported to the surface of the filter wall according to mechanisms such as interception, gravity, hydrodynamic effects, inertial impaction, and diffusion etc. Second, once transported, particles have to adhere to the filter wall by various forces, such as Van der Waals, hydrodynamic, surface tension (wetting), electrostatic etc. This thesis deals with the transport mechanism- interceptional and gravitation collision and adhesion mechanism- wetting of Al-filter and Al- inclusion in filtration. Meanwhile, we hope to investigate alternative filter materials from the view point of filtration efficiency and wettability.

1.2 Outline of Thesis

The main purpose of this thesis is to understand the aluminium filtration mechanisms and to study the use of possible alternative filter materials.

The chapters in this thesis are (see Figure 1.3):

Chapter 2 summarizes work from the literature which includes: 1) inclusion removal from molten aluminium- focusing on filtration and 2) wetting of aluminium on ceramics.

Chapter 3 contains the wetting experimental results for the Al-Al_2O_3, Al-SiC, and Al-graphite systems. The wetting behaviour of Al-filter and Al-inclusions is investigated, which include SiC, as an alternative choice for filter materials.

Chapter 4 gives plant experimental results using Al_2O_3 and SiC industrial filters.

Chapter 5 investigates with particle collision on a single cylinder, as a basis for the branch model.

Chapter 6 presents the theory of removal of particles in ceramic foam filters, treating the ceramic foam as a collection of branches (or cylinders).

Chapter 7 discusses the results from wetting experiments, filtration experiments compared with the branch model.

Chapter 8 states the main conclusions and proposes future work.

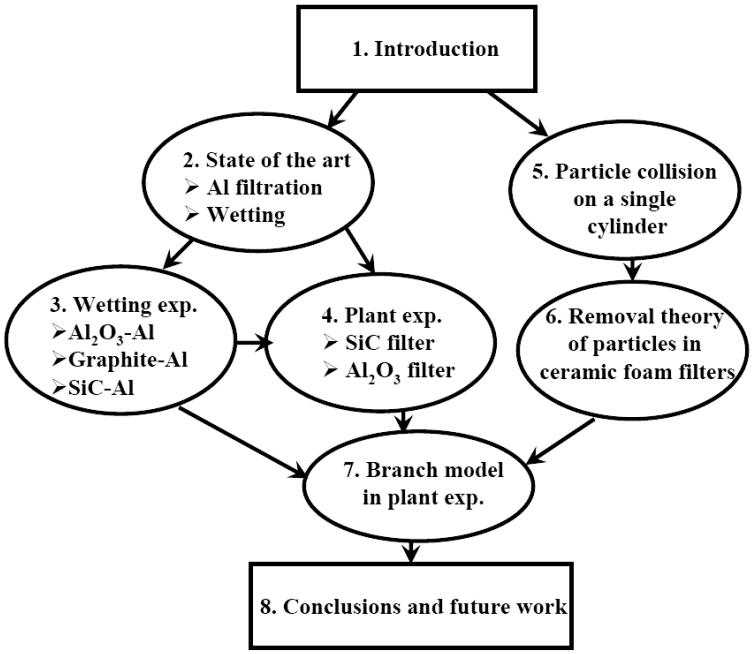

Figure 1.3 Outline of thesis

Chapter 2 STATE OF THE ART

2.1 Inclusion Removal from Molten Aluminium – Focusing on Filtration

2.1.1 Inclusions in Aluminium

Much time has transpired since Hans Oerstad of Denmark chemically isolated aluminium from aluminium chloride in 1825, and Charles Martin Hall and Paul Heroult (1886) invented the process of producing pure aluminium by passing an electric current through a mixture of aluminium oxide dissolved in molten cryolite [6]. During the last 50 years, aluminium has evolved into one of the most important materials; it is used in a variety of diverse applications-construction, automotive, aerospace, packaging, furniture, jewelry and a vast number of products, which once were made from ferrous or other materials. Specifically, during the last few years, we have seen significant increases in the production of aluminium. See Figure 2.1.

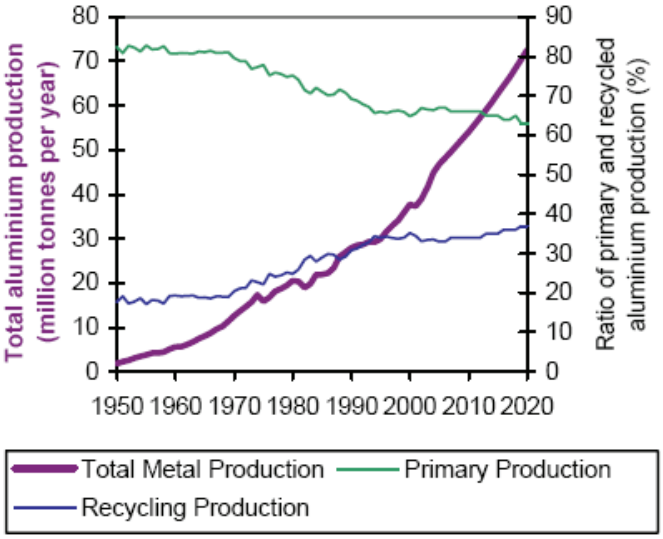

Figure 2.1 Reported and predicted world Al production [7]

The factors that influence the behaviour of aluminium can be classified in three groups: trace elements in the melt (such as alkali elements in aluminium), dissolved gases (hydrogen in aluminium), and non-metallic inclusions [8, 9].

Treatment methods of molten aluminium for removal of impurities are given in Table 2.1. The operations utilized for the removal of trace elements and hydrogen commonly employs inert- reactive gas sparging in batch devices, or in continuous reactors.

Inclusions have long been recognized as a problem in molten aluminium. The presence of microscopic inclusions, on the order of 10 to 50 μm in size, in aluminium alloys can lead to poor surface finish, increased internal porosity, and a tendency to increased corrosion. Non-metallic inclusions act as stress-raisers, and can cause premature failure of components. The size, shape, type, and distribution of non-metallic inclusions in a finished metal product are considered the performance fingerprints in a casting shop [8]. The presence of non-metallic inclusion in aluminium may destroy the continuity of the matrix, provide the nuclei for fatigue cracks, reduce mechanical properties, promote porosity formation, form hard spots and lead to very poor machinability. Moreover, it is also the main limiting factor to effective degassing due to the interaction between the inclusions and the dissolved hydrogen [10]. The detrimental effects of inclusions are summarized in Figure 2.2.

Table 2.1 Treatment of molten Al [11]

Refining	Target
Settling	Removal of particles
Gas purging	Removal of hydrogen and oxides
(N_2,Ar, Cl_2)	Flotation of solid inclusions
Chlorination	Removal of alkali metals
(Salt treatment, ‘solid’ Cl)	Flotation of inclusions
Filtration	Removal of inclusions
Slag treatment	Removal of inclusions
Vacuum treatment	Removal of Mg, Zn and Pb
Addition of primary Al	Dilution of impurities
Addition of alloys for Al	Charge make-up of alloys

There are three forms of inclusions in aluminium: oxide, extraneous particles such as refractory materials, and particles from treatment of molten aluminium. See Figure 2.3. The purification of aluminium alloy melts, before casting, is a necessary step in manufacturing high-quality finished aluminium products. Various kinds of inclusions inherent to the melting and casting process have to be eliminated. For example, indigenous inclusions exist, primarily as alumina or spinel, which result from the oxidation of molten aluminium combined with the presence of alloying agents like Mg. Another example, TiB_2, originates principally from grain refiner added to the melt just prior to casting. Exogenous inclusions must also be removed. These include refractory particles, such as alumina, silica, SiC, etc., which are picked up by the molten aluminium as a result of wear and erosion of the vessel materials used to melt and transport it. In practice, the observed particle size in aluminium melts varies between

inclusion dispersoids of a few microns to oxide skins of several millimeters (See Table 2.2).

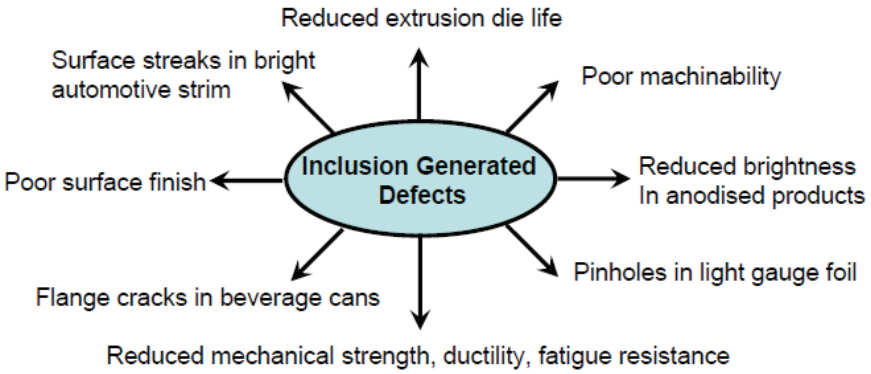

Figure 2.2 Impact of inclusions on final metal quality [12]

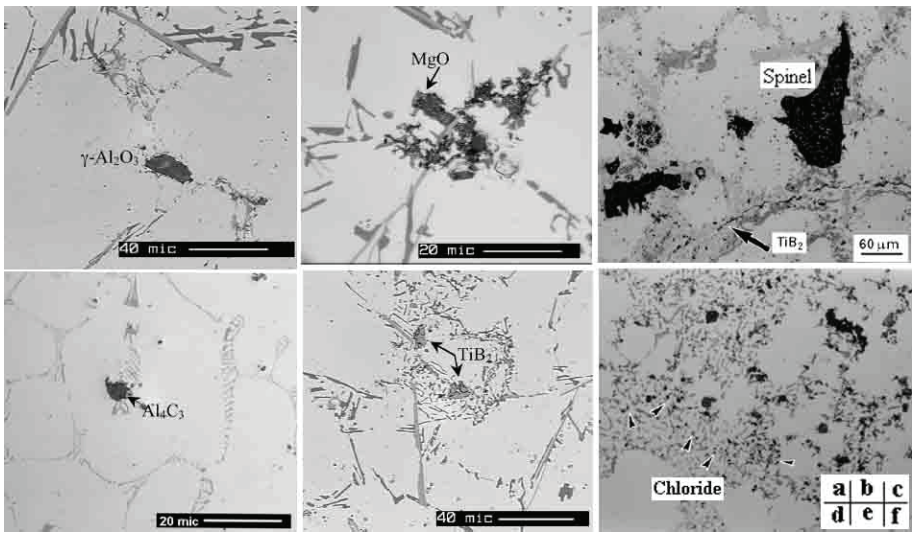

Figure 2.3 Typical inclusions in Al

(a)γ-Al_2O_3[13], (b)MgO[13], (c) $MgAl_2O_4$[14],

(d)Al_4C_3[13], (e) TiB_2[13], (f) Chloride particles[14]

Table 2.2 Inclusions in Al [9, 15-17]

Inclusion Type	Inclusion Shape	Density [g/cm^3]	Dimensions [μm]
Al_2O_3	Particles, films	3.97	0.2-30, 10-5000
MgO	Particles, films	3.58	0.1-5, 10-5000
$MgAl_2O_4$	Particles, films	3.6	0.1-5, 10-5000
Salts chlorides, fluorides	Particles	1.98-2.16	0.1-5
Al_4C_3	Particles	2.36	0.5-25
AlN	Particles, films	3.26	10-50
TiB_2	Particles, agglomerates	4.5	1-30
AlB_2	Particles, agglomerates	3.19	0.1-3

2.1.2 Methods to Remove Inclusions from the Molten Aluminium

There are several methods to remove inclusions from the molten aluminium [18]:

Filtration- molten aluminium and inclusion are separated by porous media;

Sedimentation- particles agglomerate in the bottom of the molten aluminium;

Flotation- inclusions congregate on the surface of the molten aluminium.

With the development of aluminium refining, other removal methods have appeared, such as electromagnetic separation [19] and centrifugal separation.

This section will go into the detail concerning filtration and briefly introduce the features of the remaining methods.

2.1.2.1 Filtration

Filtration – removal of inclusions by porous media has been introduced since the 1950s. Now, filters used in casting aluminium include “2-dimensional” screens, 3-dimentional strainer cores and extruded ceramic filters, and reticulated foam filter/flow modifiers [20].

Among the numerous filter media available for molten aluminium filtration, one can distinguish granular and open-pore structure filters.

Granular filters are of two types: first, bed filters with a filter medium contained within a filter bowl, which generally consists of un-bonded alumina tabs and/ or balls; second, bonded particles filters, which are made up of refractory (ceramic) grains such as Al_2O_3, mullite, silica or other ceramics, forming an assemblage of fritted grains. The grain size usually ranges from 0.7-25mm.

Open pore structure filters [21] are produced by impregnating granular polyurethane foams with ceramic slurry. Subsequent burnout of the organic foam material and firing of the ceramic foams produces a high temperature bond, with a highly porous body, presenting an open-cell structure nearly equivalent to the inverse replica of a granular structure. These ceramic foams are available with different pore sizes (nominally 20-55 pores per linear inch), which usually range from 3.0-0.6 mm.

Ceramic foam filter (CFF) appeared in late 1970s and early 1980s. Now, it is one of the best filtration technologies, which greatly improves mechanical properties of aluminium [17]. Multilayer net, pore, and tortuous channels on the CFF will remove inclusions by interception and gravity mechanisms. Inclusions become retained on the filter surface as the metal stream continues through the filter into the mould [22].

CFF operates in a mode of deep bed filtration where inclusions smaller than the pore openings are retained throughout the filter. They differ from strainers, which often only retain inclusions larger than the strainer holes. Deep bed filtration forces the molten metal to flow through a tortuous path, which allows more opportunities for inclusions to come in contact with and be retained by filter filaments.

The foam filter also minimizes turbulence and prevents entrained air from passing through. See Figure 2.4.

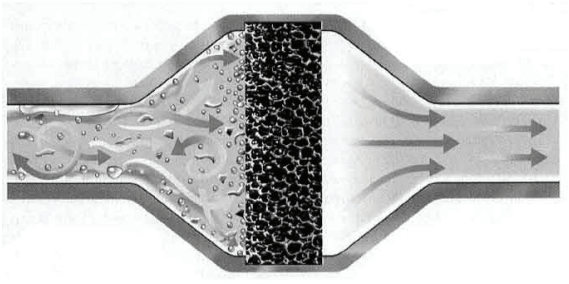

Figure 2.4 Effect of foam filter on a flow [23]

Depth filtration of molten aluminium may be governed by at least seven factors [15]:

- Texture of the porous medium, pore size distribution, and filter porosity
- Filter thickness
- Viscosity of molten metal
- Particle size distribution
- Particle density
- Flow rate through the porous medium,
- Interfacial properties between inclusions, metal, and the filter

In the late 1970, J.E. Dore [24] stated that the CFF has a number of advantages over other "in-line" filtration processes.

1. It can be incorporated in most molten metal transfer systems without major design changes, and floor space requirement are at a minimum.
2. Capital cost is substantially lower. The filter chamber is merely a steel shell with a suitable refractory lining. No special burners are required.
3. It is simple and easy to operate because it is a "one shot" disposable filter. Liquid metal does not need to be maintained in the filter chamber between casts.
4. All of the metal which passes through the filter is usable. There is no butt defect as in the case of 5252 alloy processed through the tabular alumina bed filter.
5. Operating costs are low. Indications are that the operating costs of the CFF are 30 to 75% lower than those of other in-line filtration and filtration/degassing processes.

6. Operating flexibility is improved. The same transfer system can be used to provide either filtered or unfiltered melts by merely installing or not installing a filter element.
7. It is virtually tamper proof. The operator can not channel a CFF by rabbling. Either the filter is intact or broken, and its condition is easily discernable.
8. Energy consumption is low. The filter and the filter chamber do not have to be maintained at melt temperature all of the time. In addition, the filter and filter chamber are much smaller and have a relatively low thermal mass.
9. Operator acceptance is excellent. Hourly personnel like the CFF because it eliminates such hot dirty jobs as bed rejuvenation, change of crucibles, etc.

Today the process of aluminium production includes melting, metal treatment, transfer, filtration and casting. The CFF is not a magic elixir that can overcome lack of care in other operations. The following aspects [25] are very important during the filtration operation:

- Selection of the proper filter
- Filter bowl design
- Filter gasket
- Installing the filter
- Filter and bowl pre-heating
- Priming the filter
- Stable filter operation
- Melt sampling
- Post filtration
- Cleanup

2.1.2.2 Sedimentation

Inclusions moving in the gravitational field due to the density difference between inclusions and melt are said to be removed by sedimentation or settling. A single particle in a quiescent liquid will sink with a velocity given by a balance between buoyant forces and drag forces. The stokes' velocity [26] is

$$U_S^2 = \frac{4(\rho_p - \rho_l)gR_P}{3\rho_l C} \tag{2.1}$$

Non-spherical particles or suspensions of particles will settle more slowly due to increased drag forces. Close to surfaces the settling velocity will be reduced due to wall effects [27].

Gravity sedimentation methods are usually limited to inclusion sizes greater than 100 μm, due to high drag forces and low particle terminal velocities [9]. Sedimentation is performed by long time furnace treatment [16].

2.1.2.3 Gas bubbling and bubble flotation

Bubble flotation is usually used for removal of hydrogen [28], alkaline metals [29], and inclusions. Dissolved gas, such as hydrogen is removed from the molten aluminium due to the different partial pressure of dissolved hydrogen in the melt and partial pressure in the inert gas bubble.

Particle flotation is found to be a result of two elementary capture operations: inertial impaction and interception. Inertial impaction occurs when the inertia of an inclusion particle exceeds that of a local fluid volume element resulting in departure from fluid flow streamlines around a rising gas bubble. This mechanism, unlike that responsible for particle transport in deep bed filtration, results in the impaction of an inclusion on the gas bubble surface. If attachment to the bubble occurs and viscous shear forces do not cause detachment, the inclusion is separated from the melt by flotation. Particles larger than 80μm can be removed by these means with a bubble diameter as great as 1.0 mm.

The second mechanism of particle flotation, interception, is based on contact of an inclusion and rising gas bubble. An analytical expression relating the fraction of inclusions removed to inclusion radius and bubble diameter (for spherical particles) is [9]:

$$E_f = \exp(1.0\times10^4 G_m \frac{R_p}{r_b^2}) \tag{2.2}$$

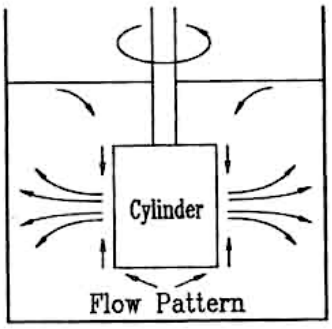

Figure 2.5 Water flow pattern around a rotating cylinder [30]

The most common in-line degassing equipments are GBF (Gas Bubbling Filtration) [30], Alpur [31], Hycast [32], ACD (Alcan Compact Degasser) [31], and Alcoa 622 process [33]. Some of them are presented in the following.

The bubble flotation device, GBF [30], as Figure 2.5, uses high speed rotors (600-950 rpm) and 2-3 baffle plates, resulting in the production of many very fine bubbles throughout the metal. The GBF is claimed to consistently show excellent efficiency in removing inclusions and hydrogen.

Figure 2.6 gives an illustration of the metal level together with the gas dispersion inside the Hycast I-60 SIR during operation. A baffle separates the reactor into two chambers; an inlet chamber with a parallel flow between gas bubbles and the metal and an outlet chamber where there is a counter flow. Each chamber is supplied with one rotor.

In the I-60 SIR the gas bubbles have approx. 50-60% longer residence time than conventional in-line refining units, which provides a better utilization of the process gas.

As the gas bubbles rise inside the reactor chamber during operation, inclusions in the melt come into contact with the gas bubbles. The inclusions are removed from the melt to the surface dross layer by the gas bubbles. The rotor is designed to create small gas bubbles. Small, well-dispersed gas bubbles increase the total surface contact area between the gas bubbles and the melt, which increases the removal of hydrogen and inclusions.

When using an upper side rotor, a vortex is created around the shaft on the surface of the metal. This increases the probability of re-entrainment of inclusions into the melt from the surface dross layer and back-leakage of hydrogen from the atmosphere above the liquid metal. A bottom installed rotor does not have this problem (see Figure 2.6).

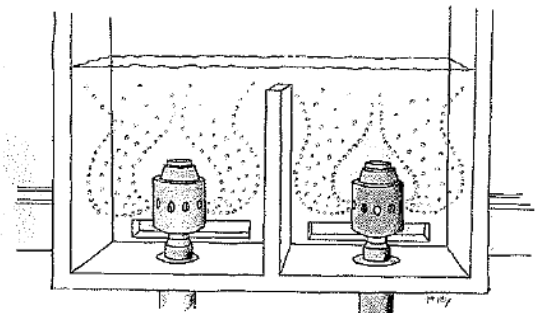

Figure 2.6 Illustration of metal level and gas dispersion inside the Hycast I-60 SIR during operation [32]

2.1.2.4 Centrifugal separation

In centrifugal separation, inclusions are removed by the rotating filters due to the density difference, but now the centripetal acceleration replaces the acceleration of gravity, compared to sedimentation. Thus $\omega^2 r$ replaces gravity g in the various relations for removal [26, 34].

2.1.2.5 Turbulent deposition

Sometimes stirring is used to remove inclusions. In turbulent flow the inclusions are carried to a surface due to (turbulent) velocity fluctuations. The influence of the

turbulence increases when the density difference gets smaller[27]. The turbulent deposition rate [27] for a smooth surface is

$$U_d = 5.1\times10^{-4} u_\tau (\frac{2u_\tau R_p}{\nu})^2 \quad (2.3)$$

Deposition at a rough surface is complex and will need an extensive treatment to describe removal. Deposition at a rough surface is more efficient than for a smooth surface. In this case U_d may possibly be proportional to the inclusion diameter [27].

2.1.2.6 Inclusion growth through agglomeration

The removal of small inclusions is difficult to attain. A solution may be agglomeration employing powerful stirring as a first step. Possible mechanisms for agglomeration [27] are:

1. Brownian (thermal) agglomeration. The particles agglomerate due to the fact that small macroscopic particles in a liquid always will be in chaotic movement.
2. Gradient agglomeration. If there are velocity gradients in a liquid, e.g. in the boundary layer near a wall, particles close to each other move at different velocities. Thus they may collide if the horizontal distance is less than the sum of the particle radii.
3. Turbulent agglomeration. Small particles in turbulent vortices migrate through the liquid in a chaotic manner resembling Brownian movement.
4. Agglomeration in polydisperse systems, i.e. suspensions with a distribution of particle sizes and particle densities. Since the forces from the gravitational field and electromagnetic fields depend on size and density difference, this may lead to collisions between particles of different sizes and/or densities.

If the agglomeration is to be important, the time constant for agglomeration must be less than the residence time.

2.1.2.7 Fluxing

Since mixed salts can remove some inclusions when they are added to molten aluminium, a simple and inexpensive method - fluxing based on stirred flux filtering and cleaning is used. A fluxing method to remove inclusions has been tested by M. Zhou [35]. The wettability of the inclusions in the molten aluminium is poorer than in molten flux. Accordingly, the surface tension of the inclusions in the molten aluminium is greater than in the molten flux. Therefore, the inclusions have the tendency to migrate from the molten aluminium to the flux because the stability of the inclusions in molten aluminium is less than in the flux. In practice the method is time consuming.

2.1.2.8 Electromagnetic separation

Electromagnetic removal of inclusions has until now hardly been utilized. Electromagnetic separation is an effective, stable and clean way to eliminate non-metallic inclusions from aluminium melt. Its principle is to expel the inclusions of poor electrical conductivity out of the melt by the differential Lorentz force [10]. This force is otherwise employed for stirring, casting, and pumping of metals. The differential Lorentz force affects the (conducting) melt, but not the non-metallic inclusions (oxides and carbides). In a melt a pressure gradient will be generated by an electromagnetic field. An inclusion in the melt will feel the pressure gradient or volume force due to the inclusion not having the same conductivity as the melt. In principle inclusions may be driven in any direction by electric and magnetic fields.

The forces may be created by:

1. Use of an applied electric field in conjunction with a magnetic field.
2. By letting the magnetic field induce a current in the melt.
3. By sending a current through the melt thereby inducing a magnetic field that interacts with the current. This gives a pinch-effect.

The conductive melt is subjected to the electromagnetic force [36],

$$F_l = j \times B \tag{2.4}$$

The net force exerted by the electromagnetic force field on a spherical particle having a different electrical conductivity can be expressed as follows in steady-state conditions and under the simplifying assumption that the fluid velocity is small [36]:

$$F_p = -\frac{3}{2}\frac{(\sigma_l - \sigma_p)}{(2\sigma_l + \sigma_p)}\frac{\pi(2R_p)^3}{6}F_l \tag{2.5}$$

For most non-metallic inclusions, where the particle is nonconductive (σ_p=0), the force becomes

$$F_p = -\frac{\pi(2R_p)^3}{8}F_l \tag{2.6}$$

Recently, various schemes based on various types of electromagnetic fields, including DC electric field with a crossed steady magnetic field, AC electric field, stationary AC magnetic field, travelling magnetic field, simultaneous imposition of AC current and AC magnetic field, and strong magnetic field created by a superconducting DC coil have been studied. The main problem, at present , is that large and homogeneous electromagnetic force densities in large volume melts are difficult to achieve, and separation efficiencies are quite low when the inclusion size is small [10].

2.1.3 Filters and Filtration Processes Used for Aluminium Purification

2.1.3.1 Filters

Commercially available porous ceramic media are surveyed and classified into the following five generic types:

- Type I: Ceramic monoliths
- Type II: Unbonded ceramic particulates
- Type III: Ceramic foams
- Type IV: Bonded ceramic particulates
- Type V : Woven ceramic fiber

The structural nature and flow properties of these filters are reported in paper [37].

Although only implemented by aluminium foundries since the late 1970s, CFFs are increasingly being used to prevent non-metallic materials from entering the mould cavity, resulting in premium-quality castings demanded by today's market [38]. Filtration with CFFs offers several key benefits that improve the quality of premium aluminium casting. They include [20]:

- A small gating system
- Improved casting yield
- Improved machining properties
- Reduced remelt scrap
- Improved mechanical properties
- Reduced dye-penetrant indications
- Reduced X-ray evidence of non-metallics

CFF (Figure 2.7) — which look very much like sponges — is characterized by an open-pore reticulated structure with porosity that may exceed 90% and a very high surface area. This structure offers low resistance to fluid flow, making it useful as a filter.

The Bonded Particle Filter (BPF®) [12] is suited for certain casthouse applications. This filter medium is an aggregate of either SiC or Al_2O_3 granules, graded to a specific particle size distribution and then bonded together using a ceramic binder. The BPF® media has several distinguishing characteristics from other filter media. Since it is constructed from "hard particles", it has substantial strength both at ambient as well as normal molten aluminium temperatures, enabling the filter to be handled easily whilst providing durability in service. The proprietary binder system provides a high degree of chemical resistance against all aluminium wrought alloys, except Al-Li, and retains this resistance for long time periods. A high content of SiC composition provides a high thermal conductivity. This is important in maintaining minimal thermal gradients between the inlet and outlet of an in-line filtering process. The affinity of the binder system to attach inclusions, a lower inherent porosity (nominally 40-45% porosity vs. 80-85% for a CFF), and a tortuous internal structure are claimed to all combine to enhance filtration efficiency. There are three principal configurations of BPF® in wrought casting applications: the Cartridge Filter (MCF), the Trough Tube Filter (TTF), and the Dual Vertical Gate Filter (DVGF).

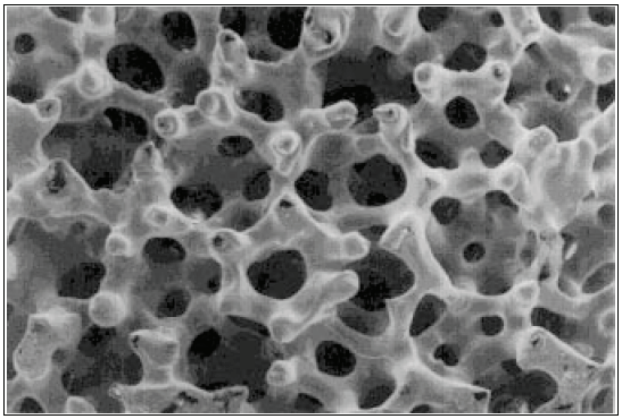

Figure 2.7 Scanning electron photograph showing the 3-D structure of a reticulated CFF [38]

Also Metaullics™ Vertical Gate Filters (VGF) [39] eliminate inclusions. Serving as walls between hearths and dip-out wells in melting or holding furnaces, these bonded particle filters remove inclusions and increase quality and productivity.
The filter can be cylindrical (some deep bed filters), tube (rigid media filters) or plate (some CFF). See Figure 2.8. The filter media may be either coherent or rigid, as in the case of the CFF or RMF (Rigid Media Filters), or consist of a loose mass of separate particles, as in the case of DBF (Deep Bed Filters). DBF, RMF, and CFF are compared in the literature [40, 41]. The filters were classified in order of decreasing efficiency as follows:

- Deep bed fine or coarse particulate material (DBF)
- Fine sintered grains featuring high filtration area and low thickness (RMF)
- CFF characterized by low thickness and high melt velocity.

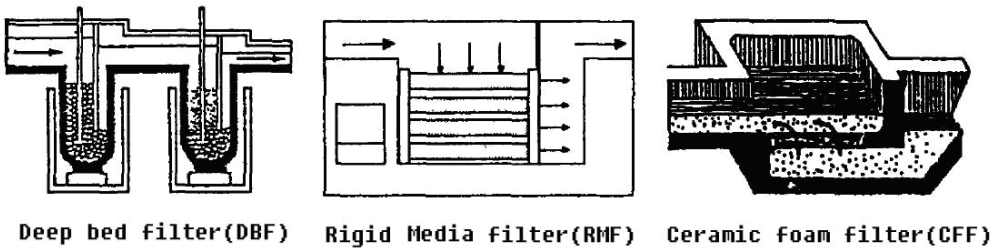

Figure 2.8 Industrial Al filtration system [15]

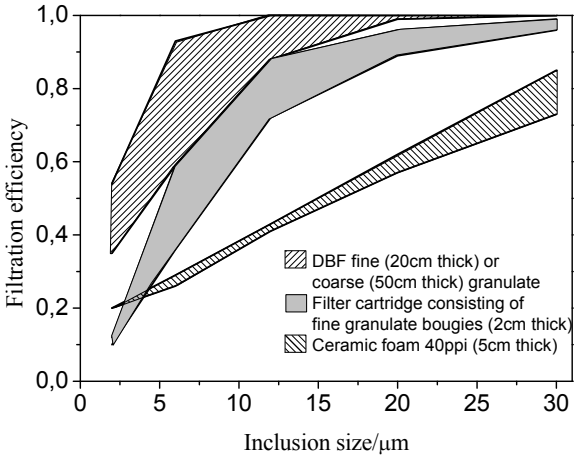

Figure 2.9 Comparison of various filtration processes [42]
The upper boundary of each hatched region corresponds to the low velocity, while the lower boundary corresponds to the high velocity

A comparison of the filtration efficiency of DBF and CFF is presented in Figure 2.9. They all have increased filtration efficiency with decreasing filtration speed and increased particle size.

K. Hoshino [43] have investigated tube (RMF). The cartridge offers a large filtering area compared to plate shape filters. If the size of the filtration box is the same, it is possible to efficiently filtrate at lower velocities compared to the plate filter.

Plate filters can be installed in the vertical or horizontal direction. See Figure 2.10.

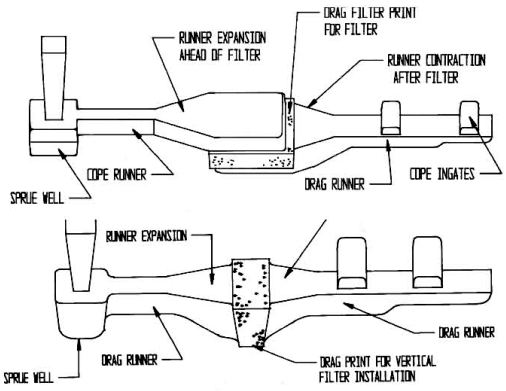

Figure 2.10 Vertical and horizontal CFF [38]

2.1.3.2 Filtration process designs

a. SELEE filtration technique

CFFs were developed by SELEE to filter molten aluminium in 1974 [44], as shown in Figure 2.11. A square and properly sized filter seat made of abrasive resistant material that slopes toward the outlet of the filter bowl so that air bubbles are not trapped underneath the filter. Air bubbles cause channelling of the metal flow in the filter and reduce effective filter area. The filter is positioned so that both major surfaces are submerged in the liquid metal during operation. This eliminates generation and entrainment of additional oxides. A refractory lining is pre-baked to a temperature of at least 650^{o}C to remove mechanical and chemical water. Filter gaskets are used to seal the annular space between the filter and the seat to prevent metal bypass and filter floating up. An easily accessible drain and a sloping floor facilitate draining and cleaning.

In 1990, about 50% of the free world aluminium consumption (i.e. 7,000,000 metric tons) was filtered using ceramic foam filters from SELEE [45]. Two types of SELEE filters with 17 inch 20 ppi and 20 inch 30 ppi combined with MINT degasser removed 51.9% and 77.5% inclusions in aluminium[46].

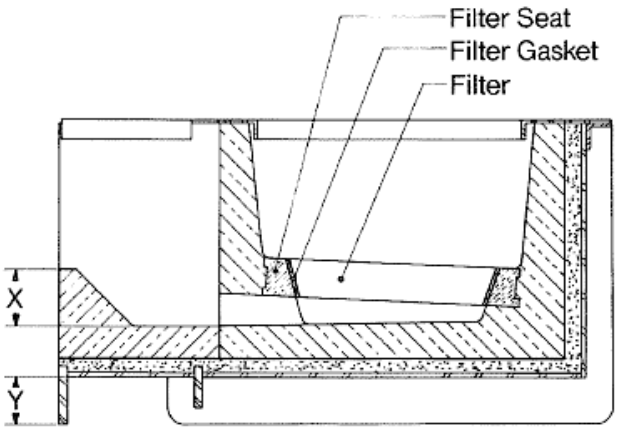

Figure 2.11 Schematic of an filter bowl for use with CFFs of SELEE® structure [25]

b. ALUDEF filtration process

A system registered as ALUDEF® (Aluminium Degassing and Filtration) [47] was developed by CENTRO TECNICO PROCESSI (Process research division of ALUMINIA S.P.A). Two versions of the ALUDEF® unit had been built, ALUDEF® 5 and ALUDEF® 20 with a maximum metal flow rate of 5 tons and 20 tons per hour respectively. The ALUDEF® process is based on the classical method of refining liquid aluminium by degassing and filtering, but it introduces some innovative ideas (Figure 2.12):

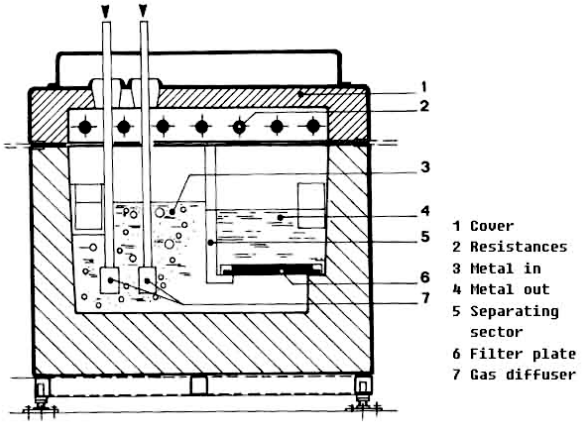

Figure 2.12 Section of ALUDEF® unit [47]

A) The process uses disposable porous ceramic plates as stable filtering medias with the following stated advantages:
   - Changing the filter plate is easier and less expensive than changing a filter bed such as Al_2O_3 balls or flakes or other granular materials;
   - Increased efficiency in removing inclusions due to the reduced dimensions of plate pores compared with filter bed pores;
   - Increased operational flexibility since it is possible to use different types of plate with porosity ranging from 20-50 ppi;
   - Ceramic filter plates are widely available all over the world in many shapes and sizes with various filter capacities.

B) The metal flows upward through the plate, thus allowing large inclusions to settle on the bottom of the unit under the filter plate. This has the following advantages:
   - It avoids clogging the first layer of the filter plate;
   - It increases plate life;
   - It reduces the number of plate changes and therefore the number of times the unit must be drained.

c. CEFILPB filtration process

CEFILPB (CEramic FIlters of Lost Packed Bed), whose structure corresponds to the negative of the organic particles packed bed used as precursor for the ceramic material, had been studied in [48]. Although somewhat similar in structure to foam filters they have a narrower pore size distribution and are more tortuous, less permeable and are much more resistant to compression. Their efficiency in short term aluminium filtration experiments compares well with commercial CFFs.

They also concluded that short time filtration of aluminium with around 1% inclusion concentration resulted in both cake and deep bed filtration modes. The last was found to be the predominant mode for inclusion retention, in the size range of 20 to 60 μm.

Three dimensional fluid flow calculations indicated that high velocities are directed toward the corners of the windows, and this behaviour agrees well with the formation of internal cakes over the windows. The flow analysis also pointed out that the window to cell diameter ratio determines the size and location of zones of very low velocity within the cell, where inclusions may be trapped.

d. Filtration processes using Coated CFF and coated deep bed filters

M. Zhou [49] investigated the deep filtration of molten aluminium using CFFs and ceramic particles with active coating, which can capture non-metallic inclusions and dissolve Al_2O_3. Figure 2.13 and Figure 2.14 sketches the models for capturing inclusions using CFF and ceramic particles with active coating. Inclusions in molten aluminium flow through the filter and are captured by the coating of filter wall or particles. Elongation of the filtered tensile specimens increased, but their tensile strength did not show a statistically significant change.

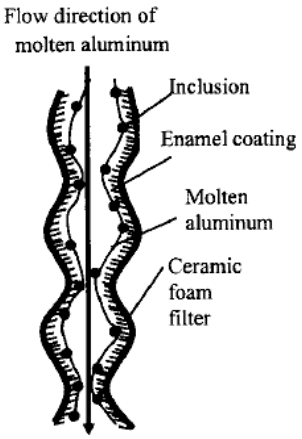

Figure 2.13 Active coating on the surface of a CFF capturing inclusions

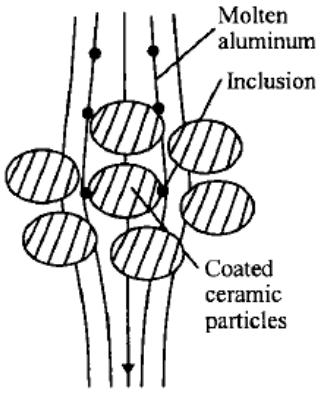

Figure 2.14 Inclusion in molten Al captured by active coating on ceramic particles

e. Multi-stage process

Purification by a single filter may give blocking due to the presence of large inclusions and different physical- chemical properties of inclusions. A solution is to use a multi-stage filter. Some of them are shown below.

e.1 SUN process

In view of the common practice of “degassing -inclusion removal-continuous casting” in most large —scale aluminium industry applications , a novel composite purification platform 973-I integrates covering flux, rotary degassing and two-stage filtration in a

multi-stage multi-media system as shown in Figure 2.15. It is found that hydrogen content is decreased by 75.5% and elongation is improved by 25-160%. The outlet of gas from bubbles in the Figure 2.15 was not indicated in the paper.

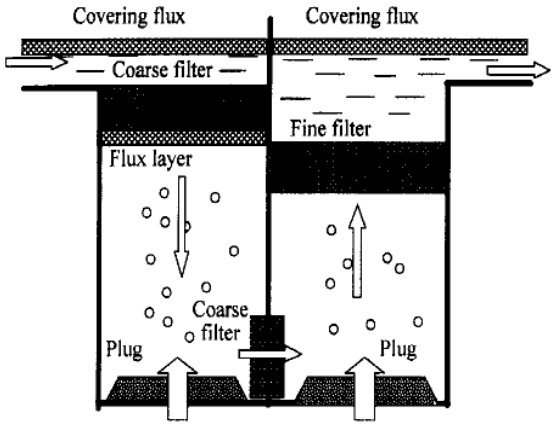

Figure 2.15 Novel purification platform 973-I for molten Al [10]

e.2 XC filter filtration process

Instone S.[50] used a filter unit called XC filter (by VAW/Hydro Aluminium and now produced by Drache) claimed to give superior filtration efficiency particularly in the size range of 15-40 μm. The XC Filter combines ceramic foam filtration (CFF) and deep bed filtration (DBF) to overcome limitations of the established technologies. A typical layout of the XC filter is shown in Figure 2.16. Metal passes first through the CFF and enters a second chamber where grain refiner is added. It then flows through the bed filter and exits the filter via the outlet chamber. The XC filter permits the addition of the grain refiner after the CFF, which can lead to significant improvements in the performance of the CFF. In this configuration the detrimental effect of TiB and AlC grain refiners on CFF performance can be avoided. The removal efficiency of the XC filter (30 ppi CFF+ Bed filter) is 88% for inclusions larger than 15μm.

Another dual stage filter bowl system is studied in [44]. There are two filters in a single bowl in order to obtain a simple compact design with minimal floor space requirements. The advantages of a dual stage system where both filters are incorporated into a single bowl are:

- Less floor space required
- May directly replace an existing filter bowl
- Fewer refractory components
- Lower installation and operation cost
- Easier start up: Only one filter to preheat and prime
- Easier cleanup and less drain metal: Only one filter bowl

Rather than simply stack the filters on top of one another, two separate filter seating surfaces were incorporated into the design in order to obtain a one inch (25 mm) gap between the two filters. The purpose of the gap was:

- To prevent an interference fit between the two filters due to the dimensional tolerance band of the filters.
- To allow each filter to be removed separately at the completion of casting.

Metallographic analysis of the spent primary or first stage filters indicated a relatively heavy inclusion loading where the filters were nearly blocked or plugged with retained inclusion material. The second stage filter by contrast exhibited a relatively low inclusion loading confirming the validity of the dual stage filter bowl concept. The introduction of the dual stage filter system resulted in statistically significant improvement in extrusion press productivity.

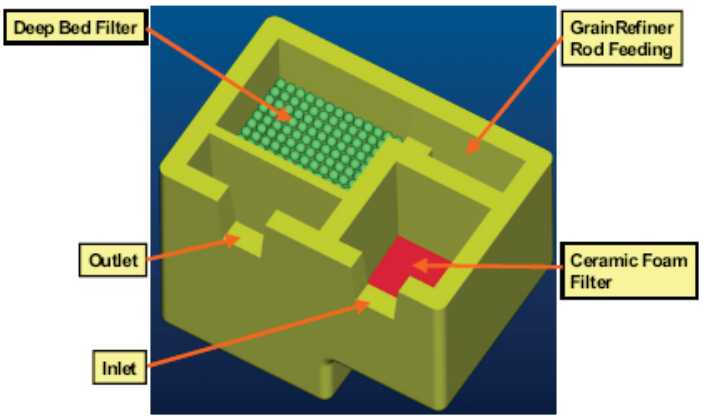

Figure 2.16 Typical layout of the XC Filter [50]

e.3 Martin process

Syvertsen et al. [51] have studied another compact deep bed filter combined with a gas pump, as Figure 2.17. A cylindrical deep bed filter with a gas (automatically controlled argon) lift pump along the centre axis was tested. The average size of the Al_2O_3 filter grains was approx. 4 mm. The filter contained 600 kg of grains on top of about 300 kg of Al_2O_3 spheres (diameter around 21 mm). The depth of the filter bed (grain part) is 0.31m. The cross section of the annular filter filled with grains or spheres was 0.93 m^2. They observed a high removal efficiency.

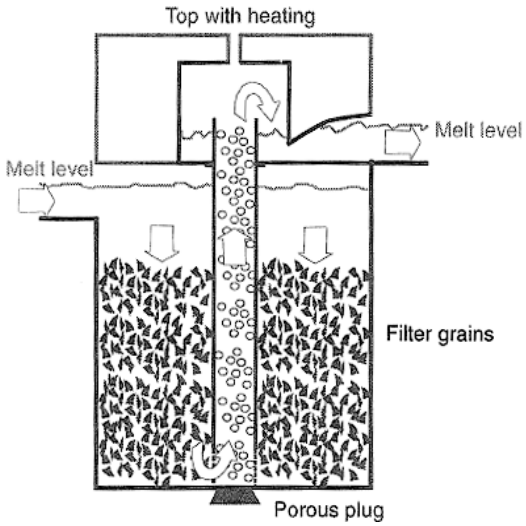

Figure 2.17 Cylindrical filter unit containing a gas-lift pump [51]

2.1.4 Inclusion Removal Mechanisms by Filtration

Particle removal depends on the properties and size of particles as well as the character of the filter. Removal is by:

- Physical separation
- Surface adhesion
- Dissolution/ chemical reaction

Physical separation. As indicated in Figure 2.18, coarse particles form a cake on a surface in the filter. The efficiency of physical separation is mainly decided by the characteristics of the filter, such as diameter of the filter pores and the filter thickness.

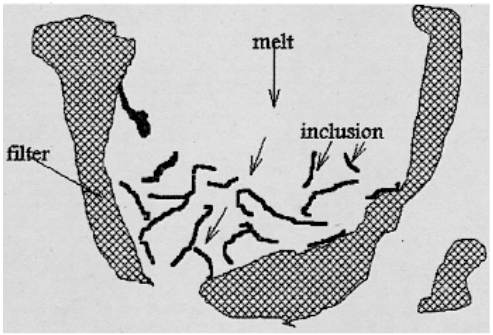

Figure 2.18 Particles blocked by filter [52]

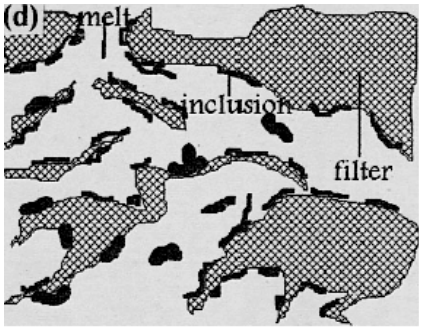

Figure 2.19 Sketch map of the surface adhesion of particles [52].

Surface adhesion refers to the phenomenon of the particle adhering to the filter wall. Figure 2.19 shows that some smaller particles are entrapped on the interior surface of the filter. Once the small blocky inclusions adhere on the surface of the filter, agglomeration occurs because these inclusions attract the same kinds of inclusions in the liquid metal. The filtration efficiency increases with the contact area between the liquid metal and the filter. Another important factor influencing filtration efficiency is the flow rate of the liquid metal passing through the filter. For inclusions to adhere and sinter to the filter wall time may be required.

Chemical reaction. Impurity elements react with components of the wall, which contribute to the effective capture of inclusions. Zhou et al. [53] investigated inclusion removal by filters coated with borophosphate enamel. They showed that Al_2O_3 reacts with molten borophosphate enamel and is converted into AlO_4 of a tetrahedral structure.

2.1.4.1 Mechanisms

Generally, there are three ways to remove inclusions [18, 54] as illustrated in Figure 2.20:

a. Sieve mode
b. Cake mode
c. Depth mode

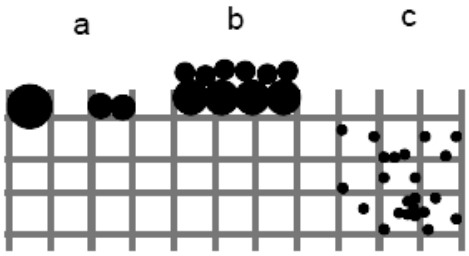

Figure 2.20 Filtration mode: (a) Sieve mode, (b) Cake mode, (c) Depth mode [55]

Sieve mode. When inclusions flow through pores smaller than their size, a filter will stop them as a sieve.

Cake mode. With the development of sieve mode, more and more inclusions will be collected outside the filter, and then they become another filter. During this time the pressure drop will increase strongly. Cake filtration is not presently used in the aluminium industry. It involves the deposition of a layer of inclusions at the inlet to the filter medium with little or no penetration of the inclusions into the internal part of the filter. This results in a very rapid metallostatic head build-up and is unacceptable for cost and practical operating reasons [5].

Depth mode. Small inclusions collide with the inner wall and are captured inside the filter. Tortuous passages in the filter improve the probability of collision. Depth filtration depends on [56]:

- The probability of a particle impinging on the filter structure;
- The probability of a particle being retained on the filter wall.

The probability that a particle will be retained depends on many variables, such as [56]:

1. Chemical composition of the particle and filter;
2. The filter microporosity, topography, and wettability;
3. The velocity (flow rate) of the metal through the filter;
4. The flow characteristics of the molten aluminium adjacent to the surface;
5. The particle size.

The three filter modes may act simultaneously.

1) Cake filtration occurs for
   - A high inclusion load
   - Large inclusions
2) Depth filtration operates at
   - Low inclusion loads
   - Small inclusions

There has been some controversy over whether the aluminium CFF operates as a deep bed or cake type filter. General characteristics of the deep bed filtration process are:

1. The inclusions caught are usually significantly smaller than the openings or pores of the filter medium and are captured inside the filter medium.
2. The accumulation of inclusion material within the filter bed during casting gradually increases the flow resistance of the filter medium. As a result the pressure drop or metallostatic head loss across the filter must increase in order to maintain constant flow.
3. Inclusion removal efficiency varies with the interstitial flow velocity within the pore structure of the filter medium.
4. The concentration of retained particles decreases from the filter inlet surface to outlet surface.

Cake filtration process is characterized by:

1. As filtration proceeds, the filter cake itself acts as the filter medium and finer and finer inclusions are captured as the cake grows.
2. The pressure drop across the filter medium and cake increases strongly with time. As filtration proceeds the layer of deposited particles becomes thicker requiring a rapidly increasing pressure to maintain a constant flow rate.
3. Inclusion capture efficiency is not affected by variations in metal velocity provided that the change in velocity does not affect the character of the cake (uncompressed or compressed).

There are several mechanisms for a particle to reach the internal surface of the filter. The following transport mechanisms shown in Figure 2.21 may play a role to determine filter efficiencies.

- **Direct interception.** A particle hits the filter surface following the fluid flow lines.

- **Gravity forces.** A particle with specific density different from the fluid leaves the fluid flow line due to gravity.
- **Brownian movement** is the microscopic movement caused by the molecular bombardment on the particles in the liquid. Brownian motion of particles in metal [57] are randomly set in motion as the result of collisions with the energetic molecules of the liquid. This phenomenon is believed to be important only for submicron particles. The higher the temperature, the faster the liquid molecules move, and the harder they bump into anything they encounter. Smaller particles move much faster than larger particles.
- **Inertial forces (Impaction)** cause the particle to proceed in a straight line due to its inertia. Thus the particles do not follow sudden change in the fluid flow lines.
- **Hydrodynamic effects.** They are due to the velocity distribution in the filter cell and the effect of the walls on flow. Depending on the shape of the particle it rotates and transfers in the flow field. Obviously the boundary layers along the filter walls play an important role.

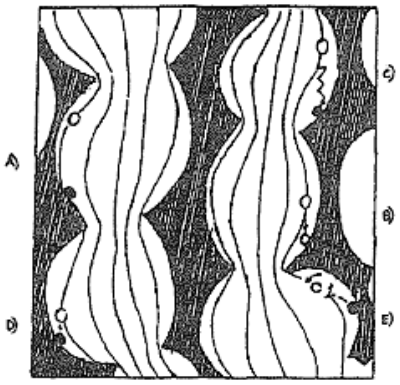

Figure 2.21 Transport mechanism of a particle in deep bed filtration [16]
A) Direct interception B) Gravity forces C) Brownian movement
D) Inertial forces E) Hydrodynamic effects

In a study of gas streamlines, Avila Ribas et al. [58] (Figure 2.22) found that gravitational settling and inertial deposition are the predominating collection mechanisms for the over-micron powder (particles). Diffusional deposition (Brownian movement) predominates for the nano-scale powder (particles).

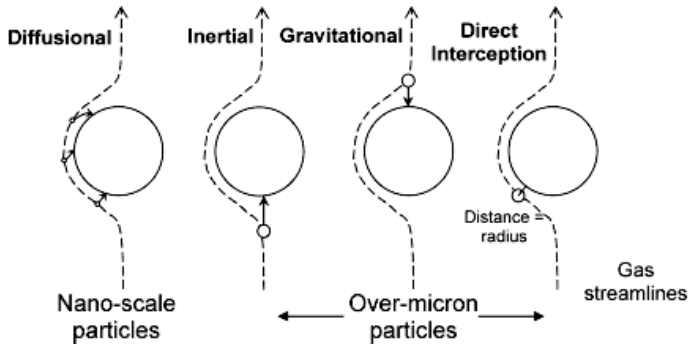

Figure 2.22 Influence of the collection mechanisms in the particles deposition behaviour [58] in gases

2.1.4.2 Flow in filters

Deep bed filtration is considered to be the dominant filtration mode for the CFFs operating at the cleanliness levels existing in aluminium plants today. In deep bed filtration of molten metal the inclusions, which are smaller than the pore size of the filter typically used, are only deposited on the pore walls and may be entrained in the liquid metal when the flow rate varies. As already pointed out, inclusion capture is considered to be a result of two sequential events: (1) transport of inclusions to walls of the filter; (2) attachment of the inclusions to the walls [9]. Flow in filters significantly influences these two events.

Particles may not be trapped directly by the filter web. The restricted flow through the neck by the previously captured particles appears to cause subsequent particles to cluster together into a large, loosely adhered mass which bridges the neck. Such bridges form a kind of cake inside the filter. The result is that the pressure increases strongly with throughput as indicated in Figure 2.23. The Reynolds number of the filter, Re_f, is based on average web diameter of the filter, d_w.

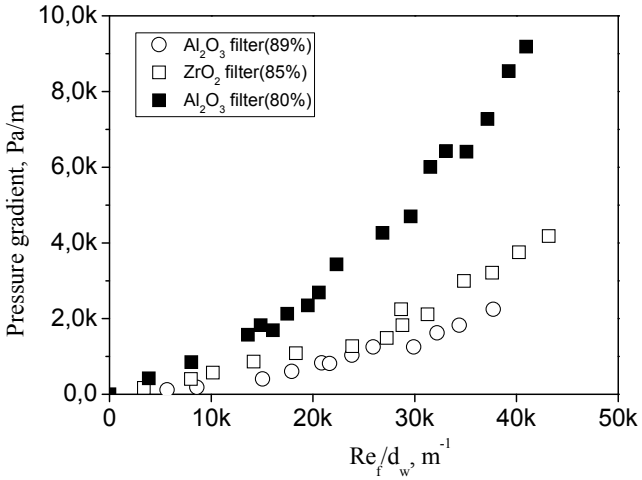

Figure 2.23 Fluid flow behaviour of various CFFs
Results from water experiments by Tian and Guthrie [59]. Percentage denotes effective porosity.

F.A. Acosta G. et al. [60] used a tube model to study the deep bed filtration. It was observed in water model that a high fluid velocity, Re=100 (for tube), promoted particle collision against the wall. Some of the particles were re-entrained into the fluid flow, while others remained circulating in the pore to settle down on the wall once the flow stopped. At the low fluid velocity, Re=0.2 (for tube), the particles closely follow the streamlines. Then, they generally did not collide against the wall of the model. A smaller number of particles were able to settle down on the wall near the window once the flow ended.

Calculation of particle trajectories [60] shows that for the highest velocities the particles tend to follow straight lines and that particles located sufficiently close to the wall will collide with it. These results are obtained when gravity acts normal to the inlet pore area. This explains filter clogging from 'cake' formation during purification of aluminium at high flow rates. The computed trajectories for the low fluid velocity condition agree with the actual observations which show that the particles follow the streamlines. They also concluded that smaller particles will need lower fluid velocities to be captured by interception or gravity inside the filter.

Flow in deep bed filtration of molten aluminium was studied experimentally in an enlarged scale water model by Laszlo [2]. A stack of rods were used to represent collector elements (bed wall) in order to create a 2D flow-field. Generally the flow in an array of tubes can be divided into two main regions, the preferred lanes and the wakes behind the tubes. See Figure 2.24. The shape of the wakes and that of the preferred channels are different in in-line and in staggered arrangement of the collector rod.

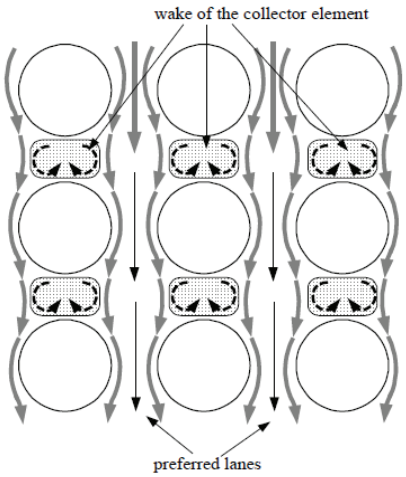

Figure 2.24 Flow regions in a tube bank with in-line arrangement [2]

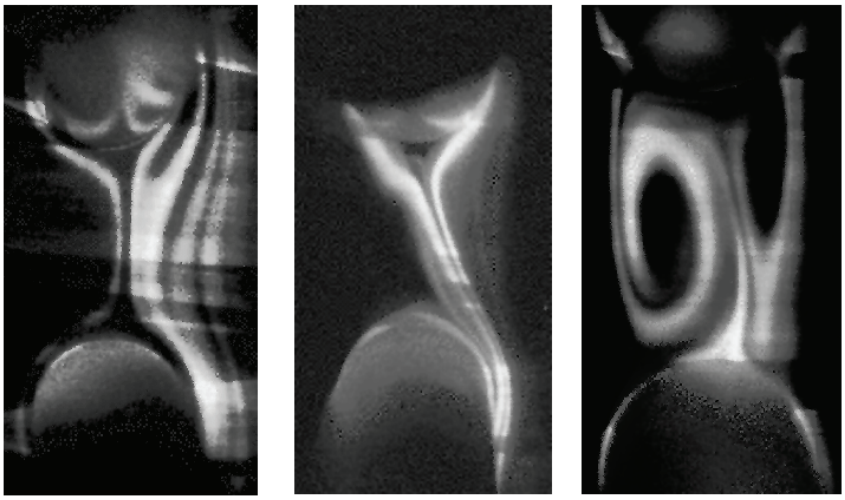

Figure 2.25 Circular cylinder in-line
Flow pattern between collector elements during the transition regime [2]
Lift: low velocity; centre: the destruction of the steady flow; right: high velocity

The flow pattern in the wake is characteristic to the velocity- more precisely to the Reynolds number-range ($Re=2RU_\infty/\nu$). Unfortunately, the authors did not give any Re data [2]. The flow pattern behind the collectors shows a similar shape in the flow around single bodies during the increase of velocity. At very low velocities, the flow is mirror- symmetrical and velocities are constant in time (left in Figure 2.25). Increasing the velocity, a pair of symmetric, counter-rotating eddies is formed in the wake. Increasing velocity further, the balance between the two vortices is destroyed, one of them becomes dominant, then separates and flows away (see Figure 2.25 right). The periodic separation of vortices with alternating sense of rotation (so called Karman

wortex sheet) is the precursor of the onset of stochastic fluctuations that characterize fully developed turbulence.

The above mentioned fluctuations are self-generated in a flow system where the boundary conditions are constant in time. At the beginning of the destruction of the steady flow, the temporal variations show a regular character, one single low frequency dominates the spectrum of velocity oscillations. This single low frequency causes a large mass of fluid to move in the same phase and this coordinated movement affects a large spatial domain inside the filter. This behaviour is characteristic to the transition fluctuating turbulent flows. As the periodic fluctuations commence around a collector element, the separation of vortices can trigger similar phenomena elsewhere- most effectively downstream- in the bed. Oscillations can be induced around cylinders that did not reach the phase of shedding alternating vortices behind them. In the centre image in Figure 2.25, the wake behind the upper cylinder is not well developed, but the streamline separating the two small, counter- rotating vortices is pushed to the right side of the inferior cylinder. This line is flipping between left and right and as a result, the upper surface of the inferior cylinder is swept by an alternating flow. The phenomenon is shown schematically in Figure 2.26.

Regularities, symmetries of the spatial arrangement of the collectors amplify these collective movements of the fluid. The onset of periodic oscillations appeared at 20-70% higher velocities in staggered than in in-line arrangement. The value depends on the geometry of the collectors and on the porosity of the system. Collectors with sharp edges, like the square and semi-circular rods, tend to trigger flow instabilities earlier.

The point of instability, where the fluid starts to oscillate, appears near the exit zone of the bed. This point moves upstream with the increase of the approach velocity. The amplitude of the fluctuations is increasing downstream.

The interaction between the collectors, the presence of these collective, “organized” movements make the transition regime inside beds of solid distinctively different from the transition of the flow around a single body.

For a single cylinder flow around a circular cylinder is steady at a very low Re_c <<1. As the Re_c increases, the symmetry disappears and two attached eddies (wakes) appear behind a cylinder. These eddies become large with increasing Re_c as in Figure 2.27. For Re_c > 45, unsteadiness arises spontaneously even though all the imposed conditions are being held steady and vortex shedding appears behind a cylinder (or an arm in filter) [61].

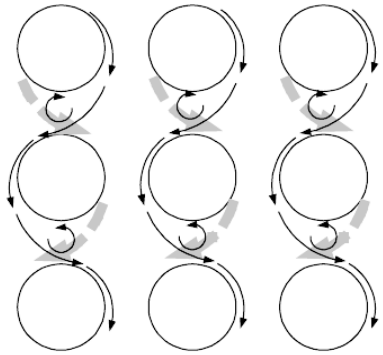

Figure 2.26 Schematic pattern of flow oscillations in a stack of rods (transition regime) [2]

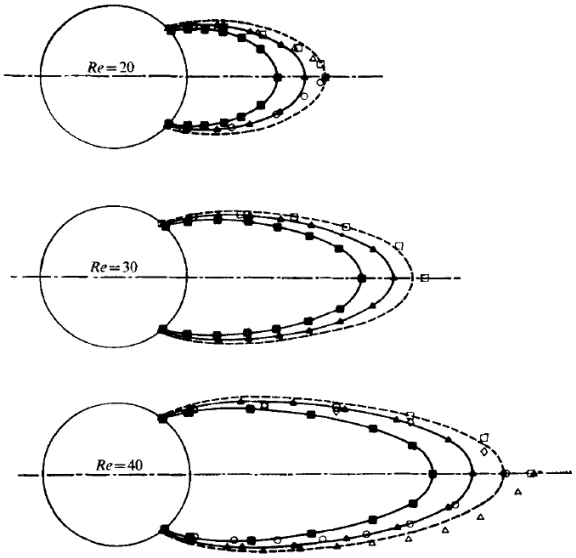

Figure 2.27 The shape of a wake boundary at the rear side of a cylinder [62]

The real velocities in a filter have to be considered. As the pore size changes, so will the velocity of the melt. This means that there are regions with turbulent flow (Re>4000) and with laminar flow (Re<2000). This change of velocity is especially important as the turbulent flow may allow very small particles to agglomerate and then be attached in the regions with laminar flow.

However, turbulent flow can lead to the release of already attached particles due to drag forces. It may be expected that the magnitude of the drag forces is proportional to the velocity in the viscous flow regime [59].

As mentioned, changing the flow rate of the liquid metal can displace the transition zone inside the bed as its position depends on the flow velocity. Already deposited

inclusions can be washed away if a large amplitude oscillating flow develops around the collector elements.

2.1.4.3 Flow transport

Transport of inclusions to the walls is the first step in inclusion removal of the filter. In general, particle transport can occur by impingement, interception, sedimentation, diffusional, and hydrodynamic effects. When the difference in density is high, the sedimentation forces may play an important role. If the difference decreases, sedimentation will become negligible and interception will become the dominant factor [63]. See Figure 2.21.

Developing boundary layers in the surface region may favour the precipitation of particles. Boundary layers form, as indicated in Figure 2.28, because there is no slip at solid interfaces. A velocity gradient develops. The boundary layers are thinnest at the point at which the fluid enters the channels (i.e. at the filter surface). A thin boundary layer is easier to penetrate than a thick, more developed one. The deposition patterns show peaks in the particles concentration in the near surface region.

It has been proposed [64] that particles preferentially deposit at channel openings or restrictions to flow, as shown in Figure 2.29. Note that a radial entry opening, such as would be expected at a pore opening, causes the build up of particles near the entrance, especially when oriented at an angle to the flow. The top surface of a reticulated ceramic filter can be visualized as several radial channel openings grouped together. If some of these openings are blocked, the flow must increase in the remaining channels to maintain a given flow or casting rate.

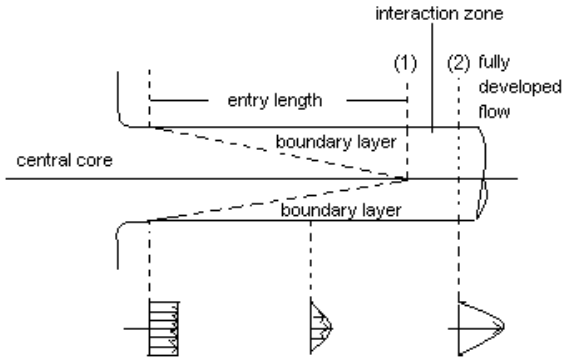

Figure 2.28 Entry region of a “pipe” [64]

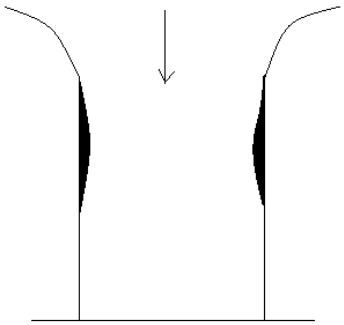

Figure 2.29 Particles build up in a radius entry nozzle [64]

2.1.4.4 Inclusion attachment to the filter walls

Particle attachment can be a result of forces developed through pressure, chemical, or Van der Waals effects. The relative dominance of each mechanism is a function of particular type and size, fluid approach velocity, as well as temperature and media characteristics.

The probability that a particle will be retained depends on many variables, as mentioned [56]: the chemical composition of the particle and filter, the particle size and morphology, the filter microporosity, topography and wettability, and the flow of the molten aluminium adjacent the filter surfaces.

If the viscous drag on the particle is not higher than the forces that cause re-entrainment, the inclusion will remain inside the filter.

The CFF forms a cellular media and can be regarded as the negative of a packed bed of granules. Therefore the flow regimes in CFFs and packed beds are essentially different. Figure 2.30 shows the different flow regimes in a CFF and in a granular media used for drinking water production.

Within these pores different flow conditions and mixing behaviour can occur, depending on flow velocity. Figure 2.31 illustrates the different flow lines inside a single pore. Notice that the flow lines are very close together at the inlets and outlets. Conditions at these points should be critical for removal and entrainment of inclusions.

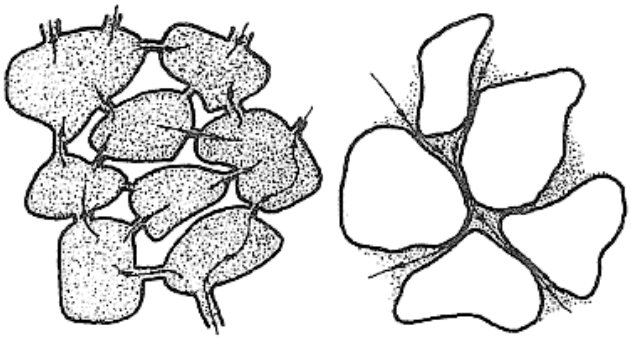

Figure 2.30 A schematic diagram illustrating the different flow regimes operating in cellular and granular media [37]

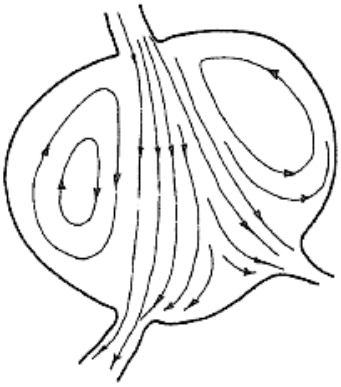

Figure 2.31 A schematic representation of flow within a cell of ceramic foam [37]

The most accepted hypothesis of aluminium deep filtration states that small inclusions at low concentrations (much less than 10ppm) are carried by the fluid through the open pores where they may attach to the walls. For large particles, inertia favours particle collision with the filter walls. When the flow rate increases, particles may be removed from the wall by the flow induced drag force, thus lowering the filtration efficiency. However, Frisvold and Engh et al. [27] calculate that the melt surface tension pressing an inclusion towards a filter wall is much larger than the typical drag forces exerted on a 10μm inclusion.

Practically all inclusions are deposited in the upper section of the collectors in the case of downward flow. Deposition is in layers, as Figure 2.32. The surface of the collectors is covered by a thin layer, in which the particles are attached to the surface by adhesion type force. The tangential force balance [2] at the edge of the deposition layer (layer 1) is as Figure 2.33.

$$f(G\cdot\cos\phi + F_A) = G\cdot\sin\phi \tag{2.7}$$

This adhesion dominated layer 1 is formed at the initial period of the life of a new filter bed. Apparently the attachment of this layer to the collector is stronger than that of the

subsequent layer to the first layer. This first, adhesion dominated layer plays a special role.

On one hand it separates or "isolates" the upper layer of inclusions from the collector, blocking the way for developing an adhesion force between the two different materials. On the other hand, it serves as a "primer" for capturing of the bigger particles, by providing an artificial roughness of the collector surface, improving retention by friction and interlocking. The structure of second upper layer is controlled mainly by the cohesion and friction between particles of the same materials. The force balance [2] between particles for the cohesion case is

$$f \cdot G \cdot \cos\phi + K = G \cdot \sin\phi \tag{2.8}$$

Experiments indicate that the cohesion forces are weak in comparison to the adhesion. For small particles the adhesion force to the collector surface is equal or greater than the gravity force. The large particles are kept on the upper surface mainly by the friction force. In a system where cohesion forces are superior to adhesion, the release of particles must have a different character, instead of "flowing" in an avalanche, the deposition layer is "peeled off", releasing chunks of particles.

Two kinds of particle loss mechanisms from the deposition layer develop [2]. First, individual particles or a small ensemble of particles (cluster) are entrained randomly from the deposition layer. The rate of this process is small, but it is nearly continuous. In the second process, a large number of particles are released suddenly in a zone around the border of the deposition layer, in the form of an avalanche. During the latter event, the deposition layer can loose 10-20% of the already captured inclusions. While the first mechanism has a quasi-continuous character, the second represents a jump in the state of the deposition layer. During avalanching, the borderline of the deposition layer is shifted upward suddenly, and then a slow process of rebuilding the layer follows (Figure 2.34).

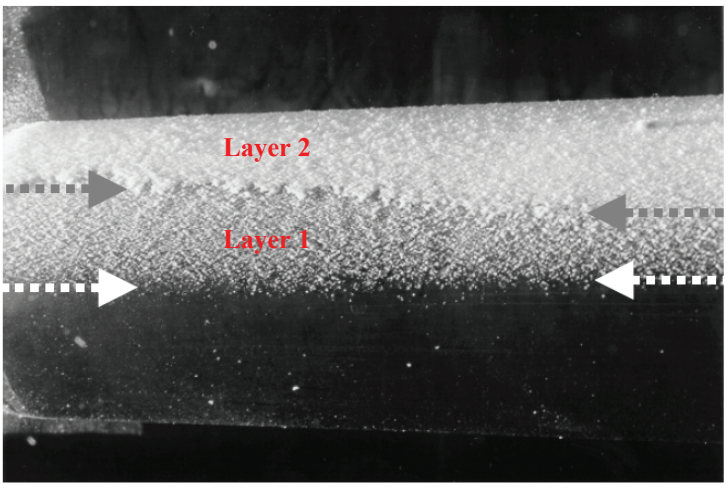

Figure 2.32 Structure of the deposition layer on a cylindrical collector [2]

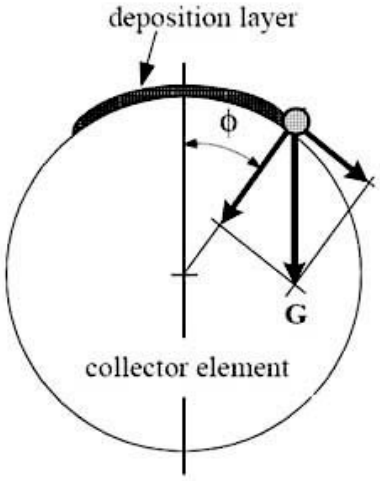

Figure 2.33 The component of the gravity force at the edge of the deposition layer [2]

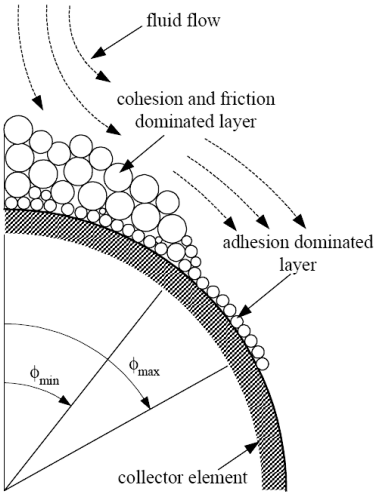

Figure 2.34 Double structure of the deposition layer [2]

When an inclusion interacts with the wall, the strength of adhesion must be great enough to resist the force of flowing metal and prevent being swept away and reintroduced to the metal stream. The adhesion strength depends on the interfacial energy between inclusion/filter, metal/filter, and metal/inclusion. The change in free energy for separation of an inclusion from the melt to the filter wall is given as [65]

$$\Delta G = \gamma_{if} - \gamma_{mf} - \gamma_{mi} \tag{2.9}$$

For the inclusion to remain fixed at the filter wall, the free energy must be less than zero. This will be enhanced by reaction between the inclusion and the filter material, or by the metal remaining non-wetting to the filter and to the inclusion.

The mechanisms of the capture may be explained as flows: First, the inclusion is trapped onto the filter surface by interception or gravity and glued there by the attraction force based on the surface tension, and then, bonded by sintering. It is concluded that the transport of inclusions from the molten metal to the filter surface is the rate controlling step [66].

The increase in filtration efficiency with decreasing pore size can be partly explained in terms of the NIFF (Near Surface Interstitial Flow controlled Filtration) theory [64]. If two filters had the same percent theoretical density but one had finer pore than the other, it would take fewer particles to bridge the necks of the finer pores. In addition, the finer pore filter would provide more convergent zones per unit volume and therefore enhance the separation of inclusions.

L. S. Aubrey et al. [67] have carried out metallographic evaluation of spent filters, filter head loss measurements, and sampling of aluminium melts for inclusion content. They agree that the primary mode of operation of CFFs in the aluminium industry is deep bed

filtration, not cake filtration. CFFs only exhibit characteristics of cake filtration under very specialized circumstances and on an infrequent basis. Further, they pointed out that when metal flow rate is less than to 900 kg/(m^2·s) the filtration mode is always deep bed. CFFs should be at least 2 inches thick and suggested metal flow rate in the range of 30 to 90 kg/(m^2·s).

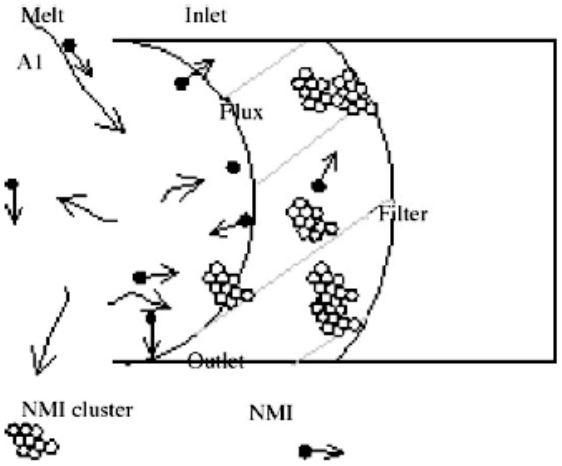

Figure 2.35 Composite filter model [68]

The removal mode of a composite filter is indicated in Figure 2.35. The mechanism is as follows [68]: (1) after dipping in flux, a flux–filter composite layer is formed on filter wall. Because flux wets the filter walls, the composite layer is stable and it cannot be brushed away by melt. (2) When aluminium melt flow passes through, a dead zone is formed near the flux layer. (3) Micro-size inclusions carried by melt move to the melt–flux interface. (4) Most particles that have moved to the interface are absorbed or melted effectively by flux layer. Some of them cluster. The inclusion cluster spans the melt–flux interface and extends towards melt. Subsequent inclusions hit it and are captured. This may be explained by the mechanism where particles tend to deposit close to "roughness elements" created by particles deposited previously [69]. A small part of them may separate from the melt–flux interface. (5) Since the melt velocity is nearly zero in the dead zone, inclusions remain in the zone until the filtration ends.

After treatment by the composite filter, no inclusions above 6.0 μm could be found in the microstructure. The tensile strength and the elongation of the samples are increased by 19.2% and 116.7%, respectively, compared with no filter. The same properties treated with the common filter only increased by 13.2% and 50%, respectively.

The inclusions are trapped throughout the filter, however, they are concentrated in the top regions [45].

Inclusion bridge generation in filters. It appears that with continued metal throughput a network of bridges comprising of oxides, fine borides and carbides accumulates. These bridges are only observed in the uppermost area of the CFF. It is believed that the

formation of these bridges is akin to the formation of a filter cake. It is the fine pore size of this filter cake that increases the capture rate of fine particles. The thicker the filter cake, the better the filtration efficiency in general and especially for fine particles. This build-up also results in changes in the filter, so that its filtration efficiency and its capacity will also be variable. This build up is also probably responsible for the eventual blocking or clogging of the filter [50].

N.J.Keegan [70] also states that the bridging is greatest in the finest filter. Very few or no bridges were found in the 30 and 50 ppi filters in his experiments. A small amount of build up was observed on a number of webs within the 65 ppi filters, but a high concentration of bridging was observed in the finest filters. See Figure 2.36.

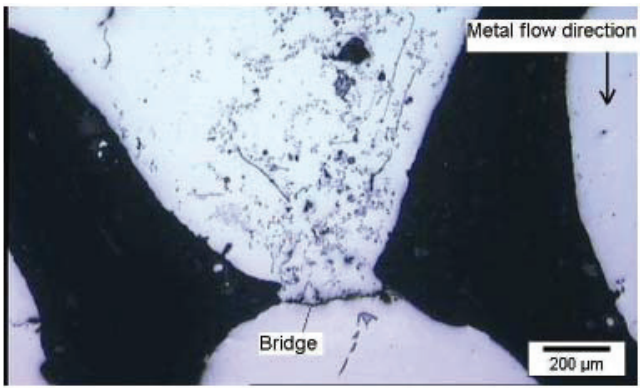

Figure 2.36 Presence of an oxide bridge at the filter inlet stopping the inclusions [71]

From investigation of rigid media filters used in casting operations, it was found that CaO particles agglomerate and form bridges at the inlet pores near the filter surface when boron free titanium alloy is used as a grain refiner. The inclusions which form bridges or clogged pores are CaO and Al_2O_3 particles. These agglomerate or bridges induce a rapid increase in pressure drop and as a result filter life is diminished. Large agglomerate or bridges of the inclusions are not formed in the melts when TiB_2 master alloys were added. It is interesting that TiB_2 may suppress the agglomeration of oxides like CaO or Al_2O_3. TiB_2 may play an important role in establishing longer filter life for the 1××× aluminium alloy series [43].

Paul Cooper [72] concluded that, in ceramic filters, if the incoming metal cleanliness was good, there was a minimal impact of the grain refiner on the performance of the filter. However, if there is an artificially high inclusion loading from the metal (achieved by deliberately vigorously stirring the metal in the furnace), then the introduction of the grain refiner leads to a reduction in filtration efficiency. In deep bed filters and tube filters [72], there is a transformation of the trapped TiB_2 particles into $(Ti,V)B_2$. V may be from the grain refiner. Subsequent growth of such particles then leads to the formation of more complex agglomerates and bridging within the filter, and thus impairs filtration and filter life.

2.1.4.5 Inclusion re- entrainment

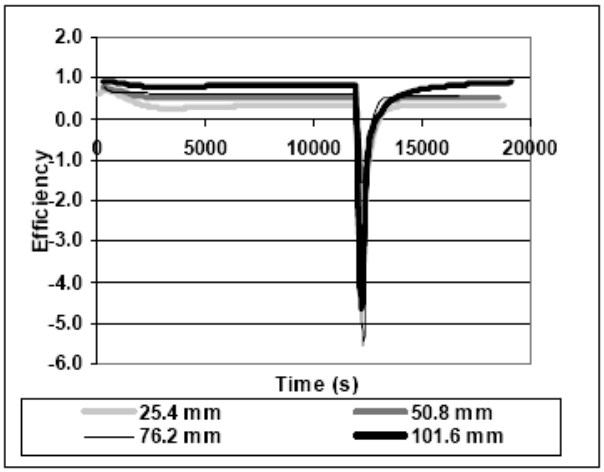

Figure 2.37 Filtration efficiency for various bed thicknesses during interrupted filtration [73]

The aluminium filtration process is semi-continuous. For a given number of ingots, there is a period of continuous filtration until the casting is completed. Then, the process is stopped, and the ingots are removed. When the subsequent batch is ready, filtration and the casting processes are re-started. During the cast stop/start periods, a significant quantity of the deposited inclusions may be released back to the metal due to flow instabilities. The deposition rate decreases, and filter efficiency is reduced due to re-entrainment. There is spontaneous and process related release, incoming flow bursts, metal head fluctuations, and vibrations release [74].

In Figure 2.37 an inclusion peak is observed during the flow interruption period. The efficiencies pass from a positive value to a negative. This shows clearly that the phenomenon of re-entrainment is present during the interruption period. Figure 2.37 also shows that the number of inclusions released is higher for a thinner bed. Unlike thicker beds, the inclusion released from the upper part of the filter will have much less chance to be re-captured again in the lower part of the filter for thinner beds [75].

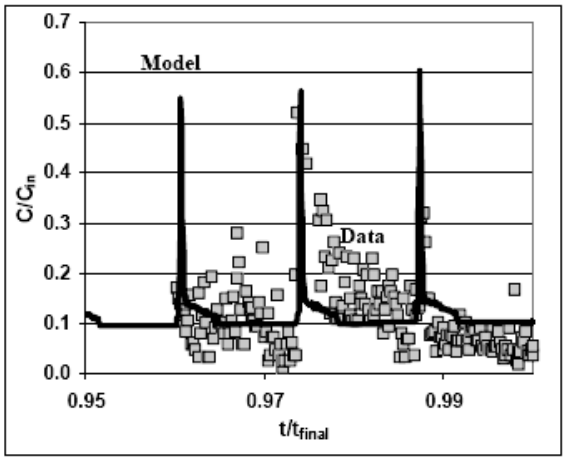

Figure 2.38 Concentration of inclusions with time [73]

Figure 2.38 shows the outlet concentration (normalized with respect to the inlet concentration) as a function of time (normalized with respect to total filter life) and compares the model predictions with industrial data for three casting cycles towards the end of the filter life. Although the data is scattered, the model predicts the general trend for all the cycles for the entire life of the filter. The peaks corresponding to release become larger as the time progresses, demonstrating the fact that the bed is aging. The study has also shown that the re-entrainment is a phenomenon which occurs during both continuous and interrupted flow filtration.

Also, increasing velocity increases the re-entrainment as expected. When the concentration is increased, re-entrainment does not change significantly for a given bed thickness.

To reduce re-entrainment of inclusions, continuous and smooth operation or at least short stop- to-start times may be recommended

2.1.5 Parametric Study of Inclusion Removal in Filtration

2.1.5.1 Effect of inclusion parameters

a. Specific gravity

An important parameter governing filtration may be the difference in specific gravities between the particulate matter and the aluminium. See Figure 2.39. Filtration efficiencies were observed to fall off somewhat as the difference in specific gravities tended to zero. An exception is possibly the 14-28 mesh deep bed filters. Where the difference was zero, the flow rate scarcely influences efficiency.

If the difference in specific gravity is zero, then the sedimentation force is zero. Filtration is then solely the result of the direct interception of particles by the filter walls [41].

b. Particle size and number

From Figure 2.39, we can see that high filtration efficiency is obtained with large particle sizes. However, large particles may block the filter.

c. Particle type

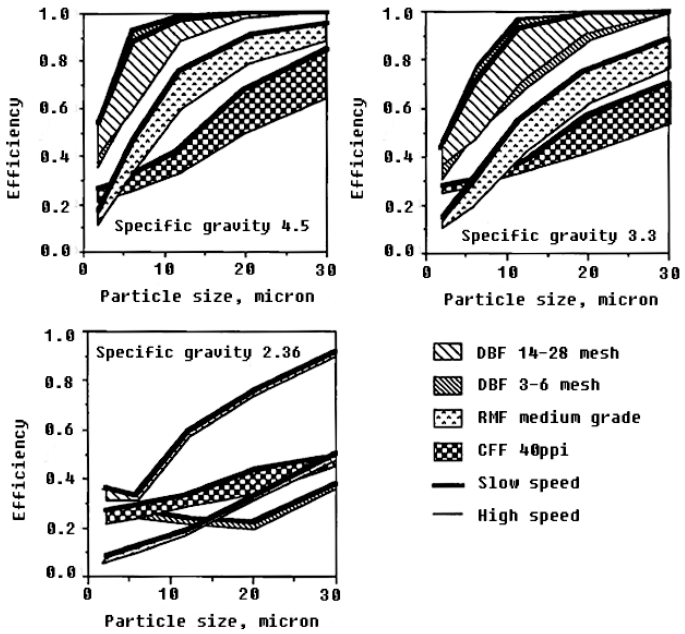

Figure 2.39 Effect of particle size on filtration efficiency for increasing specific gravity [41]

Al_2O_3 may give poorer wetting on aluminium than SiC. This may account for the more pronounced clustering effect of alumina particles. It was found that particle settling started immediately after stirring stopped in the Al-Al_2O_3 system, in the contrast to work with Al-Si -SiC where a settling front descended through the melt. It was observed metallographically that alumina particles formed clusters, together with entrained aluminium oxide films. The size of these clusters varied from single particles to over 100μm with various skeletal shapes [76].

2.1.5.2 Effect of filter parameters

a. Type of filter

In the case of specific gravity differing from that of liquid aluminium, significant differences were found for which type of filter was effective. It is possible to classify

the various types in order of decreasing efficiency, as deep bed (DBF), rigid media (RMF), and ceramic foam (CFF) [41].

b. Filter materials

C. Dupuis et al. [74] find that filtration efficiencies of phosphate bonded CFF and a fully sintered alumina ceramic filter are 6-42% and 6-48%, respectively, with flow rate 30-35 kg/(m^2·s). There is no significant difference in filtration efficiency.

The literature [77, 78] shows that AlF_3 filter is effective for removing alkali metal, Na and Ca, whereas a Al_2O_3 filter is hardly involved in the removal.

c. Depth of filtration media

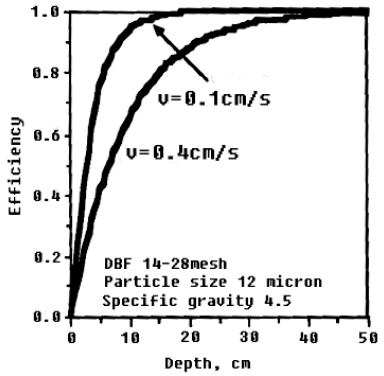

Figure 2.40 Effect of filter depth on filtration efficiency [41]

Figure 2.40 represents variations in efficiency with bed depth for 14-28 mesh media. With increasing filter depth, the filtration efficiency is increased. The equations describing these curves are exponential in form ($\eta=1-\exp(-\lambda L)$), the asymptote corresponding to maximum efficiency. The smaller the pores and the lower the speed of filtration, the more rapidly the curve reaches efficiency 1.

d. Pore size

From Table 2.3, it can be seen that the mean filtration efficiency increases as we move to finer pores. The filter efficiency performance range narrows (reliability increases) and the standard deviation of efficiency decreases for finer pores. The finer the filter, the smaller are the inclusions that will be removed. The last two columns show the inclusion size "cut-off" threshold for 75% and 95% total inclusion removal.

Table 2.3 In-line filtration system performance comparison [70]

CFF Type	Mean Filtr. efficiency [%]	Filtr. efficiency Range [%]	Standard Deviation	Reduct. of inclusions >40 µm [%]	Reduct. of inclusions >25 µm [%]	75% reduct. of inclusions >[µm]	95% reduct. of inclusions >[µm]
15"-30ppi	69	70	22.3	61		50	60
15"-50ppi	76	41	14.4	66		25	60
17"-30ppi	71	35	12.2	92	76	30	50
17"-50ppi	87	33	10.1	97	90	25	40
17"-65ppi	88	27	8.7	93	86	25	40
17"-80ppi	91	12	4.2	91	87	25	40

e. Location of filter

Filters are also used to remove turbulence and give smooth filling of moulds. In the study of casting by Bäckman Jonas [79], four different filter locations were investigated. The filters were sited as follows:

- L1, in the runner, immediately after the directional change
- L2, in the runner close to the first ingate
- L3, in the downsprue, just before the runner
- L4, in the corner between the downsprue and the runner

The filter width is 22 mm and the coarseness is 30 ppi. In Figure 2.41, the filling sequence for the different filter locations is shown for comparison.

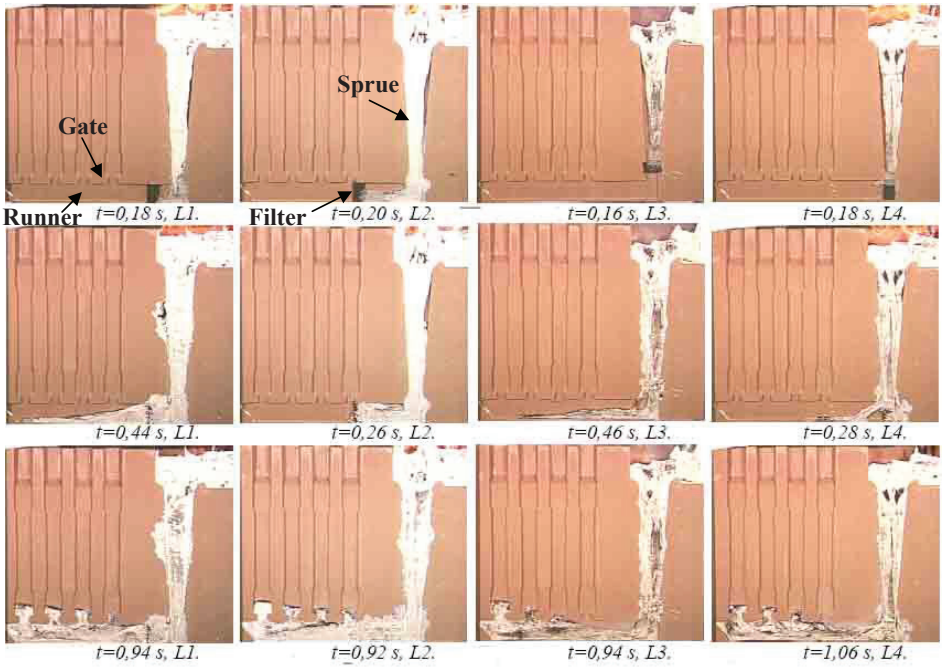

Figure 2.41 Location of the filter [79]

Filter location one (L1) shown in Figure 2.41 gives an early filling of the downsprue and furthermore a smooth filling of the runner. The runner is almost completely filled before the melt enters the gates.

Filter location two (L2) shown in Figure 2.41 gives a fairly turbulent filling of the volume prior to the filter, and the downsprue is not filled as early as in the case with filter location one. The filling sequence after the filter is smooth and similar to the filling sequence in the previous case.

Filter location three (L3) with the filter in the downsprue, shown in Figure 2.41 gives an early filling of the downsprue. After the filter the melt accelerates and the melt velocity is quite high. The high velocity of the melt leads to splashing of the melt in the runner, a late filling of the runner and a sequential filling of the specimens.

Filter location four (L4) shown in Figure 2.41 exhibits a similar filling behaviour as in the previous case with filter location three. The splashing effect in the runner after the filter is even more severe than in the case with filter location three.
So the best filter location has been shown to be in the runner directly after the downsprue, L1 when considering the influence of filters on the mould filling behaviour.

f. Filter strength

The strength [80] of a filter is classified in two ways, hot strength and cold strength. The cold strength of filters is important for handling and shipping purposes. It is important that pieces of the filters do not loosen and break off, as these may well end up in the casting. The filter must also have adequate strength to survive the closing of the mold. A filter must obviously have sufficient strength at molten metal temperatures, which is hot strength.

All foundries are different and some may not be so sensitive to some parameters than others. However, foam filters can offer good filtration efficiency, but they may lack consistency and strength [80].

2.1.5.3 Effect of process parameters

When a liquid suspension flows through a filter bed, the particulate matters deposit onto the surface of the grains of the filter medium. Such deposition is caused by various mechanisms, the four most important among them being diffusion, interception, gravity, and surface forces. Of these, diffusion dominates only for the submicron particles. Thus, for larger particles one can, by computational fluid dynamics, follow the particle trajectories to find what fraction of particulate matter is collected by the grains.

The principal forces [41] on particles are

i. The gravity (sedimentation) force
ii. The viscous drag exerted by the fluid, or fluid friction, F_f:

$$F_f = 12\pi\mu R_p U_s \tag{2.10}$$

iii. Van der Waals forces

a. Reynolds number

In a fluid, the Reynolds number is a dimensionless number that gives a measure of the ratio of inertial forces to viscous forces and quantifies the relative importance of these two types of forces for given flow conditions. For a particle and a cylinder, Re_p and Re_c are given by $2U_\infty R_p/\nu$ and $2U_\infty R/\nu$, respectively. Tian et al. [59] proposes a Reynolds number of a filter, Re_f, based on average web diameter of the filter, d_w.

$$\mathrm{Re}_f = U_\infty d_w / \nu \tag{2.11}$$

It may not be useful in describing the fluid flow inside a porous media. F.A. Acosta et al. [81] defines Re_f with pore diameter d_c and interstitial melt velocity (U_∞/ε).

$$\mathrm{Re}_f = (U_\infty / \varepsilon) d_c / \nu \tag{2.12}$$

Note that d_w and d_c here can be slightly different. C. Tian [59] describes the filter in a terms of "short cylinders of various orientation" , Acosta et al.[81] as "the collection of cells".

Increase of the flow rate may lead to a decrease in filtration efficiency as shown in Figure 2.46. Around 90% and 60% to 20% filtration efficiency were observed at high and low speed respectively.

b. The filtration efficiency

The filtration efficiency is defined as follows:

$$E = \frac{c_{in} - c_{out}}{c_{in}} \tag{2.13}$$

In the initial stage of filtration, the concentration profile throughout the filter can be described by an exponential law. Then, the initial filtration efficiency satisfies:

$$E_0 = 1 - \exp(-\lambda_0 L) \tag{2.14}$$

The filtration period where the filtration coefficient λ remains constant is known as initial or short-term filtration, while the period where the accumulation of particles starts to play an effect on the value of the filtration coefficient is known as the aging or long-term filtration period.

c. The relative size number

The relative size number N_R is defined as [82]:

$$N_R = R_p / R \tag{2.15}$$

A relation between λ_0 and N_R is shown in Figure 2.42. Whatever the value of N_G, Riviere et al. [83] observe in Figure 2.42 that $\lambda_0 L$ (and thus removal efficiency) increases for larger values of N_R. Larger values of N_R mean either larger inclusion diameter or smaller filter arm size.

Riviere et al. [83] used the filter cross section in the flow direction to create a numerical representation of a CFF. The flow rate is computed over the whole complex void space of the filter using the lattice-Boltzmann method. The trajectory analysis is derived by applying Newton's second law to suspended inclusions in the fluid flow.

The authors do not seem to take wall effects into account. Thus hydrodynamic effects such as lift forces are neglected.

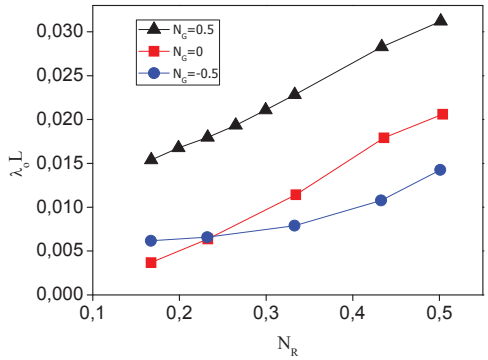

Figure 2.42 Dependence of initial filter coefficient $\lambda_0 L$ on the relative size number N_R [83] for neutrally buoyant inclusions

See N_G from Equ.(2.16).

As expected, the probability of an inclusion following the fluid streamline hitting the filter surface increases with its size and with a finer filter. As a consequence, small inclusions (small N_R) penetrate deeper into the filter as illustrated in Figure 2.43. Furthermore, inclusion collision zones are located along the preferential paths of melt streamlines. Finally, the maps of the initial capture probability density show that large inclusions are removed in the head region of the filter. This trend is observed in industry.

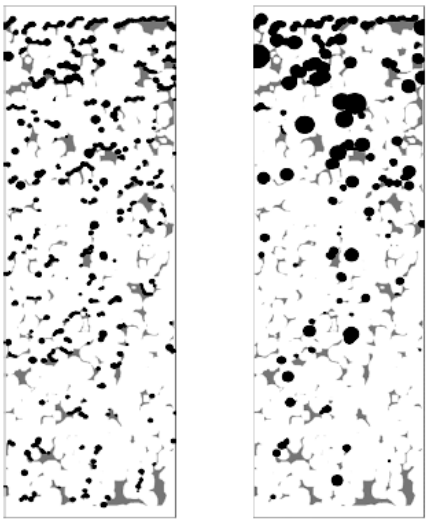

Figure 2.43 Maps of the initial capture probability density in a 50 ppi CFF for two values of the relative size number N_R [83]

The Reynolds number of the filter and the gravitational number are respectively equal to 4 and 0.15. Grey zones represent the filter and the diameters of the black circles are proportional to the number of inclusions.

d. The gravitational number

The gravitational number N_G is defined as [82]

$$N_G = 2R_p^2(\rho_p - \rho_l)g / 9\mu_s U_\infty \tag{2.16}$$

So $N_G>0$ when $\rho_p>\rho_l$, $N_G<0$ when $\rho_p<\rho_l$, and $N_G=0$ for neutrally buoyant inclusions.

Numerical simulations have been performed with a gravitational number N_G varying approximately between -0.5 and 0.5. The Reynolds number is $U_\infty l/\nu$ for the filter and the relative size number are respectively fixed at 4 and at 0.17. It is not clear how l is defined. The predicted relation between $\lambda_0 L$ and N_G is shown in Figure 2.44.

When $N_G>0$ (respectively $N_G<0$), the direction of the sedimentation velocity is the same as (opposite to) the direction of the main flow. Hence, for inclusions heavier than the melt, $N_G>0$ (respectively $N_G<0$) corresponds to a downward (respectively upward) filtration. The larger the difference between inclusion and melt densities, the better the removal efficiency is.

These findings may be illustrated by maps of the initial capture probability density for different values of the gravitational number (see Figure 2.45):

- Inclusion capture sites are not only located in the preferential paths of the flow, since new capture sites, located in the stagnant zones of the fluid, have appeared.
- If N_G is negative, the capture sites are located on the "downstream face" of the obstacles.

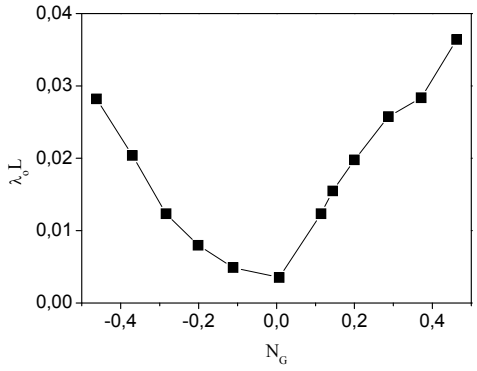

Figure 2.44 Predicted dependence of initial filter coefficient on gravitational number [83]. *N_R is equal to 0.17.*

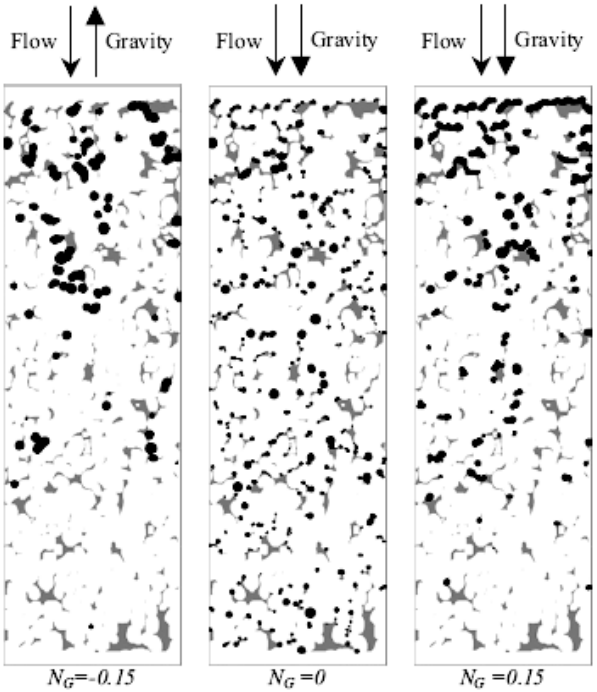

Figure 2.45 Maps of the initial capture probability density of a CFF of 50 ppi for three gravitational numbers N_G [83]

The Reynolds number of the filter, Re_f is equal to 4. Grey zones represent the filter and the diameters of the black circles diameter are proportional to the number of inclusion impacts.

For positive values of N_G, the penetration depth of the inclusions decreases when N_G increases. When N_G increases, the contribution of sedimentation to the filter coefficient rapidly becomes predominant. The contribution of interception mechanism corresponds to the value of the filter coefficient when N_G =0.

e. Filtration time

The nature of the filtration process may change with time, depending on the forces adhering particles to the filter materials [84]. Variations in filtration efficiencies with time were found in each case to be governed by the same major parameters. The filtration efficiency falls off over time and it is more obvious for the high flow rates in Figure 2.46. The filtration efficiency falls from 60% to 20% in 5000 min for high flow rate filtration. This may be due to release of inclusions during the process.

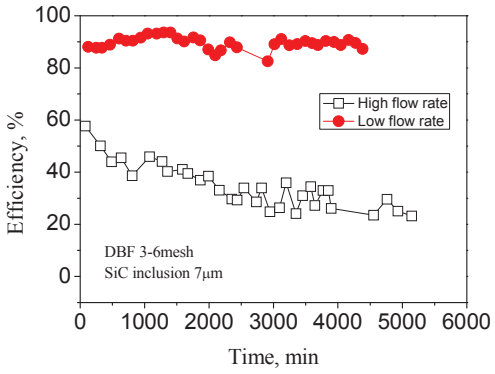

Figure 2.46 Variation in mean efficiency [41]

f. The filtration coefficient

The computed initial filtration coefficient decreased with melt velocity until reaching a minimum value at some critical melt velocity. At superficial velocities above this value, the filtration coefficient increases with the increase in melt velocity, as Figure 2.47. The critical velocity value depends on the particle size. For example for a particle size of 8 and 50 μm the critical values are around 3 and 13 mm/s respectively. The increment in the filtration coefficient is stated to be a consequence of the formation of a recirculatory flow pattern that pushes the particles toward the wall. Large particles are less sensitive to this recirculatory flow [81].

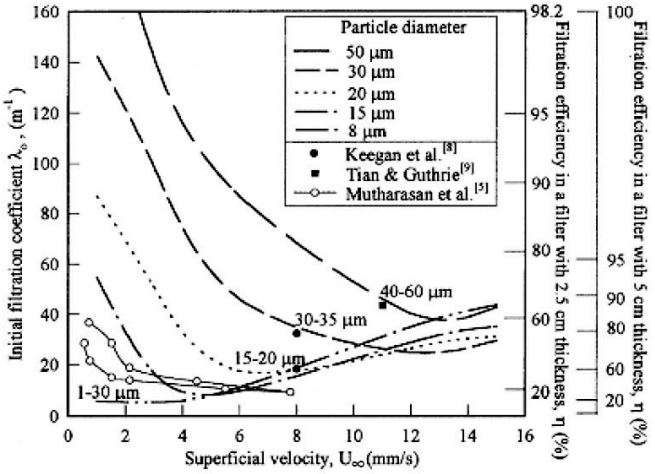

Figure 2.47 Computed initial filtration coefficient and filtration efficiencies for 30 ppi foam filters as a function of the melt velocity for various particle sizes [81]

In long-term filtration [85], the filtration coefficient depends not only on the particle size but also on concentration. For example, at a particle concentration of 1 ppm, the filtration coefficient for particles of 8 μm decreased with time as a consequence of the perturbed velocity field. This perturbation resulted from the particle accumulation on the pore wall and acted on the particles by pushing them away from the wall. The computed trajectories for particles of 50μm diameter were practically not sensitive to the perturbed flow field obtained during the filtration of molten metal with a particle concentration of 1ppm. On the other hand, particle trajectory calculation of 10ppm and Reynolds number ($(U_\infty/\varepsilon)d_c/\nu$) of 32 indicated that the change of fluid velocity, produced by the already accumulated particles in the pores, increased the filtration coefficient and efficiency. This result is a consequence of the particle cake formed at the windows, which trapped more incoming particles and decreased the flow rate. However, at a flow rate with a Reynolds number of 64, a decrease was computed in this coefficient for both particles size 8 and 50μm. At this flow rate, the domain did not favour the trapping of more incoming particles and did not decrease the flow rate either.

2.1.6 Removal of Impurity Elements from Aluminium in Filtration

One kind of impurity element filtration device is a downstream multi-stage filter [86], which has a continuous taper. It allowed any size filter between 12 and 19 inches to be used. It also gave the option of changing the gap between the top and the bottom filter. For removing salts, the gap was filled with the salt adsorption media pellets-alpha alumina bonded with frit or gamma alumina with boron nitride. The salts are readily adsorbed by capillary action because they do wet with media. Casts with the media averaged 78% reduction while casts with conventional filters alone averaged 42% reduction of impurity element. In the experiments, salts were significantly reduced by the use of salt adsorption media. The addition of salt adsorption media to the dual stage

filtration system caused no operational problem in preheating, priming, running, or removing the filters.

An "active" AlF_3 filter unit for removing Na and Ca has been studied by Görner et al. [77, 78]. The amount of Na removal increased with increasing Na concentration at the inlet. Na removal was from 6% to 59% for the conventional Al_2O_3 reference filter and from 87.5% to 99% for the "active" filter. Ca removal was from 5% to 47% for the conventional filter and from 91% to 99% for the "active" filter. Removal efficiencies for Na and Ca by the AlF_3 "active" filter as high as 98% have been achieved. Removal of Na by the AlF_3"active" filter is large compared to the Ca removal. The explanation seems to be a difference in diffusion rates for Na and Ca away from the melt-filter interface and into the bulk filter grain. Whereas the Na compound was found throughout the bulk AlF_3, Ca and its compound could be found only at and close to the surface of the filter grain with a steep gradient in concentration inwards.

Na in Figure 2.48 is enriched throughout the bulk AlF_3 and a layer covering the surface of the filter again. In this layer, Na has been found as elemental Na and as part of fluorine bearing compounds (NaF and NaAl). The flake-like Na spots throughout the bulk AlF_3 and its surface belong to a (NaAlF) compound previously determined as $Na_5Al_3F_{14}$ (chiolite).

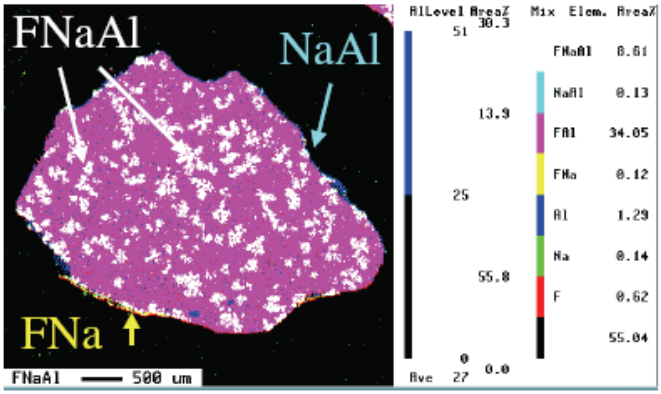

Figure 2.48 Electron probe mapping tracing Na over the cross section of an AlF_3 "active" filter grain removing Na and Ca

Ca in Figure 2.49 could be detected only in a layer at the surface and in the bulk AlF_3 close to the surface of the "active" filter grain. There is a steep gradient in concentration of Ca down from the surface. The distribution pattern for Na in Figure 2.48 gives reason to expect that Na and/or its reaction products are transported away from the melt-filter interface much faster compared to Ca.

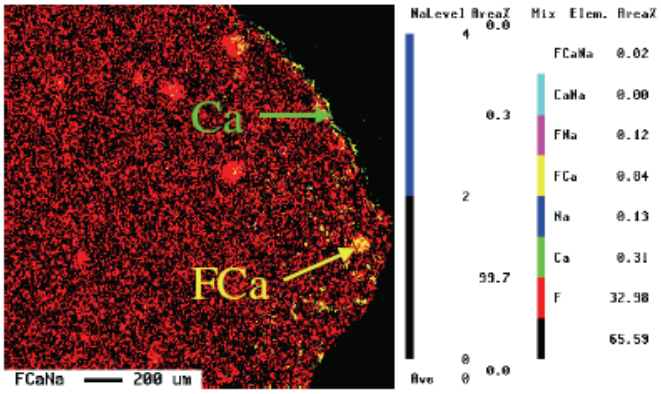

Figure 2.49 Electron prob mapping tracing Ca over the cross section of an AlF_3 "active" filter grain [77].

2.1.7 Detection Methods of Inclusions in Aluminium

Apart from mid and end-product performance results, there remain essentially three major approaches to measuring metal cleanliness [87]:

- Chemical analysis
- Metallographic Evaluation
- Techniques based upon physical principles.

2.1.7.1 Chemical method

Attempts at direct wet chemical or instrumental analysis of inclusions in aluminium have met with very limited success. This is due, in large measure to the very low concentration of inclusions, their non-uniform distribution and to the fact that the measurement of the bulk concentration of an element or compounds reveals nothing about how it is distributed within the sample. For example, no correlation has been found between the oxygen concentration (determined by neutron activation analysis) and the inclusion level ($2R_p$>20µm) in the melt. Typical oxygen levels in aluminium range between 5 to 50 ppm with most of this present either in the surface oxide or in submicron sized films.

Selective dissolution of the aluminium matrix followed by gravimetric determination of the residue has been reported. Result showed a wide degree of scatter in duplicate samples and no correlation was found between the mass of the residue and metal processing (filtration). Attempts at Alcan to analyze extraction residues by means of a counter gave no correlation between the results obtained and those provided by a metallographic technique. It was concluded that the artifacts generated in the dissolution steps completely overwhelm the actual inclusion concentration present in the metal.

2.1.7.2 Metallographic method

PoDFA

The most obvious method of assessing the inclusion content of aluminium is undoubtedly the direct examination of polished sections. However, as anyone who has ever examined a macro-section of a DC cast ingot can attest, some method of pre-concentration is required in order to observe any significant number of inclusions within a reasonable area.

Pre-concentration of inclusions by filtration has been reported by a number of authors. Figure 2.50 outlines the principle of the test of PoDFA (Porous Disc Filtration Apparatus). Metal with inclusions will be concentrated in a fine filter disk until a certain amount, e.g. 1.5 kg of metal has been filtered. The PoDFA samples containing the unfiltered part of the metal (about 5 mm) in contact with the filter were hot mounted in Bakelite and polished to a mirror-like finish. Using the grid method, the total inclusion area was obtained. This area was then divided by the mass of the metal that had passed through the filter (about 1.5 kg). The total inclusion concentration area per kilogram was calculated using the formula [14]:

$$T.[inclusion] = \frac{A_r \times a}{M} \times \frac{L_n}{L_m} \tag{2.17}$$

Where the inclusions were classified into two categories:

1. Total inclusions that take into account all types of inclusions existing in the 'cake' above the filter, and
2. Harmful inclusions which are the sum of Al_4C_3 greater than 3 μm, dispersed Al_2O_3, MgO, $MgAl_2O_4$, and potential chlorides (fine Al_4C_3 inclusions of 3 μm or less and TiB_2 have no harmful effect on the alloy mechanical properties).

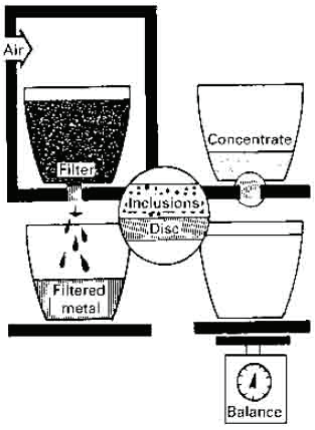

Figure 2.50 Principle of PoDFA [14]

By rigidly standardizing all aspects of materials and procedure it has been possible to reduce the variability of the results to the extent that the quantity (area) of residue present on the filter disc can be used to set release criteria for critical products [14]. The technique can also distinguish inclusions type and differentiate for instance between the level of borides, carbides and spinels present within an individual sample. This latter, qualitative, aspect of the technique has proved invaluable in establishing the cause of problems in unsatisfactory metal.

Oxides (films or clusters) are the most influential parameter in determining the filtration time when using the PoDFA technique. However, during sampling, it is rather difficult to separate the individual effects of inclusions and oxides on the filtration time, and even more so if the molten metal is disturbed or not properly skimmed [88].

2.1.7.3 On-line/ physical methods

LiMCA

Although the PoDFA technique is a powerful tool in determining not only the inclusion densities but also the inclusions, the process is fairly demanding. Thus, an on-line measuring apparatus, e.g., LiMCA/ LiMCA II, may be recommended, especially in the preparation of critical components for aeronautical applications [88].

The LiMCA (Liquid Metal Cleanliness Analyzer) technique is based on the Electric Sensing Zone (ESZ) principle, in which a constant current is maintained between two electrodes that are separated physically by an electrically insulating sampling tube. A 300 µm orifice within the non-conductive tube wall allows molten aluminium to flow into, and out of, the tube in a cyclic manner. This cycling sequence is controlled pneumatically by a differential pressure control system. When a non-conductive particle passes through the 300µm orifice, the resistance within the ESZ rises, causing a voltage pulse. See Figure 2.51.

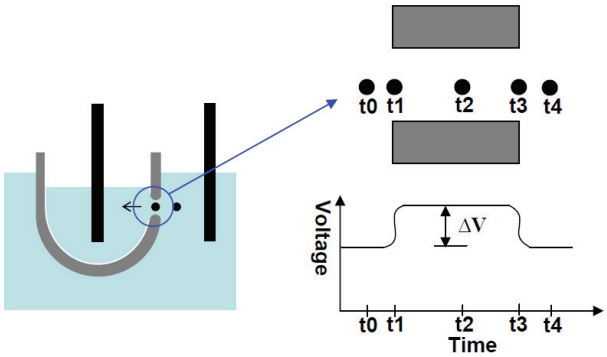

Figure 2.51 LiMCA II [89]

Since every particle registers as a pulse when passing through the ESZ, and non-conductive particles of the same size but of different type give rise to voltage pulses of the same magnitude, it has previously been impossible to discriminate between different types of inclusions within a melt. In the aluminium industry, degassing units generate micro bubbles and micro droplets of salt in molten aluminium. These relatively harmless micro-bubbles and micro-droplets interfere with the LiMCA probe and its inclusion counts. In order to attempt particle discrimination, the analogue LiMCA system was updated with Digital Signal Processing (DSP) technology to extract more information from particle signals besides pulse height. Using the McGill DSP system, each pulse was characterized by not only the peak height, but six other pulse parameters (start slope, end slope, time to maximum voltage, total signal duration, start time and end time). A previous study using an aqueous based ESZ system confirmed for the first time, both theoretically and experimentally, that inclusions of different density could be discriminated on the basis of differently shaped voltage transients generated during their passage through the electric sensing zone. The possibility of inclusion discrimination using DSP technology for molten aluminium remains to be addressed.

Some measuring methods of metal cleanliness are compared in Table 2.4. Compared with other techniques, such as sedimentation, filtration and metallography, which require considerable amounts of labour and time, the LiMCA [90] method has the advantage of providing not only information on the volume concentration of inclusions, but also on the size distribution of inclusions immediately and quantitatively.

Table 2.4 Main inclusion assessment methods for Al [64, 87, 91-93]

	PoDFA	Prefil-Footprinter	LAIS	LiMCA/ LiMCA II
Driving force	Pressure	Pressure	Vacuum	Pressure
Method for capturing inclusions	Filtration	Filtration	Filtration	Filtration
Method for sensoring inclusions	Metallographic technology	Metallographic technology	Metallographic technology	Electrical resistance
Detective range of inclusions	Depending on filter pore size	Depending on filter pore size	Depending on filter pore size	15 μm <d<140 μm
Provided information	Qualitative information, such as type of inclusions	Qualitative information, such as type of inclusions	Qualitative and qualitative information, such as type and concentration of inclusions	Quantitative and qualitative information, such as concentration, size distribution and type of inclusions
Advantage	Better indicator of inclusion content	Based on PoDFA , on-line	Similar to PoDFA	On-line
Disadvantage	Off-line	The result is not correlated well with PoDFA result and it needs improvement.	Off-line	• It does not provide information about the type of inclusions; • Cost of it is high; • Non-conducting inclusions of the same size but of different chemical contents (inclusion and gas bubble) can not be distinguished; • it is not sensitive to inclusions smaller than 15 μm; • Orifices are often blocked; • It is a semi-continuous measuring method.

2.1.8 Summary

1. Filtration provides an effective way to remove undesirable inclusions from molten aluminium. The reliability of the filtration system increases as we move to finer pore filters. The larger the inclusions, the higher the filtration efficiency. A deep filter allows recapture of released inclusions in the lower part of filter and improves the filtration efficiency.
2. Filtration and bubble flotation are the most effective ways for removing inclusions in industry. Compared to bubble flotation, filtration has the advantages of less space, time, and capital requirements and gas pollution, but filtration has the disadvantages of aging and semi-continuous behaviour.
3. It is hard to avoid re-entrainment (detaching) of inclusions from the filter. So the filter should wet the inclusions. Improvement of filter strength (or quality) should be one of the main parts of filtration research.
4. A continuous and consistent pore size should be selected to achieve optimum processing conditions of filtration and treatment capacity.
5. The capturing mechanism of inclusions is not clearly understood, and removal of liquid inclusions is difficult. Research on the filtration fundamentals concerning molten aluminium, filter body, and inclusions is required.
6. Filters can be effective means to removal trace elements using coated/composite filter, but little work has been carried out. Removing inclusions and trace elements in the same filter is interesting.
7. Filtration is not a real continuous process due to blocking and aging. To improve the effect of filtration, the multi-stage filter, reverse filter, and coated filter should be studied in future work.
8. Improved in-line cleanliness measuring methods which can detect inclusions smaller than 15μm will become necessary for strict melt quality control.
9. Most of the models regard the CFF as a net of tubes, spheres, or cells. However, CFFs are basically made from an organic foam net immersed into a slurry of ceramics. This net is dried, heated, and the organics are burned off leaving a sintered skeleton ceramic filter. In this Ph.D work, this skeleton is regarded as a collection of branches or cylinders.

2.2 Wetting of Aluminium on Ceramics

2.2.1 Fundamentals of Wetting

The wetting of a ceramic material by a metallic melt is of importance in many technical applications, such as in the preparation of composites and in the refining of metal. To improve understanding of aluminium filtration mechanisms, the main results concerning wettability of ceramic materials and aluminium are discussed and summarized in the present section.

The work needed for reversible creation of additional surface of a liquid L in contact with a vapour V, identified by the term σ_{LV}, was defined by Gibbs (1961) as:

$$\sigma_{LV} = (\frac{\partial F_{LV}}{\partial \Omega})_{T,V,n_i} \tag{2.18}$$

Similarly, the solid/ vapour surface energy can be defined by

$$\sigma_{SV} = (\frac{\partial F_{SV}}{\partial \Omega})_{T,V,n_i} \tag{2.19}$$

For a monoatomic solid, σ_{SV} is proportional to the difference in potential energy between an atom on the surface and an atom in the bulk solid, which also gives the expression of the surface energy of a crystal.

$$\sigma_{SV} = \frac{H' - H}{\omega} \tag{2.20}$$

For pure A or B, which can be either two solids, two liquids or a solid and a liquid that have a unit cross-sectional area, the quantity σ_{LV} or σ_{SV} defines the work of cohesion W_c of A (caused by the intermolecular attraction between like-molecules within a body or substance that acts to unite them), when surrounded by a vapour phase V.

$$W_c^A = 2\sigma_{AV} \tag{2.21}$$

The work of adhesion (attraction between unlike molecules) defined by Dupre (1869) is

$$W_a = \sigma_{AV} + \sigma_{BV} - \sigma_{AB} \tag{2.22}$$

Consider a flat, un-deformable, perfectly smooth and chemically homogeneous solid surface in contact with a non-reactive liquid in the presence of a vapour phase. If the liquid does not completely cover the solid, the liquid surface will intersect the solid surface at a “contact angle” θ. Sometimes it is called wetting angle. Contact angle instead of wetting angle will be used in the current work. The equilibrium value of θ,

used to define the wetting behaviour of the liquid, obeys the classical equation of Young (1805):

$$\cos\theta_Y = \frac{\sigma_{SV} - \sigma_{SL}}{\sigma_{LV}} \tag{2.23}$$

We have not taken into account the effect of the curvature of the aluminium droplet [94, 95]. Normally, we agree that a contact angle less then 90^o will identify a wetting liquid, while a greater value will identify a non-wetting liquid. Zero contact angle will be considered as perfect wetting. The Young's equation is valid in the presence of a gravitational field for the configuration of a vertical plate, as indicated in Figure 2.52 [96].

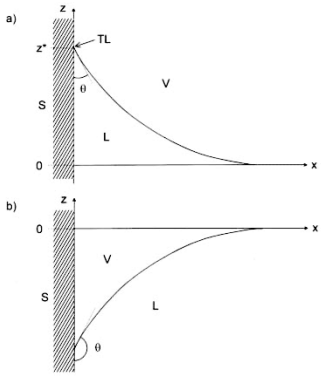

Figure 2.52 Meniscus rise on a vertical wall when θ< 90^o (a) and depression when θ >90^o (b) [96]

2.2.2 Parameters Which Influence the Wetting

a. Oxide film on aluminium drop

The surface of liquid aluminium oxidizes easily. An oxygen potential lager than 10^{-49} bar at 700 ^{o}C will promote the formation of an oxide film on liquid aluminium. The oxide film on an aluminium sample is always a problem in order to detect the real contact angle between aluminium and substrate. Removing the oxide film is one of the most serious issues in the contact angle measurement of aluminium.

Total pressure has an impact on de-oxidation, i.e. 1 bar argon with very low oxygen partial pressure may also cause oxide film, since a high total pressure hinders the diffusion of the de-oxidation product from the oxide film, $Al_2O(g)$.

De-oxidation and removal of oxide film will be discussed in Section 2.2.4.2. Vacuum conditions with very low oxygen partial pressure are recommended in the contact angle measurement of aluminium on ceramics. However, the use of high vacuum environments also enhances evaporation of the liquid aluminium and this can lead to anomalously low measured contact angles, from θ_a to θ_r, in Figure 2.53. The contact

angle after evaporation is reduced from θ_a to θ_r due to the reduced drop size. It seems that the base diameter does not change. The height of the sessile drop is reduced also.

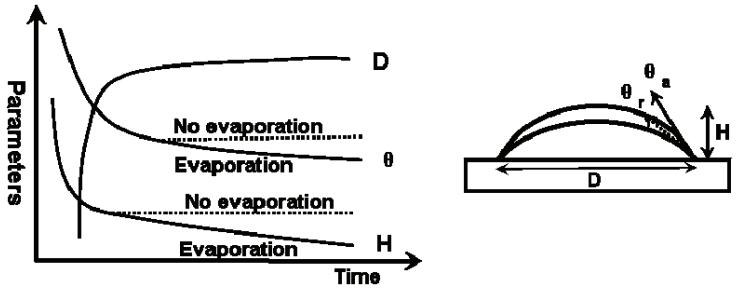

Figure 2.53 Schematic illustration of the effects of evaporation on parameters of a sessile drop

An advancing contact angle θ_a measured after spreading of the liquid on the solid is different from a receding contact angle θ_r reached when the liquid retreats [96]

This effect occurs quite frequently but the difference in the contact angle values usually lies within the range of measurement precision, unless the loss exceeds several percent. Such losses can occur when using volatile metals such as Mg or Zn or materials containing volatile components in sessile drop experiments.

b. Roughness

The roughness of solid surfaces affects wetting owing to two different effects: the first is the fact that the actual surface area is increased and the second is pinning of the triple line by sharp edges [96]. The surface roughness factor, R, was proposed by Wenzel [97]

$$R = \frac{cos\theta'}{cos\theta} \tag{2.24}$$

c. Mass

In Equ.(2.25), a value of $\beta>2$ is needed to obtain high accuracy measurements of σ_{LV} [96].

$$\beta = \frac{b^2 \rho g}{\sigma_{LV}} \tag{2.25}$$

This requirement can be satisfied using a drop with a liquid drop mass m_d for surface energy measurement,

$$m_d = (v/b)(\rho g)^{-1/2} {\sigma_{LV}}^{3/2} \beta^{3/2} \tag{2.26}$$

So the sessile drop mass should be larger then m_d and less then the designed maximum mass (or size) which fits the furnace.

d. Temperature

Better wetting with increased temperature appears to be a general rule in wetting. Rhee [97] proposed that a linear relation between cosθ and T is applicable to many liquid metal/ceramic systems.

$$\cos\theta = A + BT = 1 + B(T - T_{cs}) \tag{2.27}$$

Where A is constant, B is the slope of the line, and T_{cs} is defined as the critical temperature for spreading, i.e. the temperature at which θ approaches zero.

e. Holding time

De-oxidation of the oxide layer and evaporation of the liquid metal progresses with holding time. A decreasing contact angle will be detected with time.
In non-reactive systems, the spreading rate of aluminium drop on substrates is controlled by viscous flow and can be described (for $\theta<60^o$) by a power function of drop base radius R versus time t [98],

$$R^n \sim t \tag{2.28}$$

For reactive systems [98]

$$R^n - R_0^n \sim t \tag{2.29}$$

f. Penetration of aluminium into the substrate

When liquid penetrates into the substrate as indicated in Figure 2.54, the contact angle will be underestimated followed by sessile volume loss and spreading. Reactions at the interface are sometimes accompanied with penetration.

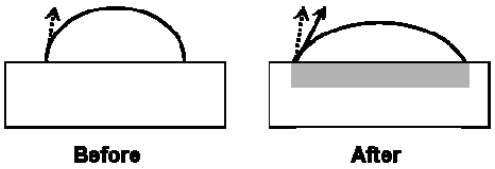

Figure 2.54 Penetration behaviour

g. "Different materials"

Various names of the same compound are often given in the literature, such as single crystal SiC, reaction bonded SiC, sintered SiC and α-Al_2O_3, β-Al_2O_3, Single crystallized Al_2O_3, sapphire, single crystallized sapphire, indicating different post treatment,

crystallization (surface orientation), defects and so on. Since they have diverse chemical structures and bondings, the contact angles with aluminium differ from each other.

The spreading process of aluminium on carbon will be strongly affected by atomic defects in carbon, which are much more numerous in vitreous carbon than in monocrystalline graphite or pyrocarbon in which the majority of graphitic hexagons are parallel to the substrate surface. Both the reaction and spreading kinetics on vitreous carbon are much faster than those on monocrystalline graphite and pyrocarbon [96].

In both C and Si-terminated faces of SiC, strong bonds with aluminium were found, but with higher adhesion energy for Al/C-SiC than Al/Si-SiC. Moreover, the Al/C-SiC bond was found to be predominantly covalent, while the Al/Si-SiC bond was rather metallic [99].

h. 2.2.9 Ridge

Ridges (see Figure 2.55), a few nanometers to several hundred nanometers in height [100] can form at the triple line in response to the vertical component of the surface tension in high-temperature systems. Ridges can largely slow or even stop spreading of the liquid. If the height of the ridge is small compared to the drop radius, the macroscopic contact angle, θ, still tends to match the one given by Young's equation. For longer times and/or small drops, fully 2-D equilibrium can be achieved [101].

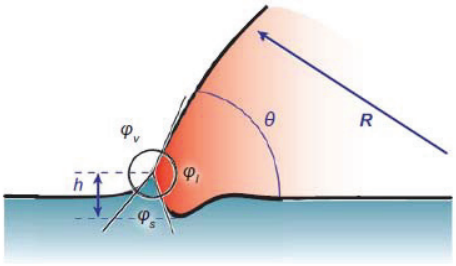

Figure 2.55 Schematic of ridge formed at the triple line [101]

2.2.3 Surface Energies and Adsorption

2.2.3.1 Surface energies

The driving force in wetting is the surface energy. Surface energy (unit: J/m^2) is also called surface tension or surface free energy with units J/m^2 or J/m. In Figure 2.56, two phases 1 and 2 are separated by a membrance AB uniformly stretched and of infinitesimal thickness. Along an element δd of the curve at a point C, there is a force σδd tangential to the interface. σ is called the surface tension or the interfacial tension at the point C. The interface is in a state of uniform tension [102] in which σ is perpendicular to the dividing line, has the same value irrespective of the direction of the line, and has the same value at all points of the interface. The force which minimizes the interface area between different phases is called surface tension in [102].

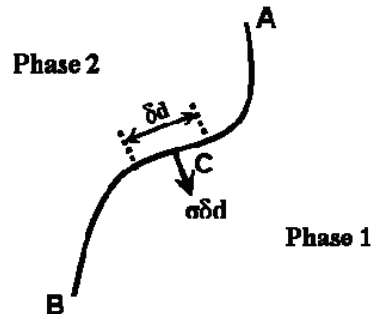

Figure 2.56 Surface tension

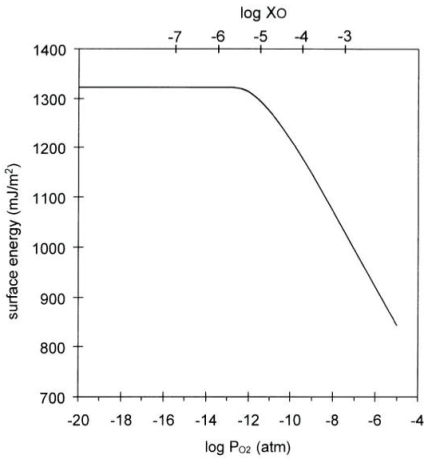

Figure 2.57 Experimental values of surface energy of liquid Cu-O mixtures as a function of partial pressure of oxygen P_{O2} or molar fraction of dissolved oxygen X_O at 1108°C.
Data from work reported in [96]

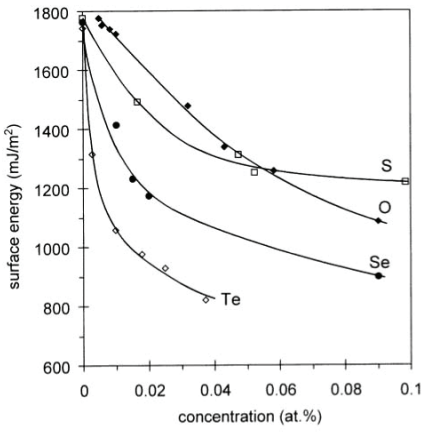

Figure 2.58 Surface energies of solutions of O, S, Se and Te in liquid Fe at 1600°C in [96]

The surface tension of a pure metal generally decreases with temperature. The presence of a surface active species decreases it further, but less at higher temperatures [102].

The surface energies of metals can be decreased by oxygen, as illustrated in Figure 2.57. This impurity can come from within the bulk of the liquid, from the gaseous environment or from the solid substrate used in wetting experiments. Oxygen dissolved in bulk metal has a strong interaction with the metal accompanied by charge transfer from the metal to oxygen. These interactions create strong perturbations of the metallic bond adjacent to an oxygen atom. There is a marked tendency for oxygen to segregate to the free surface where the perturbation is partially relaxed.

Figure 2.58 for the surface tension of Fe shows that O, S, Se and Te develop strong interactions with Fe and decrease their surface energies markedly.

Oxygen dissolved in liquid metals improves wetting even in concentrations as low as a few ppm or tens of ppm. To explain this effect, it was proposed that dissolved oxygen and metal atoms form clusters having a partially ionic character due to charge transfer from the metal to oxygen (Figure 2.59(a)). Such clusters can develop coulombic interactions with any ionic substrate and, for this reason, segregate to metal/oxide interfaces, thus improving wetting and thermodynamic adhesion. In Figure 2.59(a), the strong metal-oxide interaction results from partial rupture of the metallic bond in the cluster and its replacement by an ionic-type bonding. Formation of oxygen vacancies also can lead to a partial rupture of the ionic bond and it may be expected that some reduction in metal ions around a vacancy occur. In the diagram of Figure 2.59(b), the interface-active species is a cluster consisting of an oxygen vacancy surrounded by partially reduced metal ions. Segregation of such clusters to the oxide side of the interface ensures a gradual transition from oxidised metal atoms to metallic bonded atoms.

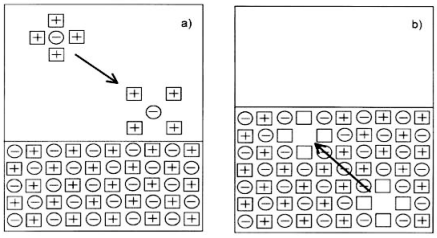

Figure 2.59 (a) Adsorption of oxygen clusters from the bulk metal at the metal/oxide interface can occur when P_{O2} is high. (b) Adsorption of a cluster centered on an oxygen vacancy from the bulk oxide at the interface can occur when P_{O2} is low.
For the sake of simplicity, total oxidation (case a) or total reduction (case b) of metal around oxygen atoms (case a) or vacancies (case b) has been assumed [96].

2.2.3.2 Adsorption

The basic mechanism of wetting is adsorption. Two types of adsorption behaviours should be distinguished, physical and chemical adsorption, in a liquid substrate system as sketched in Figure 2.60.

In physical adsorption (a), there is no reconstruction of the interface, and the liquid atoms or solvent atoms in liquid merely sit on the top of the substrate surface without displacing any underlying atom. The subsequent atoms from liquid sit on the previous monolayer due to the large affinity between like atoms. The attachment of aluminium on alumina substrate is according to this mechanism.

In physical adsorption (b), the liquid atoms or solvent atoms in liquid penetrate into the substrate until saturation, which will break the original atom bonding in substrate, but no displacement of substrate atoms takes place. The sessile volume of the liquid decreases with time due to the penetration. The liquid metal penetrates into the graphite before a chemical reaction happens.

In the (c) type of adsorption behaviour, sometimes called chemisorption, the liquid atoms or solvent atoms in liquid immerse into the substrate and realign with substrate atoms until saturation. In the chemisorption, a new atom bonding between new atom and substrate atom will be formed. The sessile volume of liquid decreases with time due to the penetration. Wettability depends on the new substrate and liquid. The interface monolayer is composed of both atoms from the liquid and the substrate. Better wetting is due to formation of the interface with the very large affinity between the atoms. A typical example is the Al-C system. Al_4C_3 is formed on the interface, which contributes to the better wetting.

Most chemical reactions (or adsorptions) involve the transfer of mass across an interface and the composition of that interface often has a determining role in controlling the kinetics of these reactions. The composition of grain boundaries, of metal-ceramic joints and of other composite interfaces may also have a strong effect on the mechanical properties of these systems [102]. The Gibbs adsorption equation is

$$d\sigma = -\frac{S^{\sigma}}{s}dT - \sum_{i=1}^{m}\Gamma_i du_i \tag{2.30}$$

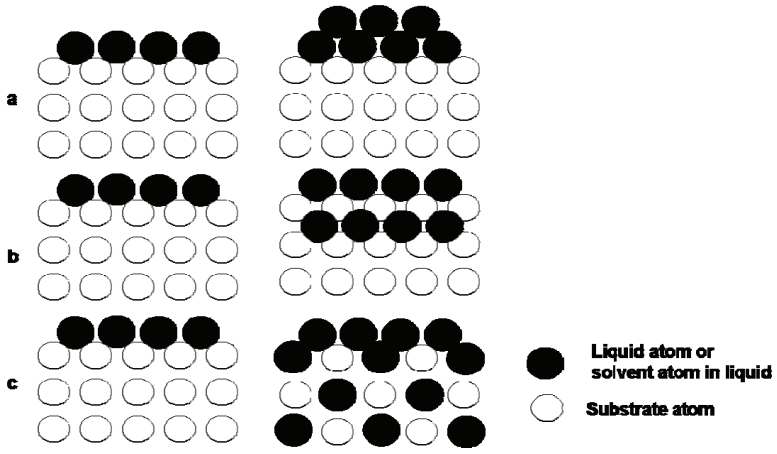

Figure 2.60 Adsorption behaviours at atomic scale

Physical adsorption: (a) Atoms absorbed merely sit on the top of the substrate surface. (b) Atoms absorbed penetrate into the substrate; Chemical adsorption: (c) Atoms absorbed and substrate atoms rearranged (the position or arrangement can be changed). ABAB type realignment is shown here.

The chemical bonding developed between aluminium and Al_2O_3 at the interface explains why the experimental work of adhesion for this metal (~900 mJ/m^2) deviates strongly from the corresponding Van der Waals value, 300 mJ/m^2, taken from the straight line of Figure 2.61.

The ease with which inclusions can attach themselves to the substrate depends on interface structure. We can imagine two different types of interface structures, as sketched in Figure 2.62. In the first, inclusion transfers from the liquid to solid takes

place over an uneven layer which comprises a diffuse interface, as Figure 2.62(a). It can form due to attachment of inclusions. In Figure 2.62 (b), it will be relatively hard to attach the first inclusion on a flat interface. But the capture becomes easier after that and the diffuse interface develops. We expect diffuse interfaces to adsorb more easily than flat interfaces.

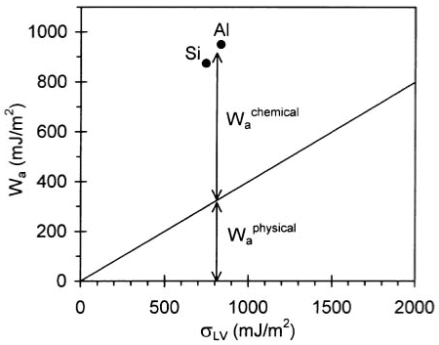

Figure 2.61 Experimental values of the work of adhesion versus the liquid surface energies for molten aluminium and Si on monocrystalline Al_2O_3. These values exceed significantly the values of the straight line for van der Waals bonded systems [96].
Van der Waals forces include attractions between atoms, molecules, and surfaces. They differ from covalent and ionic bonding in that they are caused by correlations in the fluctuating polarizations of nearby particles (a consequence of quantum dynamics). Van der Waals forces are relatively weak compared to normal chemical bonds.

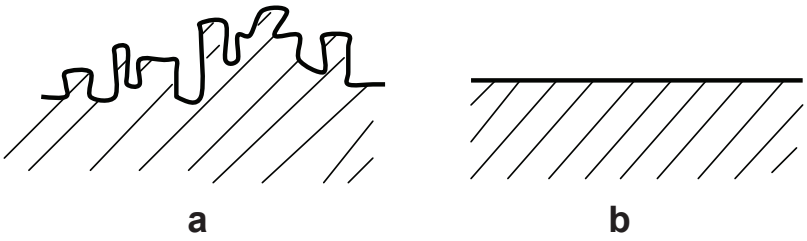

Figure 2.62 Adsorption behaviours at microscale
(a) Diffuse interface; (b) Flat interface.

2.2.4 Wetting Properties with Elements in Aluminium

2.2.4.1 Alloying elements

Wetting of aluminium alloys with ceramics has practical importance. Wide ranges of aluminium alloys are produced. Wetting of aluminium alloy with SiC has been investigated in [103]. A decreased contact angle with addition of Pb, Mg, Ca to pure aluminium has been measured. The Mg reacts with Al_2O_3 to form $MgAl_2O_4$ spinel at the interface, reducing σ_{SL} and σ_{LV}, due to the reactions,

$$3Mg(l) + Al_2O_3(s) = MgO(s) + 2Al(l) \quad (2.31)$$

$$3Mg(l) + 4Al_2O_3(s) = 3MgAl_2O_4(s) + 2Al(l) \quad (2.32)$$

which will rapidly change the oxide film. The same mechanism was elucidated for alloying elements Ca and Li [104]. But wetting is not significantly affected by Si addition [105, 106]. The progressive decrease in the contact angle with time is controlled by the dissolution of solid SiC in liquid aluminium and Al-Si alloy [104]. A reduction of contact angle of aluminium with ceramics has been achieved by adding Ti [104] and Cu [107]. The beneficial effect of Ti on wetting is believed to be due to its chemical reactivity with ceramic surfaces, producing a new phase of metallic oxide TiO, giving rise to a change in the chemistry of the metal ceramic interface.

2.2.4.2 Effect of oxygen

Since oxygen clusters cause a major perturbation of the structure and energy of the bulk metal, they are expected to segregate at two dimentional defects such as surfaces and interfaces, where the perturbation can be partially relaxed. This may explain the strong tendency for oxygen adsorption at both solid metal/vapour and liquid metal/vapour surfaces caused by the decrease in the surface energies. The adsorption energy at the metal/oxide interface i.e., the change in energy of the system when an oxygen atom segregates at the interface from the bulk, will be even higher in absolute value due to the ionic interactions between the clusters and the oxide surface (Figure 2.59a). Thus, the reduction of σ_{LV} due to oxygen adsorption will be lower than the reduction of σ_{SL} , resulting in an increase of the work of adhesion, $W_a = \sigma_{SV} + \sigma_{LV} - \sigma_{SL}$, and a decrease of θ, since $\cos\theta = (W_a/\sigma_{LV}) - 1$ [96].

a. Oxygen content in Al

The surface tension of the aluminium has been reported in two groups [108]: oxygen saturated aluminium and 'pure aluminium', i.e. with zero oxygen content. Low oxygen contents can be obtained at higher temperatures owing to the formation of $Al_2O(g)$ in reaction(2.42). Surface tension of the pure aluminium is appreciably higher than value for oxygen saturated aluminium [108]. Oxygen saturation of aluminium is considered to be the case in this work due to the low solubility of oxygen, around 1.43×10^{-4} at.% at 700°C [109].

b. Oxide films on Al

The surface of an aluminium sample oxidizes easily. On exposure to air an oxide coating about 20 Å thick forms immediately and increases to about 90 Å after a month [110]. The liquid aluminium covered by a film of Al_2O_3 results in an apparent contact angle of ~150º at 1000ºC in 1 atm Ar and 10^{-17} oxygen partial pressure [111]. A solid membrane of Al_2O_3 (melting point of 2072°C) acts as a bag and holds the liquid aluminium inside at the experimental temperature, giving a larger apparent contact angle.

Based on the ease of oxidation of aluminium it seems that the large discrepancies in contact angle measurements can be explained by the oxide film present on the liquid Al. The large variations observed for the contact angle may be caused by differences in the thickness of the initial oxide layer, holding times and above all differences in the ambient oxygen potential, whether in vacuum or in an inert atmosphere. It is therefore important to de-oxidize the aluminium before measuring the contact angle. Laurent et al. [39] propose that the de-oxidation of the oxide layer progresses in 3 stages, see Figure 2.63.

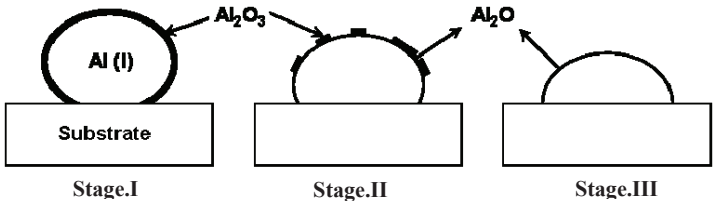

Figure 2.63 The de-oxidation of the oxide layer [39]

Stage.I: At the start, the de-oxidation process is based on the dissociative gasification of the alumina shell, reactions(2.37)-(2.42). When the oxygen partial pressure in the furnace is 10^{-5}-10^{-15} Pa (estimated vacuum ability of the sessile drop furnace), it is impossible to de-oxidize by dissociative gasification due to the extremely low equilibrium pressure of vapour species (See Figure 2.64).

Stage.II: As the gasification proceeds or if the oxide film is disrupted, the oxide layer is no longer a complete barrier between the aluminium metal and the gas phase, and then reaction(2.42) can take place. The sudden expansion of the aluminium drop by fast heating can cause cracks which increase the possibility that stage II occurs.

Stage.III: A completely de-oxidized drop of aluminium is in equilibrium with oxygen as follows:

$$2Al(l) + 1/2O_2 = Al_2O\ (g) \tag{2.33}$$

The real contact angle between aluminium and substrate can be determined in stage III and at the end of stage II. The de-oxidation time t_d for a monolayer of oxide is given by [39]

$$t_d = \frac{1}{\Omega_m(\phi_O^{ev} - \phi_O^i)} \tag{2.34}$$

Ω_m denotes the molar surface area of the oxide. Φ_o^{ev}, the flow of oxygen resulting from all evaporation process is given by [39]

$$\phi_O^{ev} = \frac{\alpha_{Al_2O} P_{Al_2O}^{eq}}{(2\pi m_{Al_2O} kT_{liq})^{1/2}} \tag{2.35}$$

Φ_o^i, the impinging flow of oxygen is given by [39]

$$\phi_O^i = \frac{2P_{O_2}^w}{(2\pi m_{O_2} kT_w)^{1/2}} \tag{2.36}$$

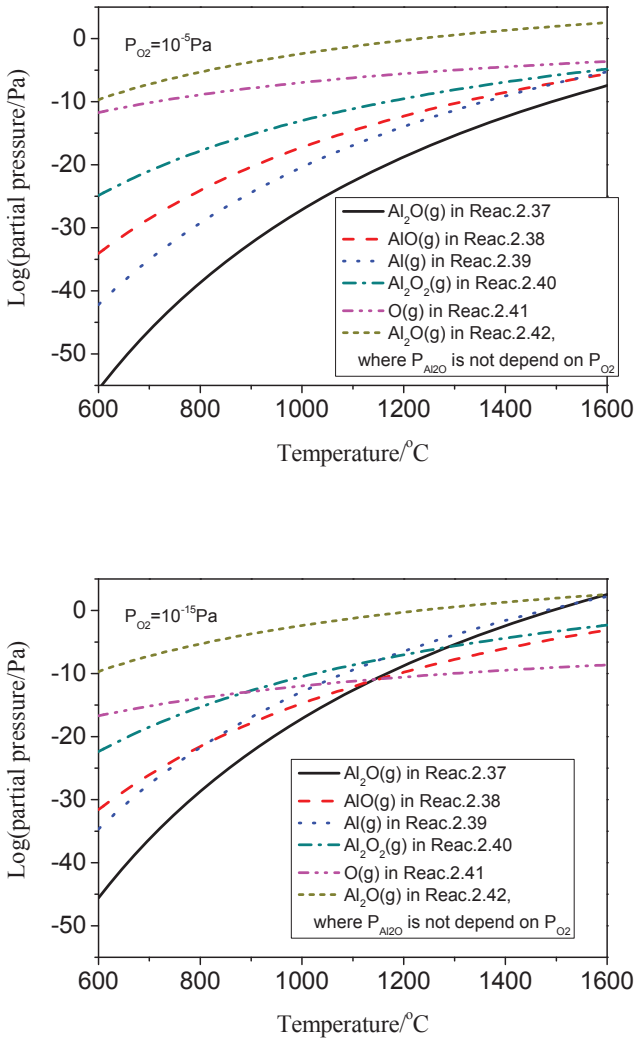

Figure 2.64 Al_2O_3 gasification and corresponding equilibrium pressure of vapour species: a) $P_{O2}=10^{-5}$Pa; b) $P_{O2}=10^{-15}$Pa.
Calculated by HSC 7.1 from Outotec

$$Al_2O_3 = Al_2O(g) + O_2(g) \quad (2.37)$$
$$Al_2O_3 = 2AlO(g) + 1/2O_2(g) \quad (2.38)$$
$$Al_2O_3 = 2Al(g) + 3/2O_2(g) \quad (2.39)$$
$$Al_2O_3 = Al_2O_2(g) + 1/2O_2(g) \quad (2.40)$$
$$1/2O_2(g) = O(g) \quad (2.41)$$
$$4Al(l) + Al_2O_3 = 3Al_2O(g) \quad (2.42)$$

The equilibrium partial pressure of $Al_2O(g)$, derived from reaction(2.42), plotted as a function of temperature is shown in Figure 2.65 [96]. For a given value of the partial pressure of oxygen in the furnace, there is a threshold temperature, T*, below which the oxide film thickens and above which it is eroded. Time t_d with temperature is shown in Figure 2.66 with unknown oxygen partial pressure and thickness of the oxide layer [39]. t_d sharply decreases with temperature to seconds at 1200K according to reaction(2.42). This can explain that the results obtained by the different authors become similar at higher temperature, as in Figure 2.67.

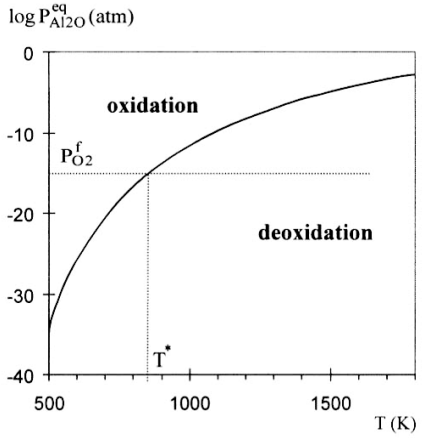

Figure 2.65 Equilibrium partial pressure of Al_2O, derived from reaction(2.42), plotted as a function of temperature [96].

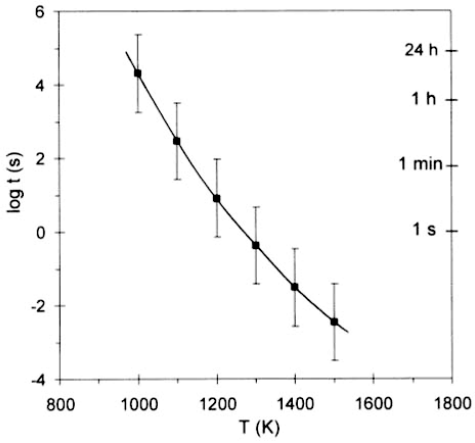

Figure 2.66 t_d at various temperatures The error bars are due to the uncertainty of the Gibbs energy of reaction(2.42) [39].

2.2.5 Wettability of Al-ceramic Systems

In many systems of aluminium and ceramics, the wetting of liquid aluminium on ceramic substrates is accompanied by reactions on interfaces. In this work, reactive systems of aluminium with SiC and graphite will be discussed as possible filter material choices. The Al-Al_2O_3 system is investigated as a non-reactive system, although it can be seen as a reactive system in [96] as (0001) faces of Al_2O_3 are known to lose oxygen, which leads to a two dimensional reconstruction of the surfaces in high vacuum at high temperature (approximately 1200°C). As discussed in Section 2.2.3.2, the common rule for ceramics is that reactive systems are more wettable than non-reactive systems.

2.2.5.1 Al-Al_2O_3 system

Understanding the wetting behaviour of aluminium on ceramics is crucial for metal-ceramic production of composites. The wettability of aluminium on ceramics also plays an important role in aluminium filtration. Alumina is the most common filter material and is one of the most typical inclusions. Contact angles between alumina and molten aluminium are used to characterize wetting. The wettability between aluminium and alumina contributes to describe how the metal and alumina inclusions or metal and alumina filter material interact.

Table 2.5 Equilibrium contact angle of molten Al on Al_2O_3 in the literature [12, 39, 112-120]

Reference	Atmosphere	Al and Substrate	Temperature [ºC]	Contact angle [º]	Remarks
John and Hausner,1986 [112]	Ar with 10^{-49} bar O_2 partial pressure	99.99% pure Al and single crystal Al_2O_3	700	90	The sessile drop method Alumina furnace tube was used.
Klinter et al.,2008 [113]	High purity Ar. Vacuum better than 10^{-9} bar	99.99% pure Al and 99.6% polycrystalline alumina	670	115	Injection technique*
			700	93	Graphite syringe and mullite furnace tube were used.
			730	94	
			750	87	
			800	88	
		99.99% pure Al and a-plane (11$\underline{2}$0) sapphire	670	122	
			700	91	
			730	84	
			750	86	
			800	86	
			850	~100	
			1000	~87	
Wang and Wu, 1994 [114]	1.2×10^{-9} bar vacuum 10^{-49} bar O_2 partial pressure at 700°C	Al and sapphire (001)	700	90±2	Injection technique Zr oxygen getter was located in the alumina tube.
Naidich et al.,1983 [115]	Vacuum, but not specified in the paper	99.995% pure Al and technical leuco sapphire with 99.97%Al_2O_3	700	~90	The sessile drop method
			800	~85	
			900	~82	
			1000	~80	
			1100	~78	
			1200	~65	
Ksiazek et al.,2002 [116]	Dynamic vacuum of 2×10^{-8} bar	99.9999% pure Al and α-Al_2O_3 (>99.9%)	680	126	The sessile drop method
			750	121	
			850	96	
			950	79	
			1050	74	

Reference	Atmosphere	Al and Substrate	Temperature [ºC]	Contact angle [°]	Remarks
Shen et al.,2003[117]	Vacuum about 5×10^{-9} bar High pure Ar+3%H_2	Al and (0001) α -Al_2O_3 single crystal (99.99%)	700 800 900 1000 1100	127 130 120 110 97	The sessile drop method Ta heater was used. Authors said that the wetting is a non-equilibrium phenomenon due to continuous oxidation.
Wolf et al.,1966[118]	1.3×10^{-7} bar vacuum	Commercially pure Al (99.1%) and single crystal sapphire	700 815 926 1037 1150	167 142 115 90 70	The sessile drop method
Carnahan et al., 1958 [12]	1.3×10^{-7} bar vacuum	99.99% pure Al and recrystallized Al_2O_3 of Triangle RR quality	1243±4	60	The sessile drop method Mo resistance heating elements were used. Authors did not attain a steady value at a given temp.
Brennan and Pask, 1968[119]	(2.6-11.7) $\times10^{-8}$ bar Vacuum	99.999% pure Al and sapphire (single crystal Al_2O_3), "water soaked" **	800 900	90 45	The sessile drop method Zr oxygen getter was located in the graphite tube.
		99.999% pure Al and sapphire (single crystal Al_2O_3), "heat treated" ***	800 900	76 55	
Nicholas, 1968[120]	Vacuum better than 3.9×10^{-8} bar	Al and AL23 grade alumina (>99.5%)	670 1018	158 90	The sessile drop method
V. Laurent et al., 1988 [39]	Total pressure of 4×10^{-9} bar and O_2 partial pressure about 10^{-20} bar	Al and single crystal Al_2O_3	660 1000	103±6 86±6	The sessile drop method Mo resistance furnace was used.

* *Injection technique: The metal drop is forced onto a substrate mechanically from a syringe once the experimental conditions are reached.*
** *Water soaked: The substrates were soaked in water at room temperature for about a week.*
*** *Heat treated: The substrates were preheated in vacuum at 1300°C just before the experiment.*

[12, 39, 112-120] measured the wettability between molten aluminium and solid alumina. Table 2.5 summarizes the measurements available in the literature. There is considerable spread in the experimental results. Therefore, we have attempted to examine the contact angle under high vacuum conditions where the oxide film on aluminium is eliminated.

All the experiments in Table I were performed under vacuum (10^{-9}-10^{-7} bar), except those of John and Hausner [112], who measured the contact angle under argon atmosphere with 10^{-49} bar oxygen partial pressure. Naidich et al. [115] reported their experimental results but did not mention the vacuum conditions. Even though the contact angles tend to decrease with the increase of temperature, the results are scattered (Figure 2.67). For example, contact angles at 700ºC measured by different authors were in the range of 88º to 167º. The scatter may be caused mainly by variations in the specimens (different purity, pre-treatment, crystallization, surface orientation, etc.) used in measurements and dissimilar experimental conditions (vacuum, oxygen potential, and the material in furnace tube), as listed in Table 2.5. The high vacuum work tends to give low contact angles as indicated by the solid dots for below 10^{-9} bar vacuum in Figure 2.67. In our experience, an aluminium sessile drop is always covered by an oxide layer when 1 bar argon with 10^{-22} to 10^{-21} bar oxygen partial pressure is employed. This leads to the anomalous high contact angle. For instance, a contact angle of 150º was measured at 1000ºC for the Al-Al_2O_3 system in our early experimental work [111].

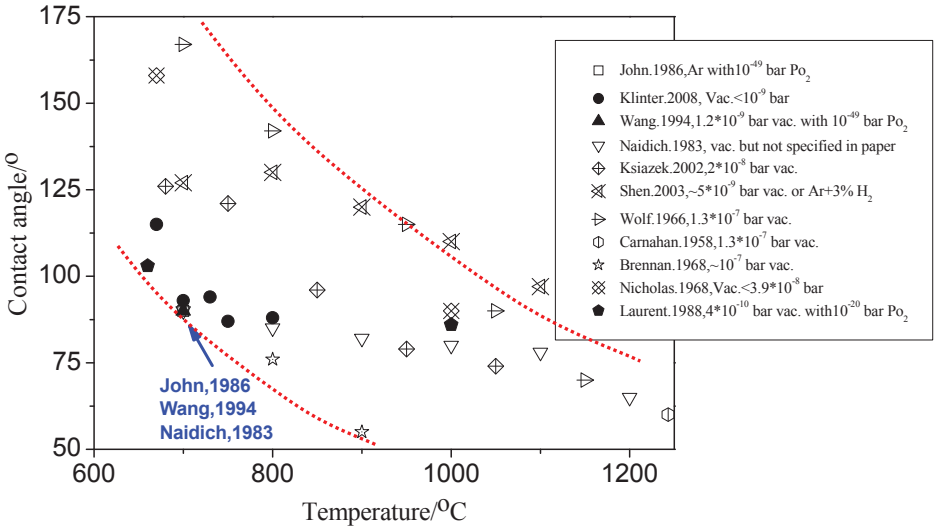

Figure 2.67 Contact angle of Al on Al_2O_3 as function of temperature reported in [12, 39, 112-120]

2.2.5.2 Al-graphite system

In the last decades, several studies had been devoted to the wetting behaviour of the Al-graphite system [121-123]. Single crystal graphite, SU-2000 vitreous carbon, and pyrographite all had contact angles around 100° at 700-900°C [115]. The wetting of the Al-graphite materials was found to depend particularly strongly on temperature.

As a reactive wetting system, it was agreed that 1) the final or steady contact angle is equal or very close to the equilibrium contact angle of the liquid on the reaction product Al_4C_3 [121]; Tomsia et al. [6] found that the wetting behaviour of the reaction product is governed by the formation of adsorption layers at the interface, rather than by the subsequent nucleation and growth of the reaction product; 2) wettability would not be improved by the chemical reaction itself. The interatomic force is not correlated to the Gibbs free energy as an exchange of atoms is involved in a chemical reaction [122]. The Al-graphite system has the peculiarity that 1) the final contact angle, θ_2 on reaction product Al_4C_3 is much lower than the initial contact angle, θ_0 on the original substrate graphite; and 2) reaction product Al_4C_3 crystals are brittle and highly sensitive to moisture. Inclusions of this type will promote accelerated fatigue crack growth rates in aluminium due to their hydrophilic nature [123].

The solubility of graphite in molten aluminium is only a few ppm at 900°C and 30ppm at 1000°C [107]. At temperatures higher than the melting point of aluminium, aluminium reacts with graphite to form Al_4C_3 as indicated in Figure 2.68.

N. Eustathopoulos [98] pointed out that the rate of spreading is controlled by the rate of the chemical reaction at the solid/liquid/vapour triple line after the drop de-oxidation. The good wetting of aluminium on Al_4C_3 is attributed to the high adhesion energy of aluminium on Al_4C_3 since aluminium has a low sp-orbital capable of forming covalent bonds.

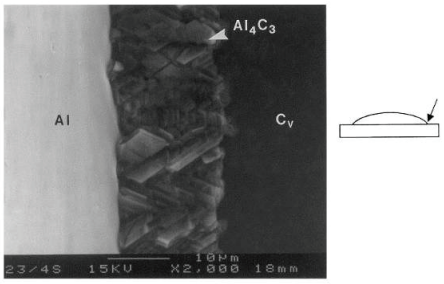

Figure 2.68 Micrograph taken from above of an Al/vitreous carbon sample cooled from 827 °C, which show an Al_4C_3 layer close to the triple line [1]

2.2.5.3 Al-SiC system

The properties of the Al-SiC interface are of basic concern in aluminium filtration with SiC filter materials. Wettabilities between molten aluminium and single crystal SiC [124], reaction bonded SiC [125] and sintered SiC [125, 126] reported in the literature

are summarized in Table 2.6. The wettability may change with 'different materials', for example, due to the various preparation processes and the various sintering aids for SiC. Figure 2.69 plots the results in Table 2.6. Aluminium has a decreasing contact angle on SiC with increasing temperature. Reaction bonded SiC has better wettability with aluminium than single crystal SiC and sintered SiC. For example reaction bonded SiC, single crystal SiC, and sintered SiC have contact angles of 41°, 60°, and 107° respectively at 830°C as shown in Figure 2.69.

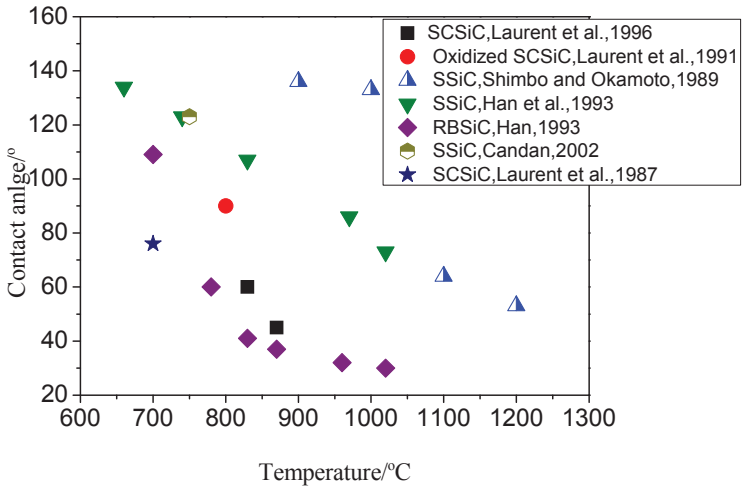

Figure 2.69 The equilibrium contact angles vs. temperature for Al on SiC from the literature [103, 105, 124-127]

SSiC- sintered SiC; RBSiC- reaction bonded SiC; SCSiC- single crystal SiC

Table 2.6 The contact angles of molten Al on SiC in the literature [103, 105, 124-127]

Reference	Atmosphere	Al and Substrate	Temperature [℃]	Contact angle[°]	Remarks
Laurent et al., 1996 [124]	Total pressure less than 5×10^{-10} bar	99.9999% pure Al and Single crystal a-SiC	830	60	The sessile drop method
			870	45	The stainless steel chamber was used.
Laurent et al., 1991 [127]	Total pressure less than 5×10^{-10} bar	Al and oxidized single crystal SiC	800	90	The sessile drop method The stainless steel chamber was used.
Shimbo and Okamoto,1989 [126]	Total pressure of 1.33×10^{-8} bar	High purity Al and pressureless sintered SiC	900	136	The sessile drop method
			1000	133	
			1100	64	
			1200	53	
Han et al, 1993 [125]	Total pressure of 10^{-8}-10^{-7} bar	99.99% pure Al and Sintered SiC	660	134	The sessile drop method
			740	123	The alumina boat was used.
			830	101	
			970	86	
			1020	73	
Han et al, 1993 [125]	Total pressure of 10^{-8}-10^{-7} bar	99.99% pure Al and reaction bonded SiC	700	109	The sessile drop method
			780	60	The alumina boat was used.
			830	41	
			870	37	
			960	32	
			1020	30	
Candan, 2002 [103]	Total pressure of 10^{-8}-10^{-7} bar	99.95% pure Al and sintered SiC	750	123	The sessile drop method The alumina boat was used.
Laurent et al., 1987 [105]	Total pressure of 10^{-9}-10^{-10} bar	99.9999% pure Al and Single crystal SiC	700	76	The sessile drop method The stainless steel chamber was used.

SiC with silica layer

In aluminium filtration, filters are primed to allow metal to flow through the filter without freezing. The SiC filter will be oxidized, during pre-heating. This oxidation may affect the wetting behaviour. The oxidation of SiC is very slow at room temperature [128], but SiC will react with air to form a silica-rich surface layer at temperatures above 700°C. SiC oxidation is controlled by the diffusion of oxygen molecules/ions through the thin oxide film [129]. The oxidation behaviour of SiC is also influenced by factors such as moisture, SiC particle size, and metal impurities[129]. Laurent et al.[127] found that silica acts as an oxygen donor to extend the life time of the Alumina layer on an aluminium drop:

$$3SiO_2 + 4Al(l) = 2Al_2O_3 + 3[Si] \tag{2.43}$$

However, this reaction does not improve the wetting of aluminium on SiC. See the circle marker (90°) at 800 °C in Figure 2.69, which is greater than the 76° for the non-oxidized SiC by the same author at 700°C. The silica layer is changed to alumina and the equilibrium contact angle becomes the same as aluminium on alumina. With time in high vacuum, a thin initial layer of silica can removed according to reaction(2.43) and (2.42), successively.

Aluminium is then in direct contact with SiC. The silica here delays the direct contact between aluminium and SiC [127].

Al alloys

Addition of Mg, Ca, Ti and Pb to pure aluminium enhances the wetting of Al-SiC [103, 106]. For example, the addition of 5wt% Mg in aluminium results in wetting of SiC ($\theta<90^o$) at 700-960°C [125]. This is due to the fact that Mg reacts with Al_2O_3 and consumes the oxide layer on the interface between aluminium and SiC. The evaporation of Mg (T_m=650°C) and Pb (T_m=372°C) in vacuum may also lead to decrease of the measured contact angle. The addition of Si to pure aluminium has little influence on the wetting of Al-SiC system.

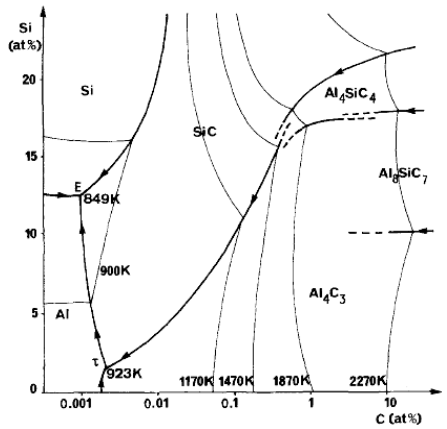

Figure 2.70 The Al rich corner in the Al-C-Si phase diagram [130]

A phase diagram of the Al-Si-C system is given in Figure 2.70. At 650°C (923K), the following ternary quasi-peritectic reaction [105] occurs isothermally:

$$3SiC + 4Al(l) = Al_4C_3 + 3[Si] \tag{2.44}$$

The addition of Si to aluminium prevents formation of Al_4C_3, but does not affect wettability between SiC and aluminium [104, 105]. The free Si in reaction bonded SiC also prevents formation of Al_4C_3 [131] and is reported to be effective in promoting wetting by liquid aluminium in the temperature range 700-1040°C [125]. This may be due to the additional Si-Al bond on the Al-SiC interface and that aluminium penetrates into the SiC along the intergranular free Si resulting from the reaction bonding process in the extensive reaction zone [132].

2.2.5.4 Other systems

AlF_3 has been shown to be an effective material to remove alkali metals, such as Na and Ca [77, 78]. Previous work [111] shows that the contact angle of liquid aluminium with an oxide layer on AlF_3 tablet (made from AlF_3 powder) at 1000°C is around 150°.

The wettability of the Al-TiB_2 system has been systematically investigated in Katrin Nord-Varhaug's thesis [133].

The oxidation rate of TiB_2 is low at temperatures below 500°C. A B_2O_3 layer that forms at low temperatures will protect the surface against further oxidation. At higher temperature, in the range 500-1000°C, other oxides will form such as Al_2O_3 and Al-B and Al-Ti products [133].

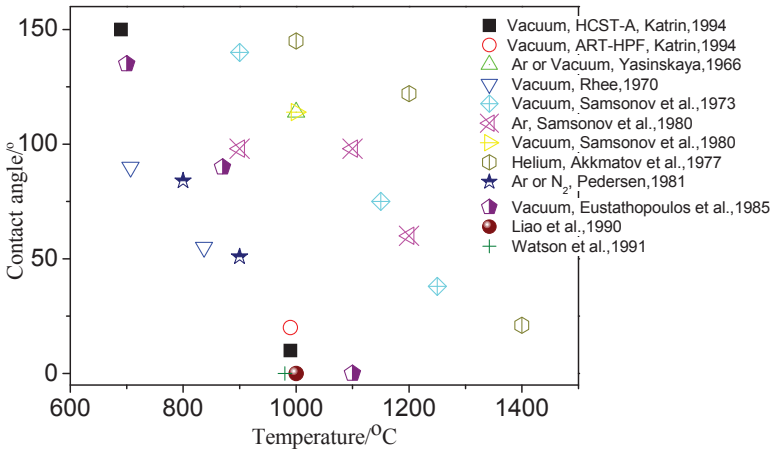

Figure 2.71 Contact angle of Al-TiB_2 system at various ambient atmospheres
Data from [133]

The high contact angle in the lower temperature range is typical of the sessile drop covered by a thin Al_2O_3 film inhibiting a real contact between the liquid and the substrate. The contact angle measured for Al-TiB_2 system in Figure 2.71 is similar to that measured for Al-Al_2O_3 system in Figure 2.67 at casting temperature around 700°C.

Particles of AlB_2 formed at the interface of Al-TiB_2, B_2O_3 on the surface of TiB_2, or BN particles present in the triple point junctions of TiB_2 might be the reason for the good wetting in the reactive system Al-TiB_2. However, AlB_2 particles may have nucleated and grown at the TiB_2 surface during cool-down after the sessile drop experiments [133].

The contact angle of aluminium on various ceramics is given in Table 2.7. The ceramics are probably covered by an oxide film. Rhee, S.K. [134] believes that the wettability increases as AlN<TiB_2<TiN<TiC. Yu. V. Naidich [115] gave the contact angles of CaF_2 and SiO_2 at 700°C as around 130° and around 80°. Possible interface reactions are:

$$3CaF_2 + 2Al = 2AlF_3 + 3Ca \quad (2.45)$$

$$3SiO_2 + 4Al = 2Al_2O_3 + 3Si \quad (2.46)$$

Table 2.7 Wettability of ceramic materials and Al [104]

Substrate	Contact angle [°]		Reference
	700 °C	1100 °C	
AlN	160	50	Ref.56 in [104]
BN	160	29	Ref.56 in [104]
C	145	57	Ref.57 in [104]
SiC	160	43	Ref.58 in [104]
Si_3N_4	160	60	Ref.56 in [104]
SiO_2	150	50	Ref.59 in [104]
UO_2	146	50	Ref.55 in [104]
ZrO_2	150	87	Ref.60 in [104]

2.2.6 Discussion

When discussing wettability in filtration, the presence of an oxide film on interface of Al-ceramic should be considered first. There may be two situations:

a. Oxide film on the interface

The contact angles have been measured in the literature with high vacuum and a long enough holding time to remove the oxide films. However, refining of aluminium through filtration is mainly carried out in 1 bar atmosphere, when the liquid aluminium is definitely covered with oxide films. Moreover, growth of oxide films would be certain with 2×10^4 Pa O_2 (1 bar atmosphere). Before filtration, priming (preheating of filter or filter bowl to avoid the blockage) is performed until the temperature of filter is sufficiently high. When the liquid aluminium flows into the filter, aluminium will be oxidized by the air in the filter box and oxide film will be captured by the filter. Thus, liquid aluminium contacts the interface with oxide film, not the ceramic itself. Hongjun Ni [68] suggests that a layer of oxide film exists between the melt and filter framework in the CFF. When the first stream of melt comes into the CFF, oxidation becomes more serious due to the large inner surface area of CFF. Thus, wettability of aluminium with oxide film and substrate is important in filtration. At 700°C, the contact angle values are ~150° and roughly independent of the nature of the substrates [104, 111].

Other metallic elements, such as Pb, Mg, Ca, Ti, Li and other interfacially active elements may give better wetting. Applying a thin metal film on the ceramic substrate surfaces, such as Ni and Ti, and Au and Cu, as well as a thin layer of metallic refractory compounds like TiB_2 and TiN [135], which can dissolve in liquid Al, was found to improve the low temperature wettability. The presence of a thin carbon layer, which reacts with aluminium to produce a carbide at the interface, was also found to give a considerable improvement of wettability[104].

A filter coated with a composite flux (containing 45%NaCl, 45%KCl and 5%LaF_3) layer was found to capture more inclusions in the filter [68].

b. No oxide film on the interface

At the beginning, when liquid aluminium flows into a hot filter after priming, an expansion of the liquid aluminium surface with oxide films occurs close to the interfaces. The dross in the launder before the filter is experienced as Al_2O_3 inclusions by the filter. Contact angles are roughly ~80^o for the Al-Al_2O_3 system at ~800^{o}C, a stable angle ~70^o of Al-graphite [1] system (or Al-Al_4C_3) at ~800^{o}C, and ~100^o for the Al-SiC system at 700^{o}C [105]. The wettability by liquid aluminium increases in the sequence of AlN<TiB_2<TiN<TiC [134]. Reactive systems are more wettable than non-reactive system is the common rule for ceramics.

The most probable situation in filtration is that the liquid Al-ceramic interface starts covered with oxide films, the metal penetrates the oxide film, and finally complete contact of aluminium with ceramics is attained.

An important point that has to be considered in filtration is whether the wetting or non-wetting with ceramics is an advantage for inclusion removal. This will be treated further in a final discussion section. The liquid aluminium comes into contact with ceramics, whether aluminium wets the ceramics or not. Capture of inclusions is determined by 1) wetting between inclusions and melt; 2) attraction between inclusions and filter (ceramics/oxide film); and 3) wetting between filter and melt.

Thus wettability of inclusion-metal (S-L) and metal-ceramic (L-S) should be considered in filtration. Of course, attraction between inclusion and ceramic is needed for removal of the inclusion. To improve the capture force of inclusions on the filter wal, flux coating on the filter wall which wets inclusions will be a good idea. The inclusions in aluminium are Al_2O_3 and Al_4C_3, MgO, $MgAl_2O_4$, SiO_2, SiC, AlN, TiB_2, and AlB_2. Sometimes, the inclusion and the filter materials have the same composition, such as Al_2O_3 and SiC inclusion/filter. The affinity of the same material may promote attraction between inclusion and filter wall.

Carbon filters have been industrialized as petrol coke filter- DUFI during 1970-1985, known for removing hydrogen, alkaline metals and non-metallic inclusions in plants operated by the ALUSUISEE Group and elsewhere [136]. However, it is not in use now. The reason might be the Al_4C_3 produced on the carbon surface. In the filtration of aluminium, inclusions such as Al_3C_4 formed in the hall electrolysis must be removed. Thus it is crucial to investigate the wetting behaviour of the Al-graphite system.

Further study should be performed on alternative filter materials, such as SiC, TiB_2, AlF_3, AlN, BN, Si_3N_4, SiO_2, ZrO_2, TiN, TiC and CaF_2.

Contact angles decrease with time in ceramic-Al systems. Reactions, spreading of aluminium, and de-oxidation of oxide films are responsible for this phenomena. During several hours of casting, the wettability between aluminium and a filter should improve.

Wettability of aluminium alloy- ceramic systems is of practical importance for a large range of aluminium alloys in filtration. Aluminium alloy containing an active element has better wetting than pure aluminium. Loss of alloying elements in filtration, such as Mg in Al_2O_3 filter, should be considered. The contact angle reduction should be taken

into account when using the sessile drop technique for alloys with volatile elements such as Mg.

The sessile drop technique as the most common method to measure wettability has developed rapidly during past few decades. The de-oxidation mechanism of Al_2O_3 film on aluminium drop is well known for reaction(2.42). This reaction is controlled by the removal of volatile compound Al_2O and becomes more noticeable when the temperature is increased. Reaction(2.42) can take place not only on the interface of liquid aluminium and oxide film, but also on Al_2O_3 substrate or surroundings. Therefore an Al_2O_3 chamber is not recommended, but a graphite chamber will be a good choice due to the reaction:

$$Al_2O(g) + C = 2Al(g) + CO(g) \tag{2.47}$$

Chapter 3 WETTING EXPERIMENTS

The wettability given by the contact angle of pure aluminium on filter materials and on inclusions is believed to be an important factor affecting the filtration of aluminium. The contact angle of molten aluminium on alumina, SiC, and graphite has been measured in the temperature range of 1000-1300ºC. To determine the wetting behaviour of the Al-ceramic system at the lower temperatures employed in filtration, a semi-empirical calculation is used.

3.1 Experimental Equipment and Procedure

The contact angle of liquid aluminium on the substrate was measured using the sessile drop technique. There are two sessile drop techniques reported in the literature. The first one uses contact heating — the metal and substrate are heated in contact, and de-oxidation of the drop is attained by evaporation of the oxide layer; The second one applies capillary purification — the molten metal is dropped onto the substrate by extrusion through a graphite capillary which breaks the superficial oxide layer [137]. The contact heating method is applied in this thesis.

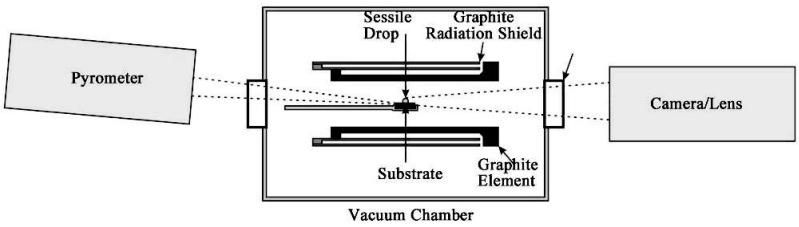

Figure 3.1 Schematic of the wetting furnace

The experimental apparatus is shown schematically in Figure 3.1. The apparatus essentially consists of a horizontal graphite heater surrounded by graphite radiation shields, located in a water-cooled vacuum chamber. The chamber was fitted with windows to allow a digital video camera (Sony XCD-SX910CR, Sony Corporation, Millersville, MD) to record the shape of the droplet. The maximum temperature of the furnace is 2400°C, and it is controlled by a pyrometer focused on the graphite sample holder. The contact angles and linear dimensions of the images were measured directly

from the image of the drop using Video Drop Shape Analysis software (First Ten Angstroms, Inc., Portsmouth, VA) [111]. We assume symmetry of the drop. This assumption was proved valid as no asymmetry was observed during the experiments.

During the preliminary experiments, argon gas was flushed through the apparatus with a flow rate 500ml/min. Argon gas was cleaned with an all-pure gas purifier from Alltech[1], followed by Mg turnings at 450°C. Inside the vacuum chamber there was also a small oxygen getter furnace which contained Ti sponge at 650°C. The oxygen potential in the gas outlet from the furnace was measured with a Rapidox 2100[2]. When the oxygen potential was below 10^{-21} bar, the sample was quickly heated to 950°C in approximately 80s, then heated to 1000, 1100, 1200, 1300, and 1400°C at a heating rate of 50°C/min (See Figure 3.2). Although the furnace temperature overshoots to 1100°C at the first 80s, this has little affect on the wettability measurements at a lower temperature such as 1000°C, since the oxide skin holds the liquid metal at the beginning. In all of the experiments, the contact angle and dimensions of the drop were recorded during the isothermal period at 1000, 1100, 1200, 1300, and 1400°C. Time = 0 was taken to be the beginning of the isothermal period.

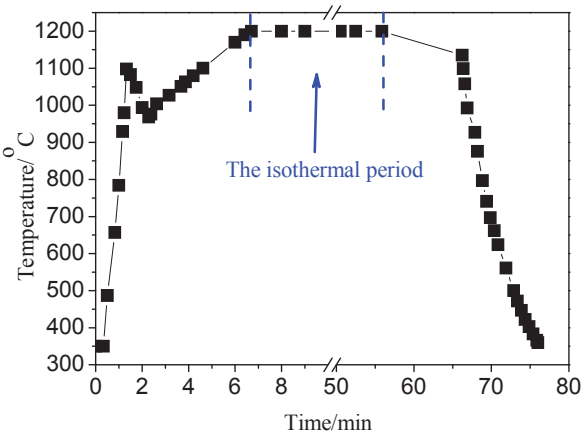

Figure 3.2 Example of the registered temperature for the experiment holding the sample at 1200 °C

The experiments were carried out with the substrate 99.7% pure alumina, graphite (ISO-88), and 98.9% single crystal SiC (Washington Mills, Norway) with 99.999% pure aluminium. The SiC single crystal was cut and ground with 1200 mesh diamond paper to get a flat surface, then dried in a closed furnace at 100°C. The average roughness of ground SiC, ISO-88 graphite (as received), and Al_2O_3 (as received) was 51.25nm,

[1] Alltech is the trade mark of Alltech Associated, Inc., 2051 Waukegan Road, Deerfield, Illinois 60015-1899, USA.

[2] Rapidox 2100 is a zirconia oxygen gas analyser from Cambridge Sensotec Limited, 31 Elizabeth Court, St Ives, CAMBS, PE27 5BQ, England.

179.76nm, and 393.13nm respectively. The average roughness is given by the arithmetic average of the absolute values in Figure 3.3. The roughness profiles were obtained by the Infinite Focus IFM G4[3]. The aluminium rod with a diameter of 2 mm was cut into small pieces around 2 mm in length, then polished by 500 mesh sandpaper and cleaned with ethanol in order to prevent subsequent oxidation.

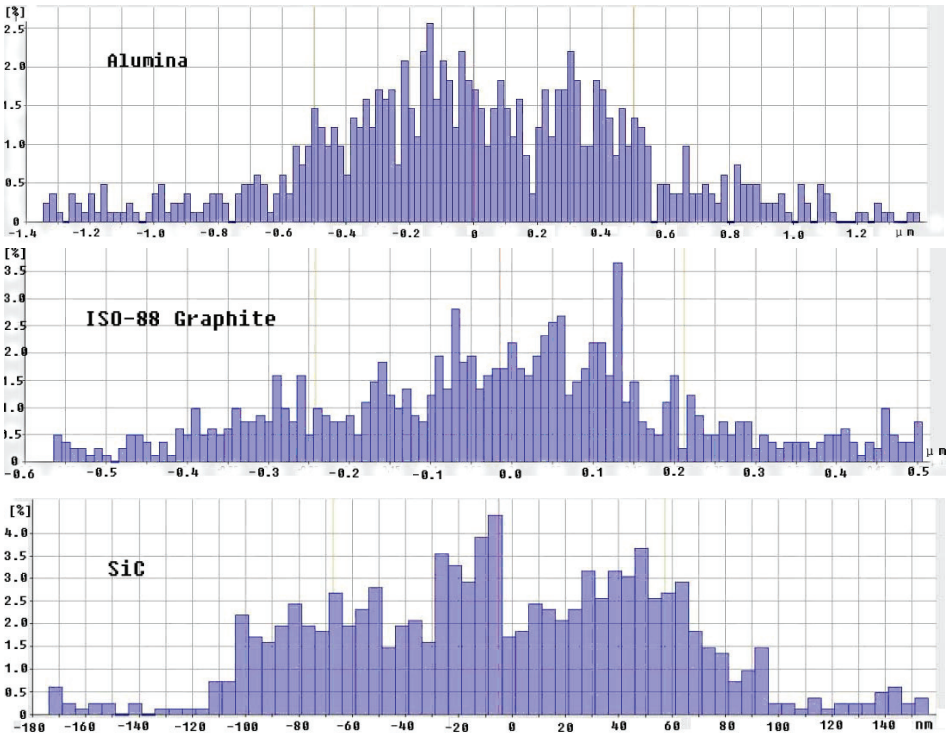

Figure 3.3 The roughness profile of the substrates

3.2 Removal of Aluminium Oxide Skin

The wettability of aluminium on solid substrates depends strongly on the experimental conditions, particularly the atmosphere. A high vacuum environment will promote aluminium evaporation and results in low contact angles, as illustrated in Figure 2.53. To evaluate the influence of the atmosphere on the contact angle of the Al-ceramic system, preliminary experiments were carried out. The samples were held 60 minutes at 1200°C and 1400°C under the 10^{-8} bar vacuum and 1 bar argon with 10^{-22}-10^{-21} bar oxygen partial pressure, respectively. The results are shown in Figure 3.4.

The contact angles obtained in an argon atmosphere were higher than those determined under vacuum conditions. As shown in Figure 3.4, at 1200ºC the apparent contact angle

[3] Infinite Focus IFM G4 is an optical coordinate system for form and roughness measurement from Alicona Imaging GmbH, Teslastrasse 8, 8074 Grambach, Austria – Graz.

was approximately 160º under the argon atmosphere, whereas the contact angle decreases from 138º to 80º in vacuum at the same temperature. Similar results were found for the contact angles at temperature 1400ºC. However, the aluminium droplet disappeared rapidly in vacuum at 1400ºC due to evaporation. The alumina film, with the melting point 2072ºC, acts as a solid shell, encloses the molten aluminium, and leads to the overestimate of the contact angle. The thinner the oxide layer, the less the measured contact angle is until the surface of molten aluminium is uncovered. Obviously, it takes less time to remove the oxide skin in vacuum than in argon as the argon atmosphere impedes gasification as shown by Coudurier et al. [135]. Under an argon atmosphere, contact angles at 1400ºC are comparable to those in vacuum at 1200ºC. High temperature and a long time are necessary to remove the oxide skin in an argon atmosphere.

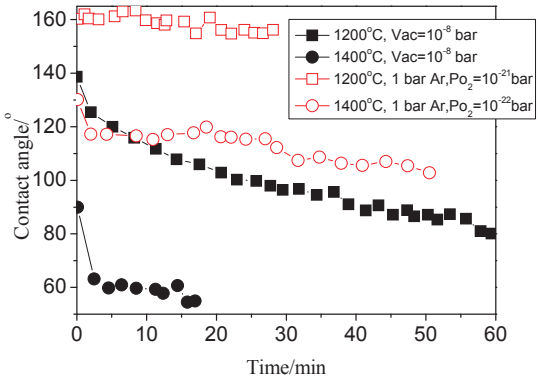

Figure 3.4 Contact angle vs. time for Al on Al_2O_3 at 1200ºC and 1400ºC in Ar and vacuum

Figure 3.5 shows the preliminary experimental results obtained from 3 step-heating experiments. The samples were isothermally held at 1200ºC, 1400ºC, and 1600ºC for 1 hour at each temperature. Contact angles in argon are approximately 40º higher than in vacuum. Again, this indicates that the oxide skin is more stable under an argon atmosphere. Every 200ºC increase of temperature results in a reduction of the contact angle by 20-25º in an Ar atmosphere. The contact angles at 1400ºC and 1600ºC could not be measured under vacuum, mainly due to the strong aluminium evaporation.

Based on these preliminary experimental results, we conclude that the atmosphere has a significant impact on the wetting behaviour of molten aluminium. Due to the low diffusion rate of $Al_2O(g)$ at high pressure, it is difficult to reduce the oxide layer according to reaction(2.42) at 1 bar atmosphere even with a low oxygen potential. Hence it is recommended to use high vacuum. 10^{-8} bar vacuum is employed in this study. The de-oxidation mechanism is discussed in detail in Section 2.2.4.2 and Section 3.4.

The atmosphere, mass of aluminium droplet and the oxide film thickness are reasonably the same in the current study. However, the substrate roughness and holding times are different for various substrates.

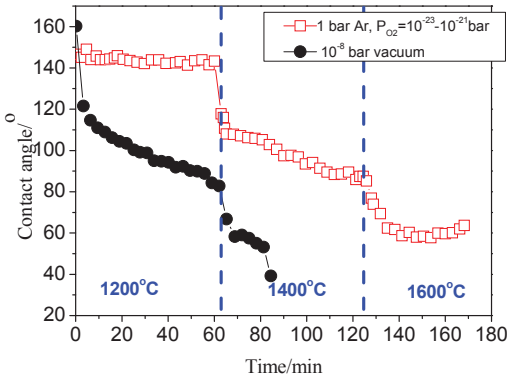

Figure 3.5 Contact angle vs. time for Al on Al_2O_3 at 1200- 1600ºC in Ar and vacuum

3.3 Wetting Results

Wetting of Al- ceramic systems under 10^{-8} bar vacuum is measured.

3.3.1 Al-Al_2O_3 system

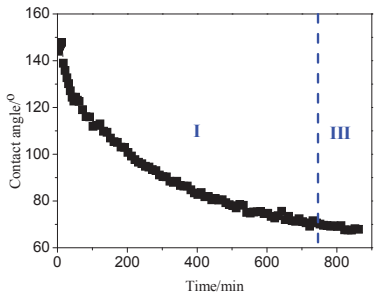

Figure 3.6 Contact angle vs. time for Al on Al_2O_3 at 1000ºC

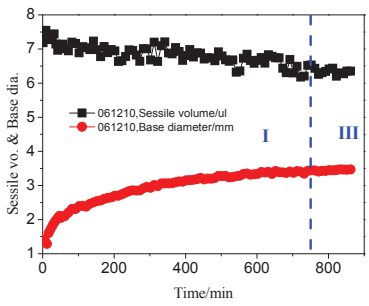

Figure 3.7 Sessile volume and base diameter vs. time for Al on Al_2O_3 at 1000ºC

Figure 3.6 and Figure 3.7 present measured time dependent contact angles of aluminium on alumina at 1000°C. The diagrams are somewhat arbitrarily divided into two stages. In the final stage, the contact angle is nearly constant. The contact angle decreases from

145° to approximately 70° during the first 750 min in the stage I. Removal of the oxide layer and evaporation of molten aluminium result in a reduction of the contact angle. In the next stage, the base diameter is nearly stable, and the contact angle is approaching a stable value (67-70°).

Figure 3.8 and Figure 3.9 are the experimental results at 1100°C. Similar to the results at 1000°C, the contact angles decrease from 158° to approximately 63° (approximately 259 min) in stage I. A decreasing sessile drop volume indicates that the reduction of the oxide layer and evaporation of aluminium take place simultaneously. In the next stage, the base diameter becomes nearly stable and the contact angle is approaching the equilibrium value (60-63°). The contact angles seem to decay exponentially with time at 1000ºC and 1100ºC.

Figure 3.10 and Figure 3.11 show similar results at 1200°C. They clearly present two stages for the change of contact angles. A sharp decrease of contact angles from 118° to 53° (approximately 80 min) has been observed in stage I due to the high aluminium evaporation rate. In the second stage, the sessile drop base diameter becomes stable, which allows the equilibrium contact angle (47-57°) to be measured.

The measured contact angles for the same system at 1300ºC are shown in Figure 3.12 and Figure 3.13. Again, two stages are shown clearly in the diagrams. A decrease of both sessile drop volume and base diameter in stage I indicates that very high evaporation takes place. However, it is clear that there is a relatively stable contact angle at 50-55° (from approximately 40 min) in the last stage.

Great efforts were made to determine the Al-Al_2O_3 contact angle at even higher temperatures, for example, 1400°C under vacuum condition. Unfortunately, the rapid evaporation at temperatures higher than 1300°C prevents obtaining reliable results.

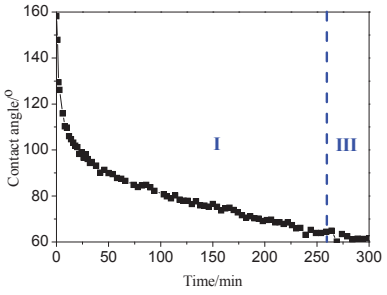

Figure 3.8 Contact angle vs. time for Al on Al_2O_3 at 1100ºC

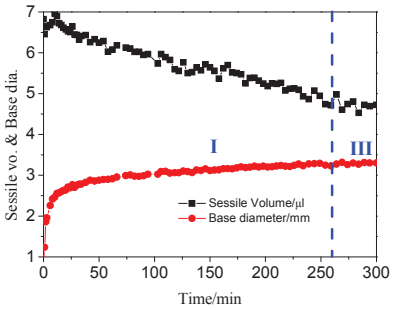

Figure 3.9 Sessile volume and base diameter vs. time for Al on Al_2O_3 at 1100ºC

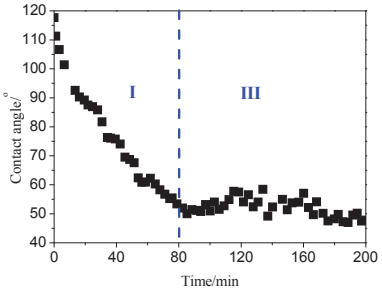

Figure 3.10 Contact angle vs. time for Al on Al_2O_3 at 1200ºC

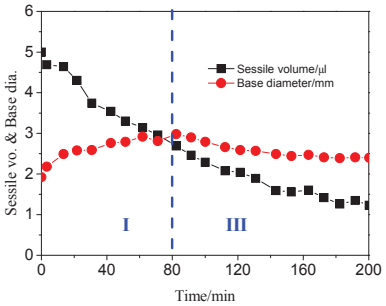

Figure 3.11 Sessile volume and base diameter vs. time for Al on Al_2O_3 at 1200ºC

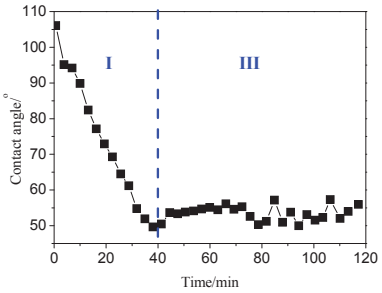

Figure 3.12 Contact angle vs. time for Al on Al_2O_3 at 1300ºC

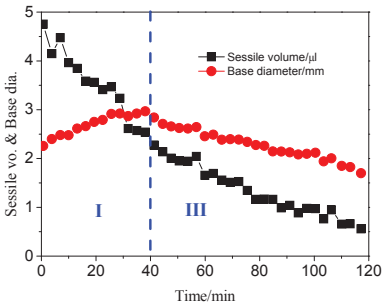

Figure 3.13 Sessile volume and base diameter vs. time for Al on Al_2O_3 at 1300ºC

3.3.2 Al-Graphite system

Wettability between aluminium and graphite at 1000°C as a function of time is shown in Figure 3.14 and Figure 3.15. Three kinetic stages can be distinguished: the first stage, where the contact angle decreases rapidly (in 64 min) from the initial contact angle $\theta_0 \approx 152^o$ to $\theta_1 \approx 120^o$; the second stage where the contact angle continues to decrease to a relatively low value of $\theta_2 \approx 80^o$, but at a slower rate; and the third stage where the contact angle stabilized at θ_2 after approximately 500 min. The nearly stable base diameter and the sessile volume allow the stable contact angle in the third stage to be measured.

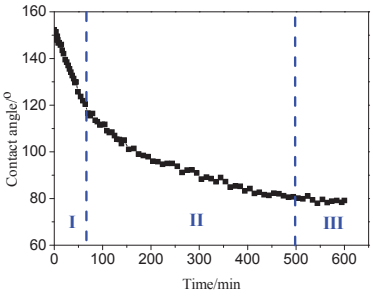

Figure 3.14 Contact angle vs. time for Al on graphite at 1000ºC

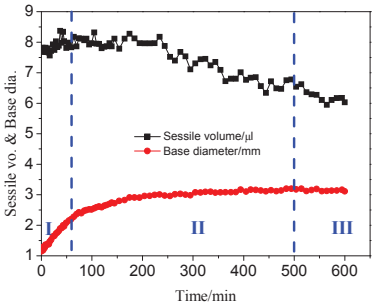

Figure 3.15 Sessile volume and base diameter vs. time for Al on graphite at 1000ºC

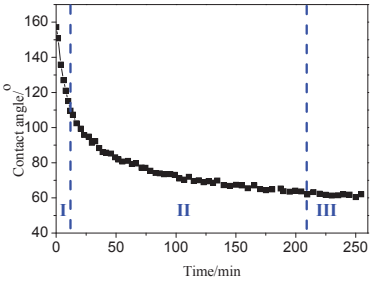

Figure 3.16 Contact angle vs. time for Al on graphite at 1100ºC

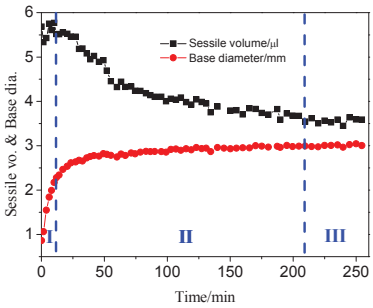

Figure 3.17 Sessile volume and base diameter vs. time for Al on graphite at 1100ºC

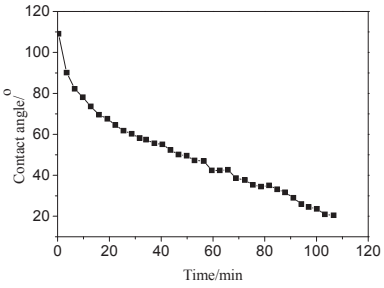

Figure 3.18 Contact angle vs. time for Al on graphite at 1200ºC

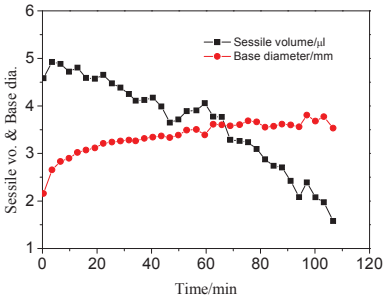

Figure 3.19 Sessile volume and base diameter vs. time for Al on graphite at 1200ºC

Similarly three stages: (I) rapid decrease, (II) slow decrease and (III) stable contact angle at 1100°C are shown in Figure 3.16 and Figure 3.17. The constant base diameter and the sessile volume allow measurement of the stable contact angle in the third stage. A lower stable contact angle is obtained in a shorter time at 1100°C than at 1000°C.

Efforts to obtain the Al- graphite contact angle at even higher temperatures, for example 1200°C, were made as shown in Figure 3.18 and Figure 3.19. Unfortunately, the evaporation of aluminium at higher temperatures is so high that the aluminium droplet disappeares quickly.

Experimental results of aluminium on graphite are summarized in Table 3.1.

Table 3.1 Wetting results of Al on graphite

Tempe-rature	Stage.I	Stage.II		Stage.III	
	θ_0[°]	θ_1[°]	t_1[min]	θ_2[°]	t_2[min]
1000°C	152	120	64	80	500
1100°C	157	107	14	62	209

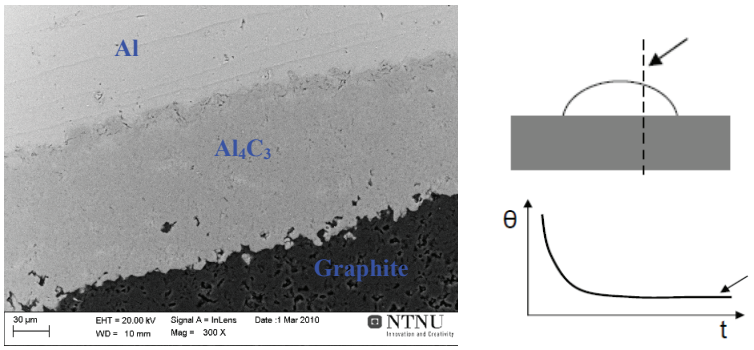

Figure 3.20 SEM micrograph of a cross section in an Al-graphite specimen cooled naturally after 250 min at 1100°C

Figure 3.20 shows the presence of a continuous layer of reaction product, Al_4C_3 at the Al-graphite interface with a thickness of 130 µm. The graphite-Al_4C_3 interface is rougher than the graphite substrate before the experiments and pores are present around some particles. Aluminium in the Al_4C_3 layer and the discrete Al_4C_3 particles indicate that the reaction proceeds by dissolution of carbon into aluminium. The final contact angle is determined by the Al-Al_4C_3 system.

3.3.3 Al-SiC system

Figure 3.21 and Figure 3.22 show the time dependent wetting properties of aluminium on SiC at 1000°C under vacuum conditions. The contact angles decrease rapidly from 121° to 81° during the first 45 min, followed by a relatively slow reduction in the stage II until approximately 150 min. Removal of the oxide layer and evaporation of molten aluminium lead to the reduction of the contact angle in stage I. In the third stage, the base diameter is nearly stable and the equilibrium contact angle (60-65°) is obtained.

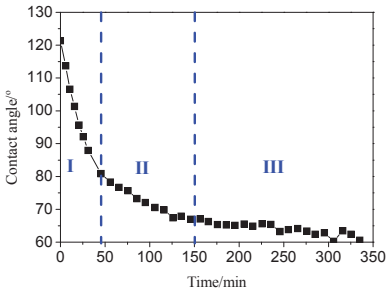

Figure 3.21 Contact angle vs. time for Al on SiC at 1000ºC

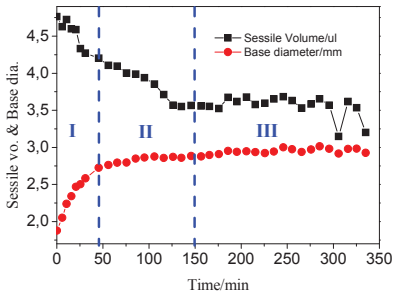

Figure 3.22 Sessile volume and base diameter vs. time for Al on SiC at 1000ºC

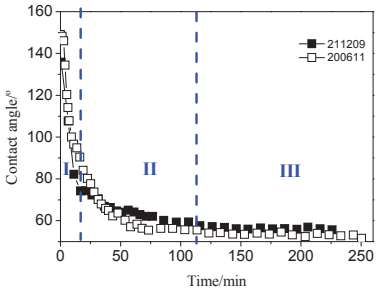

Figure 3.23 Contact angle vs. time for Al on SiC at 1100ºC

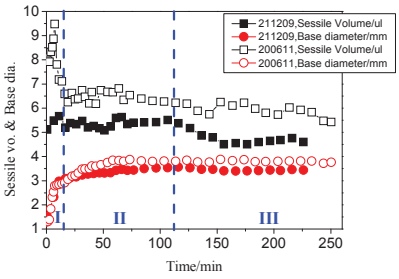

Figure 3.24 Sessile volume and base diameter vs. time for Al on SiC at 1100ºC

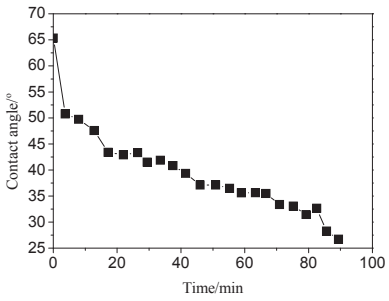

Figure 3.25 Contact angle vs. time for Al on SiC at 1200ºC

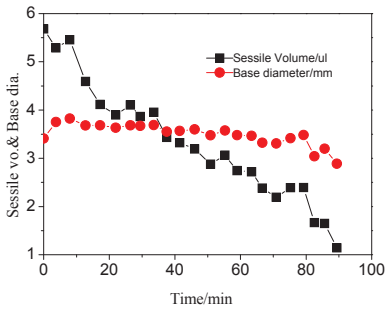

Figure 3.26 Sessile volume and base diameter vs. time for Al on SiC at 1200ºC

Two measurements of the wetting properties of Al-SiC system at 1100°C are shown in Figure 3.23 and Figure 3.24. Compared with the results obtained at 1000°C, both the

first and second stages were short in time. After approximately 112 minutes, the equilibrium contact angle is determined. The second measurement (200611) with a relatively larger aluminium drop gives nearly the same contact angle.

Efforts to obtain the Al-SiC contact angle at even higher temperatures, for example 1200°C, were made, as shown in Figure 3.25 and Figure 3.26. Unfortunately, no stable contact angle was measured, probably due to high evaporation rates.

Experimental results of aluminium on SiC are summarized in Table 3.2.

Table 3.2 Wetting results of Al on SiC

Tempe-rature	Stage.I	Stage.II		Stage.III	
	θ_0[°]	θ_1[°]	t_1[min]	θ_2[°]	t_2[min]
1000ºC	121	81	46	60-65	150
1100ºC	149	75-83	16	51-56	112

Figure 3.27 shows the presence of a continuous layer of reaction product, Al_4C_3 at the Al-SiC interface with a thickness approximately 10 μm. Aluminium in the Al_4C_3 layer and the discrete Al_4C_3 particles indicate that the reaction proceeds by dissolution of carbon into aluminium.

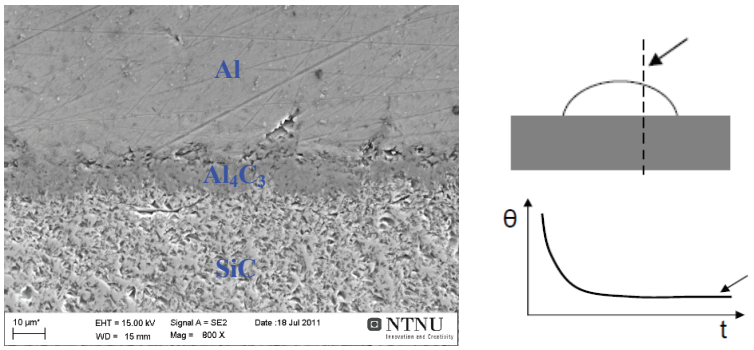

Figure 3.27 SEM micrograph of a cross section in an Al-SiC specimen cooled naturally after 250 min at 1100°C

3.4 Time Dependent Wetting Properties

The three successive stages of wetting kinetics in Figure 3.6 to Figure 3.26 are discussed successively.

Stage.I- De-oxidation of oxide layer

The sharp decrease of the contact angle on both Al-SiC and Al-graphite is similar to the contact angle curve observed for Al-Al_2O_3 for the same stage in the same wetting furnace. This reduction is due to de-oxidation of the oxide layer according to reaction (2.42).

Aluminium is oxidized (reaction(3.1)) even at oxygen partial pressure of 10^{-49} bar at 700°C (Figure 3.28) [138]. However, this pressure is impossible to achieve in the current experimental apparatus. At this pressure, a 3-liter furnace chamber contains less than 1 oxygen molecule.

$$4Al(l) + 3O_2(g) = 2Al_2O_3 \tag{3.1}$$

Nevertheless, the oxide layer on the surface of a molten aluminium drop can be removed, if the outgoing flow of gaseous Al_2O according to reaction(2.42) is greater than the incoming flow of oxygen. The equilibrium partial pressure of Al_2O (Figure 3.28), according to reaction(2.42), is 4.3×10^{-5} bar at 1000°C. Holding the total pressure in the furnace under 10^{-8} bar, the oxide skin of the aluminium drop is removed. This process allows us to measure the contact angles between molten aluminium and solid substrate. Thus the wetting behaviour of the first stage is controlled by de-oxidation of the oxide layer on the aluminium drop according to reaction(2.42).

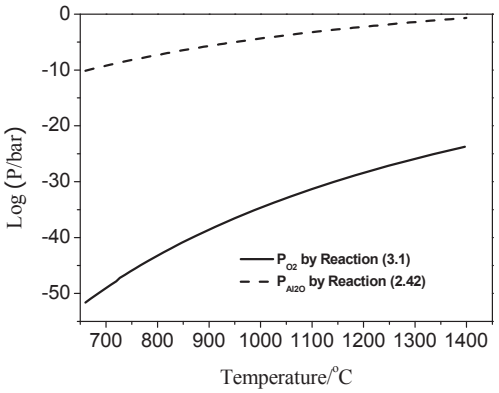

Figure 3.28 Equilibrium partial pressure of gas species in reactions(3.1) and (2.42) calculated from FactSage v6.2

The time needed for de-oxidation in stage I for the Al-Al_2O_3 system is much longer than that of the other two systems. There are two reasons. First, in the Al-Al_2O_3 system, the vacuum removing oxide from the aluminium according to reaction(2.42) has to deal with the alumina substrate also. Second, the carbon component from the substrate in the other two systems helps to remove the oxide layer by reaction(2.47).

Stage.II- De-oxidation of silica and the Al_4C_3 formation

There are three possible explanations concerning the second stage in the Al-SiC system: a) the dissolution of SiC into aluminium according to reaction(3.2), b) coverage of the interface by Al_4C_3 according to reaction(2.44) 3SiC+4Al(l) = Al_4C_3+3[Si], and c) de-oxidation of silica on the interface according to reactions (2.43) $3SiO_2$+4Al(l) = $2Al_2O_3$+3[Si] and (2.42), successively.

The maximum solubility of carbon in liquid aluminium, on the order of 30 ppm at temperatures close to 1000°C [139] is too low to support the dissolution mechanism in a).

At temperatures lower than 900°C [107], the kinetics of the reaction(2.44) is slow and leads to the limited formation of discrete particles of Al_4C_3 at the interface. Thus the spreading of de-oxidized aluminium is controlled by de-oxidation of SiO_2 on SiC with limited amounts of discrete particles of Al_4C_3 at low temperatures. This is supported by the delayed equilibrium contact angle obtained in the Al-oxidized SiC system [127] at 660-900°C.

In this investigation, temperatures were higher than 1000°C, and the formation of Al_4C_3 at the interface is accelerated [96]. The SiC-Al_4C_3 interface (see Figure 3.27) is smoother and the Al_4C_3 layer is much thinner than that on graphite (see Figure 3.20) [140] at 1100°C with the same holding time. The kinetics of reaction(2.44) forming Al_3C_4 from SiC is slower than that of reaction(3.3) forming Al_3C_4 directly, so the stable contact angle was obtained early in the Al-SiC system with formation of only a small amount of Al_4C_3. It also might be that the SiC substrate produces more densely packed Al_4C_3.

$$SiC = [Si]_{Al} + [C]_{Al} \tag{3.2}$$

$$4Al(l) + 3C(s) = Al_4C_3 \tag{3.3}$$

In the second stage in the Al-graphite system, the spreading of aluminium on the substrate is lower than the previous stage and the base diameter is a linear function with respect to time. The interfacial reaction(3.3) has Gibbs energy of -136kJ/mol to -102kJ/mol [141] at temperatures of 660 to 1300°C. The Al_4C_3 layer at the Al-graphite interface (see Figure 3.20) also supports the assumption that the second stage in the Al-graphite system is controlled by the formation of Al_4C_3.

Note that for the Al-Al_2O_3 system, there is not such a stage.

Stage.III- Stable contact angle

A relatively stable contact angle is detected in the third stage for all three systems. Good repeatability of wetting properties is observed at the same temperatures.

Schematics of stages I to III

To summarize the discussion, schematics of the wettability for the Al-ceramic systems are shown in Figure 3.29. The contact angle initially changes with time and finally approaches an “equilibrium value”. Both the Al-SiC and Al- graphite systems produce Al_4C_3 at the end. However, Si present in aluminium could prevent Al_4C_3 formation in the Al-SiC system. See reaction(2.44).

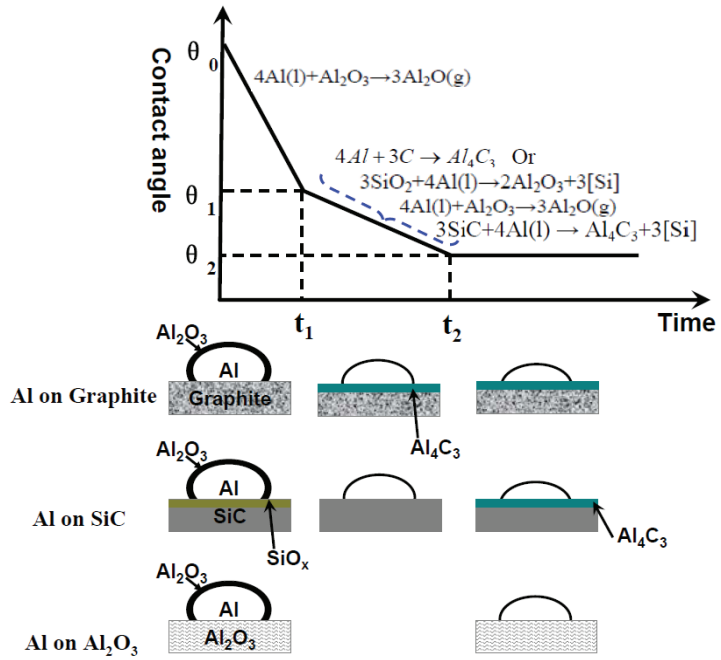

Figure 3.29 The time dependent wettability of the ceramic-Al system

In spite of the fact that roughness is greatest for Al_2O_3, it has the largest contact angle. For example at 1100°C, the equilibrium contact angle is 51-56° for SiC, 62° for graphite, 60-63° for Al_2O_3, respectively.

3.5 Extrapolation of Contact Angle to Lower Temperatures

To determine the wetting behaviour of the Al-ceramic system at the lower casting temperature, a semi-empirical calculation is employed.

The equilibrium value of the contact angle obeys the classical Young's Equ.(2.23). We have not taken into account the effect of the curvature of the aluminium droplet [94, 95].

Most of the reported surface tension measurements pertain to "oxygen-saturated" samples [108]. According to Mills and Su [108], the surface tension of oxygen saturated molten aluminium can be evaluated:

$$\sigma_{Al} = 993.86 - 0.18T(^{o}C) \text{ in mN/m} \tag{3.4}$$

3.5.1 Al-Al_2O_3 system

Eustathopoulos, Nicholas and Drevet [96] reported the experimental surface energies of alumina by the multiphase equilibrium technique. The extrapolation of the experimental data to low temperatures gives a value of 1400±500 mNm^{-1} at 700°C, which agrees roughly with first principle simulation results [142] (Figure 3.30).

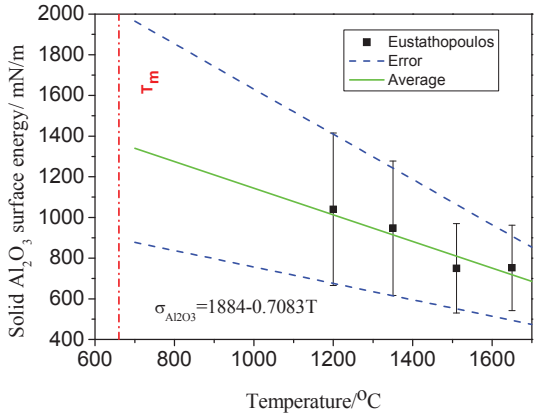

Figure 3.30 The surface energy of solid Al_2O_3 vs. temperatures

The work of adhesion W_a is equal to the sum of the surface tension of molten metal, σ_{LV}, and the surface energy of solid substrate, σ_{SV}, minus the interfacial energy, σ_{SL}.

$$W_a = \sigma_{LV} + \sigma_{SV} - \sigma_{SL} \tag{3.5}$$

When the two surfaces are brought into contact and replaced by the interface, the work of adhesion holds the two surfaces together. The work of adhesion between molten metal and the solid is a measure of the bond strength between the two media. Girifalco and Good [143] proposed that the work of adhesion is proportional to the geometric average of the surface energies of two media:

$$W_a = 2\varphi\sqrt{\sigma_{LV}\sigma_{SV}} \tag{3.6}$$

where φ is a function of the molar volumes of the liquid and the solid. In the current work, the deviation between the calculated and measured interfacial energies is minimized adjusting the temperature-dependent coefficient φ. Figure 3.31 shows the fitted line for the coefficient φ. The points are obtained by balancing the Equs.(3.5) and (3.6) where σ_{LS} is derived from the Young's Equ.(2.23) with known contact angles in the Al-Al_2O_3 system. The proportionality factor increases monotonically with temperature. The experimental results at low temperatures reported by John and Hausner [112], Klinter et al. [113], and Wang and Wu [114] have been included. They

all achieved a total pressure lower than 10^{-9} bar, except John [112]. The other results reported in the literature [12, 39, 115-120] seem to have employed either a high total pressure or less pure materials.

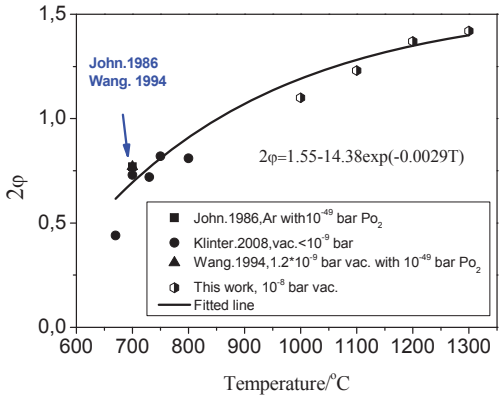

Figure 3.31 The coefficient φ fitted to literature data and this work

The following equation is obtained for the interfacial energy of aluminium and alumina, employing Equs.(3.5) and (3.6) and Figure 3.31.

$$\sigma_{Al-Al2O3} = \sigma_{Al} + \sigma_{Al2O3} - [1.55 - 14.38\exp(-0.0029T)]\sqrt{\sigma_{Al}\sigma_{Al2O3}} \tag{3.7}$$

The equation is applicable for the temperature range from 700 °C up to 1500°C. From Equ.(3.7), the contact angles of the aluminium and alumina at various temperatures under vacuum can be calculated using Equ.(2.23). At the melting point of aluminium, σ_{SL}= 1.63 J/m^2 is obtained from Equ.(3.7). P. Nikolopoulos et al. [144] proposed a similar semi-empirical relation for the metal and alumina or zirconia interface at the melting point of the metal:

$$\sigma_{SL} = (\frac{R_O}{R_{Al}} \cdot \frac{x}{y} \cdot \frac{V_{Al}}{V_{Al_2O_3}} + 1)^{2/3} \sqrt{\sigma_{LV}\sigma_{SV}} \tag{3.8}$$

where R is the radii of the ions, V is the molar volume, and x=2, y=3 for Al_xO_y. R_O/R_{Al}=2.80, V_{Al}=11.36 cm^3/mol, and V_{Al2O3}=25.62 cm^3/mol. It gives σ_{SL}= 1.66 J/m^2 at 660°C, which agrees well with our calculation results even though P. Nikolopoulos et al. [144] have not included aluminium in their correlations.

Figure 3.32 shows the calculated contact angle with the measured values at various temperatures. The contact angle between aluminium and alumina at 700°C is approximately 97°, which indicates that alumina is not wetted by molten aluminium at the casting temperature.

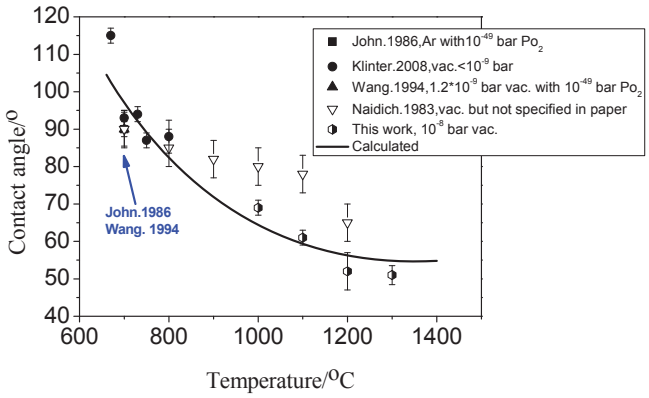

Figure 3.32 The calculated and measured contact angle vs. temperature for Al on Al_2O_3

3.5.2 Al-Graphite system

Since the surface energy of Al_4C_3 has not been reported in the literature, one may use the value of σ_{Al4C3}-σ_{Inter} to estimate the contact angle at lower temperatures. Figure 3.33 shows the σ_{Al4C3}-σ_{Inter} values as a function of temperature. The experimental data can be divided into two sets: those of Landry using the vitreous graphite substrate, the present measurements and those of Landry using single- and ploy-crystal graphite.

If we approximate the σ_{Al4C3}-σ_{Inter} values as a linear function of temperature, the contact angle of Al-Al_4C_3 system in the range of 660-1250°C can be estimated using the following equation:

$$\cos\theta = \frac{\sigma_{Al4C3} - \sigma_{inter}}{\sigma_{Al}} = \frac{2.3T(^oC) - 2125.3}{\sigma_{Al}} \tag{3.9}$$

for this work, where 2.3 is the slope of Est-2.

$$\cos\theta = \frac{2.0T(^oC) - 1430.2}{\sigma_{Al}} \tag{3.10}$$

for vitreous carbon, where 2.0 is the slope of Est-1.

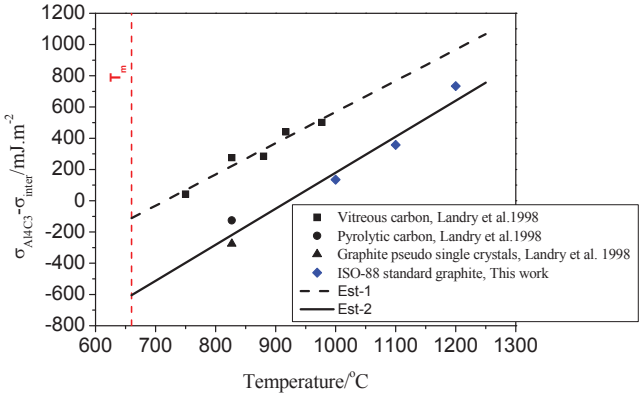

Figure 3.33 σ_{Al4C3}-σ_{inter} fitted to literature data [145] under 10^{-8} bar vacuum and this work

Figure 3.34 shows the calculated contact angle with the measured values at various temperatures. The contact angle between aluminium and Al_4C_3 (single- and ploy-crystal graphite) at 700^{o}C is around 126^o, which indicates that Al_4C_3 (graphite) is not wetted by molten aluminium at the casting temperature. If the vitreous graphite is used, the contact angle reduces to 92^o at 700 ^{o}C. This is reasonable due to the imperfectly crystallized form in vitreous graphite.

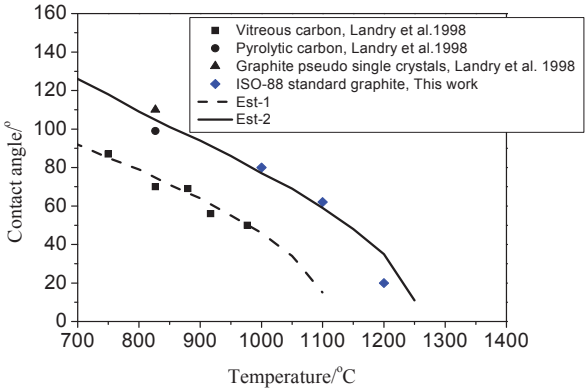

Figure 3.34 The calculated and measured contact angle vs. temperature for Al on various graphites

As suggested with Ambrose et al. [146], the decay of the contact angle with time can be fitted empirically by an exponential form:

$$\theta_t - \theta_2 = (\theta_0 - \theta_2)\exp(-t/\tau) \tag{3.11}$$

When θ_o, θ_2 and τ are known, the time dependent property of the Al-ceramic system can be estimated at the casting temperature. The initial contact angle θ_o, is not significantly altered by temperature [145] and substrate. All the contact angles occur from non-wetting, assuming θ_o=160^o. In this work, θ_o is lower than 160^o due to holding several minutes before the time zero. As shown in Figure 3.34, θ_2=126^o for single- and ploy-crystal graphite at 700^{o}C.

The characteristic time factor τ seems related to the de-oxidation time which depends on oxygen partial pressure. This needs further investigation. However, when we take τ= 23 min (the lowest de-oxidation limit from the literature [105]), the time dependent wetting behaviour of Al-graphite system at 700^{o}C can be predicted and shown in Figure 3.35. Note that τ changes the decreasing rate of the contact angle, but not the final equilibrium contact angle.

The adhesion work W_a (see Equ.(3.12)) and ratio of that with cohesion work W_c (Equ.(3.13)) at 700^{o}C are shown in Figure 3.36. The adhesion (attraction to dissimilar molecular) work is less than 25% of the work of cohesion liquid aluminium. This indicates that the Al-Al_4C_3 (graphite) interface is energetically weak, which is due to covalent bonds of Al_4C_3 [137].

$$W_a = \sigma_{LV}(1+\cos\theta) \tag{3.12}$$

$$W_c = 2\sigma_{LV} \tag{3.13}$$

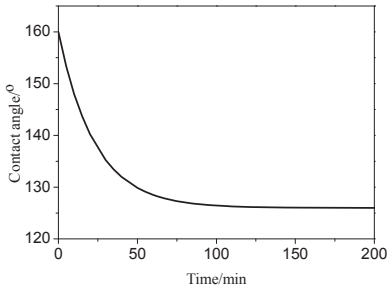

Figure 3.35 The calculated contact angle vs. time for Al on graphite at 700ºC

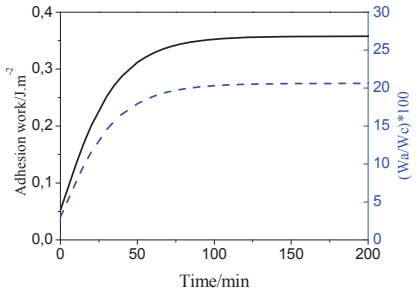

Figure 3.36 The adhesion work and the ratio W_a/W_c for Al on graphite at 700 ^{o}C according Equs.(3.12) and (3.13)

Eustathopoulos et al. [98] found out that spreading during the interfacial reaction can be described by

$$R - R_0 = Kt \tag{3.14}$$

Figure 3.37 shows a linear fit of the base diameter in the second stage with fitting factor 92.63%. The spreading rate of the triple line, K=d(diameter)/dt is equal to 1.53μm/min in the second stage at 1100°C. The spreading rates are 0.87μm/min and 7.46μm/min at 1000°C and 1200°C in the second stage.

From the changes in the sessile volume, evaporation rates of 4.2nl/min, 4.3nl/min, and 28.4nl/min at 1000°C, 1100°C, and 1200°C are found in the second stage, respectively.

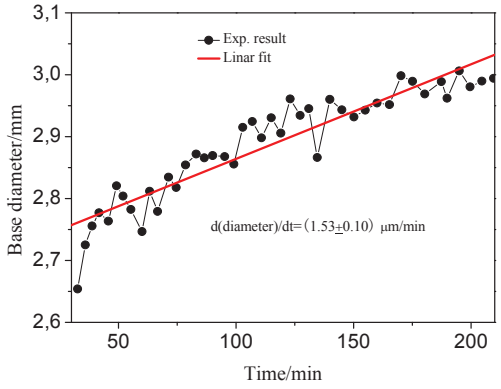

Figure 3.37 The base diameter vs. time for Al on graphite at 1100ºC

3.5.3 Al-SiC system

R.H. Bruce in [147] reported average surface energies of (110) face of β-SiC according to Equ.(3.15).

$$\sigma_{SiC} = 2851 - 0.546T(^{o}C) \text{ in mJ/m}^2 \tag{3.15}$$

As discussed in the Section 3.4, the formation of Al_4C_3 at the interface is accelerated at temperatures greater than 1000°C, but it does not significantly change the wetting [124]. This may be due to its slow reaction rate at the interface. Therefore, wettability will be discussed as in the non-reactive Al-SiC system.

With the method described in Section 3.5.1, Figure 3.38 shows the fitted line for the coefficient 2φ calculated from single crystal SiC including this work and the literature [105, 124, 127] for experiments with total pressure less than 10^{-8} bar. The points are obtained by balancing the Equs.(3.5) and (3.6) where σ_{LS} is derived from the Young's Equ.(2.23) with known contact angles in the Al-SiC system. Note that even though a thin layer of Al_4C_3 formed at the interface in this work at 1100 °C, we treat it as the Al-SiC system since according to [124], the progressive replacement at the interface, during the reaction, of a predominantly covalent carbide, such as SiC, by another carbide of the same type ($A1_4C_3$) does not significantly influence the wetting.

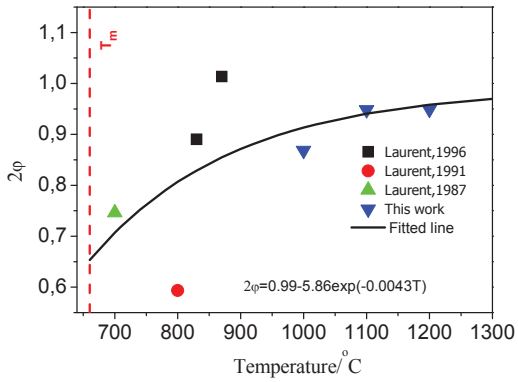

Figure 3.38 2φ fitted to the literature data [124-127, 148] and this work

Based on the preceding discussion, the following equation is obtained for the interfacial energy of single crystal SiC and aluminium, employing Equs.(3.5) and (3.6) and Figure 3.38.

$$\sigma_{Al-SiC} = \sigma_{SiC} + \sigma_{Al} - [0.99 - 5.86\exp(-0.0043T(^{o}C))]\sqrt{\sigma_{Al}\sigma_{SiC}} \tag{3.16}$$

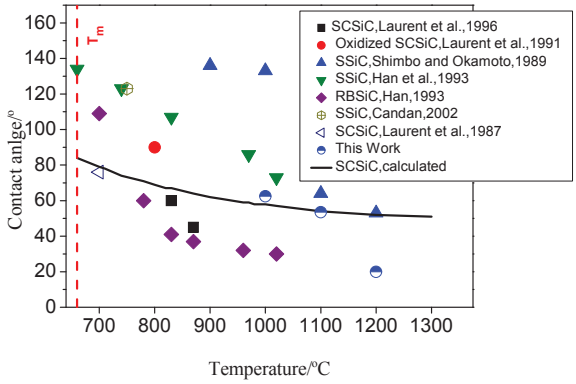

Figure 3.39 The calculated and measured contact angle vs. temperature for Al on SiC [103, 105, 124-127]
SSiC- sintered SiC; RBSiC- reaction bonded SiC; SCSiC- single crystal SiC

The contact angles of the aluminium and SiC can be calculated using Young's Equ.(2.23). Figure 3.39 shows the calculated contact angle with the measured values at various temperatures. The calculated contact angles fit well with the literature data on

single crystal SiC. The calculated equilibrium contact angle at 700°C is 79°, which indicates that SiC is wetted by molten aluminium at the casting temperature.

When we take τ= 23min (the lowest de-oxidation limit from the literature [105]), the time dependent wetting behaviour of Al-SiC system at 700°C can be predicted, and is shown in Figure 3.40. The contact angle decays exponentially and reaches the equilibrium angle at the end. Figure 3.41 shows that adhesion work reaches 60% of the work of cohesion of liquid aluminium. This indicates that the Al-SiC interface is relatively strong.

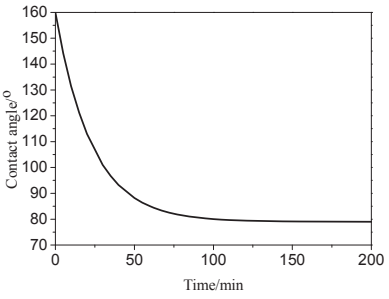

Figure 3.40 The calculated contact angle vs. time for Al on SiC at 700ºC

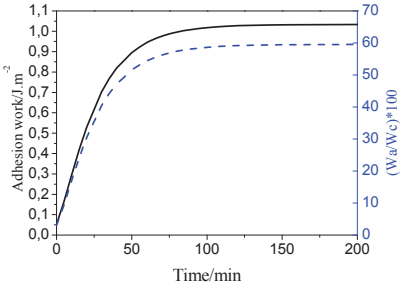

Figure 3.41 The adhesion work and the ratio W_a/W_c for Al on SiC at 700 °C according Equs.(3.12) and (3.13)

3.6 Wetting in Filtration

Filtration of aluminium is carried out in 1 bar atmosphere, when the liquid aluminium is definitely covered with oxide films. However, contact angles have been measured in high vacuum and for a long time to remove the oxide films. This addresses the case that aluminium is in direct contact with the filter material. Based on the vacuum studies, the behaviour of aluminium filtration will be discussed.

3.6.1 Priming

When replacing a filter for molten aluminium it is necessary to pre-heat the filter and the bowl in which it is seated in order to enable the filter to prime (allow metal to infiltrate the filter without freezing) and to avoid cracking the filter from thermal shock.

Liquid aluminium forms an Al_2O_3 skin rapidly when it is exposed to the atmosphere. Increasing temperature speeds up oxidation. In a typical filter start-up, the liquid aluminium is covered by oxides created by the hot atmosphere and from the filter material in the pores of the filter. Thus plugging and also freezing are common problems in the industry.

Time is required to attain wetting (equilibrium contact angle) as discussed in Section 3.4. Thus, the wetting properties of filter and aluminium improve with time during filtration.

When liquid aluminium penetrates the 'baked' filter, oxide skin covers the aluminium and the filter. One part of the oxide skin forms Al_2O_3 inclusions and the rest may adhere on the filter/Al interface. For metal to manage to enter the filter, a capillary extrusion mechanism must take place, when aluminium breaks through the oxide layer. The metal, lets say 15 tons/h, would break the oxide layer on filter/Al interface. Metal is then in direct contact with the filter material. Then oxidation is not a problem due to the low solubility of oxygen in aluminium, around 1.43×10^{-4} at.% at 700°C [109]. So wettability under high vacuum should describe closely the case where metal and ceramics are in contact.

3.6.2 The Wetting of Inclusion-Al and Al-filter

In filtration, small inclusions collide with the inner wall and are captured by the filter. Tortuous passages in the filter improve the possibility of collisions. The probability that an inclusion will be retained depends on a number of variables, such as chemical composition of the inclusion and filter, the wettability, micro-porosity, topography, flow rate, inclusion size etc [56].

Here wettability of aluminium with inclusions and filter is discussed. Aluminium may push inclusions towards the filter wall due to poor wetting between aluminium and inclusions. If the viscous drag on inclusions is not higher than the forces that cause capture, they will be retained on the filter walls.

The time dependent wettability of aluminium on various ceramics is compared in Figure 3.42. We believe that the wetting behaviour of vitreous graphite would describe wetting of the Al_4C_3 inclusion in aluminium better than the single- and poly- crystal graphite due to the imperfectly crystallized structure of Al_4C_3 inclusions. The contact angle decreases with time. SiC has the best wetting with aluminium. Note that the same characteristic time factor τ is employed here for comparison, even though the Al-SiC and Al-graphite systems should have faster de-oxidation of the oxide layer. The equilibrium contact angles at 700°C are 79° (single crystal SiC), 92° (vitreous graphite), and 97° (Al_2O_3).

Most of the inclusions have been present in liquid aluminium for a long time before filtration. Therefore contact angles of Al_4C_3 and Al_2O_3 inclusions are believed to be constant 92° and 97°, and the adhesion work is 838mJ/m^2 and 762mJ/m^2, respectively.

Based on a principle of minimum Gibbs energy it is proposed that aluminium trends to expel surfaces (particles) with poorer wetting than the Al-filter interface.

We have the following discussion based on Figure 3.42:

- When Al_4C_3 inclusions are removed with an Al_2O_3 filter, inclusions may be retained by the filter wall due to the filter microporosity, topography, and flow characteristics, rather than the wettability since Al_4C_3 inclusions have a lower contact angle with aluminium than the Al_2O_3 filter.

- When Al_2O_3 and Al_4C_3 inclusions go through a SiC filter, Al-SiC filter wettability would not help to capture inclusions since SiC gives poorer wetting with aluminium than inclusions at first. But it improves with time when wetting of aluminium with SiC is better than with inclusions.
- Al_2O_3 inclusion attachment on the Al_2O_3 filter can be explained by the agglomeration effects.

Improved inclusion removal is achieved with filter materials that have better wetting with aluminium than the inclusions.

Graphite as a filter material

Al_4C_3 reacts with water vapour according to reaction:

$$Al_4C_3 + 12H_2O = 3CH_4 + 4Al(OH)_3 \tag{3.17}$$

Release of methane and the presence of Al_4C_3 may be a reason not to use graphite as a filter in industry.

SiC as a filter material

As mentioned the presence of Si in aluminium will prevent formation of Al_4C_3 in a SiC filter. SiC should be a good alternative filter material due to its good wetting with aluminium.

Al_2O_3 as a filter material

Al_2O_3 is a common filter material. It does not react with aluminium and is poorly wetted by aluminium when compared to SiC.

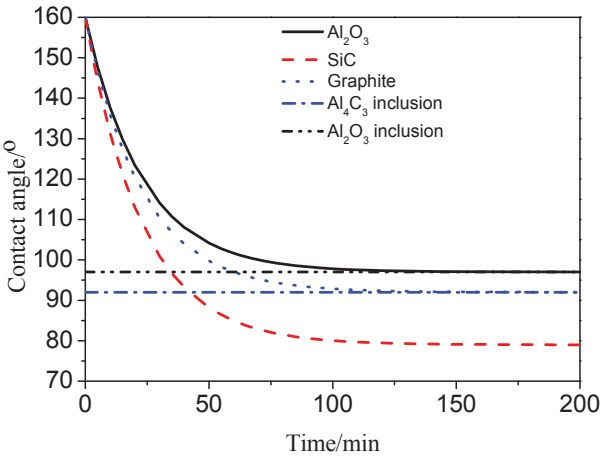

Figure 3.42 The contact angle of Al with various ceramics at 700 ^oC

3.7 Summary

In filtration of aluminium, aluminium is in contact with an alumina layer. Therefore it is important to study the wetting behaviour of initially oxidized aluminium on ceramics.

Wetting behaviour between molten aluminium and oxidized ceramics in the temperature range 1000 to 1300^{o}C is investigated.

The contact angles decrease with increasing temperatures. In order to predict the wetting behaviour of the Al-ceramic system at the lower casting temperature, a calculation for the temperature dependence of the contact angle is presented. The contact angles of Al-Al_2O_3, Al-SiC, and Al-graphite at 700^{o}C are calculated to be 97^{o}, 79^{o}, 92^{o} (vitreous graphite) and 126^{o} (single- and poly-crystal graphite), respectively. This is in good agreement with experimental values found in the literature.

It is proposed that aluminium trends to expel surfaces (particles) with poorer wetting than the Al-filter interface.

The wettability of these three Al-ceramic systems with respect to time can be divided into three stages: (I) de-oxidation of the alumina layer, (II) Al_4C_3 formation and de-oxidation of silica, and (III) the stable contact angle.

Improved wetting of aluminium on ceramics with temperature promotes infiltration. In priming of filters it is necessary to have a metal height above the filter or to increase the temperature. However, filtration may proceed at lower temperatures once metal has entered the filter.

SiC filters have better wettability with aluminium than Al_2O_3 filters. SiC reacts slowly with aluminium at the casting temperature. SiC filters will increase the Si content in aluminium due to de-oxidation of the silica layer on the interface, and also due to the presence of free Si in reaction bonded SiC. Si in aluminium will prevent formation of Al_4C_3.

It is more difficult to remove Al_4C_3 inclusions then Al_2O_3 inclusions due to the better wettability of aluminium on Al_4C_3.

Graphite reacts with aluminium and produces Al_4C_3 at the interface, which is hydrophilic. It may be a problem to use graphite as a filter material.

Chapter 4 PLANT EXPERIMENTS

In this chapter a set of aluminium filtration plant experiments is presented. The results are used to throw light on the aluminium filtration mechanisms and will be compared to the branch filtration model discussed in Chapter 7.

4.1 Experimental Equipment and Procedure

Four filtration experiments were performed with two types of 10"×10"×2", 30 ppi filters in the reference center of Hydro Sunndalsøra: one high in Al_2O_3 and one high in SiC. These two types of filters were produced in the same line by the same supplier, giving similar porosity and wall thickness. The filters were Al_2O_3 industrial filters in experiments 1 and 3, SiC industrial filters in experiments 2 and 4.

4.1.1 Filtration Loop

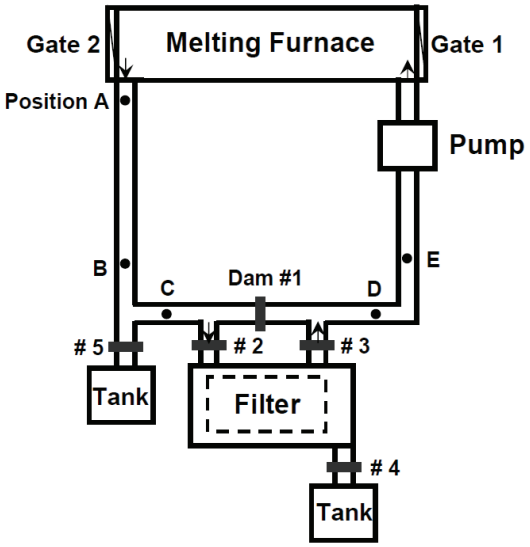

Figure 4.1 The schematic top view of the filtration loop

A top view of the filtration loop is shown in Figure 4.1. The melting furnace contains 15 tons of aluminium alloy, melted by burner inside. A porous plug through the furnace bottom with argon gas is used to stir the metal. Argon is injected with 35-50 Nl/min (Nl for normal liter at the atmosphere pressure) for 10min each time. Mechanical stirring from gate 1 is employed especially after standing a long night. The pump is used to control the mass flow of the metal. The pumping speed is 250rpm here, which gives a flow rate of 47-88mm/s.

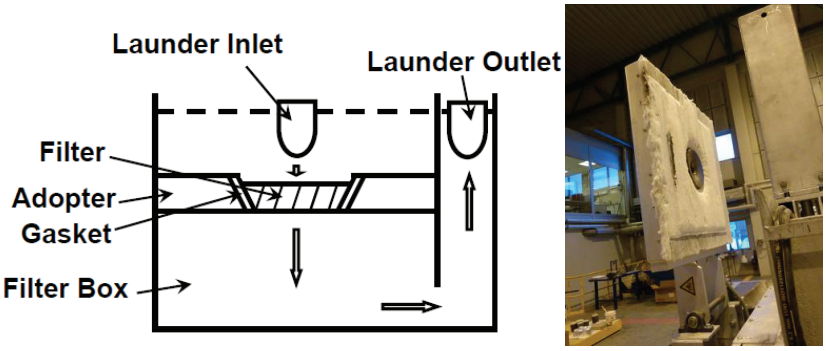

Figure 4.2 The schematic side view of the filter bowl (left) and the preheating lid (right)

Initially metal runs in the launder from position A through E and goes back to the melting furnace. The Liquid Metal Cleanliness Analyser (LiMCA) and laser give real time data for the metal. The filter in a filter bowl is preheated by a gas flush in the lid for 10 min; see Figure 4.2 right. Dam 2 is opened when LiMCA shows a relatively stable inclusion level and metal is led through the preheated filter, fills the lower space of the filter bowl, and goes out (see Figure 4.2, left). Dam 3 is opened when the right side groove of the filter bowl is full of metal. Then dam 1 is closed to ensure a constant mass flow through the filter. Dam 4 is opened to drain the metal in filter bowl after each experiment. Dam 5 is opened afterwards to drain the metal in launder at the end of the day.

See Figure 4.1 and Table 4.1 for position of instruments. LiMCA, and laser give on-line data for inclusion level (in k/kg), metal height in the launder (in mm) and temperature (in ^{o}C), respectively. Disk samples are for spectrographic analysis. The PoDFA give information on inclusion concentrations and types.

Table 4.1 Position of instruments

Position	Note
A	Position 1: Melting furnace temperature, Disk # 1
B	Position 1: LiMCA # 1
C	Position 1: Laser # 1, PoDFA # 1
D	Position 2: Laser # 2, PoDFA # 2, Disk # 2
E	Position 2: LiMCA # 2

Filtration lasts 1 hour in each experiment. 3 groups of PoDFA and disk samples from both position 1 and 2 are taken in each experiment when the LiMCA shows a stable

inclusion level at approximately 0 min, 30 min, and 60 min. Dam 1 is opened after each experiment, and then dam 2 and 3 are closed.

2 trials were made for each industrial filter: Exp.1 and 3 for Al_2O_3, Exp.2 and 4 for SiC. Spent filters in whole pieces are taken out from the filter bowl for further study. Sample numbering follows a rule: sample type + experimental number + position number + sample number. For example, for Exp.1, we have:
PoDFA samples: P111, P121, P112, P122, P113, P123;
Disk samples: D111, D121, D112, D122, D113, D123;

4.1.2 Materials

Table 4.2 provides the filter properties from the supplier. The densities of filter materials were tested by AccuPyc 1330[4] in SINTEF. The average porosities are shown in the last row in Table 4.2. The porosity is calculated on the basis of mass and volume measurements using the relation:

$$\varepsilon = 1 - \textit{the bulk density} / \textit{the material density} \tag{4.1}$$

Table 4.2 Properties of the filters

	Al_2O_3 industrial filter		SiC industrial filter	
Max. application temperature	1000°C		1250°C (depending on application)	
Chemical characterization	Al_2O_3	85-90%	Al_2O_3	5-9%
	P_2O_5	Approx.6%	SiC	58-64%
	SiO_2	Approx.6%	SiO_2	29-33%
	K_2O+Na_2O	Approx.1%		
Dilation* 20-1000 °C			0.42%	
Chemical resistance	Good			
Thermal shock resistance	Good			
Thermal expansion** 20-1000°C	Approx.8.5×10^{-6}/°C		Approx. 4.3×10^{-6}/°C	
Bending strength (3-point)	1.5 MPa			
Bulk density	0.34-0.49 g/cm^3		0.35-0.50 g/cm^3	
Material density	3.50-3.51 g/cm^3		2.76-2.89 g/cm^3	
Average porosity	88.2%		85.0%	

** Dilation refers to an enlargement or expansion in bulk or extent.*
*** Thermal expansion is the tendency of matter to change in volume in respect to a temperature change.*

The chemical composition of the aluminium alloy 5005 with approximately 1% Mg was used. See Table 4.3.

[4] AccuPyc 1330 is a density analyser from Micromeritics, 4356 Communications Dr. Norcross, GA 30093-2901, U.S.A.

Table 4.3 The standard chemical composition of the 5005 alloy [149]

								Unspecified other elements		
	Mg	Fe	Si	Zn	Cu	Mn	Cr	Each	Total	Al
wt%	0.5-1.1	0.7	0.3	0.25	0.2	0.2	0.1	0.05	0.15	Remain

4.1.3 Measurement Methods

Inclusions were measured in several ways. During filtration, 2 LiMCA II were used before and after the filter. The LiMCA II gives on-line readings of the inclusion number and the size distribution. In addition, 6 PoDFA off-line samples were taken. 6 disk samples for spectrographic analysis were taken at the same time as the PoDFA samples. Dissolved hydrogen content is measured by Alspek continuously. The Alspek results will not be discussed here, but will be reported in [150].

4.1.3.1 PoDFA

Introduced in Section 2.1.7.2, the Porous Disc Filtration Apparatus (PoDFA) was used. The PoDFA gives quantitative information on inclusion type and concentrations. The PoDFA system includes a PoDFA sampling station, crucible heater, crucible and filter. See Figure 4.3.

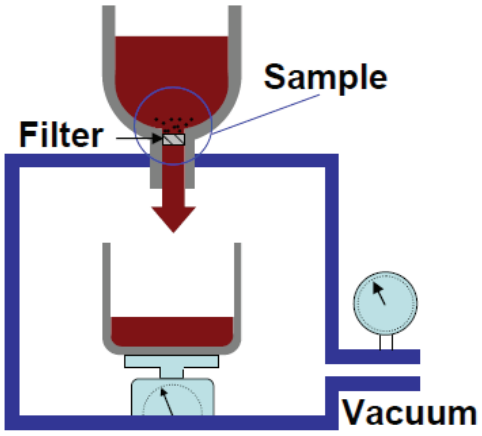

Figure 4.3 Principle of PoDFA apparatus

The hot metal is drawn through a pre-heated filter by the vacuum until a given amount of metal is weighted in the crucible under the filter. The residue on the filter is analyzed. The PoDFA samples (circled in Figure 4.3) are hot mounted in Bakelite and polished to a mirror-like finish. Using the grid method [14], the total inclusion area is obtained. This area was then divided by the mass of the metal that passes through the filter (about

1.5 kg). The total inclusion concentration area per kilogram is calculated using the formula(2.17) [14].

3 groups of PoDFA samples are taken at the beginning, middle, and end of the filtration on positions before and after the filter.

4.1.3.2 LiMCA II

Although the PoDFA technique is a powerful tool in determining not only the inclusion concentrations but also the type of inclusions, the process is fairly slow. Thus, an on-line measuring apparatus, the Liquid Metal Cleanliness Analyser (LiMCA), is recommended.

LiMCA II [151, 152] is used to measure the size and number size distribution of the inclusions during casting. One LiMCA II is placed at the inlet of the filter with the other at the outlet in the current work. See position B and E in Figure 4.1.

Figure 4.4 LiMCA II in operation, positioned after the filter

When a non-conductive inclusion between 20 and 320 μm passes through the orifice with the flow, the overall resistance of the orifice is increased momentarily and can be detected as a voltage pulse. Figure 4.4 shows the LiMCA II in operation. There are two main disadvantages for the LiMCA II: two inclusions sticking to each other are measured as one with a greater size; and gas bubbles are measured as inclusions. For more information about the theoretical basis of the LiMCA II, refer to the Section 2.1.7.3.

4.1.3.3 The filter wettability

The new filters shown in Figure 4.5 were crushed, ground, and sieved. The ground powder of size less than 40μm is pressed into tablets under 3.6 bar pressure. The wettability is tested in 10^{-8} bar vacuum at temperatures 1000 and 1100^{o}C, as described in Section 3.1.

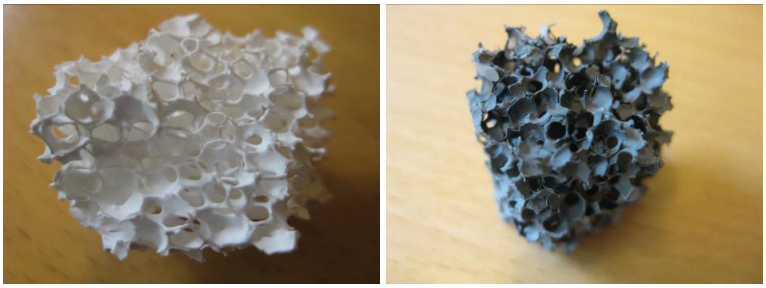

Figure 4.5 The new Al_2O_3 industrial filter (left) and SiC industrial filter (right)

4.1.4 The Remelting of PoDFA Samples

PoDFA samples were re-taken after the pilot experiments from around 2 kg of metal sample taken from each PoDFA position as described in Section 4.1.3.1, due to lack of PoDFA filters during the pilot trial. One PoDFA sample was taken from each remelted metal sample.

Metal is remelted according to the heating program as shown in Figure 4.6. Temperatures are logged every 10 seconds. 100% power is used to heat the solid sample until approximately 900°C, and melt starts at approximately 650°C. The melting point of approximately 1 wt% Mg alloy is approximately 10°C lower than the pure aluminium. At 70% power the metal is heated to 720°C and manually held at this temperature.

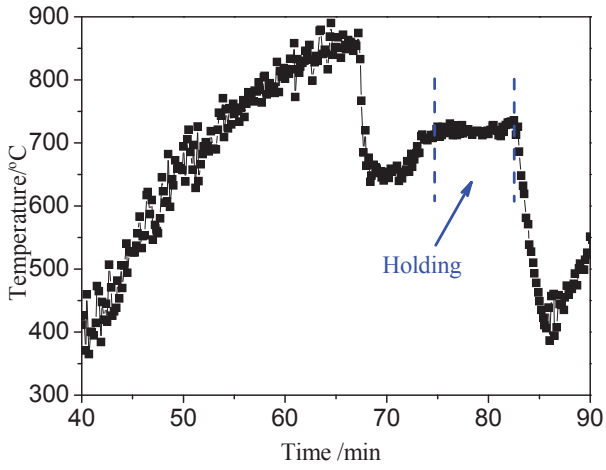

Figure 4.6 Example of the registered temperature for the sample P213

Meanwhile the crucible with a PoDFA filter is preheated and the temperature is measured. Then metal is poured into preheated crucible. There is a bowl inside the

PoDFA apparatus used to measure the filtrated metal mass. The standard filtrated mass is set at 1.25kg. When the mass reaches 1.25kg, filtering is stopped automatically. -610 mm Hg (-0.81 bar) pressure is employed.

Remelting will change the properties of the metal. It may adsorb hydrogen from the atmosphere during remelting and push hydrogen out as solidification proceeds.

However, the inclusion content probably is not influenced. The original PoDFA sample (Figure 4.7) is melted in the crucible upside down. After pouring all the metal, a layer of oxide skin with the label is left inside the melting crucible (Figure 4.8). During melting, no breakage of the oxide layer on top of the metal is observed even when we used the 100% heating power. This indicates that a strong oxide skin protects against further oxidation of the metal. Inductive stirring of the crucible should give an even distribution of inclusions in the metal.

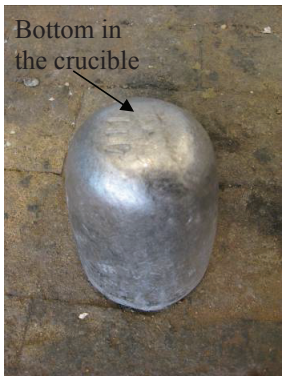

Figure 4.7 The ingot before melting

Figure 4.8 The oxide skin left in crucible after melting

4.2 Experimental Results

4.2.1 Chemical Composition of the Metal

Figure 4.9 to Figure 4.12 show composition of the alloying elements in Exp.1 to Exp.4 from the spectrographic analysis. This alloy contains approximately 1.00 wt% of Mg, 0.15 wt% of Fe, 0.075 wt% of Si, and the other elements are all less than 0.05 wt%. The minor elements are presented in an enlarged scale. All experiments give relatively stable inlet and outlet composition, except for a sudden increase of inlet level at 60min in Exp.1 and outlet level at 0 min in Exp.3 for Ca.

No apparent change of Si and Mg content was detected. This indicates that reactions(2.44), (2.31), and (2.32) are very slow at the casting temperature for this alloy. Industrial Al_2O_3 and SiC filters did not change the metal composition.

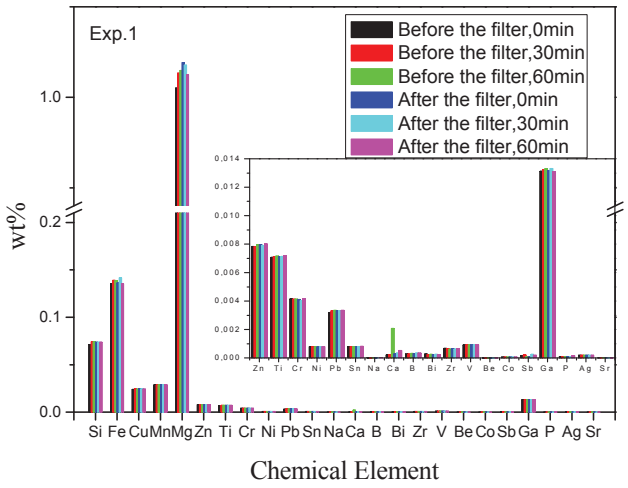

Figure 4.9 The composition of alloying elements before and after the filter in Exp.1

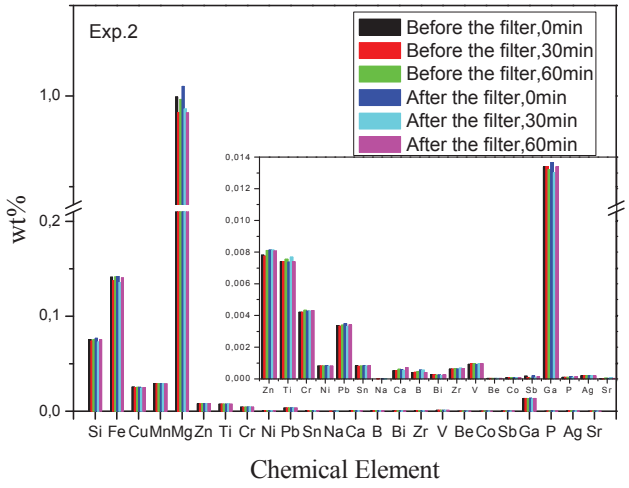

Figure 4.10 The composition of alloying elements before and after the filter in Exp.2

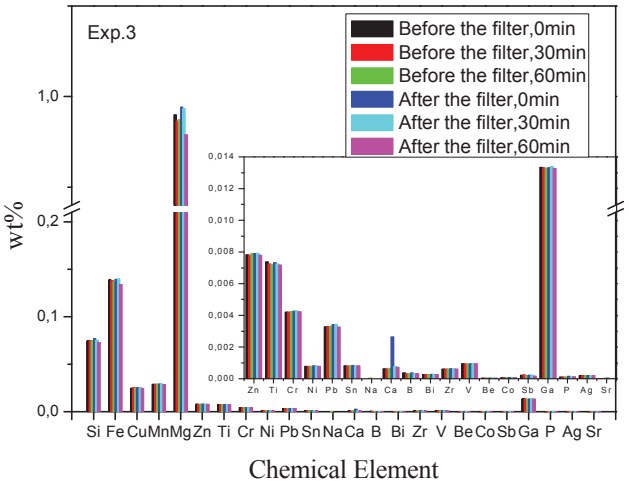

Figure 4.11 The composition of alloying elements before and after the filter in Exp.3

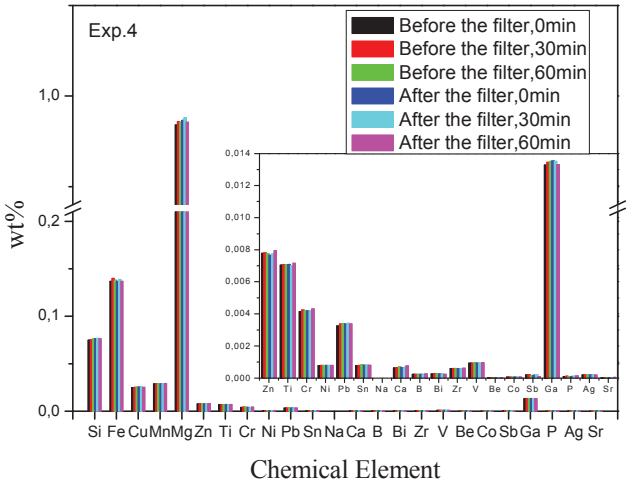

Figure 4.12 The composition of alloying elements before and after the filter in Exp.4

4.2.2 Filter Wettability

The wetting of aluminium and industrial filters was tested. The time dependent contact angles for aluminium on filter materials are presented in Figure 4.13 to Figure 4.16.

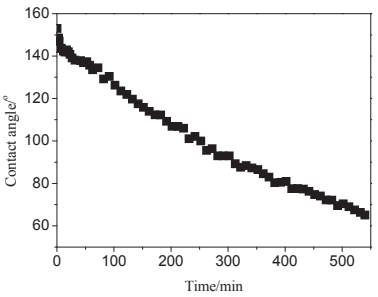

Figure 4.13 Contact angle vs. time for Al on Al_2O_3 industrial filter at 1100ºC

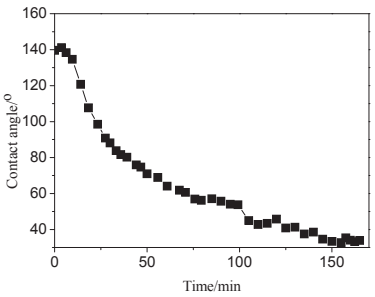

Figure 4.14 Contact angle vs. time for Al on Al_2O_3 industrial filter at 1200ºC

Similar trends as on pure substrates are observed. Contact angles decrease with time and are close to a stable angle. It shows nearly stable contact angle of 32° on Al_2O_3 industrial filters at 1200 °C and 92° on SiC industrial filters at 1100 °C. However, no stable contact angle was reached for Al_2O_3 industrial filters at 1100 °C even though we

held it for 9 hours due to the penetration. The repeated two experiments in Figure 4.16 show that the aluminium droplet on SiC industrial filters at 1200°C evaporates so fast that no stable contact angle was detected. Due to the carbon present, aluminium evaporation is enhanced for SiC industrial filter according to reaction(2.47).

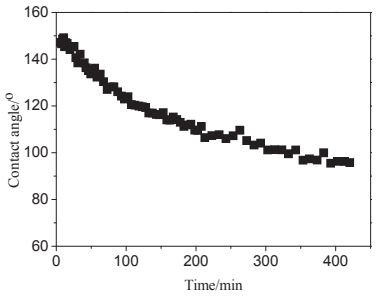

Figure 4.15 Contact angle vs. time for Al on SiC industrial filter at 1100ºC

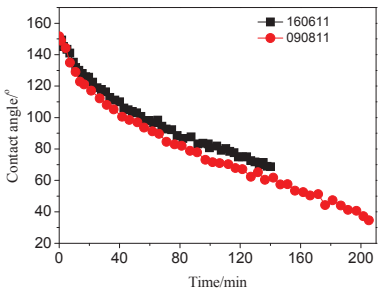

Figure 4.16 Contact angle vs. time for Al on SiC industrial filter at 1200ºC

Industrial Al_2O_3 filters give lower contact angles than pure Al_2O_3 as shown in Table 4.4. It is mainly due to the increased roughness of the pressed powders, and may also be due to that the components, P_2O_5 and K_2O+Na_2O, improve the wetting. However, industrial SiC filters show larger contact angles than pure SiC as shown in Table 4.4. The Al_2O_3 component in SiC industrial filters has impaired its wetting with aluminium.

Regarding the roughness of pressed powder, we conclude that both sintered filter materials (not pressed powder) are non- wetted by aluminium at casting temperature since wettability decreases with lower temperatures. SiC industrial filters are probably better wetted by aluminium than Al_2O_3 industrial filters due to its SiC components.

Table 4.4 Contact angles of industrial filters and pure materials

Filter	1000°C	1100°C	1200°C	1300°C
Industrial Al_2O_3		<60°	32°	
Industrial SiC		92°	<32°	
Pure Al_2O_3	67-70°	60-63°	47-57°	50-55°
Pure SiC	60-65°	51-56°		

4.2.3 Pressure Drop

Figure 4.17 to Figure 4.20 show the pressure drop and the temperature. During filtration, temperatures change in the range of 718-732°C, with a stable pressure drop 31-33 mm in Exp.1. There is a similar situation in Exp.2. The temperatures change in the range of 695-737°C, with the pressure drop 29-31 mm. In Exp.3, the temperature is relatively high, 730-746 °C, while the pressure drop decreases from 27 mm to 18 mm in the beginning for 16 min and stabilizes at 16-18 mm until the end of filtration. In Exp.4,

the pressure drop decreases from 26 mm to 17 mm during the first 16 min and stabilizes. The temperatures are 719-732°C.

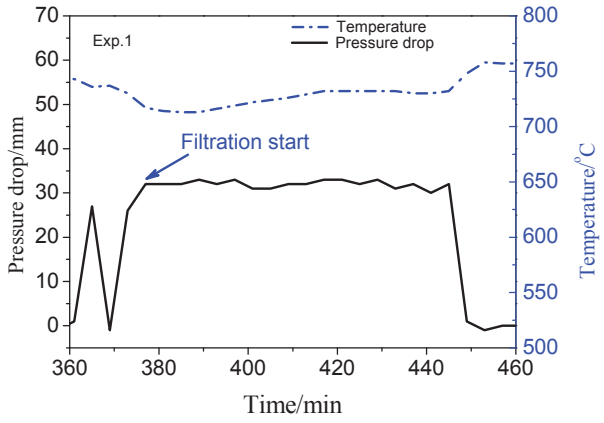

Figure 4.17 The pressure drop in Exp.1 – Al_2O_3 industrial filter

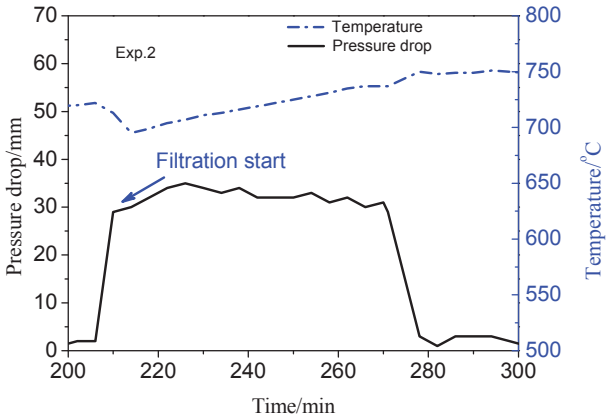

Figure 4.18 The pressure drop in Exp.2 – SiC industrial filter

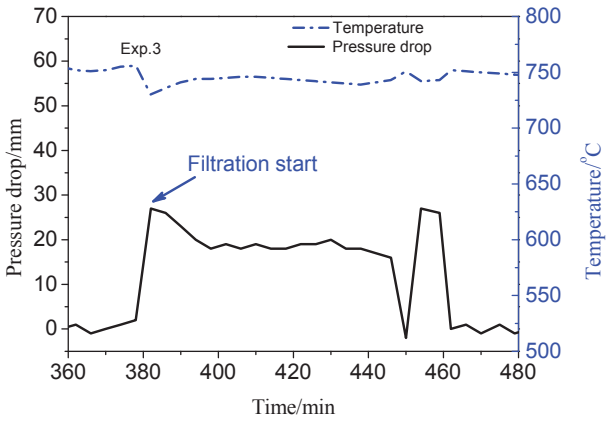

Figure 4.19 The pressure drop in Exp.3 – Al_2O_3 industrial filter

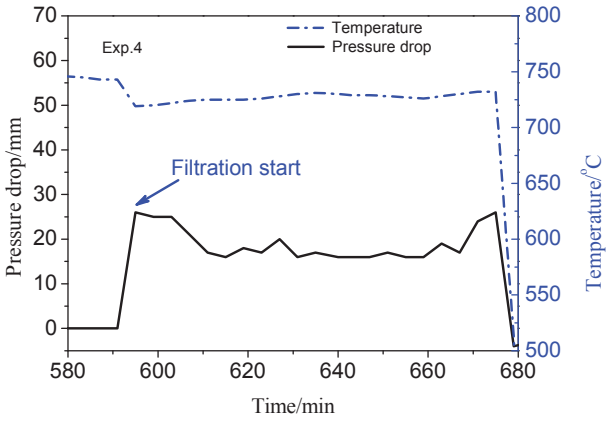

Figure 4.20 The pressure drop in Exp.4 – SiC industrial filter

4.2.4 Inclusion Levels

Figure 4.21 shows the N20 (inclusions greater than 20 µm) level. Filtration starts at the 151min on the LiMCA reading in Exp.1. Gas injection in melting furnace was started just before, which leads to the sudden increase of inlet inclusion level. As expected the outlet inclusion level is lower than the inlet level. Figure 4.22 gives the mean number inclusion size distribution and filtration efficiency in Exp.1. Most of the inclusions are less than 40µm. Approximately 50% of the inclusions are in the range of 20-25µm. For details concerning the time behaviour of the various size fractions, see Figure B.1 to Figure B.2 in Appendix B. The filtration efficiency in general increases with particle

size. The standard deviations of filtration efficiencies are discussed in Appendix C. In all four experiments, only less than 2.5% of the inclusions are larger than 60μm. The low number of large inclusions results in a huge uncertainty.

As an example, Figure 4.23 shows the filtration efficiency for N35-40 inclusions with time in Exp.1 with mean filtration efficiency of 60% except spurious points. The time dependent filtration efficiencies for N20-25, N25-30, and N30-35 inclusions in Exp.1 are shown in Figure B.9 to Figure B.11 in Appendix B.

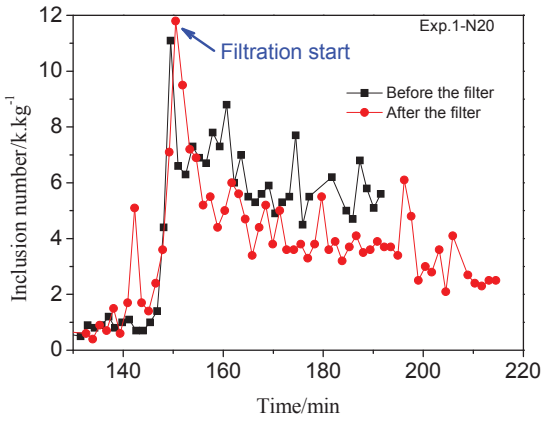

Figure 4.21 The inclusion level N20 in Exp.1 – Al_2O_3 industrial filter

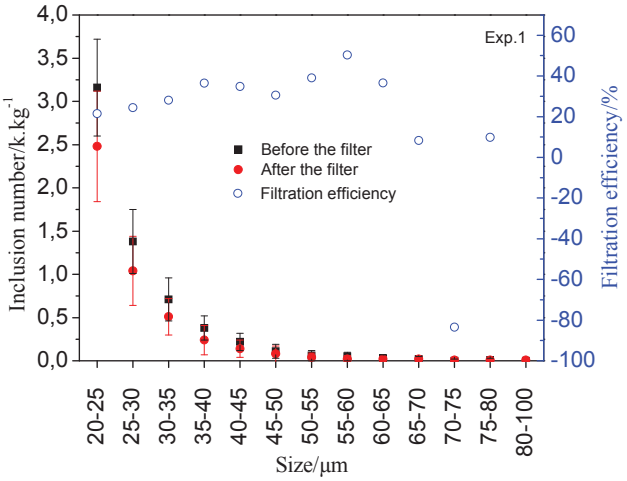

Figure 4.22 The mean number inclusion size distribution and filtration efficiency in Exp.1 – Al_2O_3 industrial filter

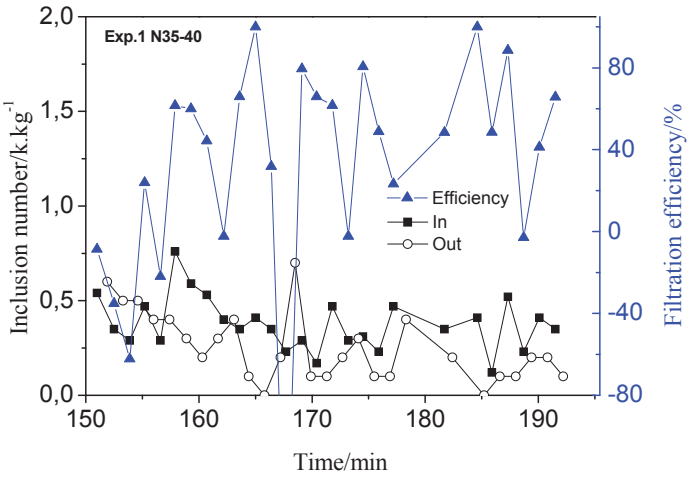

Figure 4.23 The filtration efficiency vs. time for inclusions 35-40 µm in Exp.1

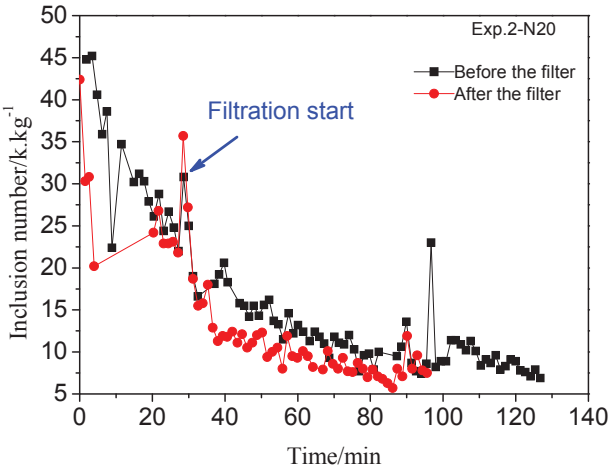

Figure 4.24 The inclusion level N20 in Exp.2 – SiC industrial filter

A similar situation was observed in Exp.2. The incoming inclusion levels fade with time due to the sedimentation in the melting furnace (Figure 4.24). The sudden increase of mass flow and fluctuation in metal flow causes an abrupt increase in inclusion level at the start of filtration as illustrated in Figure 4.24. Figure 4.25 gives the mean number inclusion size distribution and filtration efficiency in Exp.2. The number of inclusions is greatest in the range of 20-40µm. For details concerning the time behaviour of the

various size fractions, see Figure B.3 to Figure B.4 in Appendix B. The filtration efficiency in general increases with particle size.

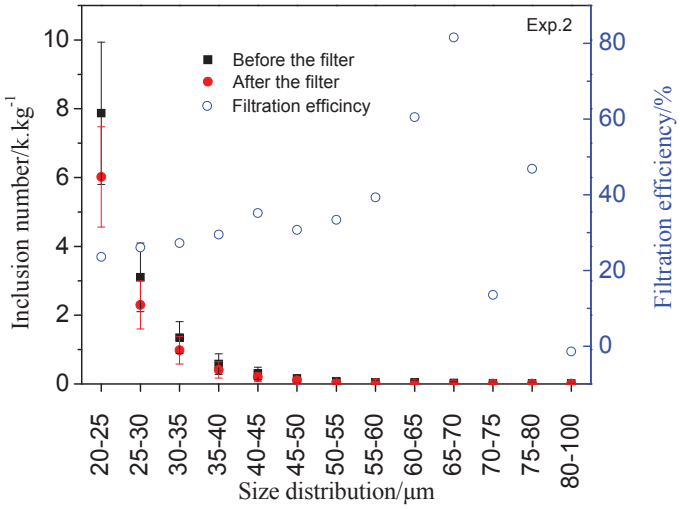

Figure 4.25 The mean number inclusion size distribution and filtration efficiency in Exp.2 – SiC industrial filter

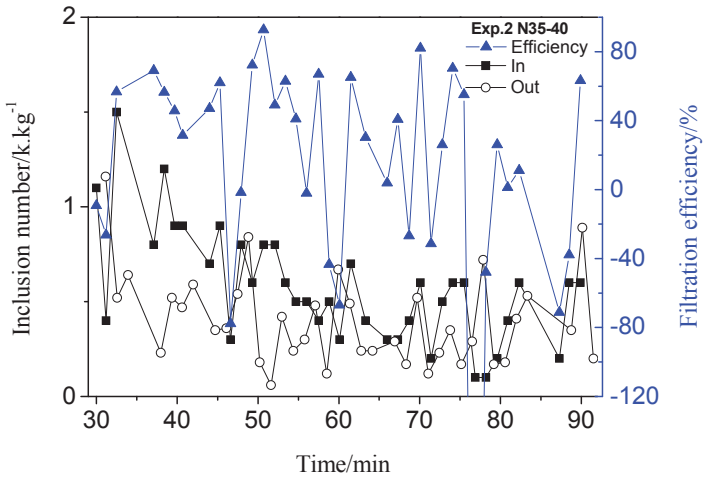

Figure 4.26 The filtration efficiency vs. time for inclusions 35-40 µm in Exp.2

As an example, Figure 4.26 shows the filtration efficiency for N35-40 inclusions in Exp.2, which shows a huge fluctuation of filtration efficiency. The time dependent filtration efficiencies for N20-25, N25-30, and N30-35 in Exp.2 are shown in Figure B.12 to Figure B.14 in Appendix B.

In Exp.3, 35Nl/min argon gas was injected through a porous plug for 13.5 min. Then the incoming inclusion level increased from approximately 5k/kg to 20k/kg. See Figure 4.27. The second inclusion increase at approximately 32 min is due to the increased metal flow and fluctuation at the filtration start. Figure 4.28 gives the mean number inclusion size distribution and filtration efficiency in Exp.3. The inclusion number is greatest in the range of 20-40μm. For details concerning the time behaviour of the various size fractions, see Figure B.5 to Figure B.6 in Appendix B. The filtration efficiency in general increases with particle size.

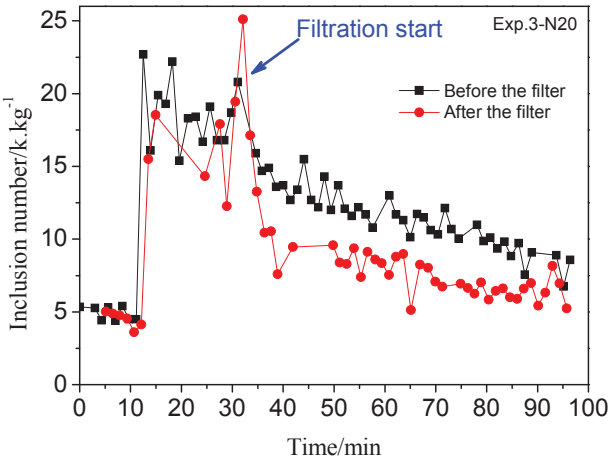

Figure 4.27 The inclusion level N20 in Exp.3 – Al_2O_3 industrial filter

As an example, Figure 4.29 shows the filtration efficiency for N35-40 inclusions with time in Exp.3, which shows a huge fluctuation of filtration efficiency. The time dependent filtration efficiencies for N20-25, N25-30, and N30-35 in Exp.3 are shown in Figure B.15 to Figure B.17 in Appendix B.

50Nl/min argon gas was injected into the melting furnace 34 min before the filtration in Exp.4. Filtration starts at the 39 min on the LiMCA reading, see Figure 4.30. Figure 4.31 gives the mean number inclusion size distribution and filtration efficiency in Exp.4. Most of the inclusions are less than 40μm. For details concerning the time behaviour of the various size fractions, see Figure B.7 to Figure B.8 in Appendix B. The filtration efficiency in general increases with particle size. As an example, Figure 4.32 shows the filtration efficiency for N35-40 inclusions in Exp.4 with filtration efficiency greater than 60% for most of the particle sizes. The time dependent filtration

efficiencies for N20-25, N25-30, and N30-35 in Exp.4 are shown in Figure B.18 to Figure B.20 in Appendix B.

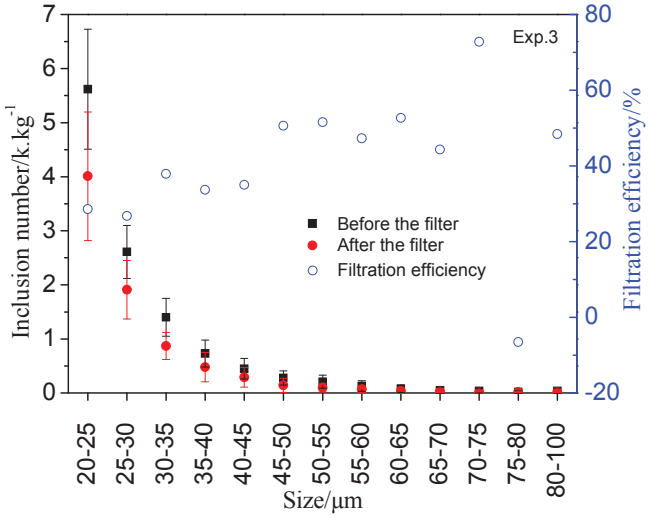

Figure 4.28 The mean number inclusion size distribution and filtration efficiency in Exp.3 – Al_2O_3 industrial filter

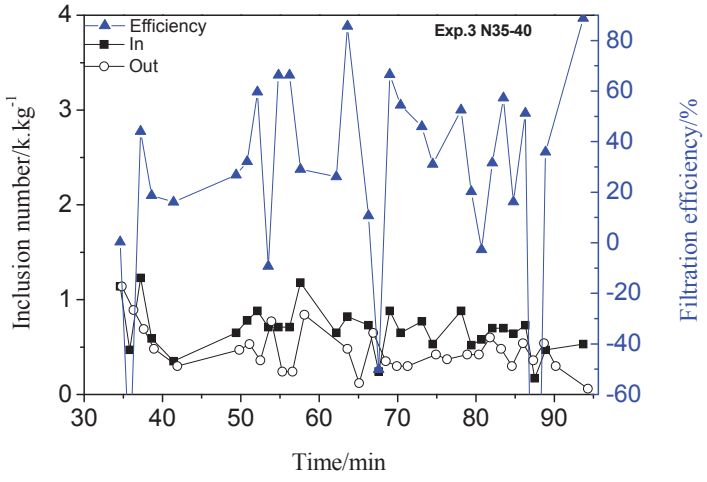

Figure 4.29 The filtration efficiency vs. time for inclusions 35-40 µm in Exp.3

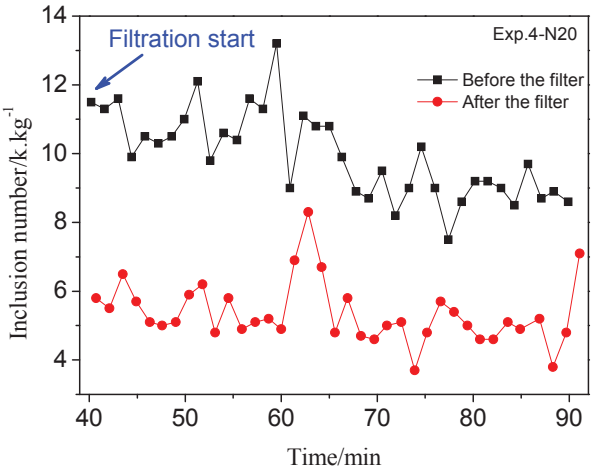

Figure 4.30 The inclusion level N20 in Exp.4 – SiC industrial filter

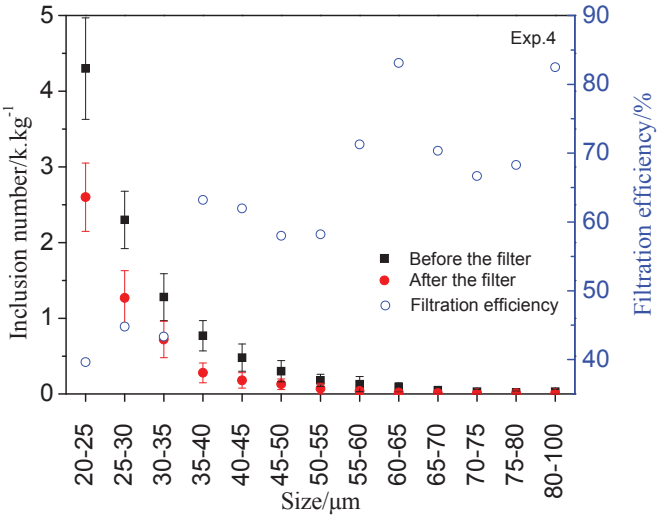

Figure 4.31 The mean number inclusion size distribution and filtration efficiency in Exp.4 – SiC industrial filter

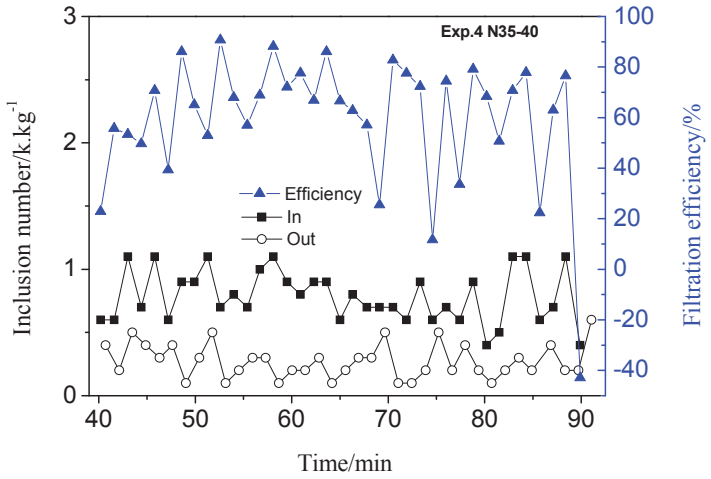

Figure 4.32 The filtration efficiency vs. time for inclusions 35-40 μm in Exp.4

The PoDFA results of the metallographic analysis are shown in Table 4.5. The filtered mass other than 1.25 kg is either due to blockage of filter, e.g. 0.93kg, or problems with the mass scale of the apparatus, e.g. 1.46kg. The results are also plotted in Figure 4.33 in the form of a bar chart that represents the proportion of each inclusion type. There are three types of inclusions, approximately 50% of mixed oxide, 10% of carbide, and 40% of TiB_2. Figure 4.34 shows the inclusion removal with the PoDFA data from Table 4.5. The mixed oxides were removed from 0.19-0.33 mm²/kg to 0.15-0.29 mm²/kg, carbides from 0-0.19 mm²/kg to 0.01-0.04 mm²/kg, and TiB_2 from 0.09-0.47 mm²/kg to 0-0.19 mm²/kg. Total inclusions are removed from 0.33-0.78 mm²/kg to 0.28-0.45 mm²/kg.

No carbide (Al_4C_3) removal was detected with available data, except at 0 min (actually it is 2-3min from the filtration start when the inclusion level stabilized) and 60 min in Exp.4. Mixed oxide was removed, except at 0 min in Exp.4. No TiB_2 was removed at 0 min in Exp.4 and 30min in Exp.3.

The metal is relatively clean. Mixed oxide probably comes from surface turbulence, splashing, etc. TiB_2 is found due to the presence of Ti and B as seen from Figure 4.9 to Figure 4.12, since no grain refiner was involved in the experiments. Carbide is Al_4C_3 that does not come from the filters.

The content of oxide in a sample is probably underestimated. Oxide films are difficult to measure by metallographic means due to the nature of PoDFA analysis technique. An oxide film is like a paper tissue in its shape. Metallographically films are only seen as thin lines. Some oxide may be removed during remelting and the solidification.

Table 4.5 The PoDFA results

PoDFA Sample No.	Weight [kg]	Preheated PoDFA filter temp. [°C]	Mixed oxide [mm²/kg]	Carbides [mm²/kg]	TiB_2/Ti-rich [mm²/kg]	Total inclusions [mm²/kg]	Removal Eff. of Total inclusions
112	1.46	540					
122	1.34	480	0.19	0.01	0.09	0.29	
113	1.09		0.27	0.02	0.13	0.42	
123	1.27	641	0.26	0.01	0.12	0.39	7.14%
121	1.22	490					
211	1.49						
221	1.27	541	0.16	0.02	0.18	0.36	
212	1.25	492	0.31		0.47	0.78	
222	1.25	531	0.21	0.02	0.19	0.43	44.9%
213	1.25	486					
223	1.25	491	0.34		0.51	0.85	
311	1.25	485	0.33		0.22	0.55	
321	1.32	510	0.22	0.04	0.00	0.45	18.2%
312	0.93	506	0.22		0.12	0.33	
322	1.26	513	0.15	0.04	0.18	0.37	-12.1%
313	1.24	500	0.33		0.40	0.73	
323	1.06	490					
411	1.26	477	0.19	0.19	0.09	0.47	
421	1.26	523	0.23	0.02	0.17	0.42	10.6%
413	1.15	471	0.25	0.02	0.12	0.38	
423	1.25	513	0.17	0.01	0.10	0.28	26.3%

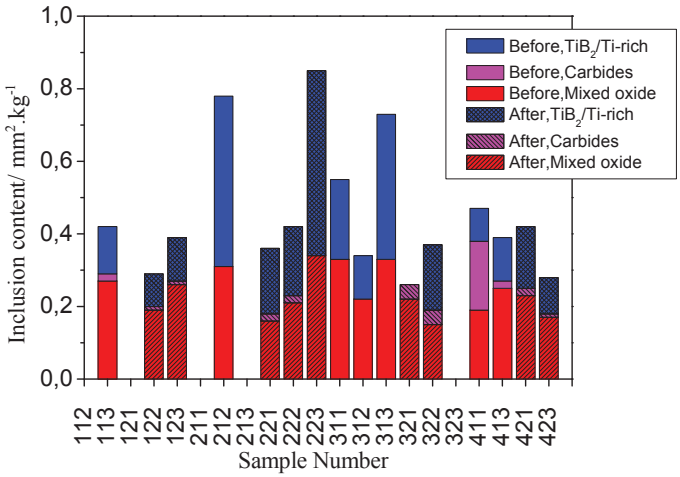

Figure 4.33 Inclusion concentration

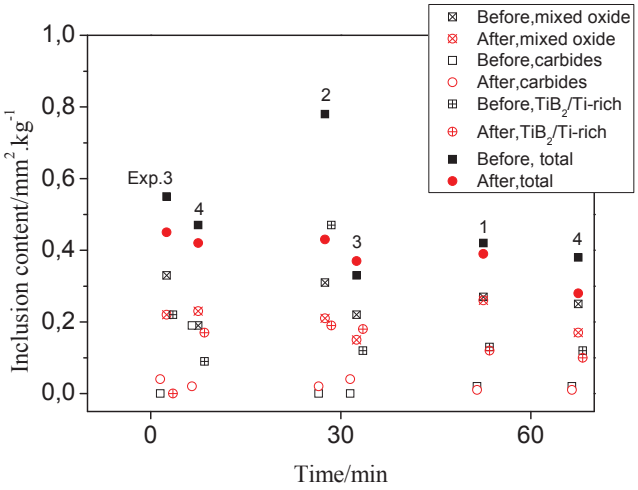

Figure 4.34 Inclusion removal analysed by PoDFA
The squares are before the filter, the circles after.

4.2.5 Spent Filter

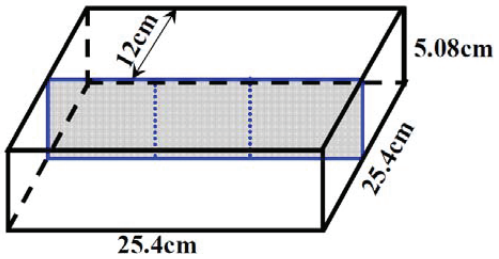

Figure 4.35 Cross sectional view of spent filters in the pilot test

The spent filters were cut along the middle (see Figure 4.35). The cross sections are shown in Figure 4.36 to Figure 4.39. Part of the filter was non-wetted by metal, and the metal was evenly loaded in the middle and two sides of the filter in Exp.1. More metal was observed in the cross section of Exp.2 (SiC) than in Exp.1 (Al_2O_3). However, it is hard to compare Exp.4 (SiC) and Exp.3 (Al_2O_3) since both filters were partly wetted by metal. Note that the rust in the Exp.3 is from saw.

We do not know if the voids were present when molten metal filled the filter or if they are due to drainage during solidification.

Figure 4.36 Cross sectional view of the spent filter in Exp.1 - Al_2O_3 industrial filter
White parts are filter material.

Figure 4.37 Cross sectional view of the spent filter in Exp.2 - SiC industrial filter
Black parts are filter materials.

Figure 4.38 Cross sectional view of the spent filter in Exp.3 - Al_2O_3 industrial filter
White parts are filter material, red is rust from saw.

Figure 4.39 Cross sectional view of the spent filter in Exp.4 - SiC industrial filter
Black parts are filter materials.

4.3 Discussion

The cross sectional views of the spent filters in Section 4.2.5 show that filters were partly wetted by the metal. Part of the metal may have drained away during solidification due to gravity and the cohesion work of the metal, especially for non-wetting filters. Both filter materials are non-wetted by aluminium at the casting temperature.

The SiC and Al_2O_3 industrial filters did not change the metal composition. Moreover, there is no indication that carbide was formed or entered the metal from the filters. An aluminium alloy with less than 10 at% Si (Figure 4.40) at 700°C could allow Al_4C_3 to be produced according to reaction(2.44).

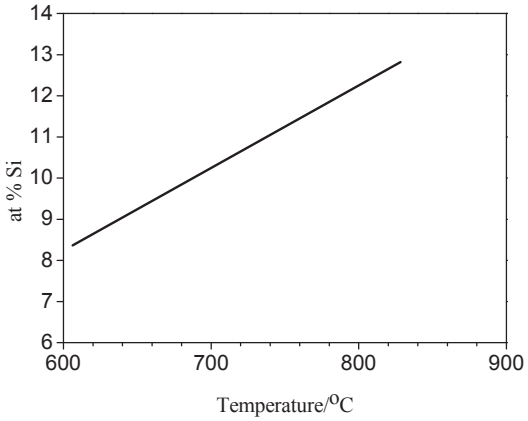

Figure 4.40 The Si level in equilibrium with Al_4C_3 and SiC in reaction(2.44) [153]

However, reaction(2.44) is probably slow. In the current one hour filtration, no increase of Al_4C_3 was measured with 0.075 wt% of Si alloy in Exp.2 and Exp.4 (SiC filters). The SiO_2 and Al_2O_3 components in the SiC industrial filters may slow down the kinetics of reaction(2.44).

Table 4.6 The pressure drop during filtration

	Exp.1	Exp.2	Exp.3	Exp.4
Temp.[°C]	718-732	695-737	730-746	719-732
Pressure drop[mm]	31-33	29-31	27 to 18 in 16 min and stabilized	26 to 17 in 16 min and stabilized

The pressure drop discussed in Section 4.2.3 is summarized in Table 4.6. Exp.3 and Exp.4 experienced a decreasing pressure drop during the first 16 min and stabilized at a lower value of 17-18 mm compared to the value of 29-33 mm in Exp.1 and Exp.2. Improved Al-filter wettability due to increased temperature is the probable reason for

the pressure drop decrease in Exps.3 and 4 compared to Exp.1 and 2. No metal leakage for filter- filter adopter and filter adopter- filter bowl (Figure 4.2) was observed in the experiments.

The preheating history of the filters is shown in Table 4.7. Exp.2 was the first experiment on the second morning, which had a relatively cold filter bowl. Although Exp.1 was heated by metal approximately 15 min, it had also a relatively cold filter bowl due to the 2 hour stop in between. Exp.3 experienced a relatively warm filter bowl heated in the previous experiment. Note that the metal in Exp.3 is approximately 10 degrees higher than the other 3 experiments. At the end of the second day, Exp.4 was carried out with the most hot filter bowl. Thus, Exp.3 and Exp.4 had a hotter filter bowl than Exp.1 and Exp.2.

Heat transfer from metal to filter including the bowl takes place in the early stage of filtration. A hot bowl is vital to keep the heat loss as low as possible [154]. From this point, the heat loss in Exp.3 and Exp.4 is expected to be low and filters are at higher temperatures then in Exp.1 and Exp.2.

Table 4.7 The preheating history of the filters

Charge No.		Note
Day 1	Exp.1	12:10 Preheated filter for 10min
		13:22 Metal (~740^{o}C) runs through filter for ~ 15min.
		15:11-16:26 Filtration Exp.1
Day 2	Exp.2	09:45 Preheat for 10min
		12:26-13:35 Filtration Exp.2
	Exp.3	14:45 Preheat for 15min
		15:17-16:29 Filtration Exp.3
	Exp.4	18:20 Preheat for 10min
		18:51-20:07 Filtration Exp.4

Thus, the wettability between the filter and the molten aluminium improves with the temperature in Exp.3 and Exp.4 requiring less pressure drop to infiltrate the filter.

Ceramic foam filters are produced by burnout of the organic foam material and firing of the ceramic foams covering it. This produces a highly porous body with a high temperature bond. CFFs do not have a large strength. One can break the tiny branches by hand. It is possible that these branches ($2R_{,SiC}$= 0.4 ± 0.1 mm, $2R_{,Al2O3}$= 0.3 ± 0.1 mm in the current study) break at high casting temperatures. Thus, micro leakage (breakage of branches) might exist in the filters in Exps.3 and 4. This might explain the pressure drop in the first 16 min in Exps.3 and 4.

Figure 4.41 shows the pressure drop with the metal temperature. At the same temperature around 727^{o}C, Exp.4 (SiC) has a lower pressure drop than Exp.2 (SiC) due to the warmer bowl. Exp.3 (Al_2O_3) with a higher metal temperature experiences a lower pressure drop than Exp.1 (Al_2O_3). It may be that improved wetting reduces the pressure drop. Exp.3 (Al_2O_3) and Exp.4 (SiC) show similar pressure drop at 743^{o}C and 727^{o}C, respectively. This may indicate that SiC industrial filters have better wettability than Al_2O_3 industrial filters.

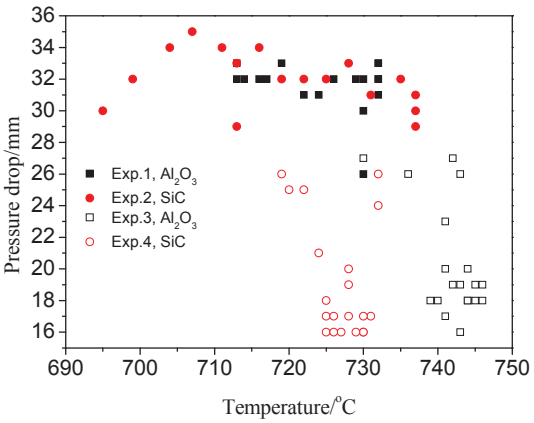

Figure 4.41 The pressure drop vs. metal temperature

The LiMCA results are influenced significantly by micro bubbles. However, no gas bubbling refining unit was involved. The hydrogen content is in the range of 0.1- 0.2 ml/100g in the current experiments. Thus, LiMCA should give a reliable inclusion reading in the range of 20-320 μm. There are no reliable results under 20 μm due to the electronic signal disturbances.

We have carried out a number of measurements per experiment: 2 LiMCA, 1 Alspek, and taken 6 PoDFA samples, 6 spectrographic analysis samples, and 12 reduced pressure drop test samples. This disturbs the aluminium and may influence the accuracy of the LiMCA readings.

The filtration efficiencies for the various inclusion sizes are shown in Figure 4.42. The standard deviations are discussed in Appendix C. In all four experiments, less than 2.5% of the inclusions are larger than 60 μm. The low number of large inclusions results in a huge uncertainty. Results regarding inclusions in 20-60 μm are plotted. Each point represents the mean value during one hour of filtration. For the time dependent filtration efficiency for various inclusion sizes, refer to Figure B.9 to Figure B.20 in Appendix B.

Filtration efficiencies increase with the inclusion size. Exps.1-3 have similar filtration efficiencies. However, Exp.4 has a higher value. The reason may be improved wetting.

Basically, no carbide and TiB_2 removal was observed in the four experiments. Oxide is obviously removed. Total removal efficiency is 7.14% in Exp.1, 44.9% in Exp.2, 18.2% and -12.1% in Exp.3, and 10.6% and 26.3% in Exp.4 from the observed PoDFA results in Table 4.5. This may indicate that SiC industrial filters capture more inclusions.

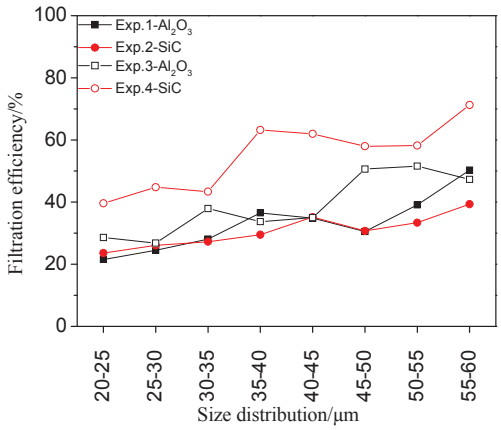

Figure 4.42 The filtration efficiency vs. the inclusion size distribution

4.4 Conclusions

Plant scale filtration experiments were carried out with Al_2O_3 and SiC industrial filters. In one hour filtration experiments, the initial behaviour of filters has been studied.

Both industrial filters are non-wetted by molten aluminium at casting temperature. However, SiC industrial filters have better wettability than Al_2O_3 industrial filters.

No metal composition change was introduced by both industrial filters. This is promising for SiC filters, considered an alternative filter material in aluminium filtration.

Improved wetting of aluminium on ceramics with temperature is an advantage in getting molten metal to infiltrate the filter. In priming filters it is necessary to have a metal height above the filter or to increase the temperature. In our plant experiments, the metal height above the filter was up to 33 mm in Exp.1 and Exp.2. With higher temperatures for the filter and filter bowl, the metal height was only 26-27 mm, and then stabilized to 17-18mm in Exp.3 and Exp.4. Filtration may proceed at lower temperatures once metal has entered the filter.

The Exp.4 with the SiC industrial filter gives higher filtration efficiency. The reason may be improved metal- filter wettability.

In addition to the filter, the bowl should be preheated at the beginning of casting.

We did not experience cake filtration or the blockage of the filter for the 5005 aluminium alloy even though we generated inclusions in the melting furnace. The alloy mainly contains oxides, carbides, and boride inclusions.

LiMCA accompanied with PoDFA measures effectively the inclusion level, size distribution, and inclusion types.

The filtration efficiency improves with inclusion size. For inclusion sizes in the range of 35-40μm, filtration efficiency was approx. 50% in all experiments even though the pore size was large using 30 ppi filters with average porosity approximately 86%.

Chapter 5 PARTICLE COLLISION ON A SINGLE CYLINDER

As a basic unit of particle removal in a ceramic foam filter (CFF), a single cylinder will first be studied in the current chapter. Mainly, collision of particles by interception and gravity is taken into account. As shown in Figure 5.1, a particle with diameter $2R_P$ approaches a cylinder with diameter 2R and collection angle θ. Schlichting [155] pointed out that the boundary layer separates and vortices (eddies) are formed at the rear side of the cylinder. Eddies are considered to scatter the particles, and collisions with the cylinder in the vortex region are neglected.

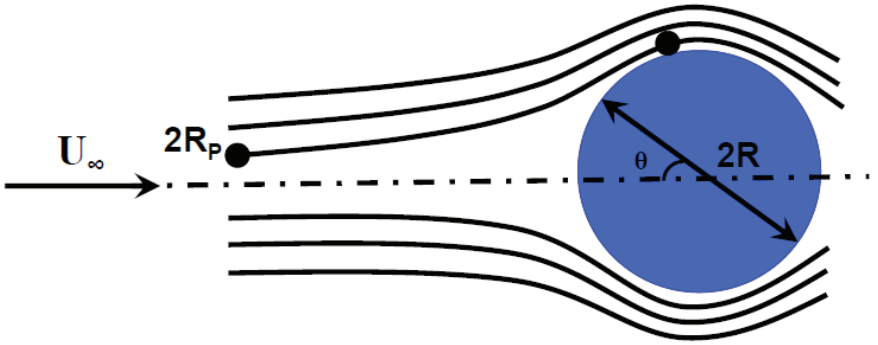

Figure 5.1 2 Dimensional view of a particle in a stream approaching a cylinder collector

5.1 Interceptional Collision

We assume that there is no slip between the liquid flow and the solid and introduce a boundary layer. Considering flow normal to the circular cylinder, the potential flow is given in the form of a series [155]:

$$U(x) = U_1 x + U_3 x^3 + U_5 x^5 + U_7 x^7 .... \tag{5.1}$$

The normal distance from the cylinder surface is y. This distance is made dimensionless by assuming [155]

$$\lambda = y\sqrt{\frac{U_1}{\nu}} \tag{5.2}$$

The coefficients U_1, U_3, U_5 depend only on the shape of the body. The stream function is

$$\Psi(x,\lambda) = \sqrt{\frac{\nu}{U_1}}\left\{U_1 x f_1(\lambda) + 4U_3 x^3 f_3(\lambda) + 6U_5 x^5 f_5(\lambda) + 8U_7 x^7 f_7(\lambda)....\right\} \tag{5.3}$$

Where x is the distance along cylinder measured from stagnation point and, x=Rθ.

$$\begin{aligned} U_1 &= 2\frac{U_\infty}{R} \\ U_3 &= -\frac{2}{3!}\frac{U_\infty}{R^3} = -\frac{U_\infty}{3R^3} \\ U_5 &= \frac{2}{5!}\frac{U_\infty}{R^5} = \frac{U_\infty}{60R^5} \\ U_7 &= -\frac{2}{7!}\frac{U_\infty}{R^7} = -\frac{U_\infty}{2520R^7} \end{aligned} \tag{5.4}$$

Then Equ.(5.2) becomes

$$\lambda = \frac{y}{R}\sqrt{\mathrm{Re}_c} \tag{5.5}$$

With Reynolds number

$$\mathrm{Re}_c = \frac{2U_\infty R}{\nu} \tag{5.6}$$

where the index c is for the cylinder. The stream function for the boundary layer becomes [155]:

$$\begin{aligned} \Psi(y,\theta) &= \sqrt{\frac{\nu}{\frac{2U_\infty}{R}}}\left[\frac{2U_\infty}{R}R\theta f_1 + 4\frac{-U_\infty}{3R^3}(R\theta)^3 f_3 + 6\frac{U_\infty}{60R^5}(R\theta)^5 f_5 + 8\frac{-U_\infty}{2520R^7}(R\theta)^7 f_7....\right] \\ &= \sqrt{\frac{\nu U_\infty R}{2}}\left[2\theta f_1(y) - \frac{4}{3}\theta^3 f_3(y) + \frac{1}{10}\theta^5 f_5(y) - \frac{1}{315}\theta^7 f_7(y)....\right] \end{aligned} \tag{5.7}$$

The functions f_1, f_3, f_5, and f_7 [155] are given in the Appendix A. The flow of liquid towards the cylinder is $2L_c\psi$. The volume flow approaching the cylinder is $2U_\infty RL_c$. Thus the collision probability for a particle of radius R_P due to interception is:

$$\eta_i = \frac{2L_c\Psi(y=R_P,\theta)}{2U_\infty RL_c} = \frac{\Psi(y=R_P,\theta)}{U_\infty R}$$
$$= \frac{2\theta}{\sqrt{\mathrm{Re}_c}}\left\{ f_1(\frac{R_P}{R}\sqrt{\mathrm{Re}_c}) - \frac{2}{3}\theta^2 f_3(\frac{R_P}{R}\sqrt{\mathrm{Re}_c}) + \frac{\theta^4}{20} f_5(\frac{R_P}{R}\sqrt{\mathrm{Re}_c}) - \frac{\theta^6}{630} f_7(\frac{R_P}{R}\sqrt{\mathrm{Re}_c})....\right\} \tag{5.8}$$

The collision efficiency increases with the θ until the maximum collision efficiency is attained at $\theta = \theta_c$, given by:

$$\frac{\partial \eta_i}{\partial \theta} = \frac{2}{\sqrt{\mathrm{Re}_c}}\left\{ f_1(\lambda_c) - 2\theta^2 f_3(\lambda_c) + \frac{\theta^4}{4} f_5(\lambda_c) - \frac{\theta^6}{90} f_7(\lambda_c)....\right\} = 0 \tag{5.9}$$

or

$$2f_7\theta^6 - 45f_5\theta^4 + 360f_3\theta^2 - 180f_1 = 0 \tag{5.10}$$

This equation is solved graphically by equating the left and right hand side of the equation. The method employed for the calculation of functions f_1 to f_7 is described in Appendix A. The solution for Equ.(5.10) is given in Figure 5.2. Inserting the collection angle θ_c in Equ.(5.8), we get Figure 5.3. The relation

$$\eta_i = A\lambda_c^{\ n} / \mathrm{Re}_c^{0.5} \tag{5.11}$$

is fitted to Figure 5.3 to give

$$\eta_i = 0.65\lambda_c^{1.73} / (\mathrm{Re}_c^{0.5}) \tag{5.12}$$

with R^2, 99%. The curve fitting employs a nonlinear least squares fitting (NLSF) [156] with a least square deviation. R^2 value gives the correlation coefficient for the fit.
Equ.(5.12) can also be written as

$$\eta_i = 0.65(R_p / R)^{1.73}(\mathrm{Re}_c^{0.365}) \tag{5.13}$$

It is seen that the collision efficiency η_i strongly depends on the ratio between particle size and cylinder size R_p/R. When streamlines are pressed together in flow around the cylinder, particles in the liquid come closer to the walls. At a distance R_p they collide with the surface. There is a moderate increase of η_i with the cylinder Reynolds number.

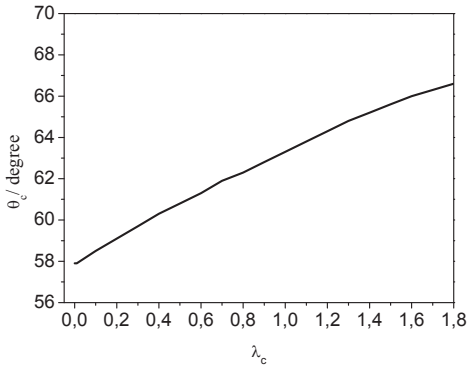

Figure 5.2 The collection angle for collision by interception

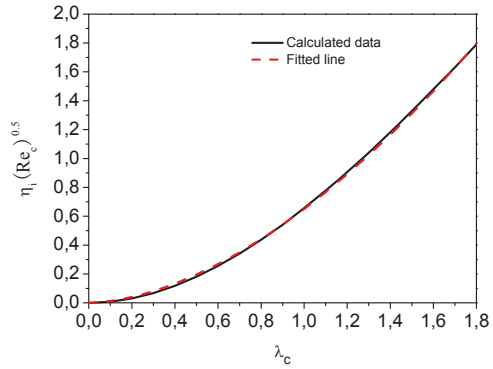

Figure 5.3 The relation of λ_c and collision efficiency according to Equ.(5.8)

It is assumed that the cylinders are oriented randomly relative to the velocity. For the flow normal to a cylinder, Equ.(5.13) gives the collision efficiency. β is the angle that the normal to the velocity makes with the cylinder axis. Following Schlichting [157], we assume that when the cylinder makes an angle β with the normal to the flow, the velocity $U_\infty \cos\beta$ determines the boundary layer behaviour (Independence principle):

$$\eta_i(\beta) = 0.65(R_p / R)^{1.73}(\mathrm{Re}_c \cos\beta)^{0.365} \tag{5.14}$$

An average collision efficiency is determined:

$$\eta_{i-avg} = \frac{2}{\pi}\eta_i \int_0^{\pi/2} \cos^{0.365}\beta d\beta = 0.8109\eta_i \tag{5.15}$$

Table 5.1 gives the calculated collision results compared with Palmer's experimental data [3] for capture. Since the error is less than 1% when including f_7, f_9 or higher grade functions are not considered. Palmer observed 50^o for the collection angle [3] which is close to our calculated collection angle of approx. 59^o in Table 5.1.

With her first nine distinct flow conditions (smooth surface cylinder), Re_c= 50-500 and R_p/R= 0.008-0.03, Palmer [3] obtained the following regression:

$$\eta_{i-Palmer} = 0.224(R_P / R)^{2.08}\,\mathrm{Re}_c^{0.718} \tag{5.16}$$

Weber and Paddock [158] showed that the interceptional collision efficiency can be given by

$$\eta_{i-weber} = \frac{\xi}{2}(\frac{R_P}{R})^2 \tag{5.17}$$

where

$$\xi = \frac{R}{U_\infty}(\frac{\partial U_\theta}{\partial y}) = \frac{R}{U_\infty}(\frac{\partial^2 \psi}{\partial y^2}) \tag{5.18}$$

ξ is the dimensionless surface vorticity at the collection angle. From Equs.(5.7) and (5.18), we obtain

$$\eta_{i-weber} = \frac{{R_P}^2}{2\sqrt{\mathrm{Re}_c}}\left[2\theta\frac{\partial^2 f_1}{\partial y^2} - \frac{4}{3}\theta^3\frac{\partial^2 f_3}{\partial y^2} + \frac{1}{10}\theta^5\frac{\partial^2 f_5}{\partial y^2} - \frac{1}{315}\theta^7\frac{\partial^2 f_7}{\partial y^2}\right] \tag{5.19}$$

Espinosa et al. [159] has simulated particles in 2-D flow around a cylinder and results are illustrated in Figure 5.4, together with Equ.(5.19). The collection angle 59^o from Table 5.1 is used for Equ.(5.19). Figure 5.4 shows the collision efficiencies compared with Palmer's experimental data.

Table 5.1 Calculation of interceptional collision efficiency with Palmer's data

Exp. Set	2R [mm]	$2R_P$ [μm]	Average U_∞ [mm/s]	ν [m^2/s]	Re_c	$R_p/R`$	$Re_c`$	λ_c	Palmer exp. [%]	θ_c [°]	η_i, our cal. [%]
1	6.35	194	10	9.33E-07	68	0.017	122	0.19	0.350	59.1	0.329
2	12.7	194	10	9.26E-07	137	0.011	191	0.15	0.140	58.8	0.180
3	25.4	194	10	9.09E-07	279	0.006	334	0.12	0.050	58.6	0.086
4	6.35	194	6	1.01E-06	38	0.017	68	0.14	0.210	58.8	0.266
5	12.7	194	6	1.01E-06	76	0.011	106	0.11	0.094	58.6	0.145
6	25.4	194	6	1.02E-06	149	0.006	178	0.09	0.032	58.4	0.069
7	6.35	194	18	9.96E-07	115	0.017	206	0.25	0.480	59.4	0.398
8	12.7	194	18	9.56E-07	239	0.011	333	0.20	0.190	59.1	0.220
9	2.54	194	18	9.40E-07	486	0.006	582	0.15	0.077	58.9	0.106

See Appendix A for the calculation of the functions f_1 to f_7.
2.5mm of silicone grease coating was included in our calculation. R`=R+0.25cm.
Gravitational collision is neglected duo to the vertical cylinder in her case.
ρ_p=1.03ρ_l.

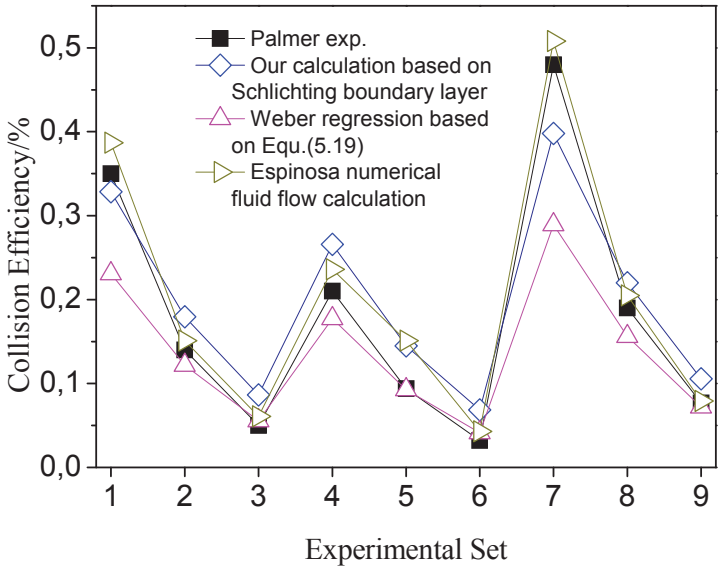

Figure 5.4 Collision efficiency for Palmer's case for neutrally buoyant particles
2.5mm of silicone grease coating was included in our calculation. R'=R+0.25cm.

The Espinosa calculation agrees well with Palmer in experiments 2, 3, 6, 8 and 9. It gives slightly higher results in experiments 1, 4, 5, and 7. The Weber calculation employing the Schlichting boundary theory agrees with the Palmer experiments 3, 5, 6, and 9. It gives lower values in experiments 1, 2, 4, 7, and 8.

The collision efficiency η_i in our calculation is slightly higher than the experimental results, except in experiments 1 and 7.

Two effects may contribute to higher results. Not all collided particles stick on the wall. The hydrodynamic effect, lift force normal to the cylinder surface, may push particles away from the cylinder.

5.2 Gravitational Collision

The other crucial collision mechanism is gravity. Hence the effect of gravity will only be outlined. If the particle density is different from that of the metal (assumed to be larger than the metal density), particles will settle out in the direction of the gravitational force. The gravity force acting on the particle [160] is

$$F_g = (\rho_p - \rho_l) g V \tag{5.20}$$

where V is the volume of the particle and equal to $4\pi R_P^3/3$ for a spherical particles.

The drag force on the particle is usually calculated in terms of an empirical factor C [161]:

$$F_d = C\rho_l U_S^2 A_p \tag{5.21}$$

where the drag coefficient C depends on the shape of the body and A_p is the projected area of the particle in the flow direction and equal to πR_P^2 for spherical particles.

The literature [161, 162] gives C versus Re_p for a sphere in an unbounded liquid, where

$$\begin{aligned} &C = \frac{24}{\mathrm{Re}_p}, \text{ when } \mathrm{Re}_p << 1 \text{ (Stokes' formula)} \\ &C = 47.91\text{-}8.04\mathrm{Re}_p \text{ , when } \mathrm{Re}_p \approx 1 \ to \ 5 \\ &C = 17.58\,\mathrm{Re}_p^{-0.62} \text{ , when } \mathrm{Re}_p \approx 5 \ to \ 10^2 \end{aligned} \tag{5.22}$$

where

$$\mathrm{Re}_p = \frac{2U_\infty R_P}{\nu} \tag{5.23}$$

The terminal settling velocity of a particle is determined by the balance between the opposing forces F_g and F_d, which gives Equ.(2.1).

For instance, for alumina particles (ρ_p=3.97 g/cm^3, R_P=10 μm) in aluminium metal (ρ_l=2.37 g/cm^3), C=240 when we set Re_p=0.1. Then the settling velocity is 0.61 mm/s. It takes 27.32 min to sink 1 m in a tank of stagnant aluminium.

Near a surface, Equ.(5.22) does not apply.

5.3 Collision in Down, Up, and Horizontal Flow

It is assumed that the flow approaching the cylinder is completely mixed with particles due to the action of the vortices from the upstream cylinders. The particle will follow the flow along the cylinder.

The velocity of the fluid along the cylinder surface is given by

$$U_\theta(y,\theta) = -\frac{\partial\psi(y,\theta)}{\partial y} = -\sqrt{\frac{\nu U_\infty R}{2}}\left[2\theta\frac{\partial f_1}{\partial y} - \frac{4}{3}\theta^3\frac{\partial f_3}{\partial y} + \frac{1}{10}\theta^5\frac{\partial f_5}{\partial y} - \frac{1}{315}\theta^7\frac{\partial f_7}{\partial y}\right] \tag{5.24}$$

The fluid velocity inwards in the radial direction is

$$U_r(y,\theta) = \frac{1}{R+y}\frac{\partial\psi(y,\theta)}{\partial\theta} = \frac{1}{R+y}\sqrt{\frac{\nu U_\infty R}{2}}\left[2f_1 - 4\theta^2 f_3 + \frac{1}{2}\theta^4 f_5 - \frac{1}{45}\theta^6 f_7 \ldots.\right] \tag{5.25}$$

Then the particle velocity along the cylinder is given by

$$V_\theta(y,\theta) = -\frac{\partial\psi(y,\theta)}{\partial y} + U_S \cos\varphi \tag{5.26}$$

The particle velocity inwards in the radial direction is given by

$$V_r(y,\theta) = \frac{1}{y+R}\frac{\partial\psi(y,\theta)}{\partial\theta} + U_S \sin\varphi \tag{5.27}$$

where

$$\begin{aligned}
&\varphi = \pi - \alpha - (\pi/2 - \theta) = \theta + \pi/2 - \alpha \text{ (See Figure 5.5)}\\
&\sin\varphi = \sin(\theta + \pi/2 - \alpha) = \sin\theta\sin\alpha + \cos\theta\cos\alpha\\
&\cos\varphi = \cos(\theta + \pi/2 - \alpha) = \cos\theta\sin\alpha - \sin\theta\cos\alpha
\end{aligned} \tag{5.28}$$

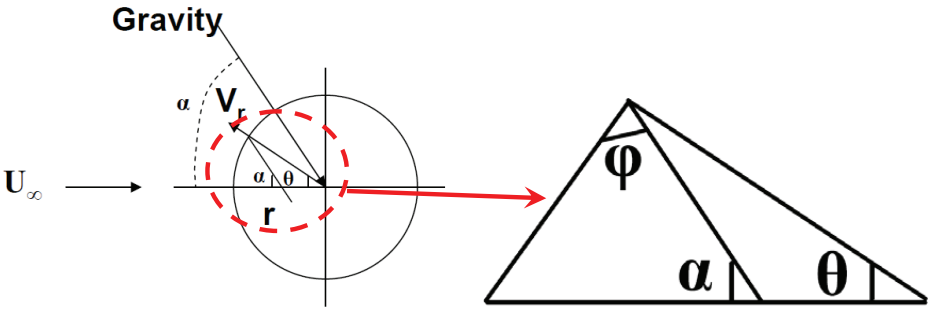

Figure 5.5 The schematic view of the cylinder cross section

Note that the velocity of the particle relative to the surrounding melt at the surface, U_s is significantly changed from the Stokes' velocity in Equ.(2.1) when it approaches the wall. It may be influenced by diffusion, hydrodynamic effects, Van der Waals force, surface tension etc. U_s is much smaller than the Stokes' velocity due to the high value of the drag coefficient near the wall.

Collision of particles with the cylinder occurs on the part of the cylinder where

$$V_r(y,\theta) = \frac{1}{y+R}\frac{\partial\psi(y,\theta)}{\partial\theta} + U_S \sin\varphi \le 0 \tag{5.29}$$

See Figure 5.5. The sign of the inequality in Equ.(5.29) corresponds to the case where the particle trajectory hits the collecting surface and the equality sign is valid when the particle trajectory touches the collecting surface.

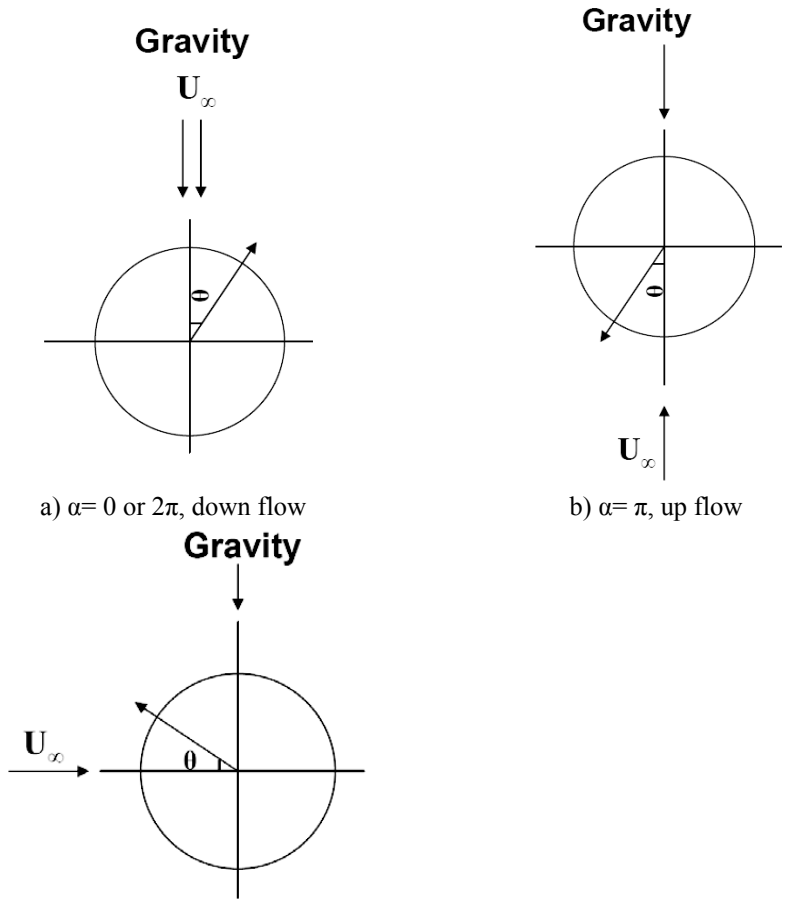

Figure 5.6 Schematic view of particles deposition on a single cylinder. θ=0 opposite to the incoming flow direction

Gravity acts in flow direction a), or against the flow direction b); and gravity acts normal to the flow c)

In order to find out where the collision start to take place, the condition (5.29) with the equality sign can be used and give $y=R_P$. One obtains

$$\frac{1}{R+R_P}\sqrt{\frac{\nu U_\infty R}{2}}\left[2f_1-4\theta^2 f_3+\frac{1}{2}\theta^4 f_5-\frac{1}{45}\theta^6 f_7....\right]=-U_S\left[\sin\theta\sin\alpha+\cos\theta\cos\alpha\right]$$

$$\left[2f_1-4\theta^2 f_3+\frac{1}{2}\theta^4 f_5-\frac{1}{45}\theta^6 f_7....\right]=-(R+R_P)U_S\sqrt{\frac{2}{\nu U_\infty R}}\left[\sin\theta\sin\alpha+\cos\theta\cos\alpha\right]$$

$$\left[2f_7\theta^6-45f_5\theta^4+360f_3\theta^2-180f_1\right]=90(R+R_P)U_S\sqrt{\frac{2}{\nu U_\infty R}}\left[\sin\theta\sin\alpha+\cos\theta\cos\alpha\right]$$

$$2f_7\theta^6-45f_5\theta^4+360f_3\theta^2-180f_1=K\left[\sin\theta\sin\alpha+\cos\theta\cos\alpha\right] \tag{5.30}$$

where

$$K=90(R+R_P)U_S\sqrt{\frac{2}{\nu U_\infty R}}=90\sqrt{\mathrm{Re}_c}\,\frac{U_S}{U_\infty}(1+\frac{R_P}{R})=90\frac{U_S}{U_\infty}(\sqrt{\mathrm{Re}_c}+\lambda_c) \tag{5.31}$$

Hence, it is not attempted to derive values for U_s. However, in order to give an indication of the effect of gravity on efficiency, U_s is included as an unknown variable in a discussion of down, up, and horizontal flow (Figure 5.6) towards a cylinder. In the following U_s and K are regarded as not dependent on the angle θ.

5.3.1 Down Flow

The case α= 0 represents down flow, when the direction of the flow and gravity coincide. See a) in Figure 5.6. Then,

$$V_r(y,\theta)=\frac{1}{y+R}\frac{\partial\psi(y,\theta)}{\partial\theta}+U_S\cos\theta=0 \tag{5.32}$$

Or

$$2f_7\theta^6-45f_5\theta^4+360f_3\theta^2-180f_1=K\cos\theta \tag{5.33}$$

All inclusions collide on the upper section of the collectors in the case of downward flow. Table 5.2 gives the collection angle in down flow. The collection angle increases from 57.9° (λ_c <<0.01 and K=0) to 90° when the settling velocity increases. Here we show the results until K=100. Data in Table 5.2 are plotted in Figure 5.7. The collection angle depends on ρ_p, ρ_l, ν, U_∞, R, and R_p. It will not exceed 90° in down flow. The collection angle increases with decreased λ_c (decreasing particle size and/or decreasing Re_c or U_∞).

The collision efficiency in down flow is

$$\eta_{\alpha=0} = \frac{2n_o(R+R_P)L_c\int_0^{\theta_c}(U_r + U_S\sin\varphi)d\theta}{n_o U_\infty \cdot 2L_c(R+R_P)} = \frac{\psi(R_P,\theta_c)+U_s\sin\theta_c}{U_\infty} = \eta_{i,\theta_c} + \eta_g\sin\theta_c \quad (5.34)$$

where we set $\eta_g = U_S/U_\infty$. However, the gravitational collision efficiency is based on time, distance, and the mass transfer coefficient for deposition, which calls for further investigation.

Table 5.2 The collection angle under various K and λ_c in down flow

K	The collection angle[°]						
	λ_c =0.01	λ_c =0.05	λ_c =0.1	λ_c =0.3	λ_c =0.6	λ_c =1.0	λ_c =1.8
1	89.7	80.2	69.7	61.6	61.9	63.6	66.6
3	89.8	85.9	78.3	64.9	62.9	63.9	66.6
10	90.0	88.7	85.4	71.8	65.7	65.1	67.1
20	90.0	89.4	87.5	77.1	69.0	66.8	67.7
30	90.0	89.7	88.3	80.0	71.4	68.2	68.3
40	90.0	89.7	88.8	81.8	73.5	69.3	68.8
50	90.0	89.8	89.0	83.1	75.0	70.5	69.4
60	90.0	89.8	89.1	84.0	76.3	71.4	69.8
70	90.0	89.9	89.3	84.8	77.5	72.4	70.3
80	90.0	89.9	89.4	85.3	78.4	73.1	70.8
90	90.0	89.9	89.5	85.8	79.2	73.9	71.2
100	90.0	89.9	89.5	86.2	79.9	74.6	71.6

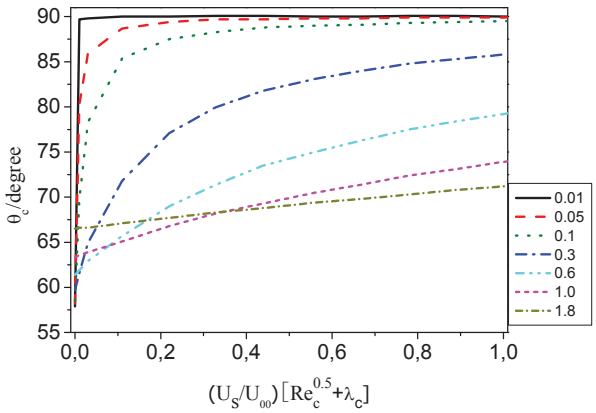

Figure 5.7 The collection angle vs. K/90 factor for various λ_c in down flow

The contribution from interception to collision efficiency is discussed in Figure 5.8. Interceptional collision increases with λ_c in down flow. However, it slightly decreases with increasing U_s (or the ρ_p) since heavy particles tend to separate from the flow line. Gravity drives particles towards the cylinder. The smaller the λ_c or the larger the K, the

greater the contribution from gravity in collision (see Figure 5.7). However at large polar angles, flow in the boundary layers is out from the cylinder and flow separates from it. The interception collision efficiency, $\eta_{i,\theta c}$ is practically independent of gravity, as shown in Figure 5.8 and is given by Figure 5.3.

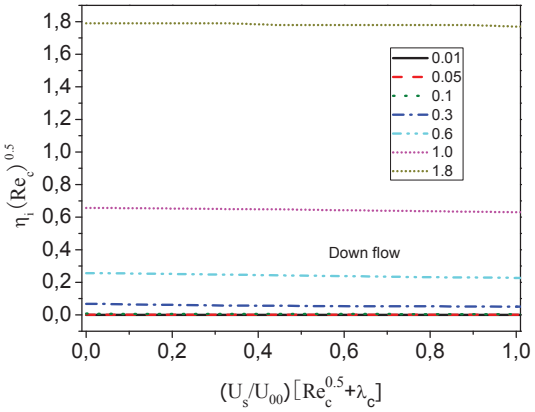

Figure 5.8 Interceptional collision efficiency vs. K/90 factor for various $\boldsymbol{\lambda_c}$ in down flow

5.3.2 Up Flow

The down low with particles lighter than the metal or the up flow with particles heavier than the metal would give $\alpha = \pi$. See b) in Figure 5.6. Then,

$$U_r(R+R_P,\theta) = U_S \cos\theta \tag{5.35}$$

Or

$$2f_7\theta^6 - 45f_5\theta^4 + 360f_3\theta^2 - 180f_1 = -K\cos\theta \tag{5.36}$$

Figure 5.9 shows the collection angle in up flow. The trend is more complicated then the other 2 cases. We can separate it into 3 areas as discussed in Figure 5.9 b, c, d, and Table 5.3. The collection angle θ_c increases with λ_c due to the increasing Re_c (or metal velocity). However, it decreases with the settling velocity (or K), except in the area b, because the K increases with Re_c in area b ($K<0.01$ and R_P is very small). The collection angle decreases with the settling velocity in the area c and d, since heavy particles tend to leave the stream line. If we compare the area c and d, the large collection angle ($>90^o$) is attained for small particles (area c) and small collection angle ($< 70^o$) for large particles (area d) in up flow.

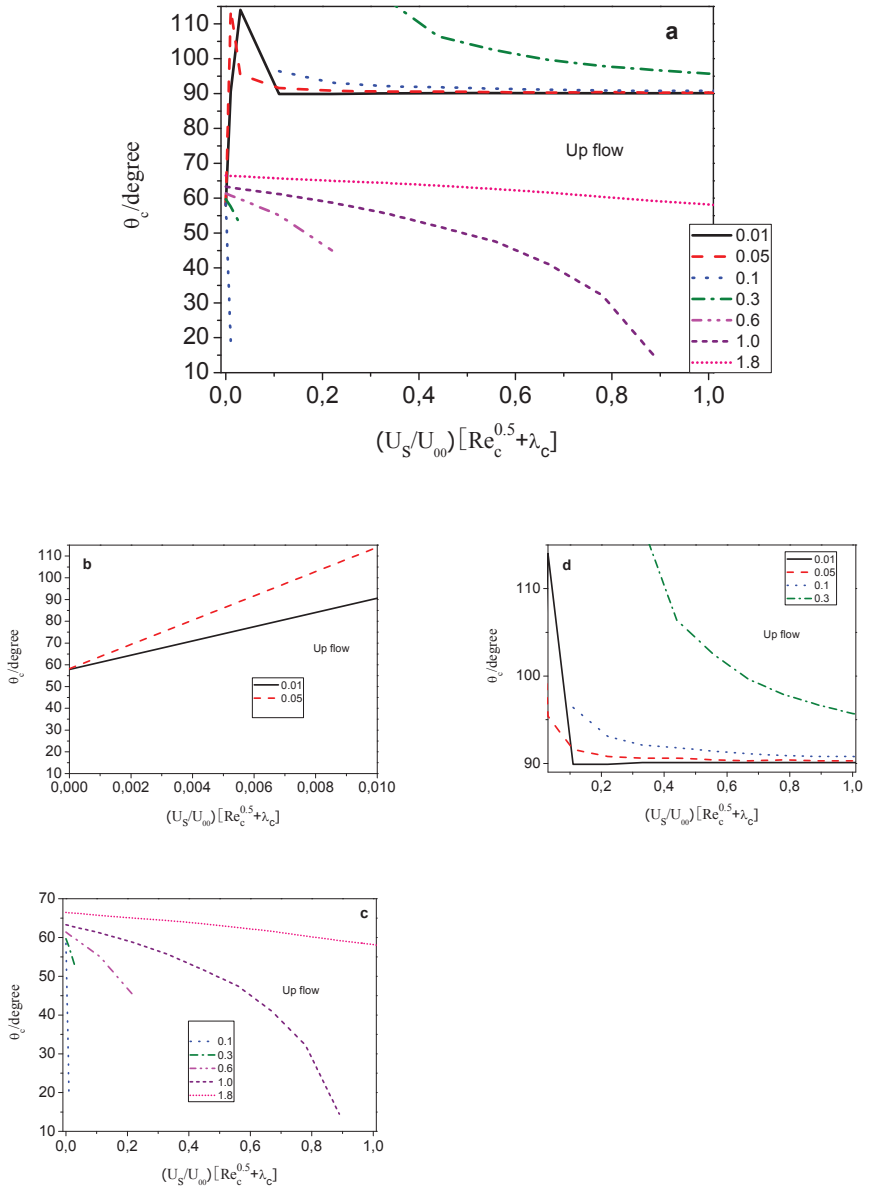

Figure 5.9 The collection angle θ_c vs. K/90 factor for various λ_c in up flow

Table 5.3 The collision angle θ_c in up flow

	λ_c and K	Note
b	λ_c=0.01, 0,05 & K/90<0.01	When K↑, θ_c↑; When λ_c ↑, θ_c↑
c	λ_c=0.01, 0,05, 0.1, 0.3 & K/90>0.03	When K↑, θ_c↓; When λ_c ↑, θ_c↑
d	λ_c= 0.1, 0.3, 0.6, 1.0, 1.8	When K↑, θ_c↓; When λ_c ↑, θ_c↑

The collision efficiency becomes

$$\eta_{\alpha=\pi} = \frac{2n_o(R+R_P)L_c\int_0^{\theta_c}(U_r + U_S\sin\varphi)d\theta}{n_o U_\infty \cdot 2L_c(R+R_P)} = \frac{\psi(R_P,\theta_c) - U_s\sin\theta_c}{U_\infty} = \eta_{i,\theta_c} - \eta_g\sin\theta_c \quad (5.37)$$

The contribution from interception to the collision efficiency is discussed in Figure 5.10. Interceptional collision increases with λ_c in up flow. However, it decreases with increasing U_s (or the ρ_p) since heavy particles tend to move away from the flow line, except area c (see Figure 5.9 c also). The large collection angle (>90°) is attained for small particles (λ_c<<0.3) in this area. These particles tend to stay on the upper side of the cylinder with increasing K. However, gravity helps a particle to escape in up flow generally.

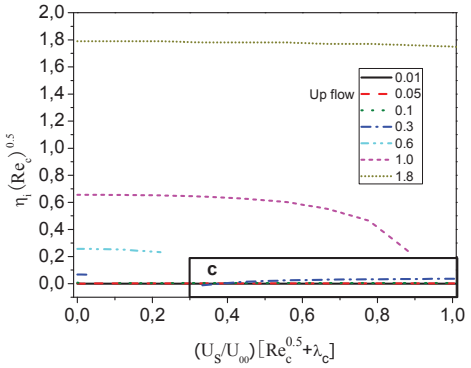

Figure 5.10 Interceptional collision efficiency vs. K/90 factor for various λ_c in up flow

5.3.3 Horizontal Flow

This case is represented by α= π/2. See c) in Figure 5.6. For the upper side of the cylinder

$$V_r(y,\theta) = \frac{1}{y+R}\frac{\partial\psi(y,\theta)}{\partial\theta} + U_S\sin\theta = 0 \quad (5.38)$$

Or

$$2f_7\theta^6 - 45f_5\theta^4 + 360f_3\theta^2 - 180f_1 = K\sin\theta \tag{5.39}$$

The upper collection angle with K/90 factor for various λ_c in horizontal flow is illustrated in Figure 5.11 a). The collection angle would increase from 58.0° to 180° when settling increases if the flow did not separate from the cylinder. We show the results until K/90=1.

However, we assume that particles beyond the separation point are captured by vortices and neglect their collision with the rear side of the collector. Schlichting [155] concluded that the separation angle is 108.8°. Thus the collection angle is limited from 58.0° to 108.8° in the upper side when settling velocity increases. The collection angle decreases with λ_c.

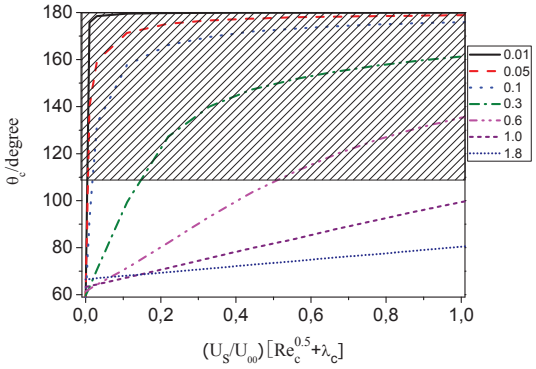

a) Upper half

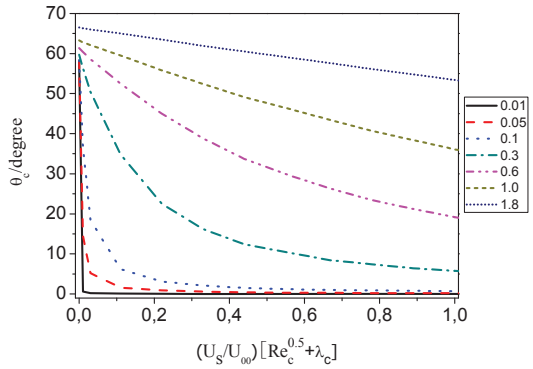

b) Lower half

Figure 5.11 The collection angle vs. K/90 factor for various λ_c in horizontal flow

For the lower side of the cylinder, the right side of the Equ.(5.39) becomes -Ksinθ. Then, the Figure 5.11 b) applies. The collection angle decreases from 66.5° (for λ_c=1.8) to 0° when settling increases.
The collision efficiency becomes

$$\eta_{\alpha=\pi/2} = \frac{n_o(R+R_P)L_c[\int_0^{\theta_{c+}}(U_r+U_S\sin\varphi)d\theta+\int_0^{\theta_{c-}}(U_r-U_S\sin\varphi)d\theta]}{n_oU_\infty L_c\cdot 2(R+R_P)}$$
$$= \frac{\psi(R_P,\theta_{c^+})+U_s[1-\cos\theta_{c^+}]+\psi(R_P,\theta_{c^-})+U_s[\cos\theta_{c^-}-1]}{2U_\infty}$$
$$= \frac{(\eta_{i,\theta_{c^+}}+\eta_{i,\theta_{c^-}})+\eta_g(\cos\theta_{c-}-\cos\theta_{c^+})}{2} \qquad (5.40)$$

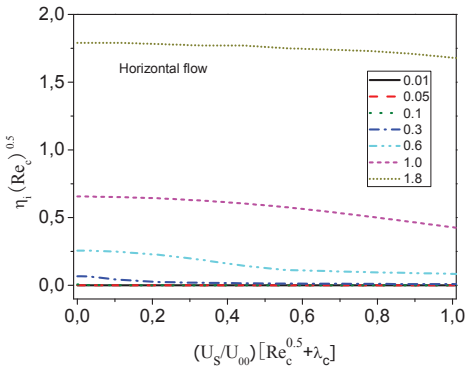

Figure 5.12 Interceptional collision efficiency vs. K/90 factor for various λ_c in horizontal flow

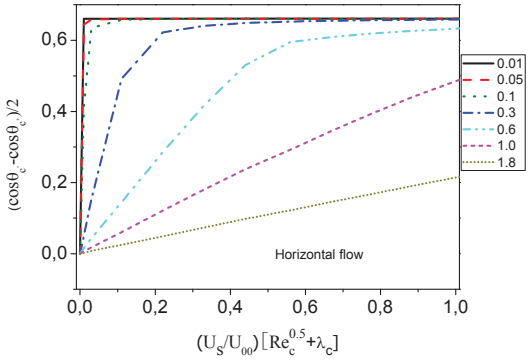

Figure 5.13 ($\cos\theta_{c-} - \cos\theta_{c+}$) vs. K/90 factor for various λ_c in horizontal flow

The contribution from interception and gravity to collision efficiency is discussed in Figure 5.12 and Figure 5.13. Interceptional collision increases with λ_c in horizontal flow. However, it slightly decreases with increasing U_s (or the ρ_p) since heavy particles tend to separate from the flow line. Gravity helps to collect particles on the upper side of the collector and it helps particles to escape on the lower side. See Figure 5.13. The smaller the λ_c or the greater the K, the greater the contribution from gravity in collision. However at large polar angles, flow in the boundary layers is out from the cylinder and the flow separates from it.

Chapter 6 REMOVAL THEORY OF PARTICLES IN CERAMIC FOAM FILTERS

Filters are a crucial step to remove inclusions and even dissolved elements from molten aluminium. Ceramic foam filter (CFF) appeared in late 1970s and early 1980s. Removal of inclusions by filtration strongly improves the mechanical properties of aluminium [17]. There are several mechanisms for a particle to reach the inner surface of the filter: interception, gravity, inertial forces, Brownian movement, and hydrodynamic effects [16]. Electromagnetic forces will not be considered. Also hydrodynamic effects are neglected. Interception and gravity are the dominant mechanisms.

The performance of a CFF is usually derived from a model of the interaction between a particle in flow stream and a single collector. Most of the models assume CFF as a net of tubes, spheres, or cells [163, 164]. However, a close look shows that the filter consists of a network of branches (See Figure 6.1). CFFs are produced by impregnating granular polyurethane foams with ceramic slurry. Subsequent burnout of the organic foam material and firing of the ceramic foams produces a high temperature bond, with a highly porous body, presenting an open-cell structure nearly equivalent to the inverse replica of a granular structure [21]. These branches, which collect the particles, are considered as cylinders. A similar assumption for capture has been used in marine biotechnology, e.g. passive settlement of larval on benthic algae [165].

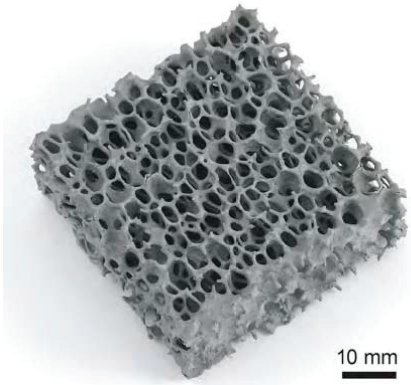

Figure 6.1 SiC CFF filter (photo by M.Gaal)

To describe the removal of inclusions in a filter, it is assumed initially that once the inclusions touch the collector, they adhere. A number balance over a control volume in a filter in Figure 6.2 gives [26]:

Inclusions through the surface z= inclusions through the surface (z+Δz) + inclusion captured inside the control volume AΔz

or

$$c(z)AU_{\infty}\varepsilon = c(z+\Delta z)AU_{\infty}\varepsilon + k_t a_s A\Delta z\varepsilon c \tag{6.1}$$

where

$$k_t = \eta U_{\infty} b \tag{6.2}$$

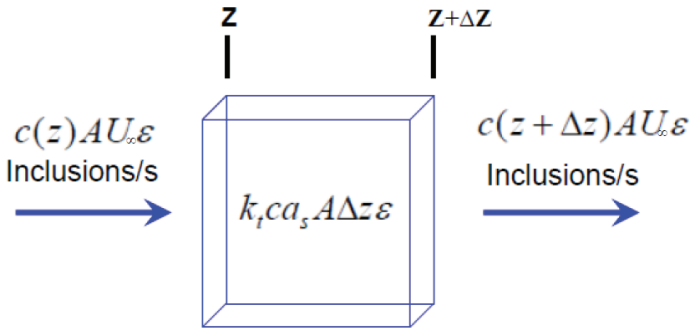

Figure 6.2 A control volume in a filter

Insert Equ.(6.2) into Equ.(6.1) and it becomes

$$\frac{dc}{dz} = -\eta a_s b c \tag{6.3}$$

Rearranging Equ.(6.3) and integrating between c_{in} and c_{out}, yield

$$\frac{c_{out}}{c_{in}} = \exp(-\eta a_s b L) \tag{6.4}$$

The filtration efficiency is defined in terms of c_{in} and c_{out} and as follows:

$$E = \frac{c_{in} - c_{out}}{c_{in}} = 1 - \exp(-\eta a_s b L) \tag{6.5}$$

The geometry factor $a_s b$ is equal to

$$a_s b = \frac{Surface\ area\ of\ collector}{Volume\ of\ melt} \cdot \frac{Collector\ surface\ area\ projected\ in\ flow\ direction}{Surface\ area\ of\ collector}$$
$$= \frac{Surface\ area\ of\ collector}{Volume\ of\ collector} \cdot \frac{Volume\ of\ collector}{Volume\ of\ melt}$$
$$\cdot \frac{Collector\ surface\ area\ projected\ in\ flow\ direction}{Surface\ area\ of\ collector} \tag{6.6}$$

Not all the cylinders in filter media are normal to the flow direction. We have to consider cylinders which show an angle β, in the range of -90^o to 90^o, to normal to the flow. The cylinder surface area projected in flow direction contributes in sum as:

$$Collector\ surface\ area\ projected\ in\ flow\ direction = \frac{\int_{-\pi/2}^{\pi/2} 2RL_c \cdot \cos\beta d\beta}{\int_{-\pi/2}^{\pi/2} d\beta} = \frac{2}{\pi} \cdot 2RL_c \tag{6.7}$$

Insert the Equ.(6.7) into geometry factor and get

$$a_s b = \frac{2\pi RL_c}{\pi R^2 L_c} \cdot \frac{1-\varepsilon}{\varepsilon} \cdot \frac{2RL_c \cdot \frac{2}{\pi}}{2\pi RL_c} = \frac{4(1-\varepsilon)}{\pi^2 R\varepsilon} \tag{6.8}$$

Then the filtration efficiency becomes

$$E = 1 - \exp(-\eta L \cdot \frac{4(1-\varepsilon)}{\pi^2 R\varepsilon}) \tag{6.9}$$

Insert η into Equ.(6.9) and the filtration efficiency can be determined.

Chapter 7 BRANCH MODEL IN PLANT EXPERIMENTS

In the current chapter, the aluminium flow rate in the plant experiments is calculated and the branch model is used to calculate the aluminium filtration efficiency. The results are compared with the literature. The branch model compares favourably to the other geometrical models. The effect of the wettability in aluminium filtration should be considered.

7.1 The Flow Rate

Forchheimer's equation has been successfully employed in the literature [166] to predict the flow rate through granular media due to pressure drop. This equation states that for an uncompressible fluid, the pressure drop through a rigid and homogeneous porous medium is given by:

$$\frac{\Delta P}{L} = \frac{\mu}{k_1} U_\infty + \frac{\rho_l}{k_2} U_\infty^2 \tag{7.1}$$

where k_1 and k_2 are constants only dependent on the medium properties, known respectively as Darcian and non-Darcian permeabilities, and

$$k_1 = \frac{\varepsilon^3 (2R_p)^2}{150(1-\varepsilon)^2}$$
$$k_2 = \frac{\varepsilon^3 (2R_p)}{1.75(1-\varepsilon)} \tag{7.2}$$

The major problem in the permeability evaluation of a ceramic foam filter is to reliably define structural properties of the cellular medium to replace the particle diameter $2R_p$ in Equ.(7.2). Moreira and Coury [167] measured the permeability utilizing water as flowing fluids. Ergun type calculation was employed using the pore diameter d_{pore} instead of the granular particle diameter. The final correlation using SI units has the following form:

$$k_1 = \frac{\varepsilon^3 d_{pore}^{-0.05}}{1.275 \times 10^9 (1-\varepsilon)^2}$$

$$k_2 = \frac{\varepsilon^3 d_{pore}^{-0.25}}{1.89\times10^4(1-\varepsilon)} \tag{7.3}$$

valid for Re_{pore} for water in the range of 0.6 to 2.55×10^3 [168].

We know [169]:

Density of the water at 30 °C, 996 kg/m^3,
Dynamic viscosity of water at 30 °C, 0.798×10^{-3} kg/(m·s),
Density of the aluminium at 725°C, 2360 kg/m^3,
Dynamic viscosity of aluminium at 725°C, 1.245×10^{-3} kg/(m·s)

Thus,

$$\frac{\mathrm{Re}_{Al}}{\mathrm{Re}_{water}} = \frac{\mu_{water}\rho_{Al}}{\mu_{Al}\rho_{water}} = 1.52 \tag{7.4}$$

Therefore, Equ.(7.3) is expected to be valid for Re_{pore} for aluminium at 725°C in the range of 0.91 to 3.88×10^3. The pore diameter of the filter was obtained by image analysis: $d_{pore,SiC}$= 2.2 ± 0.4 mm, $d_{pore,Al2O3}$= 2.1 ± 0.6 mm. It was also measured 10 times randomly with the vernier calipers to study the 3 dimential pore size. The Re_{pore} in the plant experiments is in the range of 213 to 374, which indicates that the Equ.(7.3) is valid in the current case.

The use of reliable equations is essential for the correct flow rate prediction. The permeability of a CFF slows down as inclusions accumulate. It is hard to predict the permeability correctly as inclusions accumulate.

The permeabilities in the current case are shown in Table 7.1.

Table 7.1 The permeability calculation in plant experiments

k_1[m^2]		k_2[m]		μ/k_1[kg/m^{3}s]		ρ_l/k_2[kg/m^4]	
SiC	Al_2O_3	SiC	Al_2O_3	SiC	Al_2O_3	SiC	Al_2O_3
2.91E-08	5.26E-08	1.00E-03	1.44E-03	4.28E+04	2.37E+04	2.36E+06	1.64E+06

Inserting Table 7.1 into Equ.(7.1), we get the flow rate and Reynolds numbers given in Table 7.2, in which the branch diameter of the filter was determined by image analysis: $2R_{,SiC}$= 0.4 ± 0.1 mm, $2R_{,Al2O3}$= 0.3 ± 0.1 mm, the cross section area of the filter A_x is 6.45×10^{-2} m^2 (10``×10``), and the thickness of the filter L is 0.0508 m (2``). The flow rate increases with the pressure drop.

Table 7.2 The flow rate calculation in plant experiments ($Re_c=2RU_\infty/\nu$)

ΔP_1[mm]	ΔP_2[mm]	ΔP_3[mm]	ΔP_4[mm]	$U_{\infty 1}$[mm/s]	$U_{\infty 2}$[mm/s]	$U_{\infty 3}$[mm/s]	$U_{\infty 4}$[mm/s]	Re_{c1}	Re_{c2}	Re_{c3}	Re_{c4}
26	29	27	26	78.04	66.32	79.66	62.37	44.4	50.3	45.3	47.3
26	29	27	26	78.04	66.32	79.66	62.37	44.4	50.3	45.3	47.3
26	29	27	26	78.04	66.32	79.66	62.37	44.4	50.3	45.3	47.3
32	30	26	25	87.31	67.59	78.04	61.00	49.6	51.2	44.4	46.3
32	32	26	25	87.31	70.07	78.04	61.00	49.6	53.1	44.4	46.3
32	32	26	25	87.31	70.07	78.04	61.00	49.6	53.1	44.4	46.3
32	32	23	25	87.31	70.07	73.01	61.00	49.6	53.1	41.5	46.3
32	34	23	25	87.31	72.47	73.01	61.00	49.6	54.9	41.5	46.3
32	34	23	25	87.31	72.47	73.01	61.00	49.6	54.9	41.5	46.3
32	35	20	21	87.31	73.65	67.64	55.26	49.6	55.8	38.5	41.9
32	35	20	21	87.31	73.65	67.64	55.26	49.6	55.8	38.5	41.9
32	35	20	21	87.31	73.65	67.64	55.26	49.6	55.8	38.5	41.9
33	34	18	17	88.76	72.47	63.84	48.94	50.5	54.9	36.3	37.1
33	34	18	17	88.76	72.47	63.84	48.94	50.5	54.9	36.3	37.1
33	34	18	17	88.76	72.47	63.84	48.94	50.5	54.9	36.3	37.1
32	33	19	16	87.31	71.28	65.77	47.25	49.6	54.0	37.4	35.8
32	33	19	16	87.31	71.28	65.77	47.25	49.6	54.0	37.4	35.8
32	33	19	16	87.31	71.28	65.77	47.25	49.6	54.0	37.4	35.8
33	34	18	18	88.76	72.47	63.84	50.58	50.5	54.9	36.3	38.4
33	34	18	18	88.76	72.47	63.84	50.58	50.5	54.9	36.3	38.4
31	34	19	18	85.83	72.47	65.77	50.58	48.8	54.9	37.4	38.4
31	32	19	17	85.83	70.07	65.77	48.94	48.8	53.1	37.4	37.1
31	32	19	17	85.83	70.07	65.77	48.94	48.8	53.1	37.4	37.1
32	32	18	17	87.31	70.07	63.84	48.94	49.6	53.1	36.3	37.1
32	32	18	20	87.31	70.07	63.84	53.74	49.6	53.1	36.3	40.7
32	32	18	20	87.31	70.07	63.84	53.74	49.6	53.1	36.3	40.7

Time increasing →

ΔP_1[mm]	ΔP_2[mm]	ΔP_3[mm]	ΔP_4[mm]	$U_{\infty 1}$[mm/s]	$U_{\infty 2}$[mm/s]	$U_{\infty 3}$[mm/s]	$U_{\infty 4}$[mm/s]	Re_{c1}	Re_{c2}	Re_{c3}	Re_{c4}
32	32	18	20	87.31	70.07	63.84	53.74	49.6	53.1	36.3	40.7
	32	18	16		70.07	63.84	47.25		53.1	36.3	35.8
	33	19	16		71.28	65.77	47.25		54.0	37.4	35.8
	33	19	17		71.28	65.77	48.94		54.0	37.4	37.1
	33	19	17		71.28	65.77	48.94		54.0	37.4	37.1
	31	19	17		68.84	65.77	48.94		52.2	37.4	37.1
	31	19	17		68.84	65.77	48.94		52.2	37.4	37.1
	31	20	16		68.84	67.64	47.25		52.2	38.5	35.8
	32	20	16		70.07	67.64	47.25		53.1	38.5	35.8
	30	20	16		67.59	67.64	47.25		51.2	38.5	35.8
	30	18	16		67.59	63.84	47.25		51.2	36.3	35.8
	30	18			67.59	63.84			51.2	36.3	
		18				63.84				36.3	

Time increasing →

The average flow rate and mass flow are shown in Table 7.3.

Table 7.3 The average calculated flow rate and Reynolds number in ceramic foam filters

Experiment	1	2	3	4
U_∞[mm/s]	86.38	70.39	67.98	52.61
Q[m^3/s]	5.6E-03	4.5E-03	4.4E-03	3.4E-03
Q_m[ton/h]	47.3	38.5	37.2	28.8
Re_c	49.1	53.4	38.7	39.9

where the volumetric flow rate is given by:

$$Q = U_\infty A_x \tag{7.5}$$

and the mass flow rate is:

$$Q_m = 3.6 \rho_l Q \tag{7.6}$$

The Al_2O_3 industrial filters (Exps.1 and 3) give higher velocities than the SiC filters (Exps.2 and 4). This may be due to the poor wettability of aluminium on Al_2O_3 industrial filter. Better wettability due to increased temperature in Exp.3 should give lower velocities than in Exp.1, the same for Exp.4 compared to Exp.2.

The inclusion travels around 10m in between the two LiMCA taking into account movement through the filter and bowl in plant experiments. The inclusion readings at 149.5 min (before the filter) and 150.5 min (after the filter) in Exp.1 (Figure 6.21) give similar peaks. This probably is due to the movement of same group of inclusions. Considering the LiMCA reading step width of 1.5min, it gives a flow rate in Exp.1 larger than 56 mm/s. Similarly, Figure 6.27 give flow rate larger than 56 mm/s in Exp.3. Figure 6.30 give flow rate 26 to 555 mm/s in Exp.4. Thus, movements of the peaks are roughly agreed with the calculated results in Table 7.3. This also indicates that velocity is rather high in Exps.1-4.

7.2 The Collision Efficiency

The interceptional collision efficiencies with particle size distribution in down flow are shown in Table 7.4. The λ_c are in the range of 0.36 - 2.10. The interceptional collision efficiencies increase with particle size.

As shown in Figure 2.47, the filtration efficiency decreases with the flow rate until it reaches a minimum, and then increases. The greater the velocity the less time particles have to settle. Gravitational collision efficiency decays with increasing flow rate. Gravitational collision must be taken into account at the lower flow rates. Interceptional collision efficiency increases with the velocity since then more liquid and particles come into contact with the collector. See Figure 7.1.

Gravitational collision dominates at the superficial flow rate 11 to 12mm/s for 40- 60 μm inclusions in Tian and Guthrie's case [170].

An interpretation of Figure 2.47 is that interceptional collision dominates at the superficial flow rates greater than 50mm/s for 20- 100 μm inclusions since the filtration coefficient increases with velocity. Thus, the contribution from the gravity is neglected in this work.

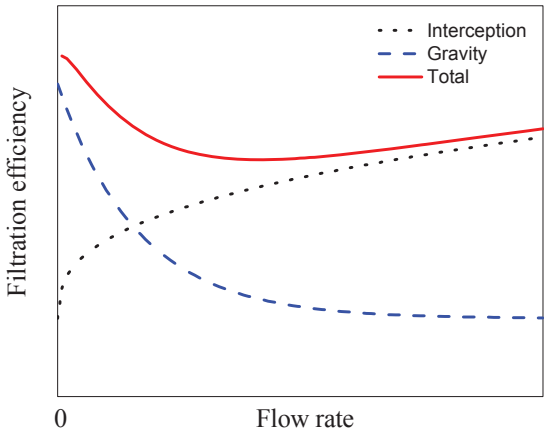

Figure 7.1 Sketch of collision efficiency vs. flow rate

Table 7.4 The interceptional collision efficiency in down flow calculated in plant experiments

R_p [μm]	R_p-avg [μm]	$\lambda_{c,1}$	$\lambda_{c,2}$	$\lambda_{c,3}$	$\lambda_{c,4}$	$\eta_{i\text{-}avg,1}$	$\eta_{i\text{-}avg,2}$	$\eta_{i\text{-}avg,3}$	$\eta_{i\text{-}avg,4}$
20-25	22.5	0.53	0.41	0.47	0.36	2.47E-02	1.55E-02	2.27E-02	1.39E-02
25-30	27.5	0.64	0.50	0.57	0.43	3.50E-02	2.19E-02	3.21E-02	1.97E-02
30-35	32.5	0.76	0.59	0.67	0.51	4.67E-02	2.93E-02	4.28E-02	2.63E-02
35-40	37.5	0.88	0.68	0.78	0.59	5.98E-02	3.75E-02	5.48E-02	3.37E-02
40-45	42.5	0.99	0.78	0.88	0.67	7.43E-02	4.65E-02	6.81E-02	4.19E-02
45-50	47.5	1.11	0.87	0.98	0.75	9.00E-02	5.64E-02	8.25E-02	5.07E-02
50-55	52.5	1.23	0.96	1.09	0.83	1.07E-01	6.71E-02	9.81E-02	6.03E-02
55-60	57.5	1.34	1.05	1.19	0.91	1.25E-01	7.85E-02	1.15E-01	7.06E-02
60-65	62.5	1.46	1.14	1.30	0.99	1.45E-01	9.07E-02	1.33E-01	8.16E-02
65-70	67.5	1.58	1.23	1.40	1.07	1.65E-01	1.04E-01	1.52E-01	9.32E-02
70-75	72.5	1.69	1.32	1.50	1.14	1.87E-01	1.17E-01	1.71E-01	1.05E-01
75-80	77.5	1.81	1.42	1.61	1.22	2.10E-01	1.32E-01	1.92E-01	1.18E-01
80-100	90.0	2.10	1.64	1.87	1.42	2.72E-01	1.70E-01	2.49E-01	1.53E-01

7.3 The Filtration Efficiency

The filtration efficiencies are shown in Figure 7.2 to Figure 7.5 according to Equ.(6.9). qη instead of η is used. The factor q, in between 0 to 1, can be interpreted as the number of particles that stick to the cylinder relative to the number that hit it. According to the deep bed filtration theory, for a particle to be captured, two steps have to be undertaken: transport and adhesion. The filtration efficiency will be a function of both transport efficiency (collision efficiency) η and adhesion efficiency q.

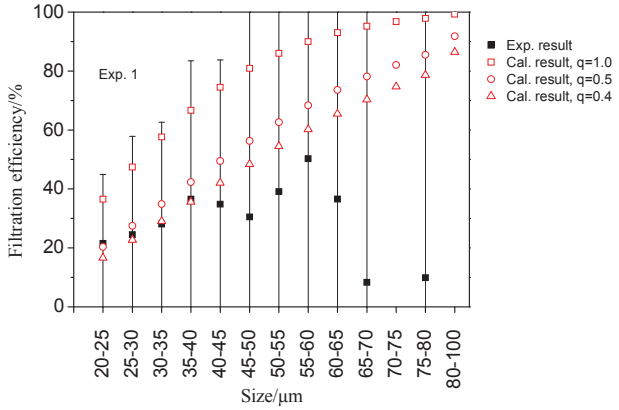

Figure 7.2 The filtration efficiency vs. inclusion size in Exp. 1 with various q

In Figure 7.2 to Figure 7.5, the filtration efficiencies increase with the particle size. There are very small numbers for particles larger than 60μm, as discussed in Section 4.2.4. For particles less than 60μm, q= 0.4, 0.5, and 0.4 for Exp.1 to Exp.3 gives the best match between calculated and experimental data. Around 40% of collided particles attach on the filter interface in alumina filters, and 50% in SiC filters. The SiC industrial filter in Exp.4 has q larger than 1. This might be due to that the porosity in Exp.4 is higher than average value 85.0%, which leads to the larger flow rate (or Re_c) than in Table 7.3. Then, the filtration efficiency becomes larger than the calculated value. The improved wettability in Exp.4 due to the increased temperature may contribute to more inclusion attachment on the filter walls, as well.

The difference between the experimental values and the model may be due to errors in the model, variations in the branch diameter, and the contributions from wettability, e.g. wetting between particle- metal, and metal-filter wall, which could be influenced by factors, such as filter and bowl temperature, flow rate, particle and filter properties etc. In spite of the high velocities, gravity may play a role.

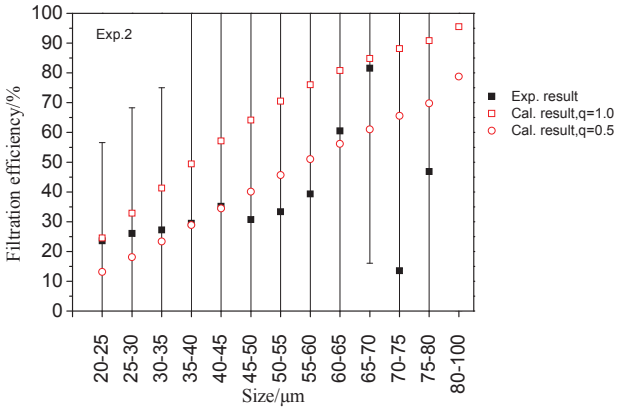

Figure 7.3 The filtration efficiency vs. inclusion size in Exp.2 with various q

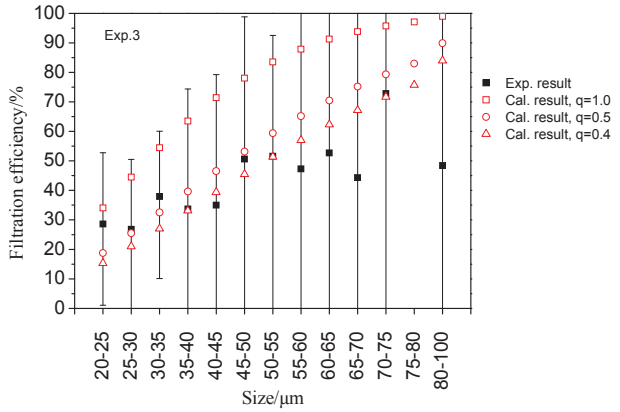

Figure 7.4 The filtration efficiency vs. inclusion size in Exp.3 with various q

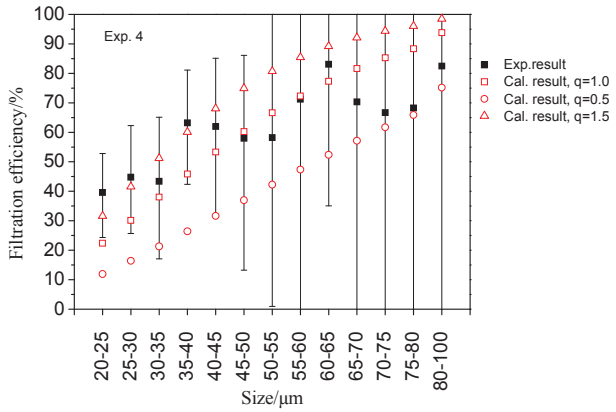

Figure 7.5 The filtration efficiency vs. inclusion size in Exp.4 with various q

7.4 Comparison with the Literature

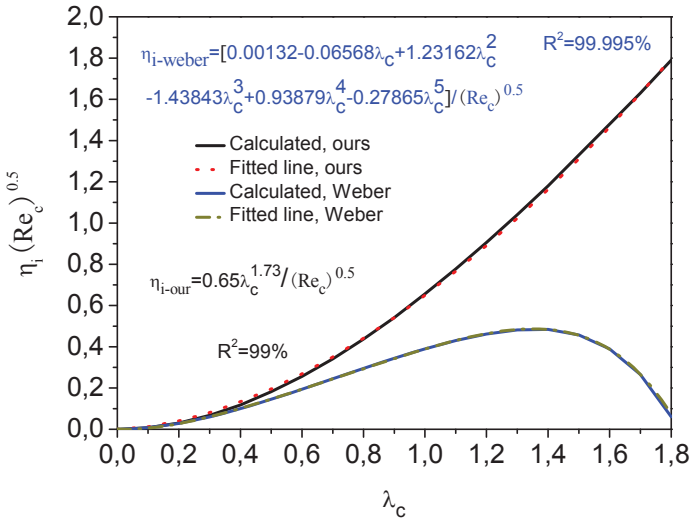

Figure 7.6 The relation of λ_c and collision efficiency according to Equ.**(5.8)** and Equ.(5.19)

Figure **7.6** compares our model and Weber's model [158] considering the Schlichting boundary layer. The collision efficiency by Weber is fitted with R square factor, 99.995%. The Weber collision efficiency (See Equ.(5.19)) employs the second

derivative of our collision efficiency (See Equ.(5.8)). Weber's model gives lower filtration efficiency than ours at higher values of λ_c. As an example, the result in Exp.1 is shown in Figure 7.7. An explanation may be that Weber approximated the stream function with a Taylor series including only the second order terms.

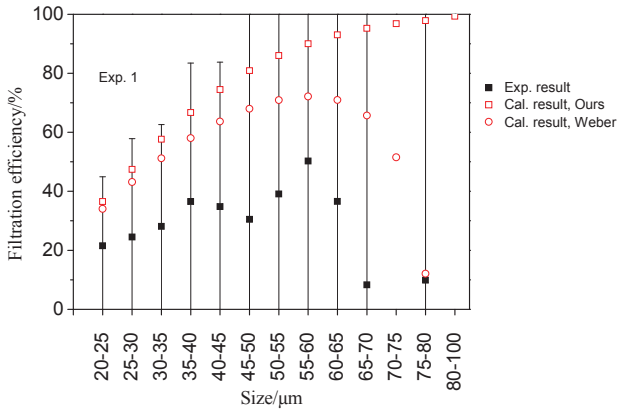

Figure 7.7 The calculated filtration efficiency in our model and Weber's model based on the Schlichting boundary layer

Various reported theoretical geometrical models, which describe ceramic foams as a collection of cells, polyhedra, etc. The specific surface area a_s is summarized in Table 7.5, where the structural parameter d_s is the strut (cylinder) diameter in the models. The specific surface areas calculated according to pore diameters are shown for porosity 88.2% (Al_2O_3 industrial filter) and 85.0% (SiC industrial filter) in Figure 7.8.

Table 7.5 The ceramic foam models

	Model	Structural parameter	Specific surface area [m^2/m^3]
Lu et al., 1998 [171]	Open-celled metal foams are treated as cylinders. 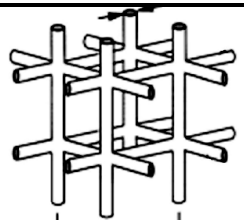	$d_s = d_{pore}(\frac{2}{\sqrt{3\pi}})(1-\varepsilon)^{1/2}$	$a_s = (\frac{2\sqrt{3\pi}}{d_{pore}})(1-\varepsilon)^{1/2}$
Innocentini et al., 1999 [166]	Ceramic foams are treated as cells. Diameter = Cylindrical form of the hydraulic cell diameter.		$a_s = \frac{4\varepsilon}{d_{pore}(1-\varepsilon)}$
Richardson et al., 2000 [172]	The pores are treated as uniform, parallel cylinders, each with a constant diameter.	$d_s = \frac{0.5338 d_{pore}(1-\varepsilon)^{1/2}}{1-0.971(1-\varepsilon)^{1/2}}$	$a_s = \frac{4\varepsilon}{d_{pore}(1-\varepsilon)}$
Fourie and Plessis, 2002 [173]	Cellular metallic foams are treated as an array of tetrakaidekahedra. 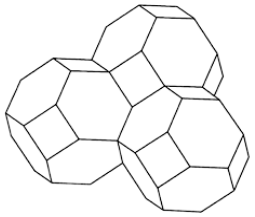	$d_s = d_{pore}\left(\frac{2}{3-\chi}-1\right)$	$a_s = (\frac{3}{d_{pore}+d_s})(3-\chi)(\chi-1)$ with $\chi = 2+2\cos(\frac{4\pi}{3}+\frac{1}{3}\cos^{-1}(2\varepsilon-1))$
Buciuman and Kraushaar-Czarnetzki, 2003 [174]	Open-cell ceramic foams are treated as a package of tetrakaidekahedra. 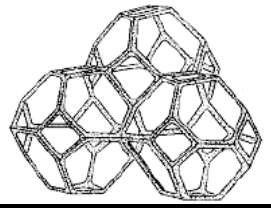	$d_s = d_{pore}\left[\frac{1-\varepsilon}{2.59}\right]^{1/2}$	$a_s = 4.82\frac{(1-\varepsilon)^{1/2}}{d_{pore}+d_s}$

Reference	Model	Structural parameter	Specific surface area [m^2/m^3]
Moreira et al., 2004 [167, 168]	Ceramic foam is treated as cellular structure. The same as Richardson et al. [172]		$a_s = \frac{12.979\left[1-0.971(1-\varepsilon)^{1/2}\right]}{d_{pore}(1-\varepsilon)^{1/2}}$
Giani et al., 2005 [175]	Open-celled metal foams are treated as cubic cells. The same as Lu et al. [171]	$d_s = d_{pore}\left[\frac{4}{3\pi}(1-\varepsilon)\right]^{1/2}$	$a_s = \frac{4}{d_s}(1-\varepsilon)$
Lacroix et al., 2007 [176]	SiC foam bed is treated as the dodecahedra. 	$d_s = \frac{d_{pore}\left[\frac{4}{3\pi}(1-\varepsilon)\right]^{1/2}}{1-\left[\frac{4}{3\pi}(1-\varepsilon)\right]^{1/2}}$	$a_s = \frac{4}{d_s}(1-\varepsilon)$
This work	Ceramic foams as treated as a collection of cylinders.		$a_s = \frac{2(1-\varepsilon)}{R\varepsilon}$

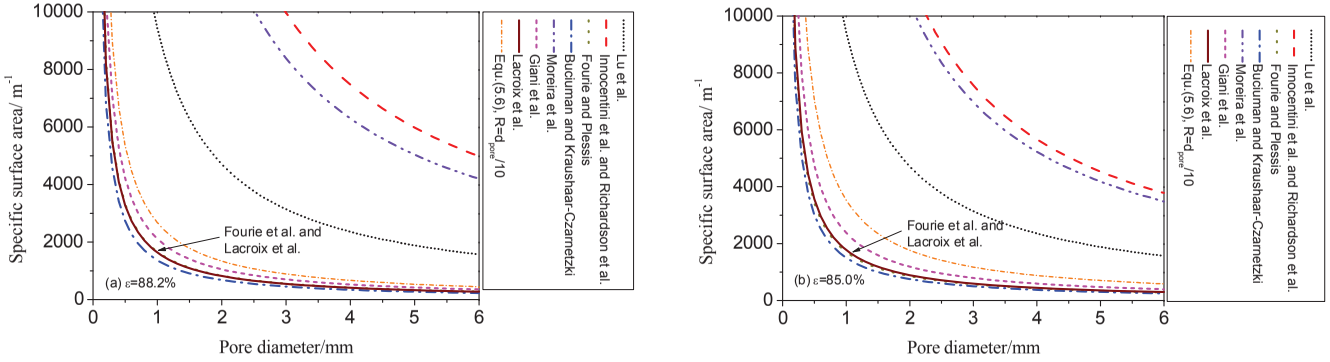

Figure 7.8 The specific surface area vs. pore diameter with various models

The models from Innocentini et al. [166], Richardson et al. [172], Moreira et al. [167, 168], Lu et al. [171], us, and Giani et al. [175] (in sequence from high to low surface area) give specific surface area higher than models by Lacroix et al. [176], Fourie and Plessis [173], and Buciuman and Kraushaar-Czarnetzki [174], regarding the ceramic foams as polyhedra (12 or 14 faces). Polyhedra seem to simulate the open cell metallic foams better than ceramic foams.

Figure 7.9 to Figure 7.12 compare the filtration efficiencies based on the specific surface area by various models. Innocentini et al. [166], Richardson et al. [172], Moreira et al. [167, 168], Lu et al. [171], and this work (from high to low) give filtration efficiencies higher than experimental values in Exps.1-3, except in Exp.4. They are expected to have higher calculated filtration efficiency than the experimental value since we assume that all inclusions that hit the wall are captured by the filter.

Innocentini et al., 1999 [166] and Richardson et al. [172] replace the particle diameter in deep bed filters with the structural parameters in the cellular media. Poor agreement with experimental permeability was obtained [166]. Lu et al. [171] and Giani et al.[175] investigated the open-cell metal foam, considering it made up of uniform distributed, equal sized cubic cells. Apparently, the structure of the ceramic foam filters is more complicated than that. Moreira et al. [167, 168] obtained the specific surface area by image analysis. They measured the perimeter of the solid phase of a cross section and multiplied it by the length of the tortuous path, obtained from the tortuosity measurements. They did not explain how they derived the specific surface area equation.

In our calculation, we may overestimate (or underestimate) the specific surface area, when we give the branch radius as 1/10 pore diameter. The reason is that the ceramic branches are not ideal cylinders.

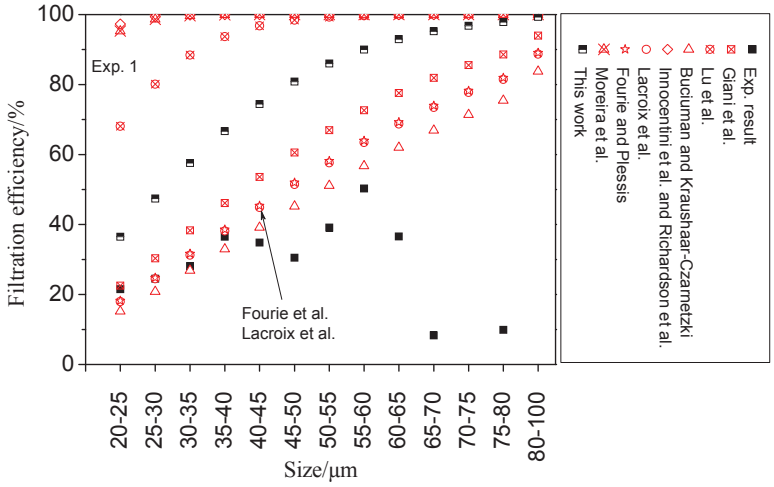

Figure 7.9 Filtration efficiency in Exp.1 calculated with various models

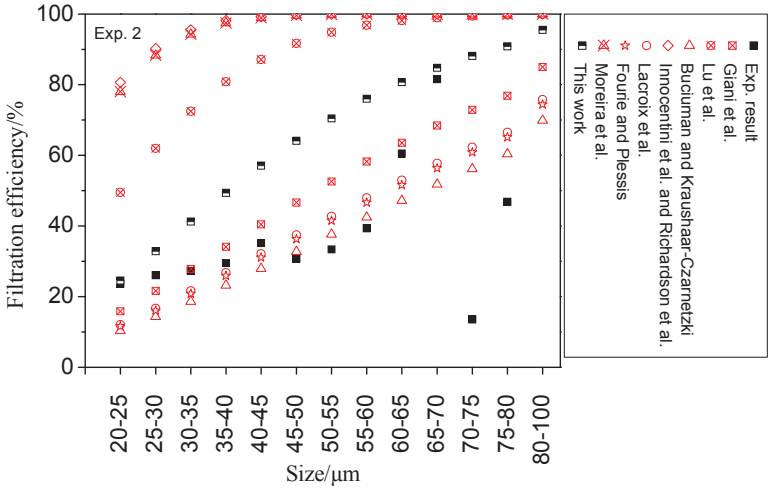

Figure 7.10 Filtration efficiency in Exp.2 calculated with various models

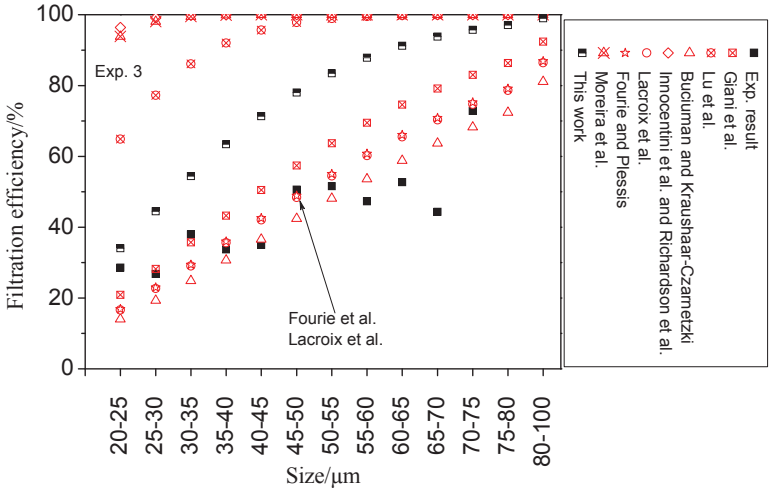

Figure 7.11 Filtration efficiency in Exp.3 calculated with various models

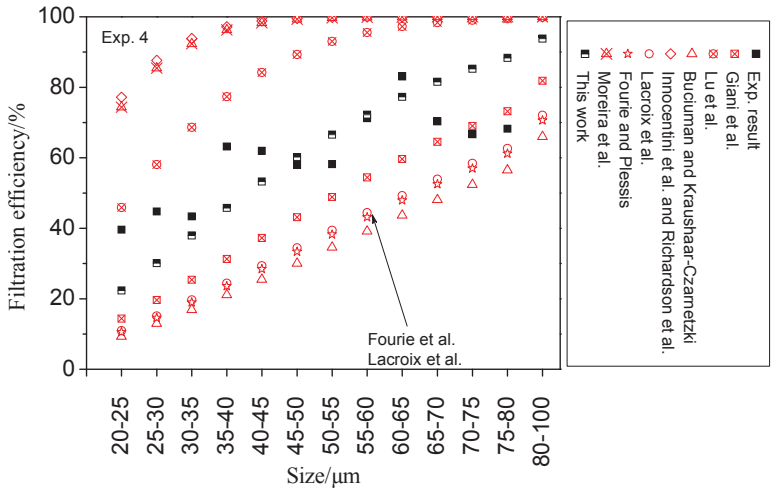

Figure 7.12 Filtration efficiency in Exp.4 calculated with various models

Figure 7.13 to Figure 7.16 show the collision efficiency as: $-\ln(1-E)= a_s bL\eta$ in plant experiments and in our model with a fitted q value. Experiments and calculation match well for particles less than 60 μm, especially for particles 20-40μm (approx. 90% of all inclusions). This indicates that we use reasonable specific surface area in our model.

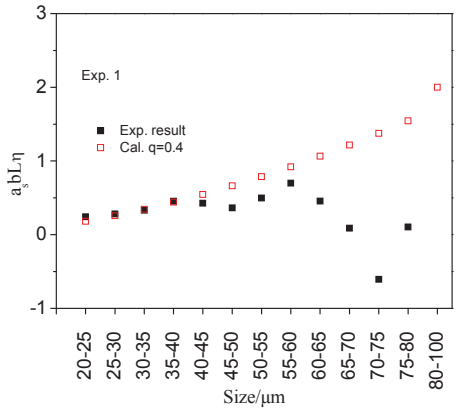

Figure 7.13 The collision efficiency factor vs. inclusion size in Exp.1

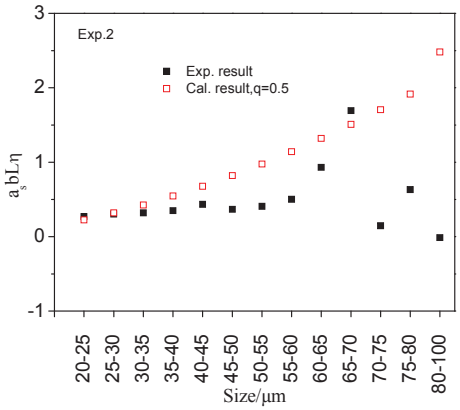

Figure 7.14 The collision efficiency factor vs. inclusion size in Exp.2

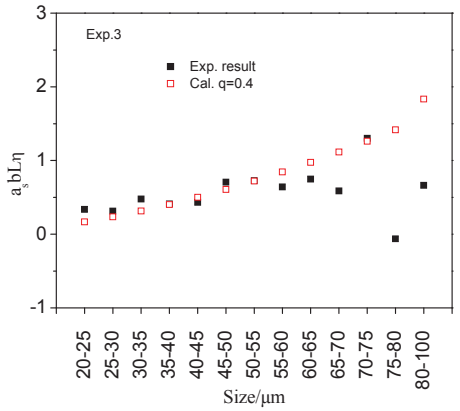

Figure 7.15 The collision efficiency factor vs. inclusion size in Exp.3

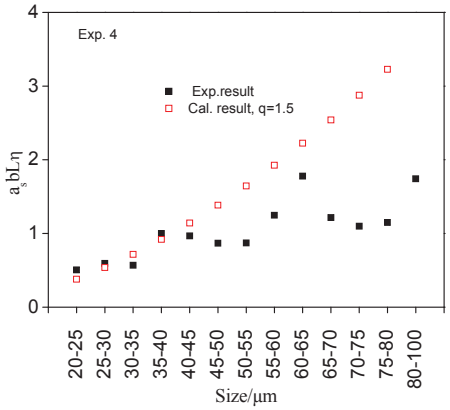

Figure 7.16 The collision efficiency factor vs. inclusion size in Exp.4

7.5 Conclusion

A branch model where the ceramic foam filter is treated as a collection of cylinders is used to describe the plant experiments.

The flow rate in the industrial filters is calculated using Forchheimer's equation and empirical results for permeability. At higher temperatures, better wetting contributes to the lower pressure drop and also lower flow rates, e.g. in Exps.3 and 4. The Al_2O_3 industrial filter gives a larger flow rate than SiC industrial filters probably due to its poor wetting. The mass flow in the plant experiments is 29-47 ton/h and the Reynolds number based on the branch diameter is in the range of 39-53.

The calculated collision efficiency and the filtration efficiency increase with inclusion size. The filtration efficiencies according to Equ.(6.9) agree with the experimental values when introducing the factor q, in between 0 to 1, which is interpreted to give the number of particles that stick to the cylinder relative to the number that hit it. Around 40% of collided particles attach on the filter interface in Al_2O_3 industrial filters, and 50% in SiC industrial filters. The increased wettability between the SiC industrial filter and molten aluminium at a higher temperature in Exp.4 may be the reason that q is larger than 1.

The difference between the experimental values and the model may be due to errors in the model, variations in the branch diameter, and the contributions from wettability, e.g. wetting between particle- metal, and metal-filter wall, which could be influenced by factors, such as filter and bowl temperature, flow rate, particle and filter properties etc. Gravity effects have not been taken into account.

Considering the Schlichting boundary layer, the collision efficiency obtained from Weber gives lower values than ours and does not increase with inclusion size for

inclusions larger than 60μm. This may be due to that Weber approximated the stream function in a Taylor series including only second order terms.

The branch model also has been compared to other geometrical models. Polyhedra seem to simulate the open cell metallic foams better than ceramic foams. Uniform distributed cells may be too simple to describe ceramic foams. The branch model in our case proves to give a reasonable specific surface area and the filtration efficiency.

In conclusion, the Equ.(7.7) together with Equs.(5.15) and (5.13) give the filtration efficiency for ceramic foam filters in aluminium filtration. The model is based on inclusion and branch diameters, Reynolds number, filter thickness, filter specific surface area, and the wettability.

$$E = 1 - \exp(-q\eta L \cdot \frac{4(1-\varepsilon)}{\pi^2 R\varepsilon}) \tag{7.7}$$

Chapter 8 CONCLUSIONS AND FUTURE WORK

In this work, removal mechanisms of inclusions in ceramic foam filter have been studied. This includes measurement of wetting between aluminium, inclusion, and filter materials. A branch model is also carried out to study the inclusion transport mechanism. An objective has been to find alternative filter materials. Also plant filtration experiments have been carried out.

Wetting

When liquid aluminium flows into a pre-heated filter, aluminium is further oxidized due to the hot air inside. One part of the oxide goes into the metal as Al_2O_3 inclusions, and the rest adheres on the Al-filter interface. This superficial oxide layer will be broken due to capillary infiltration of the molten metal through the filter and oxide. Then, oxidation is less of a problem due to the low saturated oxygen content in aluminium.

Wetting behaviour between aluminium and ceramics: graphite, oxidized SiC and Al_2O_3 in the temperature range 1000 to 1300^oC is investigated in the current work. The wettability with respect to time goes through three kinetic stages: de-oxidation of the alumina layer, interface reaction, and finally the stable contact angle. In order to predict the wetting behaviour of the Al-ceramic system at the lower casting temperatures, a semi-empirical calculation for the temperature dependence of the contact angle is presented. The contact angles of Al-Al_2O_3, Al-SiC, and Al-graphite at 700^oC are calculated to be 97^o, 79^o, 92^o (vitreous graphite) and 126^o (single- and poly-crystal graphite), respectively. This is in good agreement with experimental values in the literature.

SiC filters have better wettability with aluminium than Al_2O_3 filters. SiC filters may react slowly with aluminium at the casting temperature. SiC filters will increase the Si content in aluminium due to de-oxidation of the silica layer on the interface, and also free Si in reaction bonded SiC. The presence of Si in aluminium will prevent reaction between SiC and aluminium and formation of Al_4C_3.

It is harder to remove Al_4C_3 inclusions than Al_2O_3 inclusions probably due to the better wettability of aluminium on Al_4C_3.

Graphite reacts with aluminium and produces Al_4C_3 at the interface, which is hydrophilic. It may be a problem to use graphite as a filter material.

SiC and Al_2O_3 industrial filters are non-wetted by molten aluminium at casting temperature.

Improved wetting of aluminium on ceramics with temperature is an advantage in getting molten metal to infiltrate the filter. In priming filters it is necessary to have a metal height above the filter or to increase the temperature. In our plant experiments, the metal height above the filter was up to 33 mm in Exp.1 and Exp.2. With higher temperatures for the filter and filter bowl, the metal height was only up to 27 mm in Exp.3 and Exp.4. Filtration may proceed at lower temperatures once metal has entered the filter.

It is believed that improved metal – filter wetting gives higher filtration efficiency. A hot filter bowl is as important as a pre-heated filter in filter priming.

Filtration

Plant scale filtration experiments were carried out with Al_2O_3 and SiC industrial filters. No metal composition change was introduced by the industrial filters. This is promising for the use of SiC filters, considered an alternative filter material in aluminium filtration.

We did not experience cake filtration or the blockage of the filter for the 5005 aluminium alloy even though we added inclusions in the melting furnace. The alloy mainly contains oxides, carbides, and borides inclusions.

LiMCA accompanied with PoDFA measures effectively the inclusion level, size distribution, and inclusion types.

The filtration efficiency improves with inclusion size. For inclusion size in the range of 30-40 μm, filtration efficiency was approx. 50% in all experiments even though the pore size was large using 30 ppi filters with average porosity approximately 50%.

SiC industrial filters have better wettability with aluminium than Al_2O_3 industrial filters. At a higher temperature, the SiC industrial filter in Exp.4 showed a much higher filtration efficiency than the other three.

Modelling

The collision of particles on a cylinder is investigated based on the Schlichting boundary layer theory, focusing on interceptional and gravitational collision. The deposition by interception is determined by the cylinder radius R, particle radius R_p and cylinder Reynolds number Re_c. The interceptional collision efficiency η_i increases with λ_c ($=Re_c^{0.5}R_p/R$), and

$$\eta_i = 0.65\lambda_c^{1.73} / (Re_c^{0.5}) \tag{8.1}$$

Three collision cases in filtration: down flow, up flow, and horizontal flow are discussed in order to illustrate the role of gravity.

A branch model where the ceramic foam is treated as a collection of cylinders is proposed and compared with other models. The branch model gives a reasonable specific surface area and filtration efficiency. Inclusion removal in aluminium filtration is based on the ratio between the inclusion and ceramic foam branch diameters, the

branch Reynolds number, filter thickness, filter specific surface area, porosity, and the wettability etc:

$$E = 1 - \exp(-q\eta L \cdot \frac{4(1-\varepsilon)}{\pi^2 R\varepsilon}) \tag{8.2}$$

Future work

The gravitational collision efficiency should be investigated. Then it is necessary to figure out the velocity of the particles on hitting the collector surface. This is a difficult task.

A more extensive study should be carried out on that aluminium tends to expel inclusions with poorer wetting than the Al-filter interface.

Pre-heating of the filter bowl is as important as the preheating of filter itself due to problems with heat loss and infiltration at the beginning of the filtration. Pre-heating deserves further study including variables such as pre-heating gas, time and temperature distribution.

The possible introduction of wettability into permeability in Forchheimer's equation (7.1) calls for further study.

The SiC filter, as an alternative filter material, is promising. Its reaction rate with molten aluminium at casting temperatures should be further investigated.

The factor q here described as the ratio of inclusions that stick to the wall and inclusions that hit the wall, in Equ.(7.7) may be employed to compare the efficiency of various Al-ceramics in filtration.

References

1. Landry, K. and N. Eustathopoulos, *Dynamics of Wetting in Reactive Metal/Ceramic Systems: Linear Spreading.* Acta Metallurgica et Materialia, 1996. **44**(10): p. 3923-3932.
2. Laszlo Istvan Kiss, R.T.B., *Flow Structure and Stability of the Deposition Layer in Deep-bed Filters.* Light Metals, 2001: p. 999-1005.
3. Palmer, M.R., et al., *Observations of Particle Capture on a Cylindrical Collector: Implications for Particle Accumulation and Removal in Aquatic Systems.* American Society of Limnology and Oceanography, 2004. **49**(1): p. 76-85.
4. *International Aluminium Industry`s Perfluorocarbon Gas Emissions Reduction Programme - Update 2009*. 2009; Available from: http://www.world-aluminium.org/Downloads/Publications/Download.
5. Waite, P., *A Technical Perspective on Molten Aluminum Processing* Light Metals, 2002: p. 841-848.
6. Apelian, D., *Aluminum Solidification Processing-Prospective and Retrospective View of The Industry and The Field.* Light Metal, 2000: p. 27-29.
7. (IAI), I.A.I., *Aluminium for Future Generations.* http://www.world-aluminium.org/, Sustainability Update 2006, 2006.
8. Fei, M. and R. Ludwig, *Electromagnetic detection and infrared visualizaiton techniques for non-metallic inclusions on molten aluminum.* Review of Quantitative Nondestructure Evaluation, 2002. **21**: p. 1719-1726.
9. Eckert, C.E., R.E. Miller, and D. Alelian, *Molten aluminum filtration: fundametals and models.* Light Metals, 1984: p. 1281-1304.
10. Sun, B., et al., *Purification Technology of Molten Aluminium.* Journal of Central South University of Technology, 2004. **11**(2): p. 134-141.
11. *European Collaboration -Molten Aluminium Purification- End of Programme Report.* Aluminium International Today, 2006: p. 52-55.
12. Carnahan, R.D., T.L. Johnston, and C.H. Li, *Some Observations on the Wetting of Al_2O_3 by Aluminum.* Journal of the American Ceramic Society, 1958. **41**(9): p. 343-347.
13. Khalifa, W., F.H. Samuel, and J.E. Gruzleski, *Nucleation of solid aluminum on inclusion particles injected into Al-Si-Fe alloys.* Metall. & Mater. Trans. A, 2004. **35A**(10): p. 3233-3250.
14. Liu, L. and F.H. Samuel, *Assessment of melt cleanliness in A356.2 aluminium casting alloy using the porous disc filtration apparatus technique: Part I Inclusion measurements* Journal of Materials Science, 1997. **32**: p. 5907-5925.
15. C. Conti, P.N., *Deep filtration of liquid metals: application of a simplified model based on the limiting trajectory method.* Sep. Technol., 1992. **2**: p. 46-56.
16. L. J. Gauckler, M.M.W.e.a., *Industrial Application of Open Pore Ceramic Foam for Molten Metal Filtration.* Light Metals, 1985: p. 1261-1283.
17. Yuan, Q., et al., *Experimental research on purification of molten aluminum through electromagnetic field.* Yunnan Metallurgy, 2003. **32,Supplementary**: p. 106-108.

18. Qu, Z., *Structure Characteristic and Filtration Mechanism of CFF.* Process Technology for Alunimum Alloy, 2002. **30**(10): p. 10-13.
19. Masaaki Iwatsuki, S.N., *Determination of Inclusions in Molten Aluminum Alloy by X-ray Diffractometry after Selective Dissolution.* Analytical Sciences, 1998. **14**: p. 617-619.
20. *Metal Pouring / Filtering.* Foundry Management & Technology, 2004: p. 29-31.
21. Binner, J. and R. Sambrook, *Ceramic Foams - Processing and Applications as Filters, Interpenetrating Composites and Biomedical Materials.* http://www.azom.com/Details.asp?ArticleID=1869, 2003.
22. Kyle Adams, E.J.W.e.a., *FILTERING BASICS: Who, What, Where, Why & How.* Modern Casting, 2002: p. 19-21.
23. Braun, B., *Molten Aluminum Flow Control via Foam Filtration.* Modern Casting, 2004. **94**(3): p. 21-24.
24. Dore, J.E. and J.C. Yarwood, *Ceramic Foam Filter: a Unique Method of Filtering Molten Aluminum Alloys.* Light Metals, 1977: p. 171-189.
25. Dore, J.E., *A practical guide on how to optimize ceramic foam filter performance.* Light Metals, 1990: p. 791-796.
26. Engh, T.A., *Principles of Metal Refining*. 1992: Oxford University Press. 61.
27. Frisvold, F., T.A. Engh, and S.T. Johansen, *Removal of Inclusins — A Survey and Comparison of Principle.* Light Metal, 1992: p. 1125-1132.
28. S.T. Johansen, S.G., *The bubble size and mass transfer mechanisms in rotor-stirred reactors.* Light Metals, 1997: p. 663-666
29. S.T. Johansen, R.A., *Bubble size and removal rate of sodium in impeller stirred refining reactors.* Light Metals, 1999: p. 657-661
30. Ohno, Y., Hampton Duane T. et al, *The GBF rotary system for total aluminum refining.* Light Metals: Proceedings of Sessions, TMS Annual Meeting (Warrendale, Pennsylvania), 1993: p. 915-921.
31. B. Rinderer, P.A., *Casthouse Modifications for improved Slab Quality.* Light Metals, 2003: p. 741-746.
32. Geir M., E.M., *Hycast I-60 SIR- a New Generation Inline Metal Refining System.* Light Metals: Proceedings of Sessions, TMS Annual Meeting (Warrendale, Pennsylvania), 2006: p. 855-859.
33. Judith G. Stevens, H.Y., *Mechanism of Sodium, Calcium and Hydrogen Removal from an Aluminum Melt in a Stirred Tank Reactor- the Alcoa 622 Process.* Light Metals, 1988: p. 437-443.
34. F. R. Mollard, J.E.D.e.a., *High Temperature Centrifuge for Studies of Melt Cleanliness.* Light Metals, 1972: p. 483-501.
35. Zhou, M., et al., *A Fluxing Method to Remove Inclusions from Molten Aluminum.* Journal of Materials Science Letters, 2002. **21**: p. 1285-1287.
36. Shu, D., et al., *Study of Electromagnetic Separation of Nometallic Inclusions from Aluminum Melt.* Metallurgical and Materials Transactions A, 1999. **30**(11): p. 2979-2988.
37. D. Apelian, R.M.e.a., *Commercially Available Porous Media for Molten Metal Treatment: A Property Evaluation.* Light Metals, 1982: p. 935-968.
38. James. R. Schmahl, N.J.D., *Ceramic Foam Filter Technology for Aluminum Foundries.* Modern Casting, 1993: p. 31-33.

39. Laurent, V., et al., *Wettability of Monocrystalline Alumina by Aluminium between Its Melting Point and 1273K.* Acta Metallurgica et Materialia, 1988. **36**(7): p. 1797-1803.
40. Netter, P. and C. Conti, *Efficiency of Industrial Filters for Molten Metal Treatment Evaluation of a Filtration Process Mode.* Light Metals, 1986: p. 847-860.
41. Desmoulins, J.P., et al., *Which Filter What Plant? The Pechiney Research Approach.* Light Metals, 1989: p. 757-767.
42. P. Netter, C.C., *Efficiency of Industrial Filters for Molten Metal Treatment Evaluation of a Filtration Process Model.* Light Metals, 1986: p. 847-860.
43. K. Hoshino, T.N.e.a., *The Filtration of Molten 1××× Seties Aluminum Alloys with Regid Media Tube Filter.* Light Metals, 1996: p. 833-838.
44. Leonard S. Aubrey, M.A.C.e.a., *The development and performance evaluation of a dual stage ceramic foam filtration system.* Light Metals, 1996: p. 845-855.
45. Butcher, K., R. and D. Rogers, B, *Update on the filtration of aluminum alloys with fine pore ceramic foam.* Light Metals 1990: p. 797-803.
46. Alexandre Vianna da Silva, A.M.e.a., *Filtration Efficiency and Melt Cleanness Evaluation using LAIS Sampling at Valesul Aluminio S.A.* Light Metals, 2005: p. 957-960.
47. G. Lazzaro, L.P., *ALUDEF: a New System for in Line Refining of Liquid Aluminum.* Light Metals, 1990: p. 1001-1006.
48. A. H. Castillejos E., F.A.A.G., *Metal Filtration with a New Ceramic Porous Medium: CEFILPB.* Light Metals, 1992: p. 1113-1122.
49. Zhou, M., Shu, D. et al, *Deep filtration of molten aluminum using ceramic foam filters and ceramic particles with active coatings.* Metallurgical and Materials Transactions A (Physical Metallurgy and Materials Science), 2003. **34A**(5): p. 1183-1191.
50. Instone, S., Badowski, M., Schneider, W et al, *Development of molten metal filtration technology for aluminium.* Light Metals, 2005: p. 933-938.
51. Syvertsen, M., Frisvold, Frede et al, *Development of a compact deep bed filter for aluminum.* Light Metals: Proceedings of Sessions, TMS Annual Meeting (Warrendale, Pennsylvania), 1999: p. 1049-1055.
52. Fuwang Chen, X.H.e.a., *Investigation on the foam filter to remove inclusions in revert superalloy.* Materials letters, 1998(34): p. 372-376.
53. Zhou, M., *Effect of filtration condition on melt filtration through ceramic particles with active coating* Journal of Aeronautical Materials, 2003. **23**: p. 43.
54. Morgan, E., *Analyzing Steel Alloy Filtration.* Modern Casting, 2003. **93**(9): p. 42-45.
55. GUI, Q., *Application of Ceramic Foam Filter in Aluminum Manufacture.* Aluminum processing, 2003(1): p. 23.
56. McCollum, N.J.K.a.J.M., *Depth of ceramic foam filter vs. filtration efficiency.* Light Metals, 1992: p. 1085-1091.
57. Dahmen, U., *Brownian Motion Observed in Metals.* http://www.lbl.gov/~msd/PIs/Dahmen/05/05_6_Brownian.html, 2005.
58. Morgana de AVILA RIBAS, H.N., *Mathematical Model of Over-micron and Nano-scale Powders Accumulation in a Coke Fixed-Bed Filter.* ISIJ International, 2005. **45**(3): p. 303-311.

59. Tian, C. and R.I.L. Guthrie, *Rheological Aspects of Liquid Metal Filtration Using Reticulated Ceramic Foam Filters.* Light Metals, 1993: p. 1003-1007.
60. F. A. Acosta G., A.H.C.E.e.a., *A Study of the Role of Fluid Velocity and Particle Size on Deep Bed Filtration Behaviour.* Light Metals, 1996: p. 823-831.
61. Tritton, D.J., *Physical fluid dynamics*. 1988, Oxford: Clarendon Press. XVII, 519 s.
62. Coutanceau, M. and R. Bouard, *Experimental Determination of The Main Features of The Viscous Flow in The Wake of A Circular Cylinder in Uniform Translation. Part 1. Steady Flow.* Journal of Fluid Mechanics, 1977. **79**(02): p. 231-256.
63. B.Hubschen, et al. *A new approach for the investigation of the fluid flow in ceramic foam filters*. 2000: The Minerals, Metals, and Materials Society, Warrendale, PA.
64. L. A. Strom, J.W.B., *Non-ferrous Alloy Filtration Efficiency Study of Fully Sintered Reticulated Ceramics Utilizing LIMCA and LAIS.* Light Metals, 1992: p. 1093-1100.
65. Rudolph A. Olson III, L.C.B.M., *Cellular Ceramics in Metal Filtration.* Advanced Engineering Materials, 2005. **7**(4): p. 187-192.
66. Uemura, K., *Filtration Mechanism of Non-metallic Inclusions in Steel by Ceramic Loop Filter.* ISIJ Int., 1992. **32**(1): p. 150-156.
67. L. S. Aubrey, J.E.D., *Ceramic Foam- a Deep Bed or Caking Filter in Aluminum Cast Shop Operations.* Light Metals, 1993: p. 1009-1020.
68. Ni, H., *Purifying effects and mechanism of a new composite filter.* Materials Science and Engineering, 2006: p. 53-58.
69. T. A. Engh, B.R.e.a., *Deep Bed Filtration Theory Compared with Experiments.* Light Metals, 1986: p. 829-836.
70. N. J. Keegan, W.S.e.a., *Evaluation of the efficiency of fine pore ceramic froam filters.* light Metals, 1999: p. 1031-1040.
71. Lae, E., et al. *Experimental and numerical study of ceramic foam filtration*. in *Light Metals 2006. Proceedings of the Technical Sessions Presented by the TMS Aluminum Committee at the 135th TMS Annual Meeting*. 2006: The Minerals, Metals, and Materials Society, Warrendale, PA.
72. Cooper, P., *Trends in Rod Addition Point Increase Demands on TiBAl Quality*. Metallug Aluminium, 2006.
73. D. Kocaefe, A.M.-C., *Investigation of Inclusion Re-entrainment During Filtration.* Light Metals, 2003: p. 873-879.
74. C. Dupuis, G.B., *Filtration efficiency of ceramic foam filters for production of high quality molten aluminum alloys.* Light metal processing and applications, 2004: p. 1-11.
75. Kocaefe, D., Murray-Chiasson, A. et al, *Study of inclusion re-entrainment in a filter bed.* Metallurgical and Materials Transactions B: Process Metallurgy and Materials Processing Science, 2004. **35**(5): p. 999-1009.
76. C. Tian, G.A.I., *Settling of Multisized Clusters of Alumina Particles in Liquid Aluminum.* Metallurgical and Materials Transactions B, 1999. **30B**: p. 241-247.
77. Görner, H., T.A. Engh, and M. Syvertsen, *Kinetics of an AlF_3 Aluminum Filter.* Light Metals, 2006: p. 765-770.

78. Görner, H. and M. Syvertsen, *AlF_3 as an Aluminum Filter Medium.* Light Metals, 2005: p. 939-944.
79. J. Bäckman, I.L.S., *Influence of filter on the mould filling of aluminium melts in vacuum-sealed moulds.* Research Report of Jönköping University, 1999.
80. I.A. Andrews, A.L.M., *Molten Metal Filtration-An Engineered Balance.* Ductile Iron News, 1999: p. http://www.ductile.org/magzine/1999_1/.
81. F. A. ACOSTA G., A.H.C.E., *A Mathematical Model of Aluminum Depth Filtration with Ceramic Foam Filters: Part I. Validation for Short-Term Filtration.* Metallurgical and Materials Transactions B, 2000. **31B**: p. 491-502.
82. Rajamani Rajagopalan, C.T., *Trajectory Analysis of Deep-bed Filtration with the Sphere-in-cell Porous Media Model.* AlChE Journal, 1976. **22**(3): p. 523-533.
83. Riviere, C., H. Duval, and J. Guillot. *A 2D lattice-Boltzmann model of aluminium depth filtration*. 2004: The Minerals, Metals, and Materials Society, Warrendale, PA.
84. Stein Tore Johansen, N.M.A., *A Mathematical Model for Large Scale Filtration of Aluminum.* 119th AlMe Annual Meeting, 1990.
85. F. A. ACOSTA G., A.H.C.E., *A Mathematical Model of Aluminum Depth Filtration with Ceramic Foam Filters: Part II. Application to Long-Term Filtration.* Metallurgical and Materials Transactions B, 2000. **31B**: p. 503-514.
86. Fig.Butcher, K.R., Smith, Dawid D. et al, *Performance evaluation of a filtration unit developed to remove liquid salts from molten aluminum.* Light Metals: Proceedings of Sessions, TMS Annual Meeting (Warrendale, Pennsylvania), 2000: p. 803-807.
87. D. Doutre, B.G.e.a., *Aluminium Cleanliness Monitoring: Methods and Applications in Process Development and Quality Control.* Light Metals, 1985: p. 1179-1195.
88. Liu, L., F.H. Samuel, *Assessment of melt cleanliness in A356.2 aluminium casting alloy using the porous disc filtration apparatus technique: Part II Inclusion analysis.* Journal of Materials Science, 1997. **32**: p. 5927-5944.
89. Shi, X., *Upgrading liquid metal cleanliness analyzer (LiMCA) with digital signal processing (DSP) technology*. 1996: National Library of Canada.
90. Li, M. and R.I.L. Guthrie, *Liquid Metal Cleanliness Analyzer (LiMCA) in Molten Aluminum.* ISIJ Inter., 2001. **41**(2): p. 101-110.
91. T.A. Utigard, I.D.S., *Cleanliness of Aluminum and Steel: a Comparison of Assessment Methods.* Light Metals, 2005: p. 951-956.
92. Velasco E., P.J., *Metal Quality of Secondary Alloys for Al Castings.* Light Metals, 2006: p. 721-724.
93. Martin Syvertsen, T.A.E., *Error Analysis of LIMCA II Data.* Light Metals, 2001: p. 957-963.
94. Gaydos, J. and A. Neumann, *The Dependence of Contact Angles on Drop Size and Line Tension.* Journal of Colloid and Interface Science, 1987. **120**(1): p. 76-86.
95. Zhang, L. and S. Taniguchi, *Fundamentals of Inclusion Removal from Liquid Steel by Bubble Flotation.* International Materials Reviews, 2000. **45**(2): p. 59-82.

96. Eustathopoulos, N., M.G. Nicholas, and B. Drevet, *Wettability at high temperatures.* Amsterdam: Pergamon, 1999. **XVII**: p. 420 s.
97. Rhee, S.K., *Wetting of Ceramics by Liquid Metals.* Journal of the American Ceramic Society, 1970. **54** (7): p. 332 - 334.
98. Eustathopoulos, N., J.P. Garandet, and B. Drevet, *Influence of reactive solute transport on spreading kinetics of alloy droplets on ceramic surfaces.* Philosophical Transactions of the Royal Society London A, 1998. **356**(1739): p. 871-884.
99. Hoekstra, J. and M. Kohyama, *Ab initio calculations of the beta -SiC(001)/Al interface.* Physical Review B, 1998. **57**(4): p. 2334-2341.
100. *Getting "Wet": it`s more complicated than scientists thought.* http://www.lbl.gov/science-articles/archive/MSD-getting-wet.html, 2002: p. 1-5.
101. Saiz, E., R.M. Cannon, and A.P. Tomsia, *High-Temperature Wetting and the Work of Adhesion in Metal/Oxide System.* Annu. Rev. Mater. Res, 2008. **38**: p. 197-226.
102. Lupis, C.H.P., *Chemical Thermodynamics of Materials* 1983, New York: Prentice-Hall, Inc. 581.
103. Candan, E., *Effect of Alloying Elements to Aluminium on the Wettability of Al/SiC system.* Turkish J. Eng. Env. Sci., 2002. **26**: p. 1-5.
104. Li, J.G., *Wetting of ceramic materials by liquid silicon, aluminium and metallic melts containing titanium and other reactive elements: a review.* Ceramics international, 1994. **20**: p. 391-412.
105. Laurent, V., D. Chatain, and N. Eustathopoulos, *Wettability of SiC by aluminium and Al-Si alloys* Journal of Materials Science, 1987. **22**(1): p. 244-250.
106. Moraes, E.E.S., M.L.A. Graça, and C.A.A. Cairo, *Study of Aluminium Alloys Wettability on SiC Preform.* Congresso Brasileiro de Engenharia e Ciência dos Materiais, 2006. **15**(19): p. 4217-4224.
107. M, M.J., et al., *The surface tension of liquid aluminium in high vacuum : The role of surface condition.* International journal of adhesion and adhesives, 2007. **27**(5): p. 394-401.
108. Mills, K.C. and Y.C. Su, *Review of surface tension data for metallic elements and alloys: Part 1 Pure metals.* International Materials Reviews, 2006. **51**(6): p. 329-351.
109. Tang, K., *Wettability of Al on Al_2O_3.* SINTEF report, 2009: p. 6.
110. Ha*B,* V.G., *Growth and Structure of Thin Oxide Films on Aluminum.* Optik, 1946. **1**(2): p. 134-143.
111. Bao, S., et al., *Wetting of Pure Aluminium on Filter Materials Graphite, AlF_3 and Al_2O_3.* Light Metals, 2009: p. 767-773.
112. Jone, H. and H. Hausner, *Influence of oxygen partial pressure on the wetting behaviour in the system Al/Al_2O_3.* Journal of Materials Science Letters, 1986. **5**: p. 549-551.
113. Klinter, A.J., G. Mendoza-Suarez, and R.A.L. Drew, *Wetting of pure aluminum and selected alloys on polycrystalline alumina and sapphire.* Materials Science and Engineering A, 2008. **495**(1-2): p. 147-152.
114. Wang, D.J. and S.T. Wu, *The influence of oxidation on the wettability of aluminum on sapphire.* Acta Metallurgica et Materialia, 1994. **42**(12): p. 4029-4034.

115. Yu.V.Naidich, Y.N.C., N.F.Ishchuk, and V.p. Krasoskii, *Wetting of Some Nonmetallic Materials by Aluminum.* Sov. Powder Metall. Met. Cer, 1983. **2**: p. 481-483.
116. M.Ksiazek, et al., *Wetting and Bonding Strength in Al/Al_2O_3 System.* Materials Science and Engineering, 2002. **A324**: p. 162-167.
117. Shen, P., et al., *Wetting of (0001) a-Al_2O_3 Single Crystals by Molten Al.* Scripta Materialia, 2003. **48**: p. 779-784.
118. Wolf, S.M., A.P. Levitt, and J. Brown, *Whisker-metal matrix bonding.* Chemical Engineering Progress, 1966. **62**(3): p. 74-78.
119. Brennan, J.J. and J.A. Pask, *Effect of Nature of Surfaces on Wetting of Sapphire by Liquid Aluminum.* Journal of American Ceramic Society, 1968. **51**: p. 569-573.
120. Nicholas, M., *The Strength of Metal/Alumina Interfaces.* Journal of Materials Science, 1968. **3**: p. 571-576.
121. Kalogeropoulou, S., C. Rado, and N. Eustathopoulos, *Mechanisms of reactive wetting: the wetting to non-wetting case.* Scripta Materialia, 1999. **41**(7): p. 723-728.
122. Zhou, X.B. and J.T.M.D. Hosson, *Reactive wetting of liquid metals on ceramic substrates.* Acta Materialia, 1996. **44**(2): p. 421-426.
123. Etter, T., et al., *Aluminium carbide formation in interpenetrating graphite/aluminium composites.* Materials Science and Engineering A, 2007. **448**(1-6).
124. Laurent, V., C. Rado, and N. Eustathopoulos, *Wetting Kinetics and Bonding of Al and Al Alloys on α-SiC.* Materials Science & Engineering A, 1996. **205**: p. 1-8.
125. Han, D.S., H. Jones, and H.V. Atkinson, *The wettability of silicon carbide by liquid aluminium: the effect of free silicon in the carbide and of magnesium, silicon and copper alloy additions to the aluminium. Journal of Materials Science*, 1993. **28**(10): p. 2654-2658.
126. Shimbo, M., M. Naka, and I. Okamoto, *Wettability of silicon carbide by aluminum, copper and silver. Journal of Materials Science Letters*, 1989. **8**(6): p. 663-666.
127. Laurent, V., D. Chatain, and N. Eustathopoulos, *Wettability of SiO_2 and oxidized SiC by aluminium. Materials Science & Engineering A: Structural Materials: Properties, Microstructure and Processing*, 1991. **135**(1-2): p. 89-94.
128. Guy Ervin, J., *Oxidation Behavior of Silicon Carbide.* Journal of the American Ceramic Society, 1958. **41**(9): p. 347-352.
129. Jia, Q., et al., *Effect of particle size on oxidation of silicon carbide powders.* Ceramics International, 2007. **33** p. 309-313.
130. Viala, J.C., P. Fortier, and J. Bouix, *Stable and Metastable Phase Equilibria in The Chemical Interaction between Aluminium and Silicon Carbide.* Journal of Materials Science, 1990. **25**(3): p. 1842-1850.
131. Iseki, T., T. Kameda, and T. Maruyama, *Interfacial reactions between SiC and aluminium during joinIng.* Journal of Materials Science, 1984. **19**: p. 1692-1698.
132. Foister, S.A.M., M.W. Johnston, and J.A. Little, *The interaction of liquid aluminium with silicon carbide and nitride-based ceramics.* Journal of Materials Science Letters, 1993. **12**(4): p. 209-211.

133. Nord-Varhaug, K., *Titanium Diboride Interfacial Microstructure and wettablilty by liquid aluminium*. 1994, Universitetet i Trondheim Norges Tekniske Høgskole: Trondheim.
134. Rhee, S.K., *Wetting Of Ceramics By Liquid Aluminum.* Journal of American Ceramic Society, 1970. **53**(7): p. 386-389.
135. Coudurier, L., et al., *Etude de la mouillabilité par I'aluminium liquide de I'alumine et de I'alumine recouverte d'une couche de métal ou de composé réfractaire.* Revue internationale des hautes températures et des réfractaires 1984. **21**(2): p. 81-93.
136. Bornand, J.-D. and K. Buxmann, *DUFI: A Concept of Metal Filtration.* Light Metals, 1985: p. 1249-1260.
137. Landry, K., et al., *Characteristic contact angles in the Aluminium/vitreous carbon system.* Scripta Materialia, 1996. **34**(6): p. 841-846.
138. Standards, N.B.O., *JANAF Termochemical Tables, 2nd edition.* 1971. **37**.
139. Yokokawa, H., et al., *Phase relations associated with the aluminium blast furnace. Aluminium oxycarbide metals and Al-C-X (X=Fe, Si) liquid alloys.* Metallurgical Transactions B, 1987. **18B**: p. 433-444.
140. Bao, S., et al., *Wettability of Aluminium with Aluminium Carbide (Graphite) in Aluminium Filtration*, in *TMS*. 2012: Orlando, Florida, USA. p. submitted.
141. Isaikin, A.S., et al., *Compatibility of Carbon Filaments with A Carbide Coating and an Aluminium Matrix.* Sci. Heat Treatment, 1980. **22**: p. 815-817.
142. Takematsu, S., et al., *Evaluation of surface energy by molecular dynamics simulation and discussion about cleavage fracture in alpha-Al2O3.* Journal of the Ceramic Society of Japan, 2004. **112**(1): p. 46-49.
143. Girifalco, L.A. and R.J. Good, *A Theory for the Estimation of Surface and Interfacial Energies. I. Derivation and Application to Interfacial Tension.* J. Phys. Chem., 1957. **61**(7): p. 904-909.
144. Nikolopoulos, P., S. Agathopoulos, and A. Tsoga, *A Method for the Calculation of Interfacial Energies in Al_2O_3 and ZrO_2/ Liquid-Metal and Liquid-Alloy Systems.* Journal of Materials Science, 1994. **29**(16): p. 4393-4398.
145. Landry, K., S. Kalogeropoulou, and N. Eustathopoulos, *Wettability of carbon by aluminum and aluminum alloys. Materials Science and Engineering: A*, 1998. **254**(1-2): p. *99-111*.
146. Ambrose, J.C., M.G. Nicholas, and A.M. Stoneham, *Dynamics of Braze Spreading.* Acta Metallurgica et Materialia, 1992. **40**(10): p. 2483-2488.
147. Nikolopoulos, P., S. Agathopoulos, and G.N. Angelopoulos, *Wettability and Interfacial Energies in SiC-liquid System.* Journal of Materials Science, 1992. **27**: p. 139-145.
148. W. Kohler, F., *Investigations for the wetting of Al_2O_3 and SiC - crystals by aluminum and aluminum alloys.* Aluminium, 1975. **51**: p. 443-447.
149. Davis, J.R., *Aluminum and Aluminum Alloys*. 1993, Materials Park, OH: ASM International. V, 784 s.
150. Bao, S., et al., *Alspek Measurements in Aluminium Filtration Plant Experiments.* In Plan.
151. Shirandasht, J., *Évaluation De La Technique LiMCA II Pour La Mesure D'inclusions L'aluminium Pur Et L'alliage Binaire Al-6%Si : Role De La Temperature De Coulee (Evaluation of the technique for measureing LiMCA II*

inclusions in aluminum alloy and pure binary Al-6% Si: role of the temperature of casting). 2005, UNIVERSITÉ DU QUÉBEC À CHICOUTIMI.

152. Syvertsen, M., *Removal of hydrogen and inclusions from aluminium: theory, model studies and experiments*. 2000, Norges teknisk-naturvitenskapelige universitet, Instituttfor materialteknologi og elektrokjemi: Trondheim. p. XX, 202 s.
153. Lloyd, D.J., *The solidification microstructure of particulate reinforced aluminium/SiC composites.* Composites Science and Technology, 1989. **35**: p. 159-179.
154. Rasch, B., *Activities at RTD in Hydro Sunndalsøra*. 2011, RIRA Project Meeting: Trondheim.
155. Schlichting, H., *Boundary-Layer Theory*. 7th ed. 1979, New York, NY: McGraw Hill. 599.
156. *Origin User Guide*, One Roundhouse Plaza, Northampton, MA 01060, USA: OriginLab Corporation.
157. Schlichting, H., *Boundary-layer theory*. 1960, New York: McGraw-Hill. XX, 647 s.
158. Weber, M. and D. Paddock, *Interceptional and gravitational collision efficiencies for single collectors at intermediate Reynolds numbers.* Journal of Colloid and Interface Science, 1983. **94**(2): p. 328-335.
159. Espinosa, A., et al., *Numerical Simulation of Particle Capture by Circular Cylinders*, in *17th Australasian Fluid Mechanics Conference*. 2010: Auckland, New Zealand.
160. Ciftja, A., *Solar silicon refining: inclusions, settling, filtration, wetting*. 2009, Norges teknisk-naturvitenskapelige universitet: Trondheim.
161. Landau, L.D. and E.M. Lifshitz, *Fluid mechanics*, in *Course of Theoretical Physics. Translated from the Russian by J. B. Sykes and W. H. Reid*. 1959, Pergamon Press: London. p. 536s.
162. Julien, P.Y., *Erosion and sedimentation*, Cambridge: Cambridge University Press. xvii, 371 s.
163. Acosta G, F., et al., *Analysis of liquid flow through ceramic porous media used for molten metal filtration.* Metallurgical and Materials Transactions B, 1995. **26**(1): p. 159-171.
164. Tien, C. and B. Ramarao, *Granular filtration of aerosols and hydrosols*. 2007: Elsevier Science Ltd.
165. Harvey, M., E. Bourget, and R. Ingram, *Experimental evidence of passive accumulation of marine bivalve larvae on filamentous epibenthic structures.* Limnology and Oceanography, 1995. **40**(1): p. 94-104.
166. Innocentini, M.D.M., et al., *Prediction of Ceramic Foams Permeability using Ergun's Equation.* Materials Research, 1999. **2**(4): p. 283-289.
167. Moreira, E. and J. Coury, *The Influence of Structural Parameters on The Permeability of Ceramic Foams.* Brazilian Journal of Chemical Engineering, 2004. **21**(1): p. 23-33.
168. Moreira, E., M. Innocentini, and J. Coury, *Permeability of Ceramic Foams to Compressible and Incompressible Flow.* Journal of the European Ceramic Society, 2004. **24**(10-11): p. 3209-3218.

169. Lide, D.R., ed. *CRC Handbook of Chemistry and Physics 85th ed* 2004, CRC Press LLC.
170. Tian, C. and R.I.L. Guthrie, *Direct Simulation of Initial Filtration Phenomena within Highly Porous Media.* Metallurgical and Materials Transactions B, 1995. **26**(3): p. 537-546.
171. Lu, T., H. Stone, and M. Ashby, *Heat Transfer in Open-cell Metal Foams.* Acta Materialia, 1998. **46**(10): p. 3619-3635.
172. Richardson, J., Y. Peng, and D. Remue, *Properties of Ceramic Foam Catalyst Supports: Pressure Drop.* Applied Catalysis A: General, 2000. **204**(1): p. 19-32.
173. G. Fourie, J. and J. P. Du Plessis, *Pressure Drop Modelling in Cellular Metallic Foams.* Chemical engineering science, 2002. **57**(14): p. 2781-2789.
174. Buciuman, F.C. and B. Kraushaar-Czarnetzki, *Ceramic Foam Monoliths as Catalyst Carriers. 1. Adjustment and Description of The Morphology.* Industrial & Engineering Chemistry Research, 2003. **42**(9): p. 1863-1869.
175. Giani, L., G. Groppi, and E. Tronconi, *Mass-transfer Characterization of Metallic Foams as Supports for Structured Catalysts.* Industrial & engineering chemistry research, 2005. **44**(14): p. 4993-5002.
176. Lacroix, M., et al., *Pressure Drop Measurements And Modeling on SiC Foams.* Chemical engineering science, 2007. **62**(12): p. 3259-3267.
177. Schlichting, H. and J. Kestin, *Boundary-layer Theory*. 1968, New York: McGraw-Hill. XIX, 747 s.

Appendix A. The Functions f1, f3, f5, f7

The functions *f* has been discussed by Schlichting. 1968 [177] in detail. He calculated the functions associated with the term λ^{11} and improved the accuracy, see Table 9.1 in [177] as below.

Table A.1 Functional coefficients for the first four terms of the Blasius series, required in the calculation of 2-dimentional boundary layer on a cylinder (symmetrical case) [177]

λ	f_1`	f_3`	g_5`	h_5`	g_7`	h_7`	k_7`
0	0	0	0	0	0	0	0
0.2	0.2266	0.1251	0.1072	0.0141	0.0962	0.0173	0.0016
0.4	0.4145	0.2129	0.1778	0.0117	0.1563	0.0030	0.0044
0.6	0.5663	0.2688	0.2184	-0.0011	0.1879	-0.0286	0.0096
0.8	0.6859	0.2997	0.2366	-0.0177	0.1994	-0.0637	0.0174
1.0	0.7779	0.3125	0.2399	-0.0331	0.1980	-0.0925	0.0271
1.2	0.8467	0.3133	0.2341	-0.0442	0.1896	-0.1102	0.0369
1.4	0.8968	0.3070	0.2239	-0.0499	0.1782	-0.1159	0.0452
1.6	0.9323	0.2975	0.2123	-0.0504	0.1665	-0.1114	0.0506
1.8	0.9568	0.2871	0.2012	-0.0468	0.1558	-0.0997	0.0525
2.0	0.9732	0.2775	0.1916	-0.0406	0.1469	-0.0839	0.0510
2.2	0.9839	0.2695	0.1839	-0.0332	0.1400	-0.0669	0.0466
2.4	0.9905	0.2632	0.1781	-0.0257	0.1349	-0.0507	0.0402
2.6	0.9946	0.2586	0.1740	-0.0189	0.1313	-0.0367	0.0330
2.8	0.9970	0.2554	0.1712	-0.0133	0.1288	-0.0254	0.0257
3.0	0.9984	0.2532	0.1694	-0.0089	0.1273	-0.0168	0.0191
3.2	0.9992	0.2519	0.1682	-0.0057	0.1263	-0.0107	0.0135
3.4	0.9996	0.2510	0.1675	-0.0035	0.1257	-0.0065	0.0091
3.6	0.9998	0.2506	0.1671	-0.0021	0.1254	-0.0038	0.0059
3.8	0.9999	0.2503	0.1669	-0.0012	0.1252	-0.0021	0.0036
4.0	1.0000	0.2501	0.1668	-0.0006	0.1251	-0.0011	0.0021
λ	f_1``	f_3``	g_5``	h_5``	g_7``	h_7``	k_7``
0	1.2326	0.7244	0.6347	0.1192	0.5792	0.1829	0.0076

If we set

$$f_1(\lambda) = A_0 + A_1\lambda + A_2\lambda^2 + A_3\lambda^3 + A_4\lambda^4 + A_5\lambda^5 + A_6\lambda^6 \tag{A.1}$$

Then

$$f_1^{'}(\lambda) = A_1 + 2A_2\lambda + 3A_3\lambda^2 + 4A_4\lambda^3 + 5A_5\lambda^4 + 6A_6\lambda^5 \tag{A.2}$$

$$f_1^{''}(\lambda) = 2A_2 + 6A_3\lambda + 12A_4\lambda^2 + 20A_5\lambda^3 + 30A_6\lambda^4 \tag{A.3}$$

Schlichting, 1968 [177] also gave

$$f_1(0) = A_0 = 0$$

$$f_1'(0) = A_1 = 0$$
$$f_1''(0) = 2A_2 = 1.2326 \quad \text{(A.4)}$$

Then, fit the data in Table A.1 with the function

$$f_1'(\lambda) = 1.2326\lambda + 3A_3\lambda^2 + 4A_4\lambda^3 + 5A_5\lambda^4 + 6A_6\lambda^5 \quad \text{(A.5)}$$

and we get fitted f_1` with R^2=99.993%, see Figure A.1.

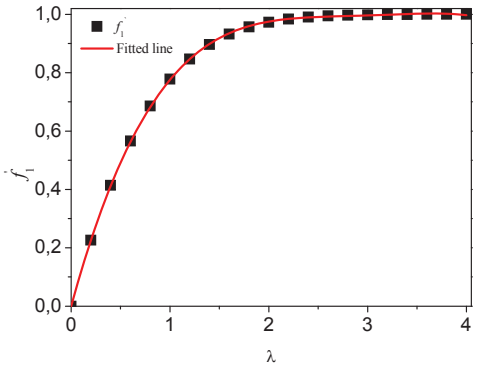

Figure A.1 The Function f_1` in the Blasius power series

Then

$$f_1(\lambda) = 0.6163\lambda^2 - 0.1825\lambda^3 + 0.0230\lambda^4 - 0.0002\lambda^6 \quad \text{(A.6)}$$

With the same way, set

$$f_3(\lambda) = B_0 + B_1\lambda + B_2\lambda^2 + B_3\lambda^3 + B_4\lambda^4 + B_5\lambda^5 + B_6\lambda^6 \quad \text{(A.7)}$$

Schlichting, 1968 [177] gave

$$f_3(0) = B_0 = 0$$
$$f_3'(0) = B_1 = 0$$
$$f_3''(0) = 2B_2 = 0.7244 \quad \text{(A.8)}$$

Then we got the function

$$f_3(\lambda) = 0.3622\lambda^2 - 0.1960\lambda^3 + 0.0512\lambda^4 - 0.0064\lambda^5 + 0.0003\lambda^6 \quad \text{(A.9)}$$

from the fitted $f_3^{`}$ with R^2=99.858% in Figure A.2.

When set

$$f_5(\lambda) = C_0 + C_1\lambda + C_2\lambda^2 + C_3\lambda^3 + C_4\lambda^4 + C_5\lambda^5 + C_6\lambda^6 \tag{A.10}$$

Schlichting, 1968 [177] gave

$$\begin{aligned} f_5^{'} &= g_5^{'} + 10h_5^{'}/3 \\ f_5(0) &= C_0 = 0 \\ f_5^{'}(0) &= C_1 = 0 \\ f_5^{''}(0) &= 2C_2 = 0.6347 + 0.1192\times 10/3 = 1.0320 \end{aligned} \tag{A.11}$$

Then we got the function

$$f_5(\lambda) = 0.516\lambda^2 - 0.4517\lambda^3 + 0.0376\lambda^4 + 0.1054\lambda^5 - 0.0375\lambda^6 \tag{A.12}$$

from the fitted $f_5^{`}$ with R^2=100% in Figure A.3.

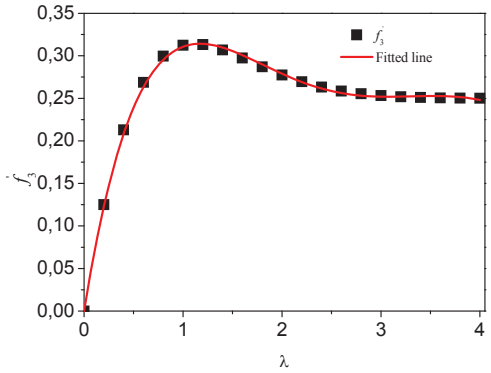

Figure A.2 The Function $f_3^{`}$ in the Blasius power series

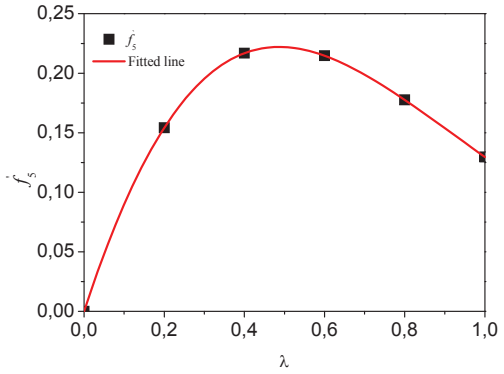

Figure A.3 The Function f_5' in the Blasius power series
R^2<98% for λ=[0, 4.0]; thus fitting in λ=[0, 1.0] is employed.

For the function f_7, set

$$f_7(\lambda) = D_0 + D_1\lambda + D_2\lambda^2 + D_3\lambda^3 + D_4\lambda^4 + D_5\lambda^5 + D_6\lambda^6 \tag{A.13}$$

Schlichting, 1968 [177] gave

$$\begin{aligned} f_7' &= g_7' + 7h_7' + 70k_7'/3 \\ f_7(0) &= D_0 = 0 \\ f_7'(0) &= D_1 = 0 \\ f_7''(0) &= 2D_2 = 0.5792 + 0.1829\times 7 + 0.0076\times 70/3 = 2.0368 \end{aligned} \tag{A.14}$$

Then we got the function

$$f_7(\lambda) = 1.0184\lambda^2 - 1.4171\lambda^3 + 0.4471\lambda^4 + 0.3319\lambda^5 - 0.1750\lambda^6 \tag{A.15}$$

from the fitted f_7' with R^2=99.997%. See Figure A.4.

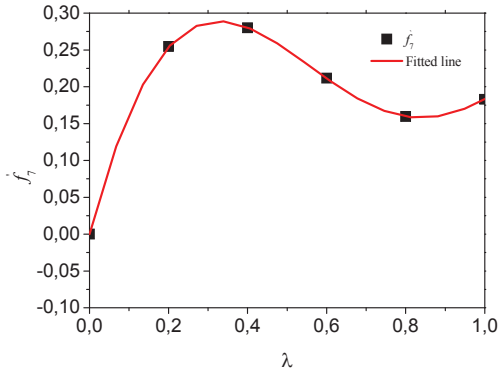

Figure A.4 The Function f_7' in the Blasius power series
R^2<98% for λ=[0, 4.0]; thus fitting in λ=[0, 1.0] is employed.

Appendix B. Inclusion Level in Filtration

The time dependent inclusion level before and after the filters are shown in Figure B.1 to Figure B.8. Approximately 50% of the number of the inclusions is in the range of 20-25 μm.

The filtration efficiencies with time for various inclusion sizes are summarized in Figure B.9 to Figure B.20. More than 87% of the number of inclusions is smaller than 40 μm. Inclusions less than 40 μm are discussed in the current appendix.

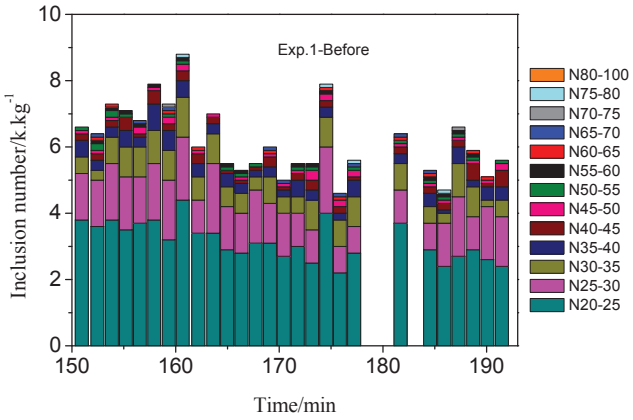

Figure B.1 The inclusion number size distribution before the filter vs. time in Exp.1 – Al_2O_3 industrial filter

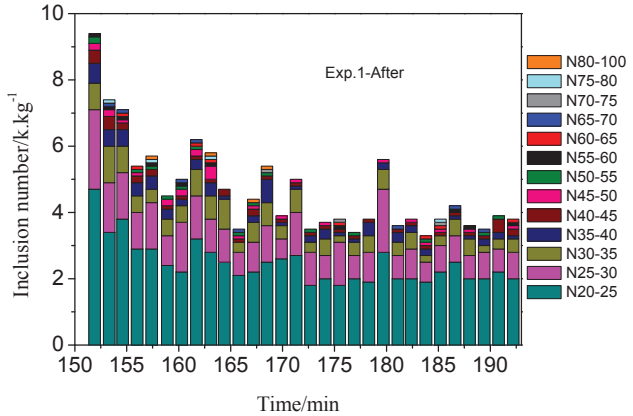

Figure B.2 The inclusion number size distribution after the filter vs. time in Exp.1 – Al_2O_3 industrial filter

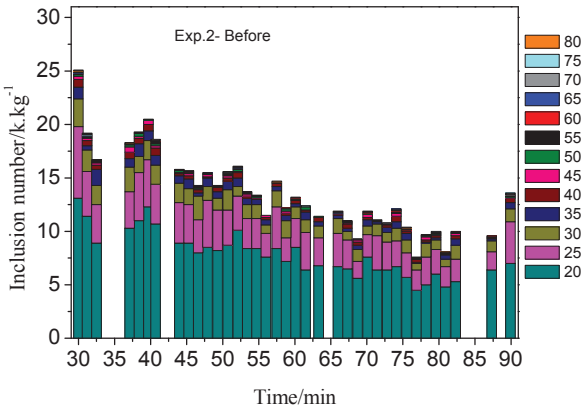

Figure B.3 The inclusion number size distribution before the filter vs. time in Exp.2 – SiC industrial filter

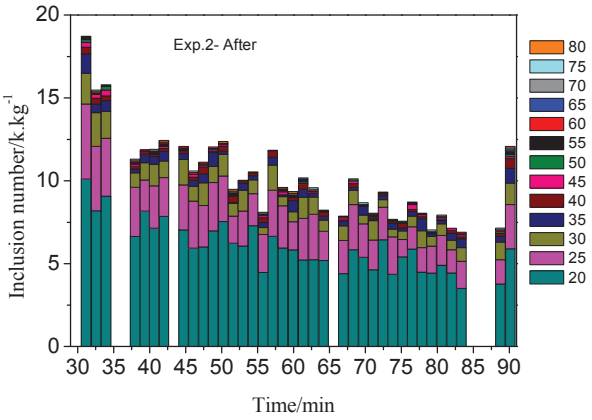

Figure B.4 The inclusion number size distribution after the filter vs. time in Exp.2 – SiC industrial filter

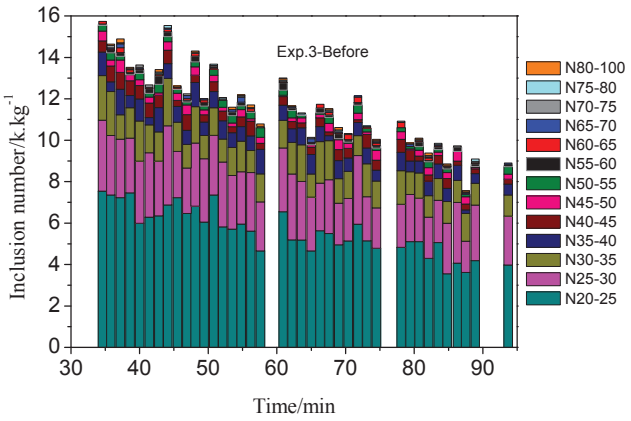

Figure B.5 The inclusion number size distribution before the filter vs. time in Exp.3 – Al_2O_3 industrial filter

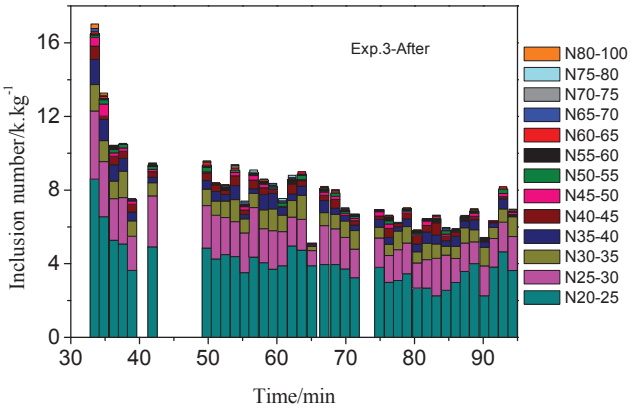

Figure B.6 The inclusion number size distribution after the filter vs. time in Exp.3 – Al_2O_3 industrial filter

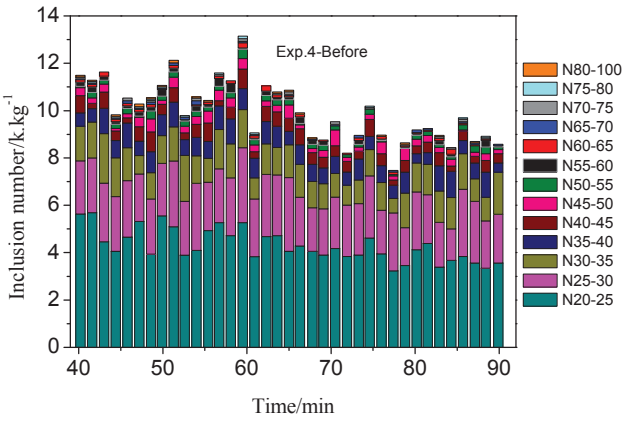

Figure B.7 The inclusion number size distribution before the filter vs. time in Exp.4 – SiC industrial filter

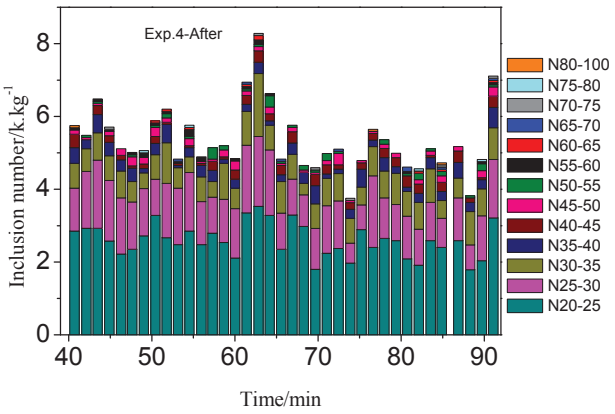

Figure B.8 The inclusion number size distribution after the filter vs. time in Exp.1 – SiC industrial filter

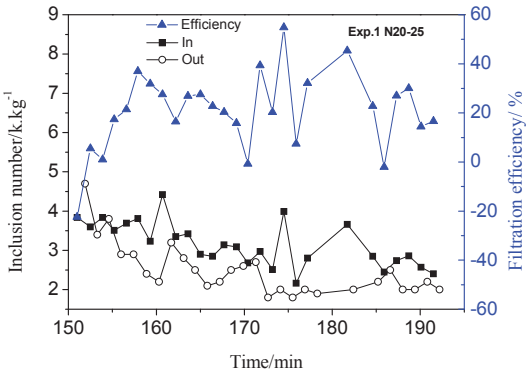

Figure B.9 The filtration efficiency vs. time for inclusions 20-25 μm in Exp.1

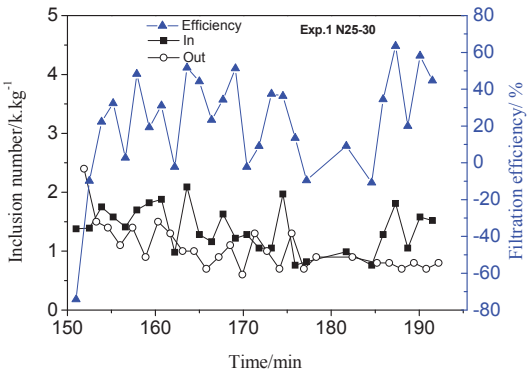

Figure B.10 The filtration efficiency vs. time for inclusions 25-30 μm in Exp.1

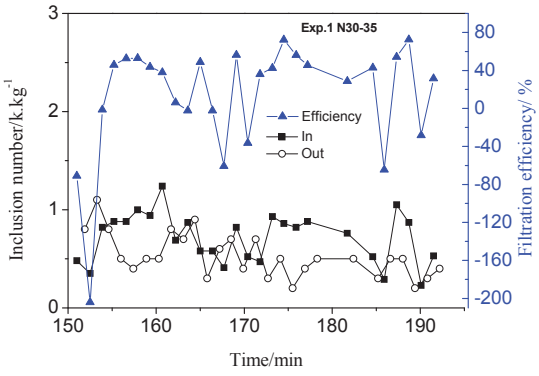

Figure B.11 The filtration efficiency vs. time for inclusions 30-35 μm in Exp.1

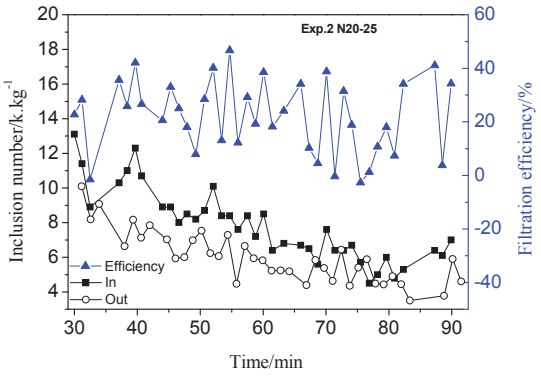

Figure B.12 The filtration efficiency vs. time for inclusions 20-25 μm in Exp.2

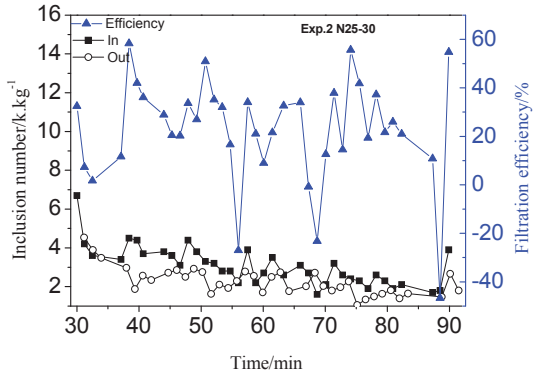

Figure B.13 The filtration efficiency vs. time for inclusions 25-30 μm in Exp.2

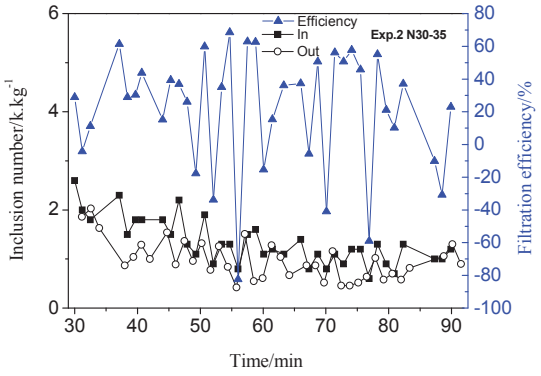

Figure B.14 The filtration efficiency vs. time for inclusions 30-35 μm in Exp.2

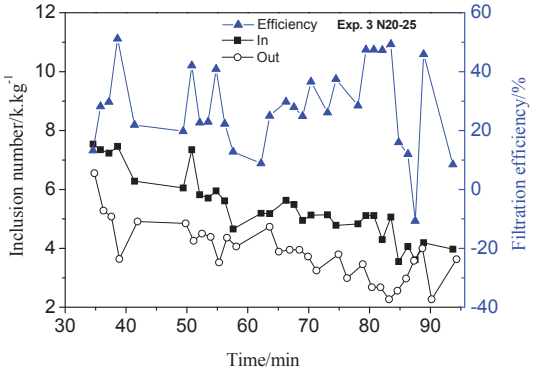

Figure B.15 The filtration efficiency vs. time for inclusions 20-25 μm in Exp.3

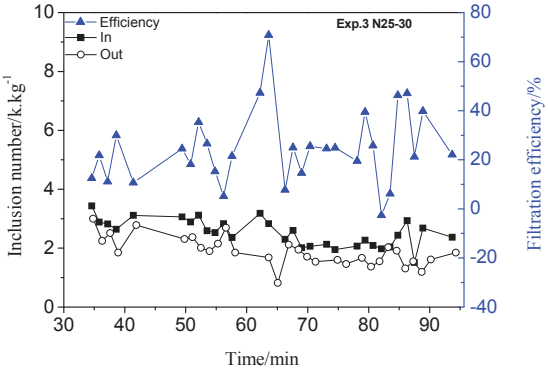

Figure B.16 The filtration efficiency vs. time for inclusions 25-30 μm in Exp.3

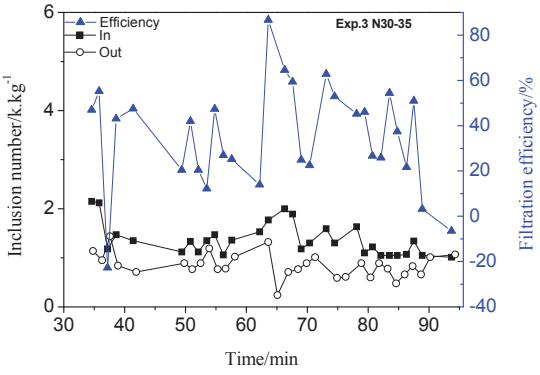

Figure B.17 The filtration efficiency vs. time for inclusions 30-35 μm in Exp.3

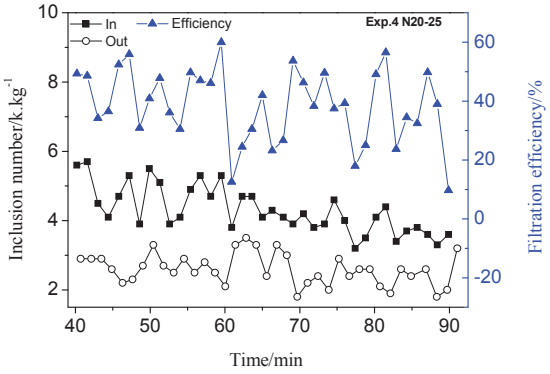

Figure B.18 The filtration efficiency vs. time for inclusions 20-25 μm in Exp.4

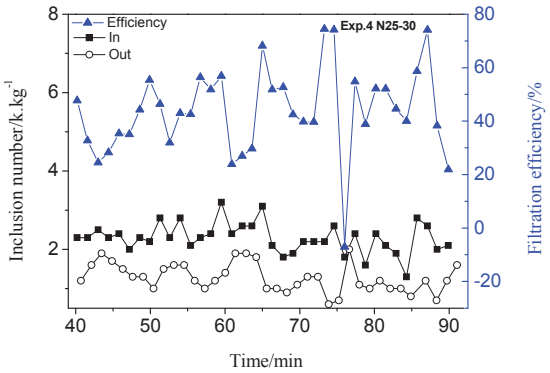

Figure B.19 The filtration efficiency vs. time for inclusions 25-30 μm in Exp.4

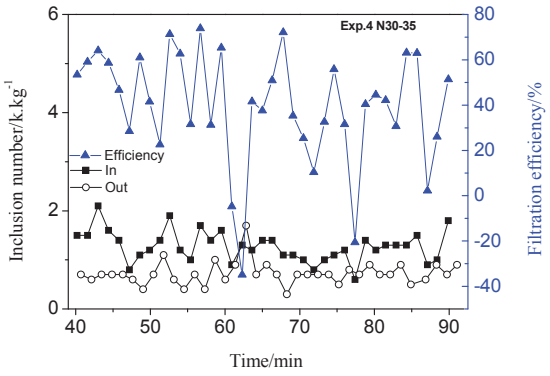

Figure B.20 The filtration efficiency vs. time for inclusions 30-35 μm in Exp.4

Appendix C. Standard Deviation for the Filtration Efficiency

Standard deviation shows how much variation there is from the "average". A low standard deviation indicates that the data points tend to be very close to the average, whereas high standard deviation indicates that the data are spread out over a large range of values.
The average is given by

$$x = \frac{1}{N}(x_1 + x_2 + x_3 + ...x_N) \tag{C.1}$$

The standard deviation is given by

$$\sigma = \sqrt{\frac{1}{N}\sum_{i=1}^{N}(x - x_i)^2} \tag{C.2}$$

The filtration efficiency E is calculated as Equ.(2.13). E is not linearly dependent on inlet inclusion number n_{in}. It is necessary to calculate the upper and lower deviation explicitly. For the detail, please refer to Syvertsen's thesis [152].

$$\begin{aligned}(\sigma_E^+)^2 &= (1 - \frac{n_{out} - \sigma_{out}}{n_{in}} - E)^2 + (1 - \frac{n_{out}}{n_{in} + \sigma_{in}} - E)^2 = (\frac{\sigma_{out}}{n_{in}})^2 + (\frac{n_{out}\sigma_{in}}{n_{in}(n_{in} + \sigma_{in})})^2 \\ (\sigma_E^-)^2 &= (1 - \frac{n_{out} + \sigma_{out}}{n_{in}} - E)^2 + (1 - \frac{n_{out}}{n_{in} - \sigma_{in}} - E)^2 = (\frac{\sigma_{out}}{n_{in}})^2 + (\frac{n_{out}\sigma_{in}}{n_{in}(n_{in} - \sigma_{in})})^2\end{aligned} \tag{C.3}$$

For deviations which give

$$\begin{aligned}E + \sigma_E^+ &\geq 1 \\ E + \sigma_E^- &\leq 0\end{aligned} \tag{C.4}$$

it is adjusted to

$$\begin{aligned}\sigma_E^+ &= 1 - E \\ \sigma_E^- &= -E\end{aligned} \tag{C.5}$$

because it is clear that

$$0 \leq E + \sigma_E \leq 1 \tag{C.6}$$

Based on the preceding discussion, Figure C.1 shows the filtration efficiency with the standard deviation. Only less than 2.5% of the inclusions are larger than 60 μm in all

four experiments, which results in a huge uncertainty (more than 100%) for inclusions in that range. The results larger than 60 μm are unreliable.

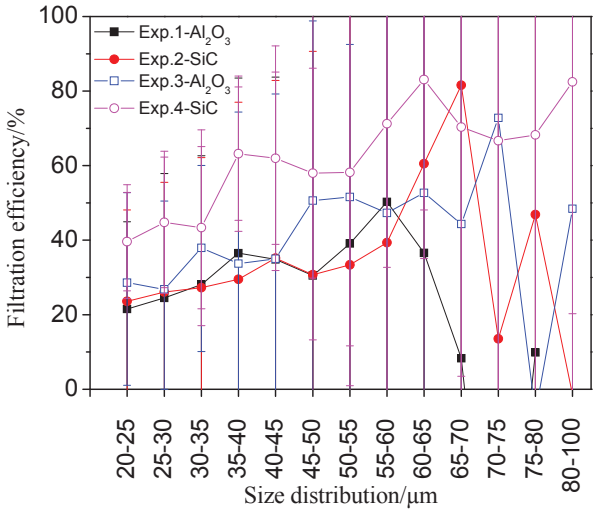

Figure C.1 The filtration efficiency vs. the inclusion size distribution with standard deviation